

REPORT DOCUMENTATION PAGE

Form Approved
OMB No. 0704-0188

The public reporting burden for this collection of information is estimated to average 1 hour per response, including the time for reviewing instructions, searching existing data sources, gathering and maintaining the data needed, and completing and reviewing the collection of information. Send comments regarding this burden estimate or any other aspect of this collection of information, including suggestions for reducing the burden, to Department of Defense, Washington Headquarters Services, Directorate for Information Operations and Reports (0704-0188), 1215 Jefferson Davis Highway, Suite 1204, Arlington, VA 22202-4302. Respondents should be aware that notwithstanding any other provision of law, no person shall be subject to any penalty for failing to comply with a collection of information if it does not display a currently valid OMB control number.

PLEASE DO NOT RETURN YOUR FORM TO THE ABOVE ADDRESS.

1. REPORT DATE (DD-MM-YYYY) 7/Dec/2001	2. REPORT TYPE THESIS	3. DATES COVERED (From - To)		
4. TITLE AND SUBTITLE AUTONOMOUS ORBITAL RENDEVOUS USING ANGLES-ONLY NAVIGATION		5a. CONTRACT NUMBER		
		5b. GRANT NUMBER		
		5c. PROGRAM ELEMENT NUMBER		
6. AUTHOR(S) 2D LT CHARI RAJA J		5d. PROJECT NUMBER		
		5e. TASK NUMBER		
		5f. WORK UNIT NUMBER		
7. PERFORMING ORGANIZATION NAME(S) AND ADDRESS(ES) MASSACHUSETTS INSTITUTE OF TECHNOLOGY			8. PERFORMING ORGANIZATION REPORT NUMBER CI01-308	
9. SPONSORING/MONITORING AGENCY NAME(S) AND ADDRESS(ES) THE DEPARTMENT OF THE AIR FORCE AFIT/CIA, BLDG 125 2950 P STREET WPAFB OH 45433			10. SPONSOR/MONITOR'S ACRONYM(S) 11. SPONSOR/MONITOR'S REPORT NUMBER(S)	
12. DISTRIBUTION/AVAILABILITY STATEMENT Unlimited distribution In Accordance With AFI 35-205/AFIT Sup 1		DISTRIBUTION STATEMENT A: Approved for Public Release - Distribution Unlimited		
13. SUPPLEMENTARY NOTES				
14. ABSTRACT				
20020204 077				
15. SUBJECT TERMS				
16. SECURITY CLASSIFICATION OF:		17. LIMITATION OF ABSTRACT	18. NUMBER OF PAGES 195	19a. NAME OF RESPONSIBLE PERSON
a. REPORT	b. ABSTRACT	c. THIS PAGE		19b. TELEPHONE NUMBER (Include area code)

AUTONOMOUS ORBITAL RENDEZVOUS USING ANGLES-ONLY NAVIGATION

by

Raja Jon Vurputoor Chari

B.S. Astronautical Engineering
United States Air Force Academy, 1999

B.S. Engineering Sciences
United States Air Force Academy, 1999

SUBMITTED TO THE DEPARTMENT OF AERONAUTICS AND ASTRONAUTICS IN
PARTIAL FULFILLMENT OF THE REQUIREMENTS FOR THE DEGREE OF
MASTER OF SCIENCE IN AERONAUTICS AND ASTRONAUTICS

at the

MASSACHUSETTS INSTITUTE OF TECHNOLOGY

June 2001

© 2001 Raja Jon Vurputoor Chari. All rights reserved.

The author hereby grants to MIT permission to reproduce and to distribute
publicly paper and electronic copies of this thesis document in whole or in part.

Signature of Author



Department of Aeronautics and Astronautics
May 11, 2001

Approved by



David K. Geller

Charles Stark Draper Laboratory, Inc.
Technical Supervisor

Certified by



John J. Deyst, Jr.

Professor of Aeronautics and Astronautics
Thesis Advisor

Accepted by

Wallace E. Vander Velde
Professor of Aeronautics and Astronautics
Chair, Committee on Graduate Studies

[This page intentionally left blank]

**THE VIEWS EXPRESSED IN THIS ARTICLE
ARE THOSE OF THE AUTHOR AND DO NOT
REFLECT THE OFFICIAL POLICY OR
POSITION OF THE UNITED STATES,
DEPARTMENT OF DEFENSE, OR THE U.S.
GOVERNMENT**

AUTONOMOUS ORBITAL RENDEZVOUS USING ANGLES-ONLY NAVIGATION

by

Raja Jon Vurputoor Chari

Submitted to the Department of Aeronautics and Astronautics
on May 11, 2001 in Partial Fulfillment of the Requirements for
the Degree of Master of Science in Aeronautics and Astronautics

Abstract

This study assesses navigation performance for rendezvous and close approach applications where on-board navigation must be accomplished through the use of angles-only measurements by developing various relative motion orbital trajectories. Chaser vehicle maneuvers designed to enhance the estimator's observability of the downrange distance to the target are considered. The target vehicle is assumed to be non-maneuvering and in a near-circular orbit. The modeled system includes representative scenarios from the Orbital Express mission.

Although a wide array of angle measurement sensors are available, their use in orbital rendezvous is generally limited by the fact that they are unable to provide direct target ranging information which leads to significant downrange error accumulation in the navigation filter. These navigation problems inherent to angles-only measurements in a natural motion environment are first qualitatively studied both analytically and through linear covariance modeling. It is shown that different target-chaser geometries lead to different navigation uncertainties in target downrange distance. The conclusions drawn from considering natural motion geometries are used to study candidate maneuver-assisted trajectories. The results from this study are used to select and combine the most promising maneuver-assisted trajectories for more in-depth consideration as potential scenarios for the Orbital Express mission. These selected trajectories are then analyzed in depth to determine the interdependency of range observability using angles-only navigation with angular sensor quality, inertial measurement accuracy, attitude determination accuracy, and trajectory design. Using the Orbital Express mission as a baseline, maneuver-assisted trajectories for angles-only navigation are tested with realistic error models to validate the rules of thumb created for improved angles-only navigation even in the presence of biases, misalignments, and degraded sensors. The results show that using well-chosen trajectories leads to navigation error uncertainties acceptable for rendezvous applications when only angular measurements are available.

Technical Supervisor: Dr. David K. Geller

Title: Senior Member of the Technical Staff, Charles Stark Draper Laboratory, Inc.

Thesis Advisor: John J. Deyst, Jr.

Title: Professor of Aeronautics and Astronautics

[This page intentionally left blank]

ACKNOWLEDGMENT

(May 11, 2001)

"If I have seen further it is by standing upon the shoulders of giants." – Isaac Newton

This thesis came about only through the time and help of a number of people and organizations. Thanks to the Charles Stark Draper Laboratory, the Air Force Institute of Technology, and the Massachusetts Institute of Technology for making this program possible.

I would like to thank all the staff at Draper Laboratory that I worked with over the last two years. First and foremost, thanks to Dr. David Geller, I couldn't have asked for a better supervisor. I'm not sure how I wound up being so lucky. He was a wonderful mentor and friend, and somehow managed to have the patience to put up with my near daily questions. Thanks for your tireless support, and the countless number of extra hours you spent at the lab helping to guide me along. Just to re-emphasize this point, I couldn't have had a better supervisor. I'm also grateful to Tim Brand for his suggestions and back-of-the-envelope ideas that helped to make this a better thesis. Thanks to Chris D'Souza, Lee Norris, and Peter Kachmar for getting me involved in the Mars Sample Return work, and for your encouraging help and wisdom throughout my time here. Thanks to George Schmidt and the education office for providing me with the opportunity to work at Draper, and thanks to Chris Stoll, Ron Proulx, and Paul Cefola who helped me get my feet wet upon first arriving at the lab.

My deepest thanks also go to the staff and incredible professors at MIT for giving me the knowledge and skills to accomplish this study. I especially thank Dr. John Deyst for his role as my advisor helping to keep me on course and providing critical insights throughout my research.

Thanks also to those who shared in my experiences as a Draper fellow. To my ex-officemate George Granholm, thanks for teaching me the ropes and providing late night study break entertainment. I also thank my new officemate, Ted Dyckman for putting up with my conversations and being a bottomless source of intriguing information. Thanks to my next-door cubicle buddies Paul Goulart, Jeremy Rea, and Andrew Grubler although I won't miss living in fear of nocturnal office pranks. Also, thanks to Rich Shertzer and Steve Clark for being my lunch-time comrades and fellow Wednesday uniform wearers.

Many thanks to my roommates, John "Moose" Fenwick, Pat "Bear" Widhelm, and Nicole "Lupus" Christoff for putting up with my dictator-like, although efficient, operation of the household. I know I wouldn't have had nearly as great of a time in Boston had it not been for you

guys. Have fun keeping up the reputation of 16 Clinton St., frequent the Phoenix Landing often in my honor, and go Red Sox (this is definitely their year).

Besides the people here in Boston, I would like to thank my family for always welcoming me home for much needed breaks and for their unconditional love and support. They have made me the person I am today. Happy 25th anniversary mom and dad, enjoy having the house to yourselves and Krishna, good luck beginning the college experience. Thanks also to the friends, faculty, and staff from St.Patrick's elementary school, Columbus high school, and the Air Force Academy who helped to mold me and continue to take an interest in my work today.

To my fiancée, Holly, thanks for being you and bringing out the best in me. Your love continues to inspire and motivate me. Thanks for sticking by me through thick and thin, and being a part of my daily life despite the physical distance between us. I look forward to spending the rest of my life with you.

Last, but surely not least, I thank God for blessing me with the people who surround me and endowing me with talents that allowed me to complete this work.

"Two roads diverged in a wood and I – I took the one less traveled by, and that has made all the difference." – Robert Frost

This thesis was prepared at The Charles Stark Draper Laboratory, Inc., under Internal Research and Development Project 13088, Rendezvous with Angles-Only Navigation.

Publication of this thesis does not constitute approval by Draper or the sponsoring agency of the findings or conclusions contained herein. It is published for the exchange and stimulation of ideas.



Raja J. Chari, 2 Lt., USAF

Table of Contents

1	INTRODUCTION.....	21
1.1	PROBLEM BACKGROUND AND MOTIVATION	21
1.2	THESIS OVERVIEW	22
1.3	ASSUMPTIONS	23
2	ANALYSIS TOOLS.....	25
2.1	KALMAN FILTER FORMULATION	25
2.1.1	<i>State and Covariance Propagation and Updating</i>	26
2.1.2	<i>Linearization.....</i>	29
	Dynamics	30
	Measurements.....	31
2.1.3	<i>Derivation of Measurement Sensitivity Matrix</i>	32
	Partials with Respect to Target and Chaser Position.....	35
	Partials with Respect to Velocity and Angular Measurement Biases	37
	Partials with Respect to Static Misalignment.....	38
	Partials with Respect to Inertial Attitude Error.....	39
2.2	LINEAR COVARIANCE ANALYSIS	41
2.2.1	<i>General Explanation and Setup</i>	41
2.2.2	<i>LINCOV Models.....</i>	46
	Un-modeled Accelerations	46
	System Biases and First Order Markov Processes	47
	Maneuver Measurement Errors	47
2.2.3	<i>Current Configuration</i>	48
3	NATURAL MOTION RANGE OBSERVABILITY	51
3.1	BACKGROUND.....	51
3.2	REFERENCE TRAJECTORY DEVELOPMENT.....	53
3.2.1	<i>Constraints.....</i>	53
3.2.2	<i>Shifted Altitude Metric</i>	55
3.2.3	<i>Station-keeping</i>	56
3.2.4	<i>Closure.....</i>	60
3.3	LINEAR COVARIANCE RESULTS	65
3.3.1	<i>Setup.....</i>	65
3.3.2	<i>Station-keeping</i>	66
	Co-circular Orbits	67
	Station-keeping Football.....	72
3.3.3	<i>Closure.....</i>	76
	Coelliptic Orbits	76
	V-bar Hop Trajectories	81
	Traveling Football Trajectories	83

3.4	ADDITIONAL ANALYSIS CONSIDERATIONS.....	86
3.4.1	<i>Error Ellipse Behavior</i>	86
Centered Station-keeping Football	88	
Offset Station-keeping Football	90	
Coelliptic	93	
3.4.2	<i>Measurement Availability</i>	96
3.4.3	<i>Noise Vs. Number of Measurements</i>	98
3.4.4	<i>Biases</i>	100
3.5	GENERAL CONCLUSIONS.....	104
3.5.1	<i>Effects of Measurement Noise</i>	106
3.5.2	<i>A Priori Effects on Benefits of Geometry</i>	108
4	MANEUVER-ASSISTED TRAJECTORY ANALYSIS	113
4.1	COMPARISON TO PREVIOUS WORK	113
4.2	REFERENCE TRAJECTORY DEVELOPMENT.....	114
4.2.1	<i>Station-keeping</i>	115
4.2.2	<i>Closure</i>	119
4.3	LINEAR COVARIANCE RESULTS	128
4.3.1	<i>Station-keeping</i>	129
4.3.2	<i>Closure</i>	137
V-bar Approaches.....	137	
R-bar Approaches.....	138	
Modified Coelliptics	139	
Modified Traveling Footballs	142	
Effects of Process Noise	144	
Results Summary.....	146	
4.4	GENERAL CONCLUSIONS AND HYBRID TRAJECTORY DEVELOPMENT	147
5	MISSION ANALYSIS.....	159
5.1	MISSION OVERVIEW.....	159
5.2	INCORPORATION OF MISSION SPECIFICATIONS.....	161
5.3	DESIGN OF MISSION TRAJECTORIES	164
5.3.1	<i>Closure</i>	165
5.3.2	<i>Station-keeping</i>	170
5.4	RESULTS	172
5.4.1	<i>End-to-End Testing</i>	182
Dispersions Due to Velocity Uncertainty	185	
Geo-Synchronous Test Case.....	187	
6	CONCLUSIONS	189
6.1	SUMMARY OF RESULTS	189
6.1.1	<i>Natural Motion Navigation</i>	189

6.1.2	<i>Maneuver-Assisted Navigation</i>	190
6.1.3	<i>Orbital Express Mission Analysis</i>	190
6.2	FUTURE WORK.....	190
6.2.1	<i>Dispersion Analysis</i>	191
6.2.2	<i>Monte Carlo Analysis</i>	191
6.2.3	<i>Formulation of problem in relative frame</i>	191
6.2.4	<i>Observability Calculation</i>	192
7	REFERENCES.....	193

[This page intentionally left blank]

List of Figures

Figure 2-1: State and covariance propagation and updating	27
Figure 2-2: Filtering equations flow diagram	29
Figure 2-3: Angular measurements from chaser to target.....	32
Figure 2-4: Filter design using LINCov analysis	45
Figure 3-1: Uncertainty with angular measurements and no relative geometry	52
Figure 3-2: Uncertainty with angular measurements and use of relative geometry.....	52
Figure 3-3: Target-centered LVLH coordinate frame.....	54
Figure 3-4: Shifted altitude method	55
Figure 3-5: Co-circular station-keeping 10km away with 10km of cross-track motion	57
Figure 3-6: Football station-keeping 100m away, 10m vertical motion with 10m of cross-track motion	58
Figure 3-7: Football station-keeping centered on target, 1km vertical motion	59
Figure 3-8: Coelliptic with 10km Δh	61
Figure 3-9: V-bar hops with 1km Δh	62
Figure 3-10: Traveling football with 10m Δh and 100m of vertical motion with 10m of cross-track motion	63
Figure 3-11: Inertial and relative RSS uncertainty for Co-circular station-keeping 1km away....	67
Figure 3-12: Relative position uncertainty for Co-circular station-keeping 1km away	68
Figure 3-13: Relative position uncertainty for Co-circular station-keeping 1km away with 87m cross-track motion.....	69
Figure 3-14: Relative position uncertainty over 4 days for Co-circular station-keeping 1km away with 87m cross-track motion.....	70
Figure 3-15: Relative position uncertainty for Co-circular station-keeping 1km away with 268m cross-track motion.....	71

Figure 3-16: Relative position uncertainty for Co-circular station-keeping 1km away with 1km cross-track motion.....	71
Figure 3-17: Station-keeping football relative motion schematic	72
Figure 3-18: Relative position uncertainty for Football station-keeping 100m away with 10m vertical motion	73
Figure 3-19: Relative position uncertainty for Football station-keeping 300km away with 100km vertical motion and 100km cross-track motion.....	74
Figure 3-20: Relative position uncertainty for Football station-keeping centered on target with 1km vertical motion	75
Figure 3-21: Relative position uncertainty for Football station-keeping centered on target with 1km vertical motion and 1km cross-track motion.....	76
Figure 3-22: Coelliptic relative motion schematic	77
Figure 3-23:Actual relative position & velocity uncertainty values for Coelliptic with 100m Δh	78
Figure 3-24: Relative position uncertainty for Coelliptic with 100m Δh	79
Figure 3-25: Relative position uncertainty for Coelliptic with 1km Δh and 1km cross-track motion	80
Figure 3-26: Relative position uncertainty for Coelliptic with 1km Δh	80
Figure 3-27: V-bar hop relative motion schematic	81
Figure 3-28: Relative position uncertainty for V-bar hops with 1km Δh and 1km cross-track motion	82
Figure 3-29: Relative position uncertainty for V-bar hops with 1km Δh	82
Figure 3-30: Traveling football relative motion schematic.....	83
Figure 3-31: Relative position uncertainty for Traveling football with 10m Δh and 100m vertical motion	84
Figure 3-32: Relative position uncertainty for Traveling football with 10m Δh and 100m vertical motion with 10m cross-track motion	85
Figure 3-33: Relative position uncertainty for Traveling football with 10m Δh and 100m vertical motion with 100m cross-track motion	85

Figure 3-34: Two dimensional error ellipse dimensions.....	87
Figure 3-35: Incorrect expected error ellipse behavior for Centered station-keeping football	88
Figure 3-36: Expected error ellipse behavior for Centered station-keeping football.....	89
Figure 3-37: Correlation coefficient time history for Centered station-keeping football	90
Figure 3-38: Error ellipse behavior for Centered station-keeping football	90
Figure 3-39: Expected error ellipse behavior for Offset station-keeping football	91
Figure 3-40: Correlation coefficient time history for Offset station-keeping football.....	92
Figure 3-41: Error ellipse behavior for Offset station-keeping football.....	92
Figure 3-42: Expected error ellipse behavior for Coelliptic.....	93
Figure 3-43: Correlation coefficient time history for Coelliptic	94
Figure 3-44: Error ellipse behavior for Coelliptic.....	94
Figure 3-45: Identical line-of-sight history for different coelliptic orbits.....	95
Figure 3-46: Relative position uncertainty for Coelliptic with 100m Δh and increased <i>a priori</i> uncertainty.....	96
Figure 3-47: Measurements available only in sunlight – Actual relative position and velocity uncertainty values for Traveling football with 100m Δh and 1km vertical motion with 1km cross-track motion.....	97
Figure 3-48: Measurements always available – Actual relative position and velocity uncertainty values for Traveling football with 100m Δh and 1km vertical motion with 1km cross-track motion	98
Figure 3-49: Actual relative position and velocity uncertainty values for V-bar hops with 1km Δh	99
Figure 3-50: Increased noise and measurement frequency – Actual relative position and velocity uncertainty values for V-bar hops with 1km Δh	100
Figure 3-51: Actual relative position and velocity uncertainty values for Football station-keeping 100m away with 10m vertical motion – With one bias.....	101
Figure 3-52: Actual relative position and velocity uncertainty values for Football station-keeping 100m away with 10m vertical motion – With both biases	102

Figure 3-53: Actual relative position and velocity uncertainty values for Football station-keeping 100m away with 10m vertical motion – Without biases	102
Figure 3-54: Filter bias value uncertainty for one bias - Football station-keeping 100m away with 10m vertical motion	103
Figure 3-55: Filter bias value uncertainty for both biases - Football station-keeping 100m away with 10m vertical motion	104
Figure 3-56: Cone of equivalent relative motion geometries.....	105
Figure 3-57: Relative position and velocity uncertainty for Co-circular station-keeping 1km away with 1km cross-track, 1°/axis 3σ angular measurement noise.....	106
Figure 3-58: Relative position and velocity uncertainty for Co-circular station-keeping 1km away with 1km cross-track motion, 5°/axis 3σ angular measurement noise.....	107
Figure 3-59: Relative position and velocity uncertainty for Co-circular station-keeping 1km away with 1km cross-track motion, 0.1°/axis 3σ angular measurement noise.....	107
Figure 3-60: Relative position and velocity uncertainty for Co-circular station-keeping 1km away with 87m cross-track motion, normal <i>a priori</i> uncertainty	108
Figure 3-61: Relative position and velocity uncertainty for Co-circular station-keeping 1km away with 87m cross-track motion, increased <i>a priori</i> uncertainty	109
Figure 3-62: Relative position and velocity uncertainty over 4 days for Co-circular station-keeping 1km away with 87m cross-track motion, increased <i>a priori</i> uncertainty	110
Figure 3-63: Relative position and velocity uncertainty for Co-circular station-keeping 1km away with 268m cross-track motion, normal <i>a priori</i> uncertainty	111
Figure 3-64: Relative position and velocity uncertainty for Co-circular station-keeping 1km away with 268m cross-track motion, increased <i>a priori</i> uncertainty	111
Figure 4-1: Football station-keeping 10m away with 1m vertical motion, 2.5 orbits of 1m cross-track motion starting at 5 hours, $\Delta V=2\text{mm/s}$	116
Figure 4-2: Co-circular station-keeping 100m away, 2.5 orbits of 1m cross-track motion starting at 5 hours, $\Delta V=2\text{mm/s}$	117
Figure 4-3: Football station-keeping centered on target with 100m vertical motion, 10m observation maneuvers every hour starting at 5 hours, $\Delta V=0.3\text{m/s}$	118

Figure 4-4: V-bar approach from 360m at 1cm/sec with damped cross-track oscillations, ΔV=1.59m/s	120
Figure 4-5: R-bar approach from 360m at 1cm/sec with multiple observation maneuvers, ΔV=27.1m/s	122
Figure 4-6:ΔV required for R-bar approaches with varying closing rates & initial separations..	123
Figure 4-7: Coelliptic with 100m Δh and damped cross-track oscillations symmetric with respect to flyby point from 2-8 hours, ΔV=8.85m/s.....	124
Figure 4-8: Traveling football with fixed 10m Δh and shrinking vertical oscillations with damped cross-track oscillations, ΔV=1.85m/s.....	125
Figure 4-9: Traveling football with shrinking Δh and shrinking vertical oscillations, ΔV=0.055m/s	126
Figure 4-10: Traveling football/spiral with shrinking Δh and shrinking vertical oscillations with multiple observation maneuvers, ΔV=1.55m/s	127
Figure 4-11: Relative position uncertainty for Football station-keeping centered on target with 100m vertical motion and 2.5 orbits of 10m cross-track motion starting at 5 hours, ΔV=0.02m/s	130
Figure 4-12: Relative position uncertainty for Co-circular station-keeping 100m away with 2.5 orbits of 1m cross-track motion starting at 5 hours, ΔV=2mm/s	131
Figure 4-13: Relative position uncertainty for Co-circular station-keeping 100m away with 2.5 orbits of 10m cross-track motion starting at 5 hours, ΔV=.02m/s	131
Figure 4-14: Relative position uncertainty for Co-circular station-keeping 100m away with 2.5 orbits of 100m cross-track motion starting at 5 hours, ΔV=.2m/s	132
Figure 4-15: Relative position uncertainty for Football station-keeping 10m away with 1m vertical motion and 2.5 orbits of 10m cross-track motion starting at 5 hours, ΔV=0.02m/s	133
Figure 4-16: Relative position uncertainty for Football station-keeping 10m away with 1m vertical motion and 10m observation maneuvers starting at 5 hours, ΔV=0.32m/s.....	133
Figure 4-17: Relative position uncertainty with process noise for Co-circular station-keeping 100m away with 2.5 orbits of 100m cross-track motion starting at 5 hours, ΔV=0.22m/s..	134

Figure 4-18: Relative position uncertainty with process noise for Co-circular station-keeping 100m away with 100m observation maneuvers every hour starting at 5 hours, $\Delta V=3.2\text{m/s}$	135
Figure 4-19: Maneuver-assisted station-keeping trajectory LINCOV results summary.....	137
Figure 4-20: Relative position uncertainty for V-bar approach from 360m at 1cm/sec with 2 orbits of 100m cross-track motion starting at 5 hours, $\Delta V=1.03\text{m/s}$	138
Figure 4-21: Relative position uncertainty for R-bar approach from 360m at 1cm/sec, $\Delta V=24.4\text{m/s}$	139
Figure 4-22: Relative position uncertainties for Coelliptic with 100m Δh case with no cross-track motion overlaid on case with damped cross-track oscillations symmetric with respect to flyby point, $\Delta V=9.63\text{m/s}$	140
Figure 4-23: Relative position uncertainty for Coelliptic with 100m Δh case with damped cross- track oscillations symmetric with respect to flyby point, $\Delta V=9.63\text{m/s}$	141
Figure 4-24: Relative position uncertainty for Coelliptic with 1km Δh case with damped cross- track oscillations symmetric with respect to flyby point, $\Delta V=96.3\text{m/s}$	141
Figure 4-25: Relative position uncertainty for Traveling football, unmodified, with 10m Δh and 100m vertical oscillations, $\Delta V=0\text{m/s}$	142
Figure 4-26: Relative position uncertainty for Traveling football with shrinking Δh and shrinking vertical oscillations, $\Delta V=0.055\text{m/s}$	143
Figure 4-27: Relative position uncertainty for Traveling football/spiral with shrinking Δh and shrinking vertical oscillations with multiple observation maneuvers, $\Delta V=1.55\text{m/s}$	144
Figure 4-28: Relative position uncertainty with process noise for Coelliptic with 100m Δh and damped cross-track oscillations symmetric with respect to flyby point from 2-8 hours, $\Delta V=8.85\text{m/s}$	145
Figure 4-29: Relative position uncertainty with process noise for Coelliptic with 100m Δh and multiple observation maneuvers, $\Delta V=50.72\text{m/s}$	145
Figure 4-30: Maneuver-assisted closure trajectory LINCOV results summary	147
Figure 4-31: Hybrid trajectory 1– Co-circular station-keeping to coelliptic to final approach....	149

Figure 4-32: Hybrid trajectory 1 – R-bar final approach, $\Delta V=3\text{m/s}$	150
Figure 4-33: Hybrid trajectory 1 – Relative position uncertainty for R-bar final approach, $\Delta V=3\text{m/s}$	150
Figure 4-34: Hybrid trajectory 1 – V-bar final approach, $\Delta V=2.97\text{m/s}$	151
Figure 4-35: Hybrid trajectory 1 – Relative position uncertainty for V-bar final approach to 17m, $\Delta V=2.97\text{m/s}$	151
Figure 4-36: Hybrid trajectory 2– Spiral to final approach.....	152
Figure 4-37: Hybrid trajectory 2 – R-bar final approach, $\Delta V=1.12\text{m/s}$	153
Figure 4-38: Hybrid trajectory 2 – Relative position uncertainty for R-bar final approach to 8m, $\Delta V=1.12\text{m/s}$	153
Figure 4-39: Hybrid trajectory 2 – V-bar final approach, $\Delta V=1.01\text{m/s}$	154
Figure 4-40: Hybrid trajectory 2 – Relative position uncertainty for V-bar final approach to 32m, $\Delta V=1.01\text{m/s}$	154
Figure 4-41: Hybrid trajectory 3– Centered football station-keeping to final approach.....	155
Figure 4-42: Hybrid trajectory 3 – R-bar final approach, $\Delta V=0.81\text{m/s}$	156
Figure 4-43: Hybrid trajectory 3 – Relative position uncertainty for R-bar final approach, $\Delta V=0.81\text{m/s}$	156
Figure 4-44: Hybrid trajectory 3 – V-bar final approach, $\Delta V=0.85\text{m/s}$	157
Figure 4-45: Hybrid trajectory 3 – Relative position uncertainty for V-bar final approach to 8m, $\Delta V=0.85\text{m/s}$	157
Figure 5-1: Orbital Express system elements.....	160
Figure 5-2: Orbital Express mission endpoints.....	161
Figure 5-3: Orbital Express trajectory option 1 schematic.....	166
Figure 5-4: Orbital Express trajectory option 2 schematic.....	167
Figure 5-5: Orbital Express trajectory option 3 schematic.....	168
Figure 5-6: Orbital Express trajectory option 4 schematic.....	169
Figure 5-7: Orbital Express station-keeping trajectory schematics.....	171

Figure 5-8: Orbital Express trajectory testing results legend.....	174
Figure 5-9: Results for closure trajectories with quiet chaser vehicle using nominal error cases and stress cases.....	178
Figure 5-10: Results for closure trajectories with noisy chaser vehicle using nominal error cases and stress cases.....	179
Figure 5-11: Results for station-keeping trajectories with quiet chaser vehicle using nominal error cases and stress cases	180
Figure 5-12: Results for station-keeping trajectories with noisy chaser vehicle using nominal error cases and stress cases	181
Figure 5-13: Orbital Express end-to-end trajectory schematic	183
Figure 5-14: End-to-end trajectory results for quiet chaser with all errors at nominal values and varying measurement availability conditions.....	184
Figure 5-15: Relative position dispersions resulting from velocity uncertainty at maneuver execution times for Orbital Express end-to-end trajectory	186
Figure 5-16: Geo-synchronous end-to-end trajectory results for quiet chaser with all errors at nominal values and constant measurement availability	188

List of Tables

Table 3-1: Natural motion station-keeping reference trajectories	60
Table 3-2: Natural motion closure reference trajectories.....	64
Table 4-1: Maneuver-assisted station-keeping reference trajectories	119
Table 4-2: Maneuver-assisted closure reference trajectories	128
Table 4-3: Maneuver-assisted station-keeping trajectory LINCOV results summary	136
Table 4-4: Maneuver-assisted closure trajectory LINCOV results summary	146
Table 5-1: Summary of results for Orbital Express trajectories with quiet chaser vehicle.....	175
Table 5-2: Summary of results for Orbital Express trajectories with noisy chaser vehicle	176

[This page intentionally left blank]

1 INTRODUCTION

The purpose of this study is to make a qualitative and quantitative assessment of angles-only navigation performance for orbital rendezvous and close approach applications through the development and description of relative motion trajectories. This opening chapter addresses the background of the problem and the motivation for an angles-only approach. The following sections will present the major assumptions of the study and an overview of the remaining chapters.

1.1 PROBLEM BACKGROUND AND MOTIVATION

Although orbital rendezvous has been a well-studied problem since the Gemini era, it has generally taken place with the benefit of a man-in-the-loop. A new generation of planned missions such as the NASA Mars Sample Return Mission, ASTRO Orbital Express Project, and the Air Force's XSS-11 are driving a demand for the ability to autonomously capture, inspect, or dock with on-orbit objects. Effective space rendezvous requires a navigation system to measure the relative position between the chaser and target vehicle. Measurement techniques used in the past include relative GPS (which requires a high degree of cooperation from the target spacecraft) or radar and lidar systems that can place significant power and weight requirements on the chaser. Additionally, the use of active sensing techniques is a non-stealthy approach in the case of a non-cooperative target.

In light of these drawbacks, angles-only relative navigation is an attractive alternative if adequate accuracy in all components of relative position can be achieved. Many simple sensors are capable of providing line-of-sight direction, such as optical or infrared cameras and trackers. Another attractive alternative is a radio direction finder, which only requires a simple radio frequency (RF) tone generator on the target. This technique, which has the potential to work at very long ranges as well as short distances, uses multiple antennas on the chaser to measure the direction to the target using interferometry. Although these sensors all provide line-of-sight information, the use of angles-only measurements creates inherent problems in the ability of the navigation system to determine the range to the target.

This thesis first seeks to study relative motion orbital trajectories that make the use of angles-only navigation feasible. In addition to trajectory design, though, there are a number of other factors that potentially affect the ability of a navigation system to accurately determine range along the line-of-sight including inertial measurement unit (IMU) accuracy, attitude determination accuracy, and the accuracy of the angular measurements themselves. Thus, as a secondary objective, the degrading effects of these error sources is examined using several selected trajectory designs and realistic error models based on the Orbital Express mission.

1.2 THESIS OVERVIEW

The ability to determine the distance along the line-of-sight is enhanced by a combination of two techniques. First, the relative motion trajectory between the chaser and target is designed to create changes in the line-of-sight, thereby enhancing the observability of all relative position components. Second, the chaser executes maneuvers which are designed to further enhance the observability of the position component along the line-of-sight.

Chapter 2 presents the linear covariance analysis tool used for this study and briefly covers the basic navigation filtering equations. Chapter 3 qualitatively examines the navigation problems inherent to angles-only measurements in natural motion orbital trajectories. A wide range of natural motion trajectories are considered across different operating ranges from meters to hundreds of kilometers. The well-known problem of unbounded downrange uncertainty growth in the navigation filter due to a lack of range observability when using only angular measurements is demonstrated. It is shown that changes in target-chaser relative geometry can decrease the navigation uncertainty of the target's downrange distance. A study of the evolution of the navigation uncertainties as functions of time shows their dependence on the line-of-sight motion associated with natural orbital mechanics, and motivates the use of maneuvers to sever this dependence. Additional factors such as measurement availability, measurement noise levels, *a priori* uncertainty values based on delivery conditions, and system biases are examined with regard to their interdependence and influence on the angles-only navigation problem.

Chapter 4 makes use of the conclusions drawn from considering natural motion trajectories to develop candidate maneuver-assisted trajectories. The maneuvers that create these trajectories are shown, and the trajectories themselves are briefly compared with results from dual-control literature. Based on performance analysis and a brief consideration of the effects of un-modeled accelerations, the most promising trajectories are selected for more in-depth consideration. Also,

several hybrid trajectories are designed that combine the best characteristics of various approaches and create the basis for eventual mission testing.

Chapter 5 develops and tests several maneuver-assisted trajectories designed for the Orbital Express mission environment. The analysis takes the chaser from its anticipated initial conditions through final approach using realistic specifications for sensor models. These selected trajectories are then explored to better understand and quantify the sensitivity of the navigation filter solution to different maneuver-assisted trajectories and un-modeled accelerations, as well as to IMU, attitude determination, and angular measurement errors. The results show that using well-chosen maneuver-assisted trajectories leads to navigation error uncertainties acceptable for rendezvous applications even when only angular measurements are available.

Chapter 6 presents conclusions drawn from the overall study and discusses potential topics for future work.

1.3 ASSUMPTIONS

For this study, it is assumed that the target and chaser vehicles are in nearly circular orbits since the vast majority of current potential rendezvous missions involve circular or near-circular orbits. Specifically, the author's work on the Mars Sample Return Mission and ASTRO Orbital Express Mission involved maximum eccentricity values of 0.04. Similarly, the current analysis considers only Low-Earth orbits (LEO) although the conclusions should easily extend to higher altitude orbits just as easily as they would extend to modestly elliptical orbits. The planetary constants for earth come from [16] although once again the extension of the results to other planetary central bodies would have no adverse effects.

The other major assumption is that higher order gravity terms, including J2, are not considered in the current analysis. The differential effects of such terms on target and chaser vehicles in close proximity are generally negligible. When this is not the case, the higher order terms should improve the results since they will introduce additional motion into the relative motion trajectory. There are a number of additional assumptions throughout this work that will be mentioned as they are made and used.

[This page intentionally left blank]

2 ANALYSIS TOOLS

This chapter covers the development of the tools that will be employed for analysis of the angles-only navigation problem. First, a general review of the equations governing Kalman filtering is presented, and then the topic is expanded to briefly explain the principles behind linear covariance (LINCov) analysis. Finally, some of the more specific implementation issues as they pertain to this problem are addressed.

2.1 KALMAN FILTER FORMULATION

The concept of Kalman filtering was first put forward by R.E. Kalman in 1960. The idea is to create a recursive algorithm that is capable of processing measurements that are corrupted by errors. Ideally, one would like to know the exact values of state variables over time. However, in practice this is usually not possible, so the next best option is to estimate these values in a least squares optimal fashion. The Kalman filter equations provide a methodology to do exactly that in the case of linear systems.

Kalman filtering caught on quickly as it had immediate applications to guidance and navigation problems, specifically within the Apollo space program. Since then, the original algorithm, along with many variations, has been applied to numerous situations where it is desirable to know the state of a dynamic system in the presence of uncertainties. Although there are many sources available detailing the development of the Kalman Filter equations and their use (see [11][13][14][17][21]), this section will be a short review of the development of the equations in their general form as presented by Vander Velde [29].

One of the most common ways to approaching a filtering application is by thinking of the process in terms of the evolution of a continuous time system augmented by discrete time measurements. For the case of a linear system driven by zero-mean white Gaussian noise the state equation can be written

$$\dot{\bar{x}} = \mathbf{A}(t)\bar{x} + \mathbf{B}(t)\bar{n} \quad (2.1)$$

where \bar{x} is the state vector, $\mathbf{A}(t)$ is the state dynamics matrix, $\mathbf{B}(t)$ is the noise dynamics matrix, and \bar{n} is the noise with zero-mean and strength \mathbf{N} , or alternatively:

$$\begin{aligned} E[\bar{n}(t)] &= 0 \\ E[\bar{n}(t)\bar{n}(\tau)^T] &= \mathbf{N}\delta(t-\tau) \end{aligned} \quad (2.2)$$

where $E[]$ is the expectation operator and δ is the Dirac delta function. The measurements occur at discrete intervals in the form

$$\bar{z}_k = \mathbf{H}_k \bar{x}(t_k) + \bar{v}_k \quad (2.3)$$

where \mathbf{H}_k is the measurement sensitivity matrix at time k and \bar{v}_k is an unbiased, finite variance random variable with

$$\begin{aligned} E[\bar{v}_k] &= 0 \\ E[\bar{v}_k \bar{v}_k^T] &= \mathbf{R}_k \end{aligned} \quad (2.4)$$

In the presence of uncertainty, the actual value \bar{x} is not known so an estimate $\hat{\bar{x}}$ is formed with the error defined as:

$$\bar{e} = \bar{x} - \hat{\bar{x}} \quad (2.5)$$

Further the state covariance matrix is defined as:

$$\mathbf{P} = E[\bar{e}\bar{e}^T] \quad (2.6)$$

These definitions will be the basis for the filtering equations.

2.1.1 State and Covariance Propagation and Updating

It is useful to think of the filtering process as shown in Figure 2-1. A process is evolving over time and at discrete points in time (t_{k-1}, t_k) measurements are available which provide information about the state. The state estimate and covariance are propagated in time from t_{k-1} to t_k and the instant before the measurement they have values $\hat{\bar{x}}_k^-$ and \mathbf{P}_k^- respectively. After the measurement at t_k is incorporated, improved estimates $\hat{\bar{x}}_k^+$ and \mathbf{P}_k^+ are formed.

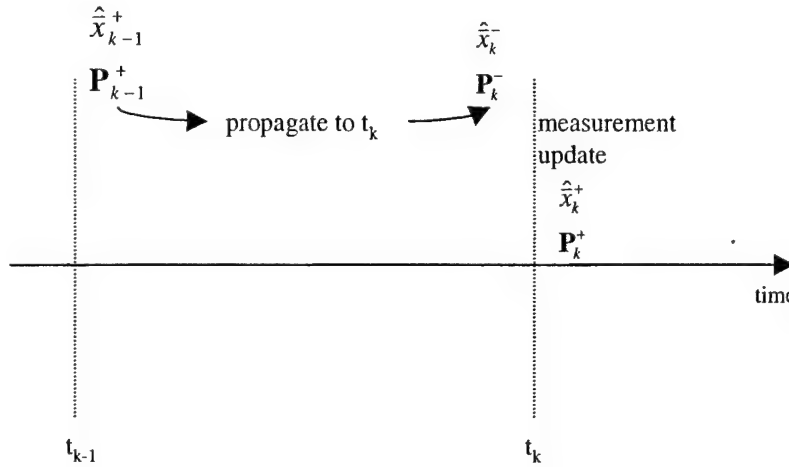


Figure 2-1: State and covariance propagation and updating

For the continuous time case we can define the propagation equations for the state and state covariance as:

$$\begin{aligned}\dot{\hat{x}} &= \mathbf{A}\hat{x} \\ \dot{\mathbf{P}} &= \mathbf{A}\mathbf{P} + \mathbf{P}\mathbf{A}^T + \mathbf{B}\mathbf{N}\mathbf{B}^T\end{aligned}\tag{2.7}$$

where the time dependence notation has been dropped for simplicity.

However, from an implementation standpoint, since it is usually more convenient to propagate these variables to discrete times, specifically times where measurements are available, an alternate formulation is useful. Defining the evolution of the true state in discrete time as:

$$\bar{x}_{k+1} = \Phi_k \bar{x}_k + \bar{w}_k\tag{2.8}$$

with Φ being the state transition matrix satisfying the differential equation

$$\dot{\Phi}(t, \tau) = \mathbf{A}\Phi(t, \tau) \quad \text{with} \quad \Phi(t_{k-1}, t_{k-1}) = \mathbf{I}\tag{2.9}$$

and \bar{w}_k being a zero-mean discrete white noise process with covariance \mathbf{Q} or

$$\begin{aligned}\bar{w}_k &= \int_{t_k}^{t_{k+1}} \Phi(t_{k+1}, \tau) \mathbf{B}(\tau) \mathbf{N}(\tau) d\tau \\ E[\bar{w}_k \bar{w}_i^T] &= \begin{cases} \mathbf{Q}_k & i = k \\ 0 & i \neq k \end{cases}\end{aligned}\tag{2.10}$$

The state and covariance propagation equations become

$$\begin{aligned}\hat{\bar{x}}_{k+1}^- &= \Phi_k \hat{\bar{x}}_k^+ \\ \mathbf{P}_{k+1}^- &= \Phi_k \mathbf{P}_k^+ \Phi_k^T + \mathbf{Q}_k\end{aligned}\quad (2.11)$$

where

$$\mathbf{Q}_k = E \left[\vec{w}_k \vec{w}_k^T \right] = \int_{t_k}^{t_{k+1}} \Phi(t_{k+1}, \tau) \mathbf{B}(\tau) \mathbf{N}(\tau) \mathbf{B}(\tau)^T \Phi(t_{k+1}, \tau)^T d\tau \quad (2.12)$$

With equation (2.11) providing a method to propagate the state estimate and state covariance, the other half of the problem is to incorporate new measurements in order to improve the state estimate. After a measurement is taken according to equation (2.3), the best estimate will be a combination of the existing estimate and the new information or:

$$\hat{\bar{x}}_k^+ = \hat{\bar{x}}_k^- + \mathbf{K}_k (\bar{z}_k - \mathbf{H}_k \hat{\bar{x}}_k^-) \quad (2.13)$$

where \mathbf{K}_k is, at this point, an undefined gain. Combining equations (2.13) with (2.5) and (2.6) the state covariance update equation becomes:

$$\mathbf{P}_k^+ = (\mathbf{I} - \mathbf{K}_k \mathbf{H}_k) \mathbf{P}_k^- (\mathbf{I} - \mathbf{K}_k \mathbf{H}_k)^T + \mathbf{K}_k \mathbf{R}_k \mathbf{K}_k^T \quad (2.14)$$

The optimum estimate is defined to be the one which minimizes the trace of the covariance matrix. Assigning this desire a cost function $J = \text{tr}(\mathbf{P})$ the optimum gain \mathbf{K}_k will be such that

$\frac{\partial J}{\partial \mathbf{K}_k} = 0$ where tr is the trace operator. The resulting optimum gain is termed the Kalman gain

and is written:

$$\mathbf{K}_k = \mathbf{P}_k^- \mathbf{H}_k^T \left(\mathbf{H}_k \mathbf{P}_k^- \mathbf{H}_k^T + \mathbf{R}_k \right)^{-1} \quad (2.15)$$

Equations (2.11) and (2.13)-(2.15) are typically called the filtering equations and are shown in schematic form in Figure 2-2.

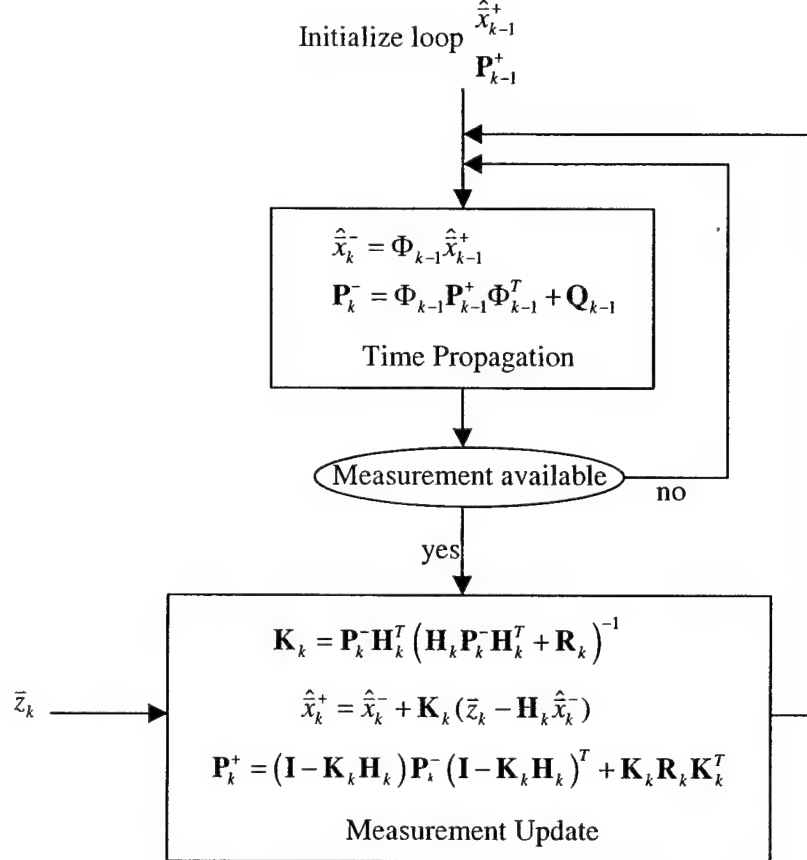


Figure 2-2: Filtering equations flow diagram

2.1.2 Linearization

Although the Kalman filter was originally devised for linear systems, it has seen extensive use in non-linear situations. Modifications to its basic form are utilized in order to apply the same methodology to a non-linear problem. As explained in [11] one of two methods is generally used. The first possibility is the development of an *extended* Kalman filter where the reference trajectory is updated with the filter estimate forming a closed loop system. The second option, and the one used in this work, is the linearized Kalman filter. In this case, a nominal state trajectory is chosen independent of the measurements and filter estimates, and then the actual trajectory is linearized about the nominal one. In addition, the angle measurements are non-linear functions of the state variables and therefore must be linearized about the same nominal trajectory.

Dynamics

The first step is to handle the non-linear dynamics of the problem. The linearization process proceeds as follows. The actual state trajectory, \bar{x} , is represented as the nominal value, \bar{x}^* , plus some corrective term, $\delta\bar{x}$ as in:

$$\bar{x} = \bar{x}^* + \delta\bar{x} \quad (2.16)$$

If the dynamics are non-linear then equation (2.1) becomes

$$\dot{\bar{x}} = f(\bar{x}) + \bar{n} \quad (2.17)$$

where f is a non-linear operator. Substituting equation (2.16) this is equivalent to

$$\dot{\bar{x}}^* + \delta\dot{\bar{x}} = f(\bar{x}^* + \delta\bar{x}) + \bar{n} \quad (2.18)$$

This non-linear equation can be linearized about the reference trajectory so that

$$\begin{aligned} \delta\dot{\bar{x}} &= \mathbf{A}\delta\bar{x} + \bar{n} \\ \text{where } \mathbf{A} &= \left. \frac{\partial f}{\partial \bar{x}} \right|_{\bar{x}}. \end{aligned} \quad (2.19)$$

In discrete time, the state transition matrix is

$$\delta\bar{x}_{k+1} = \phi(t_{k+1}, t_k)\delta\bar{x}_k \quad (2.20)$$

must satisfy the same conditions as in equation (2.9) and can then be approximated by a 4th order Taylor series expansion as

$$\phi(t_{k+1}, t_k) = e^{\mathbf{A}\Delta T} \approx \mathbf{I} + \mathbf{A}\Delta T + \mathbf{A}^2 \frac{\Delta T^2}{2!} + \mathbf{A}^3 \frac{\Delta T^3}{3!} + \mathbf{A}^4 \frac{\Delta T^4}{4!} \quad (2.21)$$

As shown in [14], the fourth order approximation introduces virtually zero error for time steps up to sixty seconds over the course of one orbit.

For orbital motion, the non-linear dynamics represented by f can be simply written in terms of position, velocity, and acceleration as

$$\begin{aligned} \dot{\bar{R}} &= \bar{V} \\ \dot{\bar{V}} &= \bar{a}_{grav}(\bar{R}) = \frac{-\mu\bar{R}}{|\bar{R}|^3} \end{aligned} \quad (2.22)$$

Recall that for this study, J2 effects are not being considered so the acceleration is simply inversely proportional to $|\bar{R}|^2$ and proportional to the gravitational parameter, μ . A point-mass gravity model is acceptable since the higher order terms have a negligible effect on the relative motion. However, this formulation can be readily extended for a higher order gravity model if desired. Combining equation (2.22) into one state, \bar{x} , gives a form identical to equation (2.20) where the state transition matrix is calculated according to equation (2.21) and

$$\mathbf{A} = \begin{bmatrix} 0 & I \\ \frac{\partial(\bar{a}_{grav})}{\partial \bar{R}} & 0 \end{bmatrix}_{\bar{x}}. \quad (2.23)$$

This transition matrix in equation (2.21) is used to propagate the state and its covariance. Although the results are nearly identical, the interested reader is directed to [14] for the more detailed formulation that is used in the actual program implementation.

Measurements

Since the measurements are also non-linear functions of the state variables, equation (2.3) becomes:

$$\bar{z} = \mathbf{h}(\bar{x}^* + \delta\bar{x}) + \bar{v} \quad (2.24)$$

where \mathbf{h} is a non-linear transformation between the state and measurement and \bar{v} is the measurement noise as before. The time dependence has been omitted for notational ease. If a first order Taylor expansion is performed about \bar{x}^* then the measurement can be expressed as [11]:

$$\bar{z} = \mathbf{h}(\bar{x}^*) + \left. \frac{\partial \mathbf{h}}{\partial \bar{x}} \right|_{\bar{x}=\bar{x}^*} \delta\bar{x} + \text{higher order terms} + \bar{v} \quad (2.25)$$

where

$$\frac{\partial \mathbf{h}}{\partial \bar{x}} = \begin{bmatrix} \frac{\partial h_1}{\partial x_1} & \frac{\partial h_1}{\partial x_2} & \dots & \frac{\partial h_1}{\partial x_n} \\ \frac{\partial h_2}{\partial x_1} & \dots & \dots & \frac{\partial h_2}{\partial x_n} \\ \dots & \dots & \dots & \dots \\ \frac{\partial h_m}{\partial x_1} & \dots & \dots & \frac{\partial h_m}{\partial x_n} \end{bmatrix} \quad (2.26)$$

and the \mathbf{H} matrix is then found by evaluating equation (2.26) along the nominal trajectory, $\bar{x}^*(t)$, or

$$\mathbf{H} = \left. \frac{\partial \mathbf{h}}{\partial \bar{x}} \right|_{\bar{x}^*} \quad (2.27)$$

The evaluation of equation (2.27) is not a simple task so section 2.1.3 will deal with this topic extensively.

2.1.3 Derivation of Measurement Sensitivity Matrix

The measurement sensitivity matrix, \mathbf{H} , must be formed using equation (2.27). In order to get to this point, though, it will be necessary to write the measurements as functions of the state variables. This in itself is a non-trivial task and the preliminary steps are laid out here.

In the present problem, the measurements of azimuth, α and elevation, e , are taken from the chaser vehicle as shown in Figure 2-3. Since the current study uses the chaser and target inertial states to generate relative information, taking meaningful angular measurements implies that the chaser vehicle has a sensor, such as a star tracker, to determine its inertial orientation.

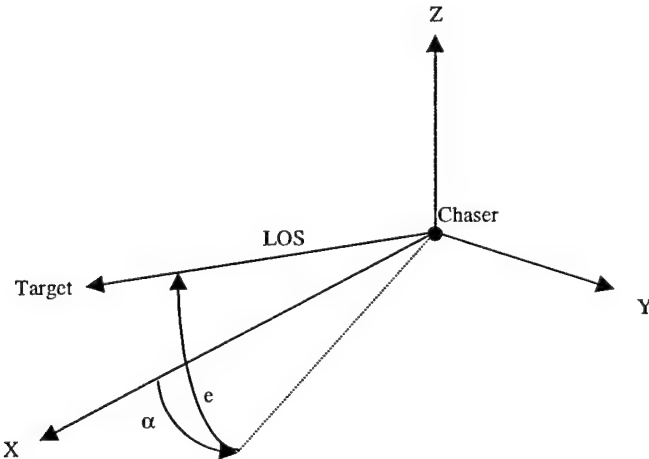


Figure 2-3: Angular measurements from chaser to target

The line-of-sight unit vector in the frame of the angular measurement sensor is written:

$$\hat{i}_{LOS}^s = \begin{bmatrix} \cos e \cos \alpha \\ \cos e \sin \alpha \\ \sin e \end{bmatrix} \quad (2.28)$$

so that the target position vector is simply $\bar{r}^s = \hat{r}_{\text{los}}^s$ where $r = |\bar{r}_{\text{rel}}^s|$ is the range to the target. If the effects of potential measurement biases on the azimuth and elevation are also included, then the new representation of relative range along the line-of-sight would be:

$$\bar{r}_{\text{rel}}^s = |\bar{r}_{\text{rel}}| \begin{bmatrix} \cos(e - b_e) \cos(\alpha - b_\alpha) \\ \cos(e - b_e) \sin(\alpha - b_\alpha) \\ \sin(e - b_e) \end{bmatrix} . \quad (2.29)$$

where b_α and b_e are the measurement biases. Equivalently, the position vector in the sensor coordinate frame can be written by transforming the inertial relative range vector through the following:

$$\bar{r}_{\text{rel}}^s = T_{s \leftarrow b} T_{b \leftarrow I_m} T_{I_m \leftarrow I} (\bar{r}_{\text{rel}}^I) \quad (2.30)$$

where $T_{X \leftarrow Y}$ is the coordinate transformation matrix to take a vector expressed in the Y frame into its equivalent representation in the X frame. In equation (2.30), $T_{I_m \leftarrow I}$ is the transformation from the true inertial frame to the measured inertial frame. The difference between the two being due to an inertial attitude knowledge error, $\bar{\Theta}^I$ produced by the star tracker, or other IMU. $T_{b \leftarrow I_m}$ is the transformation from the measured inertial frame to the spacecraft body frame, and $T_{s \leftarrow b}$ is the transformation from the spacecraft body frame to the angular measurement sensor frame. This last transformation may include a body-fixed static alignment error, represented by $\bar{\varepsilon}^b$, between the actual sensor frame and the nominal sensor frame. Finally, $\bar{r}_{\text{rel}}^I = \bar{R}_1^I - \bar{R}_2^I$ where \bar{R}_1^I and \bar{R}_2^I are the inertial position vectors for the target and chaser respectively.

The transformation matrices can also be written in an alternate form using the rotation vector they are transforming through. For example, assuming that the sensor frame is nearly aligned with the body frame, $T_{s \leftarrow b}$ can equivalently be written as $(I - \bar{\varepsilon}_\otimes^b)$. This notation comes from a shorthand version of the cross-product operator where in general

$$\bar{A} \times \bar{B} = -\bar{B} \times \bar{A} = A_{\otimes} \bar{B} = -B_{\otimes} \bar{A} = (A_y B_z - A_z B_y) \hat{x} + (A_z B_x - A_x B_z) \hat{y} + (A_x B_y - A_y B_x) \hat{z}$$

$$\text{where } A_{\otimes} = \begin{bmatrix} 0 & -A_z & A_y \\ A_z & 0 & -A_x \\ -A_y & A_x & 0 \end{bmatrix} \quad B_{\otimes} = \begin{bmatrix} 0 & -B_z & B_y \\ B_z & 0 & -B_x \\ -B_y & B_x & 0 \end{bmatrix} \quad (2.31)$$

This reformulation of the transformation matrix is possible since the direction cosine matrix for rotations through small angles about three axes is given by

$$T = \begin{bmatrix} 1 & A_z & -A_y \\ -A_z & 1 & A_x \\ A_y & -A_x & 1 \end{bmatrix} \quad (2.32)$$

Note that equation (2.32) is identical to $I - A_{\otimes}$ and therefore, the relative position vector in the sensor frame can be written in yet a third form as

$$\bar{r}_{rel}^s = \underbrace{(I - \bar{\epsilon}_{\otimes}^b)}_{T_{s \leftarrow b}} \underbrace{T_{b \leftarrow I_m} (I - \bar{\Theta}_{\otimes}^l)}_{T_{I_m \leftarrow I}} |\bar{r}_{rel}| \hat{i}_{LOS}^l \quad (2.33)$$

This formulation is useful because it explicitly includes all of the filter states which will allow the partial derivatives of the measurements to be calculated. For this study, the complete set of filter states are

$$\bar{R}_1^l, \bar{V}_1^l, \bar{R}_2^l, \bar{V}_2^l, b_e, b_{\alpha}, \bar{\epsilon}^b, \bar{\Theta}^l \quad (2.34)$$

which are the inertial position and velocity vectors of the target and chaser respectively, the angular measurement biases, the body-fixed static alignment bias, and the inertial attitude knowledge error. Now using a technique from Battin [3] the partial derivative of the relative position vector in the sensor frame with respect to itself gives

$$\begin{aligned}
\frac{\partial \bar{r}_{rel}^s}{\partial \bar{r}_{rel}^s} &= \mathbf{I} = \frac{\partial |\bar{r}_{rel}|}{\partial |\bar{r}_{rel}|} \frac{\partial |\bar{r}_{rel}|}{\partial \bar{r}_{rel}^s} + \frac{\partial \bar{r}_{rel}^s}{\partial e} \frac{\partial e}{\partial \bar{r}_{rel}^s} + \frac{\partial \bar{r}_{rel}^s}{\partial \alpha} \frac{\partial \alpha}{\partial \bar{r}_{rel}^s} \\
&= \hat{i}_{los}^s \frac{\partial |\bar{r}_{rel}|}{\partial \bar{r}_{rel}^s} + |\bar{r}_{rel}| \bar{P}_e^b \frac{\partial e}{\partial \bar{r}_{rel}^s} + |\bar{r}_{rel}| \bar{P}_\alpha^b \frac{\partial \alpha}{\partial \bar{r}_{rel}^s} \\
\text{where } \bar{P}_e^b &= \begin{bmatrix} -\sin(e - b_e) \cos(\alpha - b_\alpha) \\ -\sin(e - b_e) \sin(\alpha - b_\alpha) \\ \cos(e - b_e) \end{bmatrix} \\
\bar{P}_\alpha^b &= \begin{bmatrix} -\sin(\alpha - b_\alpha) \cos(e - b_e) \\ \cos(\alpha - b_\alpha) \cos(e - b_e) \\ 0 \end{bmatrix}
\end{aligned} \tag{2.35}$$

A key result of this technique is that the vector coefficients, $\hat{i}_{los}^s, \bar{P}_e^b, \bar{P}_\alpha^b$ are actually orthogonal unit vectors so that $(\bar{P}_\alpha^b)^T \bullet \bar{P}_e^b = (\bar{P}_e^b)^T \bullet \hat{i}_{los}^s = (\bar{P}_\alpha^b)^T \bullet \hat{i}_{los}^s = 0$ which will be a useful feature when trying to solve for partial derivatives with respect to filter states. Also note that

$$\begin{aligned}
(\bar{P}_\alpha^b)^T \bullet \bar{P}_\alpha^b &= \cos^2(e - b_e) \\
(\bar{P}_e^b)^T \bullet \bar{P}_e^b &= 1
\end{aligned} \tag{2.36}$$

With these preliminaries aside, it is possible to finally begin solving for the partial derivatives of the azimuth and elevation measurements with respect to different states in the navigation filter. These partials are evaluated along the nominal reference trajectory as in equation (2.26) to form the measurement sensitivity matrix, \mathbf{H} . The states of interest are the chaser and target inertial position and velocity vectors, the static misalignment of the angles-only sensor in the chaser body frame, and the inertial attitude error produced by measurement error of a star tracker, or equivalent sensor.

Partials with Respect to Target and Chaser Position

To begin with, the measurement partial derivatives with respect to the position vector of the target are determined by first calculating

$$\frac{\partial \bar{r}_{rel}^s}{\partial \bar{R}_1^I} = \frac{\partial (T_{s \leftarrow b} T_{b \leftarrow I_m} T_{I_m \leftarrow I} (\bar{R}_1^I - \bar{R}_2^I))}{\partial \bar{R}_1^I} = T_{s \leftarrow b} T_{b \leftarrow I_m} T_{I_m \leftarrow I} \tag{2.37}$$

Then using equation (2.29) and the technique in equation (2.35), it also can be found that

$$\begin{aligned}\frac{\partial \bar{r}_{rel}^s}{\partial \bar{R}_1^I} &= \frac{\partial \bar{r}_{rel}^s}{\partial |\bar{r}_{rel}|} \frac{\partial |\bar{r}_{rel}|}{\partial \bar{R}_1^I} + \frac{\partial \bar{r}_{rel}^s}{\partial e} \frac{\partial e}{\partial \bar{R}_1^I} + \frac{\partial \bar{r}_{rel}^s}{\partial \alpha} \frac{\partial \alpha}{\partial \bar{R}_1^I} \\ &= \hat{i}_{los}^s \frac{\partial |\bar{r}_{rel}|}{\partial \bar{R}_1^I} + |\bar{r}_{rel}| \bar{P}_e^b \frac{\partial e}{\partial \bar{R}_1^I} + |\bar{r}_{rel}| \bar{P}_\alpha^b \frac{\partial \alpha}{\partial \bar{R}_1^I}\end{aligned}\quad (2.38)$$

Now solving for the partial of azimuth with respect to the target position state by setting the right hand sides of equations (2.37) and (2.38) equal and multiplying through by $(\bar{P}_\alpha^b)^T$ to produce

$$\begin{aligned}(\bar{P}_\alpha^b)^T \bullet \hat{i}_{los}^s \frac{\partial |\bar{r}_{rel}|}{\partial \bar{R}_1^I} + |\bar{r}_{rel}| (\bar{P}_\alpha^b)^T \bullet \bar{P}_e^b \frac{\partial e}{\partial \bar{R}_1^I} + |\bar{r}_{rel}| (\bar{P}_\alpha^b)^T \bullet \bar{P}_\alpha^b \frac{\partial \alpha}{\partial \bar{R}_1^I} &= (\bar{P}_\alpha^b)^T T_{s \leftarrow b} T_{b \leftarrow l_m} T_{l_m \leftarrow I} \\ |\bar{r}_{rel}| \cos^2(e - b_e) \frac{\partial \alpha}{\partial \bar{R}_1^I} &= (\bar{P}_\alpha^b)^T T_{s \leftarrow b} T_{b \leftarrow l_m} T_{l_m \leftarrow I} \\ \frac{\partial \alpha}{\partial \bar{R}_1^I} &= \frac{(\bar{P}_\alpha^b)^T T_{s \leftarrow b} T_{b \leftarrow l_m} T_{l_m \leftarrow I}}{|\bar{r}_{rel}| \cos^2(e - b_e)} = \frac{(\bar{P}_\alpha^b)^T (I - \bar{\epsilon}_\otimes^b) T_{b \leftarrow l_m} (I - \bar{\Theta}_\otimes^I)}{|\bar{r}_{rel}| \cos^2(e - b_e)}\end{aligned}\quad (2.39)$$

Evaluating this partial along a nominal error free trajectory, \bar{x}^* , produces

$$\begin{aligned}\left. \frac{\partial \alpha}{\partial \bar{R}_1^I} \right|_{\bar{x}^*} &= \frac{(\bar{P}_\alpha^b)^T T_{b \leftarrow I}}{|\bar{r}_{rel}| \cos^2(e)} \\ \left(\left. \frac{\partial \alpha}{\partial \bar{R}_1^I} \right|_{\bar{x}^*} \right)^T &= \left(\frac{(\bar{P}_\alpha^b)^T T_{b \leftarrow I}}{|\bar{r}_{rel}| \cos^2(e)} \right)^T = \frac{T_{I \leftarrow b} \bar{P}_\alpha^b}{|\bar{r}_{rel}| \cos^2(e)}\end{aligned}\quad (2.40)$$

The process is almost identical for the partial with respect to the chaser position state except that

$$\frac{\partial \bar{r}_{rel}^s}{\partial \bar{R}_2^I} = \frac{\partial (T_{s \leftarrow b} T_{b \leftarrow l_m} T_{l_m \leftarrow I} (\bar{R}_1^I - \bar{R}_2^I))}{\partial \bar{R}_2^I} = -T_{s \leftarrow b} T_{b \leftarrow l_m} T_{l_m \leftarrow I}\quad (2.41)$$

so that the resulting partial is only different by a negative sign

$$\left(\left. \frac{\partial \alpha}{\partial \bar{R}_2^I} \right|_{\bar{x}^*} \right)^T = \frac{-T_{I \leftarrow b} \bar{P}_\alpha^b}{|\bar{r}_{rel}| \cos^2(e)}\quad (2.42)$$

The next step is to compute the partial derivative of the elevation measurement with respect to the target and chaser position vectors. The steps are identical to those used for the azimuth

calculations. First set the right hand sides of equations (2.37) and (2.38) equal and multiply through by $(\bar{P}_e^b)^T$

$$\begin{aligned} & (\bar{P}_e^b)^T \bullet \hat{i}_{los}^s \frac{\partial |\vec{r}_{rel}|}{\partial \bar{R}_1^I} + |\vec{r}_{rel}| (\bar{P}_e^b)^T \bullet \bar{P}_e^b \frac{\partial e}{\partial \bar{R}_1^I} + |\vec{r}_{rel}| (\bar{P}_e^b)^T \bullet \bar{P}_\alpha^b \frac{\partial \alpha}{\partial \bar{R}_1^I} = P_e^T T_{s \leftarrow b} T_{b \leftarrow I} T_{I \leftarrow I} \\ & |\vec{r}_{rel}| \frac{\partial e}{\partial \bar{R}_1^I} = (\bar{P}_e^b)^T T_{s \leftarrow b} T_{b \leftarrow I_m} T_{I_m \leftarrow I} \\ & \frac{\partial e}{\partial \bar{R}_1^I} = \frac{(\bar{P}_e^b)^T T_{s \leftarrow b} T_{b \leftarrow I_m} T_{I_m \leftarrow I}}{|\vec{r}_{rel}|} = \frac{(\bar{P}_e^b)^T (I - \bar{\varepsilon}_\otimes^b) T_{b \leftarrow I_m} (I - \bar{\Theta}'_\otimes)}{|\vec{r}_{rel}|} \end{aligned} \quad (2.43)$$

Evaluating along the nominal trajectory gives the desired forms:

$$\begin{aligned} \left(\frac{\partial e}{\partial \bar{R}_1^I} \Big|_{\bar{x}^*} \right)^T &= \left(\frac{(\bar{P}_e^b)^T T_{b \leftarrow I}}{|\vec{r}_{rel}|} \right)^T = \frac{T_{I \leftarrow b} \bar{P}_e^b}{|\vec{r}_{rel}|} \\ \left(\frac{\partial e}{\partial \bar{R}_2^I} \Big|_{\bar{x}^*} \right)^T &= \frac{-T_{I \leftarrow b} \bar{P}_e^b}{|\vec{r}_{rel}|} \end{aligned} \quad (2.44)$$

Partials with Respect to Velocity and Angular Measurement Biases

The partials of the angle measurements with respect to the target and chaser velocity are simply zero since there is no explicit functional dependence between the measurements and velocity.

$$\frac{\partial e}{\partial \bar{V}_1^I} = \frac{\partial e}{\partial \bar{V}_2^I} = \frac{\partial \alpha}{\partial \bar{V}_1^I} = \frac{\partial \alpha}{\partial \bar{V}_2^I} = \bar{0} \quad (2.45)$$

The partials with respect to the measurement biases themselves are just equal to unity since the biases are additive terms.

$$\begin{aligned} \frac{\partial e}{\partial b_e} &= \frac{\partial \alpha}{\partial b_\alpha} = 1 \\ \frac{\partial e}{\partial b_\alpha} &= \frac{\partial \alpha}{\partial b_e} = 0 \end{aligned} \quad (2.46)$$

Partials with Respect to Static Misalignment

The next set of measurement partial derivatives are for the angular measurements with respect to the static misalignment bias, $\bar{\epsilon}^b$. The steps are again identical to those used for the partials with respect to position. Starting with

$$\begin{aligned}\frac{\partial \bar{r}_{rel}^s}{\partial \bar{\epsilon}^b} &= \hat{i}_{LOS}^s \frac{\partial |\bar{r}_{rel}|}{\partial \bar{\epsilon}^b} + |\bar{r}_{rel}| \bar{P}_e^b \frac{\partial e}{\partial \bar{\epsilon}^b} + |\bar{r}_{rel}| \bar{P}_\alpha^b \frac{\partial \alpha}{\partial \bar{\epsilon}^b} \\ &= \frac{\partial \left((I - \bar{\Theta}_\otimes^b) T_{b \leftarrow I_m} (I - \bar{\Theta}_\otimes^I) |\bar{r}_{rel}| \hat{i}_{LOS}^I \right)}{\partial \bar{\epsilon}^b}\end{aligned}\quad (2.47)$$

The final term of equation (2.47) is handled using

$$\begin{aligned}&\frac{\partial \left[T_{b \leftarrow I_m} (I - \bar{\Theta}_\otimes^I) |\bar{r}_{rel}| \hat{i}_{LOS}^I - \bar{\epsilon}_\otimes^b T_{b \leftarrow I_m} (I - \bar{\Theta}_\otimes^I) |\bar{r}_{rel}| \hat{i}_{LOS}^I \right]}{\partial \bar{\epsilon}^b} \\ &= \frac{\partial}{\partial \bar{\epsilon}^b} \left[\left(T_{b \leftarrow I_m} (I - \bar{\Theta}_\otimes^I) |\bar{r}_{rel}| \hat{i}_{LOS}^I \right)_\otimes \bar{\epsilon}^b \right] \\ &= \left[T_{b \leftarrow I_m} (I - \bar{\Theta}_\otimes^I) |\bar{r}_{rel}| \hat{i}_{LOS}^I \right]_\otimes\end{aligned}\quad (2.48)$$

Setting this result equal to the middle term of equation (2.47) and multiplying through by $(\bar{P}_\alpha^b)^T$ gives

$$\frac{\partial \alpha}{\partial \bar{\epsilon}^b} = \frac{(\bar{P}_\alpha^b)^T \left[T_{b \leftarrow I_m} (I - \bar{\Theta}_\otimes^I) |\bar{r}_{rel}| \hat{i}_{LOS}^I \right]_\otimes}{|\bar{r}_{rel}| \cos^2(e - b_e)}\quad (2.49)$$

Evaluating along the nominal trajectory, and using the cross-product identities in equation (2.31) gives

$$\begin{aligned}\left. \frac{\partial \alpha}{\partial \bar{\epsilon}^b} \right|_{\bar{x}^*} &= \frac{- \left[T_{b \leftarrow I_m} \hat{i}_{LOS}^I \right]_\otimes (\bar{P}_\alpha^b)^T}{\cos^2(e)} = \frac{- (\hat{i}_{LOS}^b)_\otimes (\bar{P}_\alpha^b)^T}{\cos^2(e)} \\ \left(\left. \frac{\partial \alpha}{\partial \bar{\epsilon}^b} \right|_{\bar{x}^*} \right)^T &= \frac{\bar{P}_\alpha^b \times \hat{i}_{LOS}^b}{\cos^2(e)}\end{aligned}\quad (2.50)$$

The partial of elevation with respect to static misalignment follows very much in the same manner. Starting again with equation (2.47) and this time multiplying through by P_e^T gives

$$\frac{\partial e}{\partial \bar{\epsilon}^b} = \frac{\left(\bar{P}_e^b \right)^T \left[T_{b \leftarrow I_m} \left(I - \bar{\Theta}_{\otimes}^I \right) \mid \bar{r}_{rel} \mid \hat{i}_{LOS}^I \right]_{\otimes}}{\mid \bar{r}_{rel} \mid} \quad (2.51)$$

Then finally

$$\begin{aligned} \frac{\partial e}{\partial \bar{\epsilon}^b} \Big|_{\bar{x}^*} &= - \left(\hat{i}_{LOS}^b \right)_{\otimes} \left(\bar{P}_e^b \right)^T \\ \left(\frac{\partial e}{\partial \bar{\epsilon}^b} \Big|_{\bar{x}^*} \right)^T &= \bar{P}_e^b \times \hat{i}_{LOS}^b \end{aligned} \quad (2.52)$$

Partials with Respect to Inertial Attitude Error

The final set of partial derivatives then are for the measurements with respect to the inertial attitude measurement error, $\bar{\Theta}^I$. The steps are very similar to those used for the previous partials with respect to the static misalignment. Starting with

$$\begin{aligned} \frac{\partial \bar{r}_{rel}^s}{\partial \bar{\Theta}^I} &= \hat{i}_{LOS}^s \frac{\partial \mid \bar{r}_{rel} \mid}{\partial \bar{\Theta}^I} + \mid \bar{r}_{rel} \mid \bar{P}_e^b \frac{\partial e}{\partial \bar{\Theta}^I} + \mid \bar{r}_{rel} \mid \bar{P}_{\alpha}^b \frac{\partial \alpha}{\partial \bar{\Theta}^I} \\ &= \frac{\partial \left(\left(I - \bar{\epsilon}_{\otimes}^b \right) T_{b \leftarrow I_m} \left(I - \bar{\Theta}_{\otimes}^I \right) \mid \bar{r}_{rel} \mid \hat{i}_{LOS}^I \right)}{\partial \bar{\Theta}^I} \end{aligned} \quad (2.53)$$

Where the last term of equation (2.53) becomes

$$\begin{aligned} &\frac{\partial \left[\left(I - \bar{\epsilon}_{\otimes}^b \right) T_{b \leftarrow I_m} \mid \bar{r}_{rel} \mid \hat{i}_{LOS}^I + \left(I - \bar{\epsilon}_{\otimes}^b \right) T_{b \leftarrow I_m} \left(-\bar{\Theta}_{\otimes}^I \right) \mid \bar{r}_{rel} \mid \hat{i}_{LOS}^I \right]}{\partial \bar{\Theta}^I} \\ &= \frac{\partial \left[\left(I - \bar{\epsilon}_{\otimes}^b \right) T_{b \leftarrow I_m} \left(-\bar{\Theta}_{\otimes}^I \right) \mid \bar{r}_{rel} \mid \hat{i}_{LOS}^I \right]}{\partial \bar{\Theta}^I} = \frac{\partial \left[\left(I - \bar{\epsilon}_{\otimes}^b \right) T_{b \leftarrow I_m} \left(\mid \bar{r}_{rel} \mid \hat{i}_{LOS}^I \right)_{\otimes} \bar{\Theta}^I \right]}{\partial \bar{\Theta}^I} \\ &= \left(I - \bar{\epsilon}_{\otimes}^b \right) T_{b \leftarrow I_m} \left[\mid \bar{r}_{rel} \mid \hat{i}_{LOS}^I \right]_{\otimes} \end{aligned} \quad (2.54)$$

so that multiplying through by $\left(\bar{P}_{\alpha}^b \right)^T$ yields

$$\frac{\partial \alpha}{\partial \bar{\Theta}^I} = \frac{\left(\bar{P}_{\alpha}^b \right)^T \left(I - \bar{\epsilon}_{\otimes}^b \right) T_{b \leftarrow I_m} \left[\mid \bar{r}_{rel} \mid \hat{i}_{LOS}^I \right]_{\otimes}}{\mid \bar{r}_{rel} \mid \cos^2(e - b_e)} \quad (2.55)$$

Evaluating along the nominal trajectory gives

$$\begin{aligned}\left.\frac{\partial \alpha}{\partial \bar{\Theta}^I}\right|_{\bar{x}^*} &= \frac{-\left[\hat{i}_{LOS}^I\right]_{\otimes} \left(\bar{P}_\alpha^b\right)^T T_{b \leftarrow I}}{\cos^2(e)} \\ \left(\left.\frac{\partial \alpha}{\partial \bar{\Theta}^I}\right|_{\bar{x}^*}\right)^T &= \frac{-\left[\hat{i}_{LOS}^I\right]_{\otimes} T_{I \leftarrow b} \bar{P}_\alpha^b}{\cos^2(e)} = \frac{\bar{P}_\alpha^I \times \hat{i}_{LOS}^I}{\cos^2(e)}\end{aligned}\quad (2.56)$$

The partial for the elevation measurement comes from multiplying $\left(\bar{P}_e^b\right)^T$ through equation (2.53) and evaluating along the nominal trajectory for

$$\left.\frac{\partial e}{\partial \bar{\Theta}^I}\right|_{\bar{x}^*} = \frac{T_{b \leftarrow I} \left(\bar{P}_e^b\right)^T \left[\left|\bar{r}_{rel}\right| \hat{i}_{LOS}^I\right]_{\otimes}}{\left|\bar{r}_{rel}\right|} = -\left[\hat{i}_{LOS}^I\right]_{\otimes} \left(\bar{P}_e^b\right)^T T_{b \leftarrow I} \quad (2.57)$$

so finally

$$\left(\left.\frac{\partial e}{\partial \bar{\Theta}^I}\right|_{\bar{x}^*}\right)^T = \bar{P}_e^I \times \hat{i}_{LOS}^I \quad (2.58)$$

The entire \mathbf{H} matrix can finally be constructed by combining equations (2.27), (2.40), (2.42), (2.44), (2.45), (2.46), (2.50), (2.52), (2.56), and (2.58) to yield

$$\begin{aligned}\mathbf{H} &= \left[\begin{array}{cccccccc} \frac{\partial e}{\partial \bar{R}_1^I} & \frac{\partial e}{\partial \bar{R}_2^I} & \frac{\partial e}{\partial \bar{V}_1^I} & \frac{\partial e}{\partial \bar{V}_2^I} & \frac{\partial e}{\partial b_e} & \frac{\partial e}{\partial b_\alpha} & \frac{\partial e}{\partial \bar{\varepsilon}^b} & \frac{\partial e}{\partial \bar{\Theta}^I} \\ \frac{\partial \alpha}{\partial \bar{R}_1^I} & \frac{\partial \alpha}{\partial \bar{R}_2^I} & \frac{\partial \alpha}{\partial \bar{V}_1^I} & \frac{\partial \alpha}{\partial \bar{V}_2^I} & \frac{\partial \alpha}{\partial b_e} & \frac{\partial \alpha}{\partial b_\alpha} & \frac{\partial \alpha}{\partial \bar{\varepsilon}^b} & \frac{\partial \alpha}{\partial \bar{\Theta}^I} \end{array} \right]_{\bar{x}^*} \\ &= \left[\begin{array}{cc} \frac{\bar{P}_e^I}{\left|\bar{r}_{rel}\right|} & \frac{\bar{P}_\alpha^I}{\left|\bar{r}_{rel}\right| \cos^2(e)} \\ -\frac{\bar{P}_e^I}{\left|\bar{r}_{rel}\right|} & -\frac{\bar{P}_\alpha^I}{\left|\bar{r}_{rel}\right| \cos^2(e)} \\ \bar{0} & \bar{0} \\ \bar{0} & \bar{0} \\ 1 & 0 \\ 0 & 1 \\ \bar{P}_e^b \times \hat{i}_{LOS}^b & \frac{\bar{P}_\alpha^b \times \hat{i}_{LOS}^b}{\cos^2(e)} \\ \bar{P}_e^I \times \hat{i}_{LOS}^I & \frac{\bar{P}_\alpha^I \times \hat{i}_{LOS}^I}{\cos^2(e)} \end{array} \right]_{\bar{x}^*}^T\end{aligned}\quad (2.59)$$

2.2 LINEAR COVARIANCE ANALYSIS

When it comes to simulation of a dynamic system there are two basic approaches that provide insight to the designer. The first is a Monte Carlo study. In this case, multiple samples of a stochastic process are generated and operated upon, and the results of these multiple samples are characterized statistically. The statistics allow the designer to see how factors such as measurement models, filter design, or initial conditions affect the actual state history. Although fundamentally deterministic, the drawback to this approach is that generating an adequate number of samples to make the statistical results meaningful can be very time consuming for complex systems.

The alternative approach is the use of a technique called linear covariance (LINCov) analysis. The simplest way to conceptualize LINCov is to consider it in terms of Monte Carlo analysis. The end result of the Monte Carlo analysis was a statistical representation of the errors on the states of interest. LINCov takes the approach of developing this statistical representation directly, without having to use large numbers of actual samples. Each sample of a Monte Carlo run uses random number generators to introduce stochastic effects. However, these random numbers can be described by a statistical distribution just as well. The idea then is that LINCov uses a single run where all the uncertainties are described statistically and then the statistics of the state error are propagated in time. In the end, both methods generate the same product: a statistical representation of the state errors of interest. Although LINCov is a considerably faster method of testing designs, it has the drawback of requiring both linearized models and Gaussian distributions. Therefore, the results usually require verification using deterministic methods. The details of LINCov will now be examined. This section, along with section 2.1.3 is based largely on a presentation given by Dr. David Geller [17] of the techniques that he used to develop a baseline LINCov program for the NASA/JPL Mars Sample Return project which was modified for the current study by the author.

2.2.1 General Explanation and Setup

Fortunately, the heart of the LINCov method has already been derived in the form of the Kalman filter equations in section 2.1.1. These equations are what allow LINCov to propagate the statistics of a dynamic process in time. In order to fully develop the process some new definitions are required. First, a truth model is required that includes both states and

measurements. These are similar to equations (2.1)-(2.4), and (2.8), except this time the models are non-linear and the ‘T’ subscript is added to represent the truth model

$$\begin{aligned}\dot{\bar{x}}_T &= f_T(\bar{x}_T) + \bar{w} & \bar{w} &\sim N(0, \mathbf{Q}_T \delta(t - \tau)) \\ \bar{z}_T &= h_T(\bar{x}_T) + \bar{v} & \bar{v} &\sim N(0, \mathbf{R}_T)\end{aligned}\tag{2.60}$$

where, although a slight abuse of notation, $\sim N(a, b)$ represents a normal distribution with mean a and covariance b .

Next, a reference trajectory, or nominal state history, is defined where the * superscript refers to the reference values

$$\begin{aligned}\dot{\bar{x}}_T^* &= f_T(\bar{x}_T^*) \\ \bar{z}_T^* &= h_T(\bar{x}_T^*)\end{aligned}\tag{2.61}$$

and the initial condition for the truth state is

$$\bar{x}_T(t_0) = \bar{x}_{t_0}^* \quad \bar{x}_T(t_0) \sim N(\bar{x}_{t_0}^*, \mathbf{P}_{t_0})\tag{2.62}$$

The next step is to linearize the non-linear state dynamics and measurements about this nominal trajectory as shown in sections 2.1.2 and 2.1.3. It is assumed that the linearized equations have the form

$$\begin{aligned}\delta \bar{x}_{T_{k+1}} &= \phi_T(t_{k+1}, t_k) \delta \bar{x}_{T_k} + \bar{n} & \bar{n} &\sim N(0, \mathbf{Q}_T) & \delta \bar{x}_{T_0} &\sim N(0, \mathbf{P}_{t_0}) \\ \delta \bar{z}_{T_k} &= \mathbf{H}_T \delta \bar{x}_k + \bar{v} & \bar{v} &\sim N(0, \mathbf{R}_T)\end{aligned}\tag{2.63}$$

At this point, the concepts of section 2.1.1 are used and a set of estimated states are calculated using the filtering equations. Keep in mind that in many cases, the number of estimated states may not be as large as the number of true states, and the filter models may not be the same as the truth models. This is especially true when the truth model includes numerous higher order terms. Using Figure 2-2 and the ‘F’ subscript to represent the filter states, the filtering estimation equations of the linearized system become

$$\begin{aligned}
& \text{state \& covariance propagation} \quad \begin{cases} \delta \hat{\bar{x}}_{k+1} = \phi_F(t_{k+1}, t_k) \delta \hat{\bar{x}}_k \\ \mathbf{P}_{F_{k+1}} = \phi_F \mathbf{P}_{F_k} \phi_F^T + \mathbf{Q}_F \end{cases} \\
& \text{state \& covariance update} \quad \begin{cases} \delta \hat{\bar{x}}_k^+ = \delta \hat{\bar{x}}_k^- + \mathbf{K}_k (\delta \bar{z}_{T_k} - \mathbf{H}_{F_k} \delta \hat{\bar{x}}_k^-) \\ \mathbf{P}_{F_k}^+ = (\mathbf{I} - \mathbf{K}_k \mathbf{H}_{F_k}) \mathbf{P}_{F_k}^- (\mathbf{I} - \mathbf{K}_k \mathbf{H}_{F_k})^T + \mathbf{K}_k \mathbf{R}_{F_k} \mathbf{K}_k^T \\ \mathbf{K}_k = \mathbf{P}_{F_k}^- \mathbf{H}_{F_k}^T (\mathbf{H}_{F_k} \mathbf{P}_{F_k}^- \mathbf{H}_{F_k}^T + \mathbf{R}_{F_k})^{-1} \end{cases} \quad (2.64)
\end{aligned}$$

In order to generate truth and filtering data simultaneously, an augmented system is constructed. First, the augmented state vector is defined

$$\vec{X}_A = \begin{bmatrix} \delta \bar{x}_T \\ \delta \hat{\bar{x}} \end{bmatrix} \quad (2.65)$$

where again the size of the truth and estimated states are not necessarily the same. The covariance matrix for the augmented state, \mathbf{P}_A , is constructed by calculating $E[\vec{X}_A \vec{X}_A^T]$. The augmented state propagation equation becomes

$$\begin{aligned}
\begin{bmatrix} \delta \bar{x}_{T_{k+1}} \\ \delta \hat{\bar{x}}_{k+1} \end{bmatrix} &= \begin{bmatrix} \phi_T & 0 \\ 0 & \phi_F \end{bmatrix} \begin{bmatrix} \delta \bar{x}_{T_k} \\ \delta \hat{\bar{x}}_k \end{bmatrix} + \begin{bmatrix} \bar{n} \\ 0 \end{bmatrix} \\
\vec{X}_{A_{k+1}} &= \Phi \vec{X}_{A_k} + \begin{bmatrix} \bar{n} \\ 0 \end{bmatrix} \quad (2.66)
\end{aligned}$$

and the augmented state covariance propagation equation is

$$\mathbf{P}_{A_{k+1}} = \Phi \mathbf{P}_{A_k} \Phi^T + \mathbf{Q}_A \quad (2.67)$$

where

$$\Phi = \begin{bmatrix} \phi_T & 0 \\ 0 & \phi_F \end{bmatrix} \quad \mathbf{Q}_A = \begin{bmatrix} \mathbf{Q}_T & 0 \\ 0 & 0 \end{bmatrix} \quad (2.68)$$

The augmented state update equation is

$$\begin{aligned}
\begin{bmatrix} \delta \bar{x}_{T_k}^+ \\ \delta \hat{\bar{x}}_k^+ \end{bmatrix} &= \begin{bmatrix} \mathbf{I} & 0 \\ \mathbf{K}_k \mathbf{H}_{T_k} & \mathbf{I} - \mathbf{K}_k \mathbf{H}_{F_k} \end{bmatrix} \begin{bmatrix} \delta \bar{x}_{T_k}^- \\ \delta \hat{\bar{x}}_k^- \end{bmatrix} + \begin{bmatrix} 0 \\ \mathbf{K}_k \end{bmatrix} \vec{v} \\
\vec{X}_{A_k}^+ &= \mathbf{A}_k \vec{X}_{A_k}^- + \mathbf{K}_{A_k} \vec{v} \quad (2.69)
\end{aligned}$$

and the augmented state covariance update equation becomes

$$\mathbf{P}_{A_k}^+ = \mathbf{A}_k \mathbf{P}_{A_k}^- \mathbf{A}_k^T + \mathbf{K}_{A_k} \mathbf{R}_{T_k} \mathbf{K}_{A_k}^T \quad (2.70)$$

where

$$\mathbf{A}_k = \begin{bmatrix} \mathbf{I} & 0 \\ \mathbf{K}_k \mathbf{H}_{T_k} & \mathbf{I} - \mathbf{K}_k \mathbf{H}_{F_k} \end{bmatrix} \quad \mathbf{K}_{A_k} = \begin{bmatrix} 0 \\ \mathbf{K}_k \end{bmatrix}$$

Equations (2.67) and (2.70) are all that is needed to capture all of the statistics for a linear covariance analysis. Rather than having to run multiple samples of a Monte Carlo analysis, the time history of \mathbf{P}_A is recorded and then the performance can be easily evaluated.

Note that the \mathbf{Q}_A matrix does not contain a \mathbf{Q}_F term in equation (2.68) as one might expect it should from looking at the covariance propagation expression in equation (2.64). This subtlety of LINCOV merits some comment. Recall that the covariance of the true state which represents trajectory dispersions is

$$\mathbf{P}_T = E\left[\delta \bar{x}_T (\delta \bar{x}_T)^T\right] \quad (2.71)$$

so that it propagates in time according to

$$\mathbf{P}_{T_{k+1}} = \phi_T \mathbf{P}_{T_k} \phi_T^T + \mathbf{Q}_T \quad (2.72)$$

However, the covariance of the state estimate is

$$\mathbf{P}_F = E\left[\delta \hat{\bar{x}} (\delta \hat{\bar{x}})^T\right] \quad (2.73)$$

which propagates in time according to

$$\mathbf{P}_{F_{k+1}} = \phi_F \mathbf{P}_{F_k} \phi_F^T \quad (2.74)$$

The covariance propagation expression that appears in equation (2.64) includes the \mathbf{Q}_F term solely for calculation of the Kalman gain. However, the actual covariance associated with the estimated state is simply given by equation (2.74).

In many cases, covariance analysis is used to evaluate the effectiveness of a filter design, especially when the filter is of lower order than the truth model. In that situation, one could compare the values of \mathbf{P}_F , which is the filter's guess as to the covariance of the state estimate, to the actual state error covariance which is

$$\mathbf{P}_{e_{\text{nav}}} = [-\mathbf{I} \quad \mathbf{I}] \mathbf{P}_A \begin{bmatrix} -\mathbf{I} \\ \mathbf{I} \end{bmatrix} \quad (2.75)$$

This would quickly identify whether or not the filter design was ‘good’ in the sense that it gives an accurate estimate of the state errors. Comparing the filter estimates of the error to the actual errors would yield a variation of one of the three cases shown in Figure 2-4 [17].

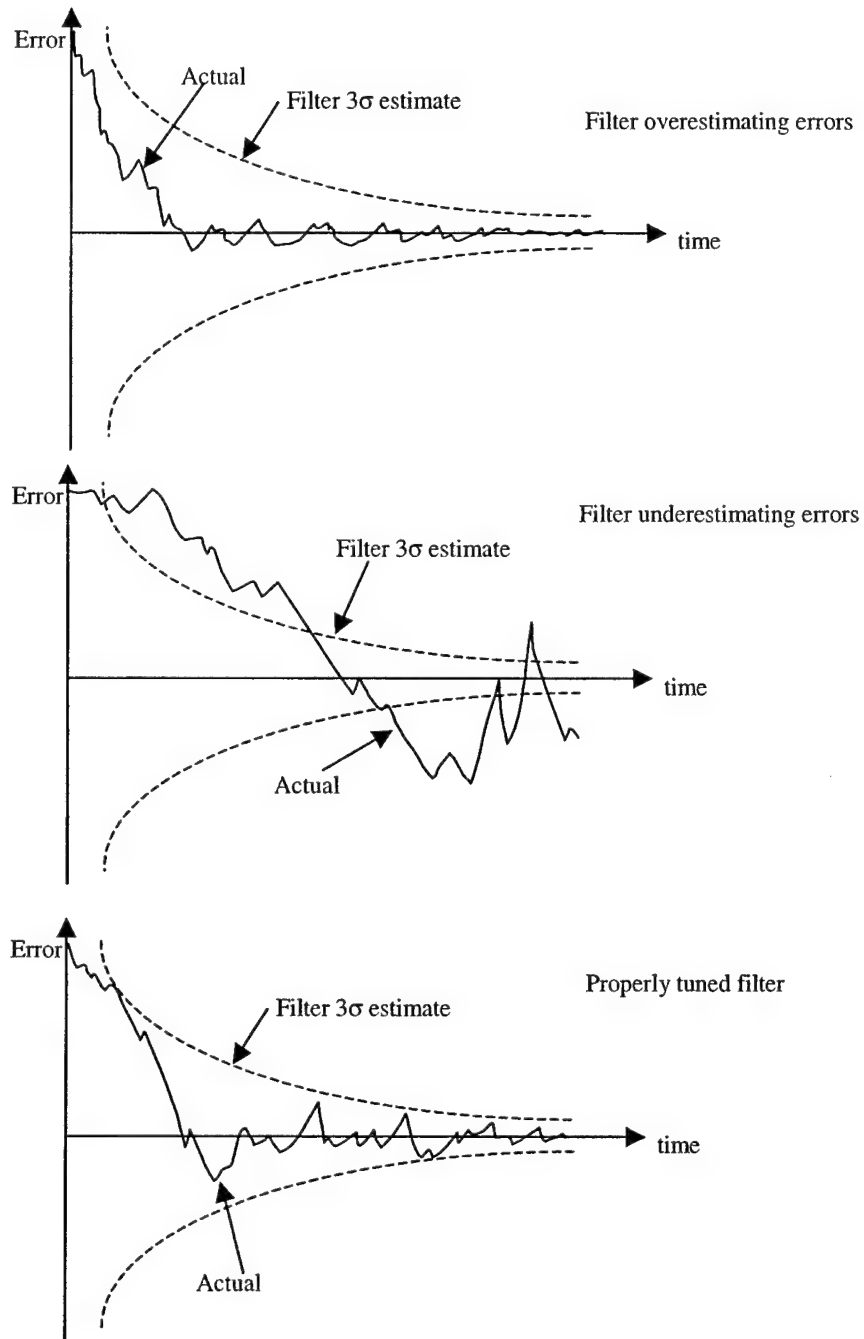


Figure 2-4: Filter design using LINCOV analysis

In this study, however, the only concern is how trajectories and maneuvers affect downrange observability when only angular measurements are used. In light of this, trajectory dispersions are not considered since the focus is only on the navigation performance. Additionally, the filter models and states are identical to the truth model and states because filter tuning is not being studied here. Therefore, the quantity of key concern will be \mathbf{P}_F , the filter covariance. The presence or lack of range observability in the navigation filter will be apparent by simply examining the behavior of the downrange position uncertainty.

2.2.2 LINCOV Models

One of the major assumptions behind LINCOV analysis is the fact that linearized models are available to represent the system error sources in addition to the previously linearized dynamics and measurements. Unfortunately, real-world interactions are rarely, if ever, linear. This section briefly covers the development of some of the models that have not already been addressed (see sections 2.1.2 and 2.1.3) that are used in LINCOV.

Un-modeled Accelerations

Un-modeled acceleration, or process noise as it is often referred to, represents the noise in the state dynamics. The amount of process noise typically depends on the fidelity of the model for the equations of motion. The lower the fidelity of the dynamics model is, the larger the process noise should be to ensure that the covariance values stay large enough to capture the state uncertainties. For example, typical effects that may be un-modeled for low-earth orbit (LEO) vehicles are drag, higher-order gravity terms, thermal cycling, solar radiation pressure, uncoupled jet firings, or spacecraft venting. Continuing with the simple model of just position and velocity from equations (2.20) and (2.22), and assuming constant disturbance accelerations over small time steps, ΔT , the un-modeled accelerations enter into the state through

$$\delta \bar{x}_{k+1} = \phi(t_{k+1}, t_k) \delta \bar{x}_k + \begin{bmatrix} I \frac{\Delta T^2}{2} & 0 \\ 0 & I \Delta T \end{bmatrix} \bar{\varepsilon}_k \quad (2.76)$$

where $\bar{\varepsilon}$ is the constant acceleration term with units of m/s^2 and $\bar{\varepsilon} \sim N(0, \sigma_\varepsilon^2)$. Assuming the acceleration disturbances are uncorrelated from one time step to another, the state noise covariance is then

$$\mathbf{Q} = \sigma_e^2 \begin{bmatrix} I \frac{\Delta T^4}{4} & I \frac{\Delta T^3}{2} \\ I \frac{\Delta T^3}{2} & I \Delta T^2 \end{bmatrix} \quad (2.77)$$

This process noise covariance matrix, \mathbf{Q} , is used in the covariance propagation equation (2.67).

System Biases and First Order Markov Processes

More often than not, system biases appear in real problems. However, these systems rarely have a truly constant bias, but rather there are biases that are functions of some time dependent condition [14][17]. In orbital applications, the time dependence may be related to the orbital period for example. These time-varying biases (no oxymoron intended) can be incorporated into the state model description as first order Markov processes:

$$\alpha_{k+1} = e^{-\Delta T/\tau} \alpha_k + \sigma_\alpha \sqrt{1 - e^{-2\Delta T/\tau}} \eta \quad (2.78)$$

where $\eta \sim N(0,1)$ & $\alpha_0 \sim N(0, \sigma_\alpha^2)$ so that

$$P_{\alpha_{k+1}} = E[\alpha_{k+1}^2] = e^{-2\Delta T/\tau} P_{\alpha_k} + \sigma_\alpha^2 \left(1 - e^{-2\Delta T/\tau}\right) \quad (2.79)$$

implying that the steady state variance approaches σ_α^2 in the absence of measurements. Although equations (2.78) and (2.79) are scalar equations, the same formulations can be applied to a vector valued random variable, $\vec{\alpha}$. The value of the time constant, τ , is usually chosen based on empirical experience. This same formulation can also be used to model a truly constant bias ($\tau = \infty$) as well as broadband noise ($\tau \ll \Delta T$).

Maneuver Measurement Errors

A key piece of information used for navigation is the direction and magnitude of any maneuvers, ΔV , executed. However, there is always some error in how well this can be measured. The ΔV measurement errors are defined here as

$$\Delta \vec{V}_{measurement\ err} = k_{sf} \Delta \vec{V}_{nominal} + \Delta \vec{V}_{quantization} \quad (2.80)$$

In this model, $k_{sf} \sim N(0, \sigma_{k_{sf}}^2)$ represents a scale factor error which creates an error in the magnitude of the measurement of the maneuver. The quantization term $\Delta\vec{V}_{quantization} \sim N(0, \sigma_q^2)$ represents the error associated with mechanized devices such as accelerometers that have some minimum threshold value that can be detected. There are no bias terms in the model since these are easily calibrated out in mission practice by measuring the 0-g environment.

Each time a maneuver takes place, the true velocity vector of the chaser is altered. Correspondingly, the covariance associated with that velocity should be adjusted to take into account that there is new uncertainty entering the system. This is modeled by altering the 3x3 partition of the covariance matrix corresponding to chaser velocity according to

$$\mathbf{P}_{\vec{v}_{chaser}}^+ = \mathbf{P}_{\vec{v}_{chaser}}^- + \sigma_q^2 \mathbf{I}_{3 \times 3} + \sigma_{k_{sf}}^2 \Delta\vec{V}_{nominal} \Delta\vec{V}_{nominal}^T \quad (2.81)$$

where the - and + superscripts refer to the instant immediately before and after the maneuver respectively.

2.2.3 Current Configuration

For the current study, actually running the LINCOV tool consists of two distinct steps. First, a reference trajectory must be generated. Besides providing a time history of the actual states in equation (2.34), the reference trajectory is used to calculate the state transition matrix used for propagating the covariance matrix in time. Creating a particular reference trajectory is a matter of selecting the initial orbital elements of both the target and chaser to induce the desired relative motion. Additionally, maneuvers can be executed at fixed times to alter the natural motion. These concepts will be covered in more detail in Chapters 3 and 4.

With a reference trajectory defined, the LINCOV parameters need to be specified in order to perform a covariance analysis about the given trajectory. Initialization in the current version includes setting the *a priori* navigation uncertainty values for the target and chaser vehicles, and defining the variance values and time constants of error models such as angle measurements, ΔV measurement, sensor alignment errors, attitude determination errors, and un-modeled acceleration. Since the target and chaser vehicle states are propagated in inertial space, the un-modeled acceleration term does not have to account for errors resulting from use of the C-W relative motion equations. Finally, an epoch date is chosen. The actual date is not relevant to the success of angles-only navigation, but it serves to provide a realistic model of the sun's position relative to the target and chaser vehicles. This sun position is used to determine lighting

conditions on the vehicles for cases when measurement availability is limited to periods of solar illumination and is further discussed in sections 3.4.2 and 5.2.

Each LINCOV run provides a variety of information relating to the navigation filter's estimation of state uncertainty. The figure that will be of primary concern in this study is the uncertainty in the relative downrange position component. For the interested reader, the tool also calculates time histories of the root sum square (RSS) inertial and relative position and velocity uncertainties, the position and velocity component uncertainties, the relative frame error ellipsoids as well as the altitude vs. downrange correlation coefficients, semi-major axis uncertainty, bias value uncertainties, and the inertial observability matrix.

[This page intentionally left blank]

3 NATURAL MOTION RANGE OBSERVABILITY

The first step towards addressing the potential of angles-only navigation is to better understand both its limitations and possibilities. It is generally well-known that relative navigation without any range information is problematic in situations where the chaser is not moving relative to the target. This situation leads to unbounded growth in downrange uncertainty because the navigation filter has no range observability. However, the problem of generating range observability is not as well understood when there are changes in the relative target-chaser geometry due to natural orbital motion. The true three-dimensional freedom of the space environment motivates the question of whether or not well-chosen orbital trajectories alone can indirectly provide range observability through angular measurements.

3.1 BACKGROUND

The term *observability* is one that can potentially carry various meanings. In filtering and control applications, observability typically means that the value of a state variable can be determined to some level of accuracy. In a strict sense, and with no sensor errors, the estimation uncertainty of an observable state would approach zero asymptotically. For the purposes of this study, however, the concept of observability is used in a looser sense. Specifically, when a trajectory is said to be more observable than another, this simply means that the filter is having more success estimating the downrange state. It does not necessarily mean that the downrange estimate will asymptotically approach its exact value.

From an intuitive standpoint, it would seem that using only angle measurements to determine the position of a target will lead to an error, or uncertainty, ellipse with a cigar-like shape due to the range ambiguity as shown in Figure 3-1

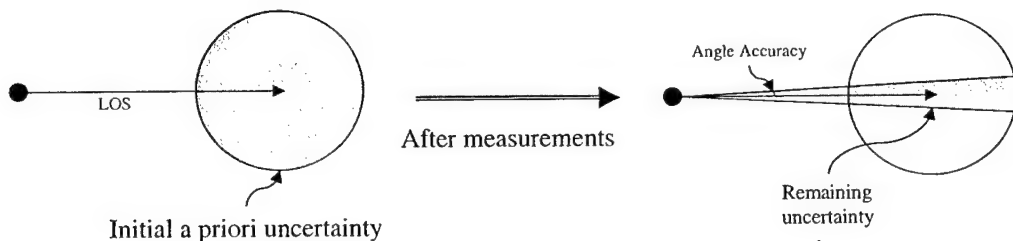


Figure 3-1: Uncertainty with angular measurements and no relative geometry

With no sensor available to help eliminate this ambiguity, the angles-only navigation approach seems doomed to failure. However, following the same line of intuitive logic, Figure 3-2 shows how the uncertainty of the range value could potentially be reduced through relative motion between the target and chaser vehicles.

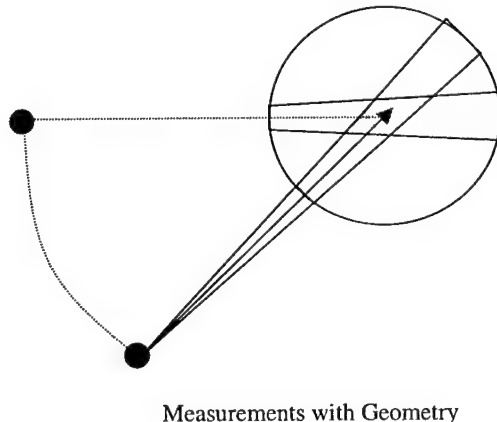


Figure 3-2: Uncertainty with angular measurements and use of relative geometry

A qualitative evaluation of natural motion trajectories is helpful for a variety of reasons. First, the simplest cases provide validation that the LINCov tool is working correctly. Secondly, not all mission phases require a high level of precision navigation. In these cases, the possibility of trajectories that generate improved range observability without the use of any maneuvers is worth study. Most importantly, the analysis of natural motion trajectories generates an appreciation of characteristics that lead to improved range observability. These characteristics, or rules of thumb, can be exploited when designing trajectories that have the benefit of using maneuvers to improve the navigation uncertainties.

Since there are a wide variety of orbital trajectories that could be considered, the possibilities are grouped by their relative motion characteristics as well as by the range regime they operate

across. In general, the chaser vehicle can be either closing on the target or station-keeping around some fixed relative offset point. Three different range regimes are defined, generally based on the initial separation distance between the target and chaser: 1) long range (10-100km) 2) short range (1-10km) and 3) proximity operations, or Prox Ops (<1km).

3.2 REFERENCE TRAJECTORY DEVELOPMENT

As explained in section 2.2 using LINCOV as an analysis tool requires a nominal reference trajectory. The number of relative natural motion trajectories that can result from placing two vehicles in different orbits is potentially limitless. However, from the standpoint of mission practicality as well as insuring the validity of analysis tools, a number of limitations are placed on the possible reference trajectories.

3.2.1 Constraints

The first constraint levied on the reference trajectories is that the target is in a circular orbit and the chaser is itself in a nearly circular orbit. The reason for this is that when both vehicles are in nearly circular orbits and the separation distance between them is small, the relative motion can be described by the Clohessy-Wiltshire (C-W) equations, also called Hill's equations as [28]:

$$\begin{aligned}\ddot{x} + 2\omega\dot{z} &= f_x \\ \ddot{z} - 2\omega\dot{x} - 3\omega^2 z &= f_z \\ \ddot{y} + \omega^2 y &= f_y\end{aligned}\tag{3.1}$$

where x , y and z are the components of the target in the positive local vertical horizontal local vertical (LVLH) frame as shown in Figure 3-3. The specific force, \vec{f} , represents non-gravitational accelerations, and ω is the orbital rate, $\omega = \frac{2\pi}{\text{Orbital Period}}$. The C-W equations represent a linear, although coupled, description of chaser vehicle motion.

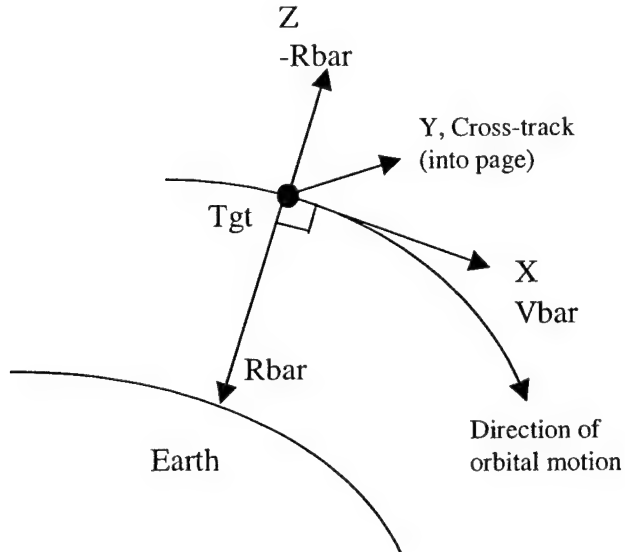


Figure 3-3: Target-centered LVLH coordinate frame

The next restriction on the trajectories of the chaser and target is an upper limit on the difference in their inclinations, and thereby the relative cross-track motion. In practice, cross-track motion could also be generated by a difference in the ascending node of the two orbits, but for this study only inclination differences are used. This cross-track motion constraint is based on the mission reality of the high fuel cost associated with performing plane change maneuvers. Even if orthogonal orbital planes proved to be the most useful from a range observability standpoint, it is very unlikely that any LEO spacecraft would have the capability to transfer into the target orbit to affect a rendezvous with acceptable closing velocity. Assuming that a simple plane change maneuver from one circular orbit to another at a different inclination through the angle θ is executed, then according to Sellers [22], the ΔV required will be

$$\Delta V = 2V_{\text{initial}} \sin\left(\frac{\Theta}{2}\right) \quad (3.2)$$

In order to keep the ΔV less than 100 m/s, the maximum plane change angle to consider would be (using the initial velocity associated with a 500km circular orbit, 7.6km/sec) less than 1 degree and would be less than 7.5° to keep the ΔV below 1km/sec.

3.2.2 Shifted Altitude Metric

Before actually looking at relative trajectories, the shifted altitude metric merits a brief explanation. This measure was first proposed as a figure of merit by Stan Shepperd of The Draper Laboratory regarding elliptic orbit rendezvous. In the current study, it is the method used only in plotting trajectories that allows an easier visualization of the relative motion. For small chaser-target separations and nearly circular orbits, the difference between this method and using the LVLH frame is very small. The method is presented simply for completeness. Figure 3-4 shows exactly what the shifted altitude value refers to. The actual target is propagated backwards in time until its velocity vector is parallel to the chaser velocity vector. The length of the normal vector intersecting both the chaser and target velocity vectors is then termed the relative altitude between the vehicles.

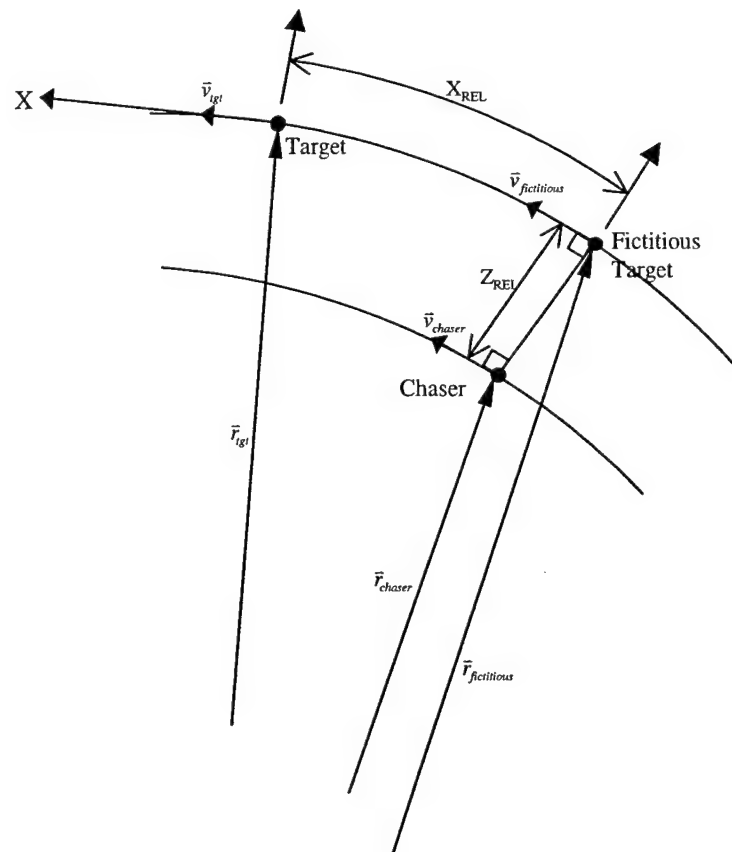


Figure 3-4: Shifted altitude method

3.2.3 Station-keeping

The two potential types of station-keeping orbits are co-circular orbits and football type orbits. Both of these can then be modified with the addition of out-of-plane, or cross-track, motion. The co-circular orbit is the simplest possible relative trajectory. Inertially, both the target and chaser are in identical orbits, and in the LVLH target centered frame the chaser is motionless. In terms of orbital elements, the chaser and target are identical except for the true anomaly, ν , of the chaser being chosen to give the desired downrange separation between the orbits.

An example of a co-circular orbit with cross-track motion is shown in the relative motion plot in Figure 3-5. The relative motion plots are broken into three views from different perspectives which are the side/in-plane profile (altitude vs. downrange), a front view (altitude vs. cross-track), and a top view (cross-track vs. downrange). In addition, the downrange axis is opposite of its actual value so that the plots are easier to read (e.g. 10km downrange in the plot actually corresponds to the chaser being 10km behind the target). In this particular case, the chaser is 10km away from the target and is oscillating 10km out-of-plane. Note that the characteristic lack of motion for a co-circular orbit is clear in the in-plane plot.

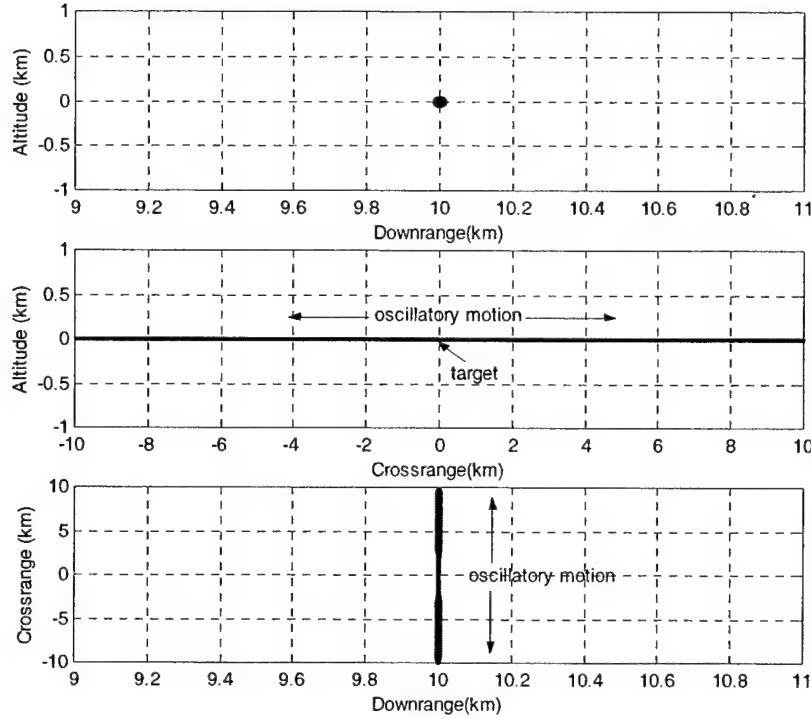


Figure 3-5: Co-circular station-keeping 10km away with 10km of cross-track motion

The second type of station-keeping is the football which gets its name because the shape of the relative motion trajectory literally looks like a football. It is actually an ellipse where the relative ellipse semi-minor axis lies along the relative altitude direction and the relative ellipse semi-major axis, which is exactly twice the value of semi-minor axis, lies along the downrange direction. This two by one shape is a result of the relative motion orbital mechanics in (3.1). From an inertial point of view, the football orbit is created by introducing eccentricity, e , in the chaser orbit according to:

$$|e|_{chaser} = \frac{\text{desired vertical motion}}{a_{\text{target}}} \quad (3.3)$$

where a is the semi-major axis. Figure 3-6 shows a football which is centered 100m away from the target and has 10m of vertical motion. Note that 10m of vertical motion refers to the altitude going between -10m and +10m. This case also has 10m of cross-track oscillation which can be added to any given orbit by modifying the chaser's orbital inclination, i , according to:

$$i_{chaser} = \left(i_{target} - \frac{\text{desired crosstrack motion}}{a_{target}} \right) rad \quad (3.4)$$

Adding cross-track motion results in a relative ellipsoid shape that does not necessarily have a two by one semi-major to semi-minor axis ratio, although the elliptical in-plane projection of the ellipsoid will still retain this characteristic.

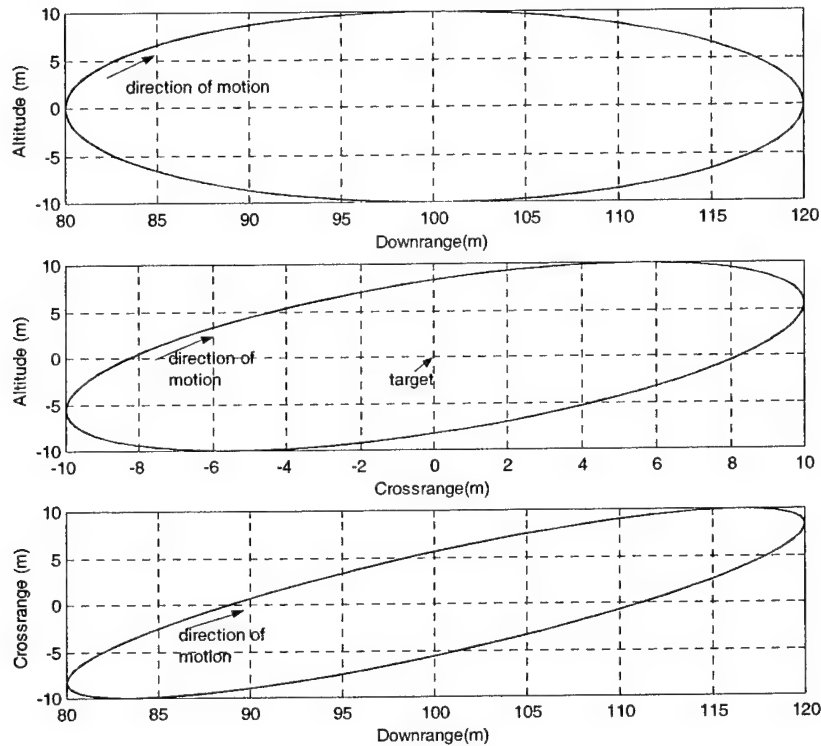


Figure 3-6: Football station-keeping 100m away, 10m vertical motion with 10m of cross-track motion

Another potential variation on the station-keeping football is the case where the target is actually enclosed by the football itself. The football still maintains its characteristic shape as in Figure 3-7. This shows the chaser in a football orbit with 1km of vertical motion centered on the target.

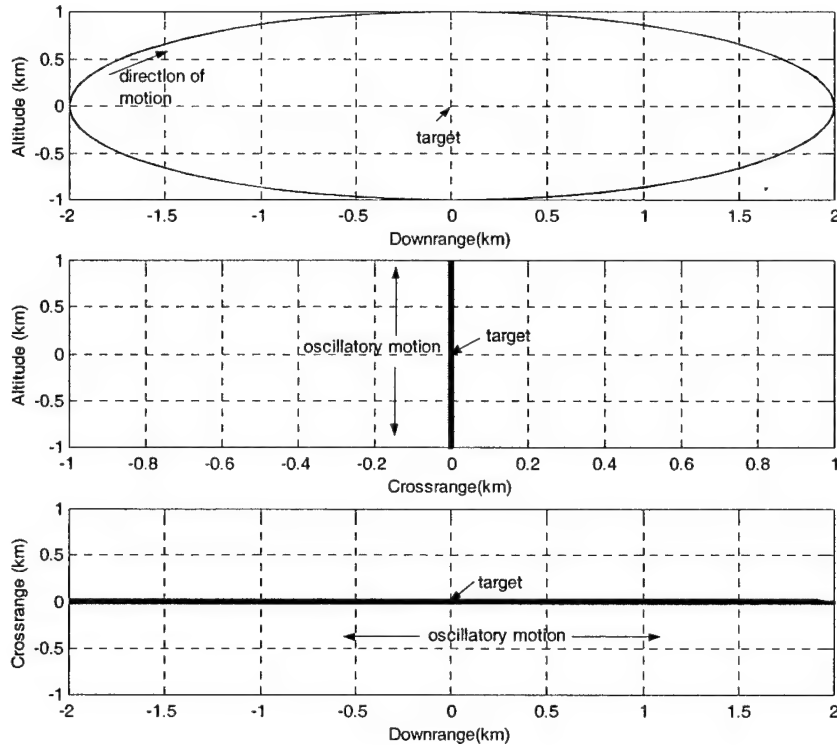


Figure 3-7: Football station-keeping centered on target, 1km vertical motion

The co-circular and football orbits were used as the basis for all of the natural motion station-keeping trajectories. The full list of station-keeping trajectories is in Table 3-1. The various cases were chosen to try to best isolate the characteristics that lead to improved range observability. For example, the case of the co-circular orbit with 1km separation is modified by incrementally increasing the amount of cross-track motion in order to gain better insight into how this particular geometric change will affect range observability at varying levels of extremity.

		Station-keeping Natural Motion Trajectories
Long Range		
	Co-circular	
		10km away
		10km away, 10km cross-track
		10km away, 100km cross-track
		100km away
		100km away, 100km cross-track
	Football	
		30km away, 10km vertical motion
		30km away, 10km vertical motion, 100km cross-track
		300km away, 100km vertical motion
		300km away, 100km vertical motion, 100km cross-track
Short Range		
	Co-circular	
		1km away
		1km away, 1.7km cross-track
		1km away, 1km cross-track
		1km away, 577m cross-track
		1km away, 268m cross-track
		1km away, 87m cross-track
	Football	
		Centered, 1km vertical motion
		Centered, 1km vertical motion, 1km cross-track
		1km away, 100m vertical motion
		1km away, 100m vertical motion, 1km cross-track
		1km away, 1km vertical motion (encircles tgt)
		1km away, 1km vertical motion, 1km cross-track (encircles tgt)
		5km away, 100m vertical motion
		5km away, 100m vertical motion, 1km cross-track
		10km away, 100m vertical motion
		10km away, 100m vertical motion, 1km cross-track
		10km away, 1km vertical motion
		10km away, 1km vertical motion, 1km cross-track
Prox Ops		
	Co-circular	
		100m away
		100m away, 10m cross-track
		100m away, 100m cross-track
	Football	
		100m away, 10m vertical motion
		100m away, 10m vertical motion, 10m cross-track
		100m away, 10m vertical motion, 100m cross-track

Table 3-1: Natural motion station-keeping reference trajectories

3.2.4 Closure

The major difference between closing and station-keeping trajectories is that there is a semi-major axis difference between the chaser and target for the closing trajectories, and no semi-

major axis difference for the station-keeping trajectories. This semi-major axis difference, which appears as a non-zero average altitude difference, or Δh , in the relative motion trajectory, causes the two orbits to have different periods, and therefore the chaser will close on or move away from the target. There are three basic types of closing orbits including coelliptics, ‘V-bar hops,’ and traveling footballs. The first and simplest of these is the coelliptic. Mathematically, a coelliptic is defined by requiring the product of the semi-major axis and eccentricity of both the chaser and target orbits to be equal as in:

$$a_{\text{target}} \hat{e}_{\text{target}} = a_{\text{chaser}} \hat{e}_{\text{chaser}} \quad (3.5)$$

Note that the eccentricity is vector valued meaning that the direction of periapsis for both orbits lies along the direction of the same unit vector, \hat{e} . Physically, the coelliptic can be visualized as the elliptical equivalent of concentric circles. The lower orbit has higher linear velocity and therefore if the chaser is below the target it will close on it. In fact, at the very low eccentricities dealt with in this study, the coelliptic is very nearly just a concentric set of circular orbits. A relative motion plot for a coelliptic with 10km Δh is shown in Figure 3-8.

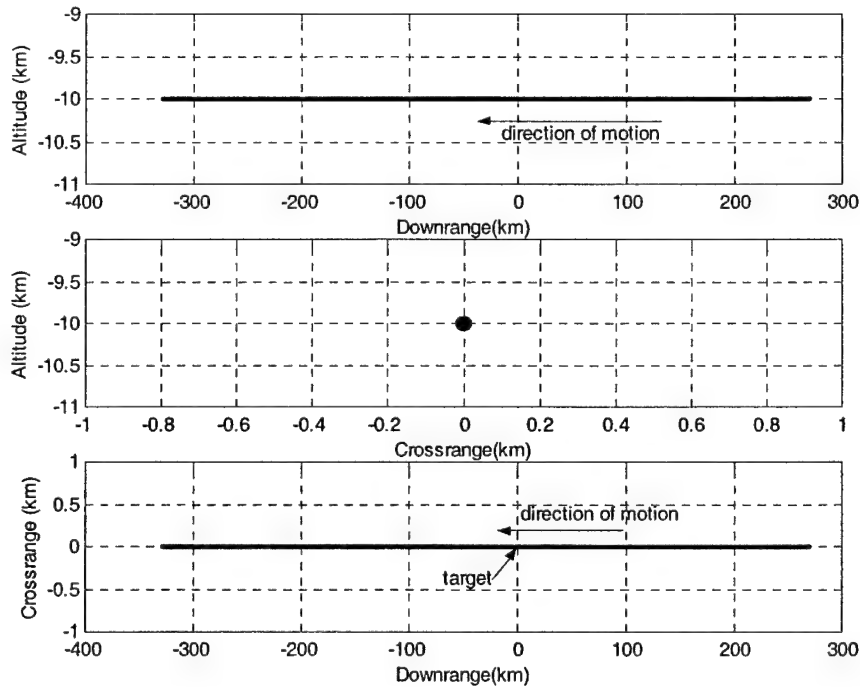


Figure 3-8: Coelliptic with 10km Δh

The next type of closing trajectory is a V-bar hop. In addition to the Δh used for the coelliptic, eccentricity is also added to the chaser orbit to induce vertical motion according to equation (3.3). By setting this vertical motion equal to the Δh , the relative motion trajectory closes on the target while also ‘hopping’ up to the V-bar. An example is shown in Figure 3-9 which shows an average $1\text{km } \Delta h$ so the chaser bounces between -2km and 0 in altitude while also closing on the target starting 30km behind it and winding up about 30km in front of it.

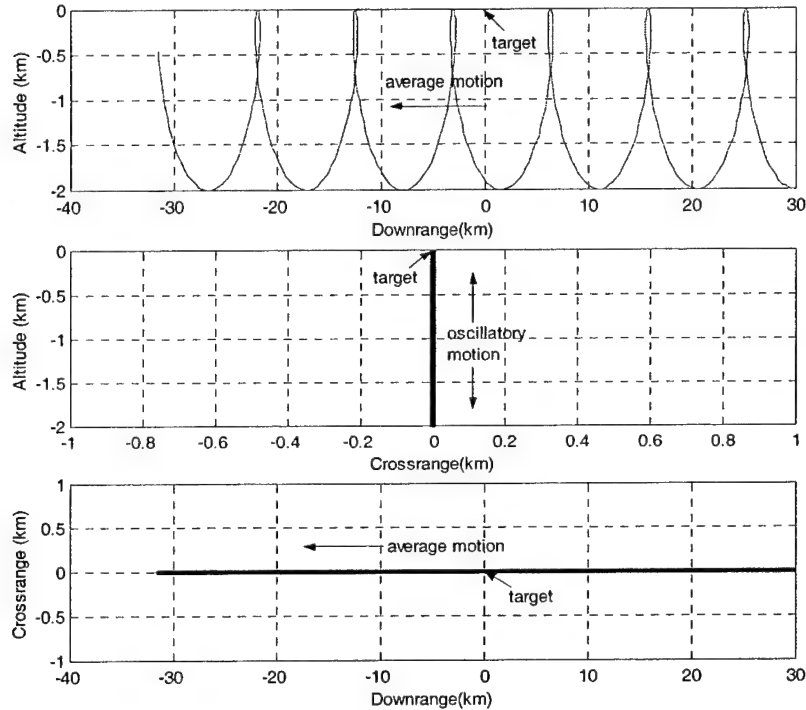


Figure 3-9: V-bar hops with $1\text{km } \Delta h$

The final type of closing trajectory is the traveling football. This is very similar to the V-bar hop except that the vertical motion is greater than the Δh resulting in a traveling ellipse when viewing the relative motion. Due to the closing velocity, the traveling football does not have the two by one aspect ratio that was characteristic of the station-keeping case. Figure 3-10 shows a traveling football with a $10\text{m } \Delta h$ and 100m of vertical motion resulting in altitude oscillations between -110m and 90m . It also includes 10m of cross-track motion which can easily be added to any of the closing trajectories by using equation (3.4).

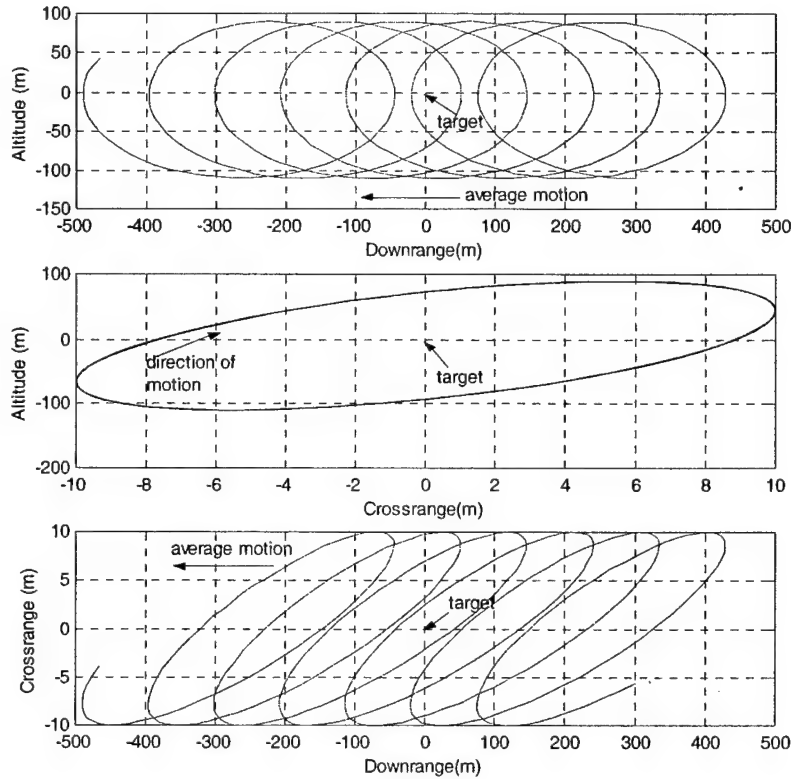


Figure 3-10: Traveling football with 10m Δh and 100m of vertical motion with 10m of cross-track motion

These three basic types of closing trajectories form the basis for all of the various trajectories that were studied. As was the case with station-keeping, the variations are chosen to provide comparisons that will hopefully yield insight into the range observability problem. Combined with the station-keeping cases, the complete listing of natural motion closing trajectories in Table 3-2 provides the basis for the natural motion range observability analysis.

		Closure Natural Motion Trajectories
Long Range		
	Coelliptic	
		10km Δh
		10km Δh , 100km cross-track
		100km Δh
		100km Δh , 100km cross-track
	V-bar 'hops'	
		10km Δh , 10km vertical motion
		10km Δh , 10km vertical motion, 100km cross-track
		100km Δh , 100km vertical motion
		100km Δh , 100km vertical motion, 100km cross-track
	Traveling Football	
		5km Δh , 10km vertical motion
		50km Δh , 100km vertical motion
Short Range		
	Coelliptic	
		1km Δh
		1km Δh , 1km cross-track
		5km Δh , 10km vertical motion
		5km Δh , 1km cross-track
	V-bar 'hops'	
		334m Δh , 334m vertical motion
		334m Δh , 334m vertical motion, 1km cross-track
		1km Δh , 1km vertical motion
		1km Δh , 1km vertical motion, 1km cross-track
	Traveling Football	
		100m Δh , 1km vertical motion
		100m Δh , 1km vertical motion, 1km cross-track
Prox Ops		
	Coelliptic	
		10m Δh
		10m Δh , 10m cross-track
		33m Δh
		33m Δh , 10m cross-track
		100m Δh
		100m Δh , 100m cross-track
	V-bar 'hops'	
		0.1m Δh , 0.1m vertical motion
		1m Δh , 1m vertical motion
		1m Δh , 1m vertical motion, 1m cross-track
		5m Δh , 5m vertical motion
		5m Δh , 5m vertical motion, 10m cross-track
		33m Δh , 33m vertical motion
		33m Δh , 33m vertical motion, 10m cross-track
		200m Δh , 200m vertical motion, R-bar approx.
		200m Δh , 200m vertical motion, 10m cross-track R-bar approx.
	Traveling Football	
		10m Δh , 100m vertical motion
		10m Δh , 100m vertical motion, 10m cross-track
		10m Δh , 100m vertical motion, 100m cross-track
		0.1m Δh , 0.5m vertical motion V-bar approx.
		0.1m Δh , 0.5m vertical motion, 1m cross-track V-bar approx.

Table 3-2: Natural motion closure reference trajectories

3.3 LINEAR COVARIANCE RESULTS

With the natural motion reference trajectories generated, the next step is to use the LINCov analysis tool to better understand range observability with angles-only measurements. As explained in section 2.2.3 these reference trajectories are the nominal state trajectories that will be used as the truth model. The LINCov tool demonstrates what the navigation filter performance would be if only angular measurements were taken and used to estimate the relative position and velocity of the target. Examining the downrange uncertainty should provide insight as to which types of behavior can potentially lead to successful angles-only navigation. As with the development of the reference trajectories, the covariance results are best understood when looking at the cases of station-keeping and closure separately. The results shown here are representative examples of patterns that arose during the analysis of hundreds of trajectory results.

3.3.1 Setup

Although the final goal of this study is to understand angles-only navigation performance in the presence of all the error sources discussed in section 2.2.3, it is first necessary to build a more intuitive understanding. In keeping with the spirit of performing only a qualitative analysis at this point, nearly all of the error sources are eliminated for now in the covariance analysis. The only exception is the placement of zero-mean uncorrelated random noise errors with 1° - 3σ , on the angular measurements themselves, as described in Figure 2-3. These measurements are taken every 60 seconds and are always available. The possibility of condition dependent measurement availability is also considered later in section 3.4.2, but will be shown to not have any significant effect on the results. The last assumption is that the chaser is always bore-sighted on the target. Thus, attitude control issues are eliminated from the analysis, except in terms of the angle measurement errors.

Another factor to consider is the setup of the *a priori* navigation uncertainties. For this study, two different methods were used. The first method is to place identical position and velocity uncertainties on both vehicles in the inertial frame regardless of their initial relative position. This would be realistic in the real-world scenario where both vehicles were being tracked and monitored by ground stations or using a form of GPS (Global Positioning Satellite) on-board orbit determination. The second alternative is to assume that the initial position and velocity uncertainties on the vehicles are a function of their initial relative separation. This has

the advantage of lending itself to easier comparison of covariance results across different range regimes. Also, it is more realistic in the sense that the absolute uncertainty values associated with the first method would prohibit a number of the short-range and proximity operations cases. For example, if 100m was selected to always be the initial inertial uncertainty this would be fine for two vehicles starting 10km apart, but unacceptable for a prox ops case when they are only 100m apart to begin with. For the results presented in sections 3.3.2 and 3.3.3, the latter method of selecting *a priori* values was used. Specifically, the standard deviation of the *a priori* position uncertainty is chosen to be 1% of the actual initial range, and the standard deviation of the velocity uncertainty is $1/10,000^{\text{th}} \text{ sec}^{-1}$ of the position uncertainty. The $1/10000^{\text{th}} \text{ sec}^{-1}$ proportion is representative of several applications such as GPS, Deep Space Network (DSN), or ground tracking where the position uncertainty is on the order of 100m and the corresponding velocity uncertainty is $1/10000^{\text{th}} \text{ sec}^{-1}$ of the position uncertainty, on the order of 1cm/sec. The first method of setting *a priori* uncertainty will also be explored later but will be shown to have no significant effects on the qualitative conclusions.

An important need that must be addressed before generating results is a method to normalize the results across different target-chaser separation distances. Consider the problem of two station-keeping footballs, one of which is 100m from the target and the other is 10km from the target. They have similar geometries with 10m and 1km of vertical motion respectively. However, the covariance results would show that the football 100m away has a lower absolute value of range uncertainty than the one further away. This can be deceptive because the difference is not caused by the geometry of the trajectory but rather the fact that the position uncertainty produced by the noise on the angular measurements increases the further the chaser is from the target. In order to normalize the results one possible approach would be to change the noise level on the angles depending on the ranges involved. However, this would generally be an unrealistic model. A simpler method, and the one used in this study, is to present the uncertainty results as a percent of the true range. This effectively removes the range dependence in the results and allows for more direct comparisons.

3.3.2 Station-keeping

The LINCOV tool is first applied to the station-keeping orbits. In looking at the results, it is easiest to consider them grouped by the general type of relative motion trajectory the orbit falls under: co-circular, or football.

Co-circular Orbits

The most immediate result that came out of the station-keeping analysis was a demonstration of the expected problem with angles-only navigation. When the chaser is in the same orbit as the target, it is impossible for the chaser to gain any downrange information about the target so the uncertainty grows with time. This can be seen in Figure 3-11 and Figure 3-12 which are the results for a case of the chaser being in a co-circular orbit separated from the target by 1km. Figure 3-11 shows that both the inertial and relative uncertainty is growing while Figure 3-12 shows that after the initial filter transient, the relative downrange error starts growing while the other components approach zero.

As an aside, Figure 3-11 also demonstrates how the target and chaser root sum square (RSS) inertial, or absolute, uncertainties grow to very large values compared to the relative RSS uncertainty. This occurs because inertial uncertainty growth that takes place identically on both vehicles does not affect the relative uncertainty. For example, if the absolute uncertainty on the target is 105m in a given direction and the absolute uncertainty on the chaser is 100m in the same direction, then the relative uncertainty is only 5m. The fluctuations in the inertial RSS uncertainty correspond to the fact that the downrange error component has both linear and periodic components.

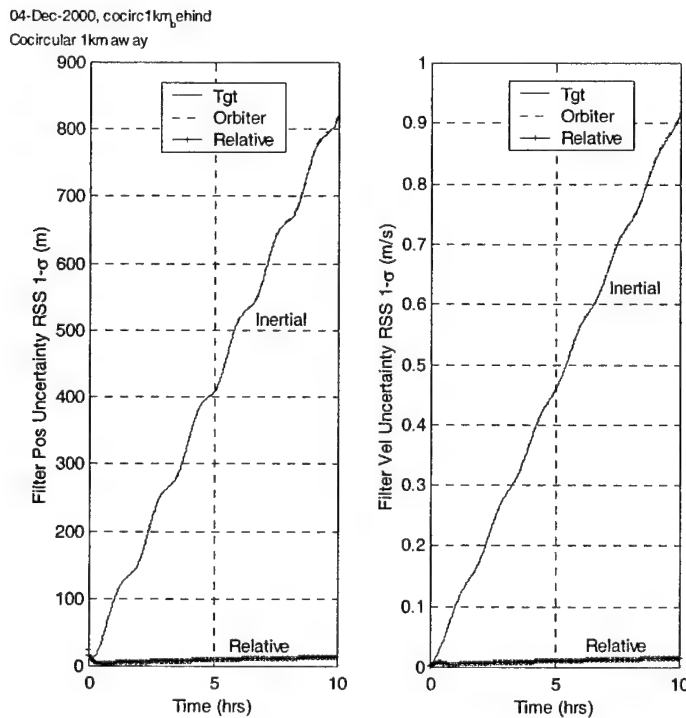


Figure 3-11: Inertial and relative RSS uncertainty for Co-circular station-keeping 1km away

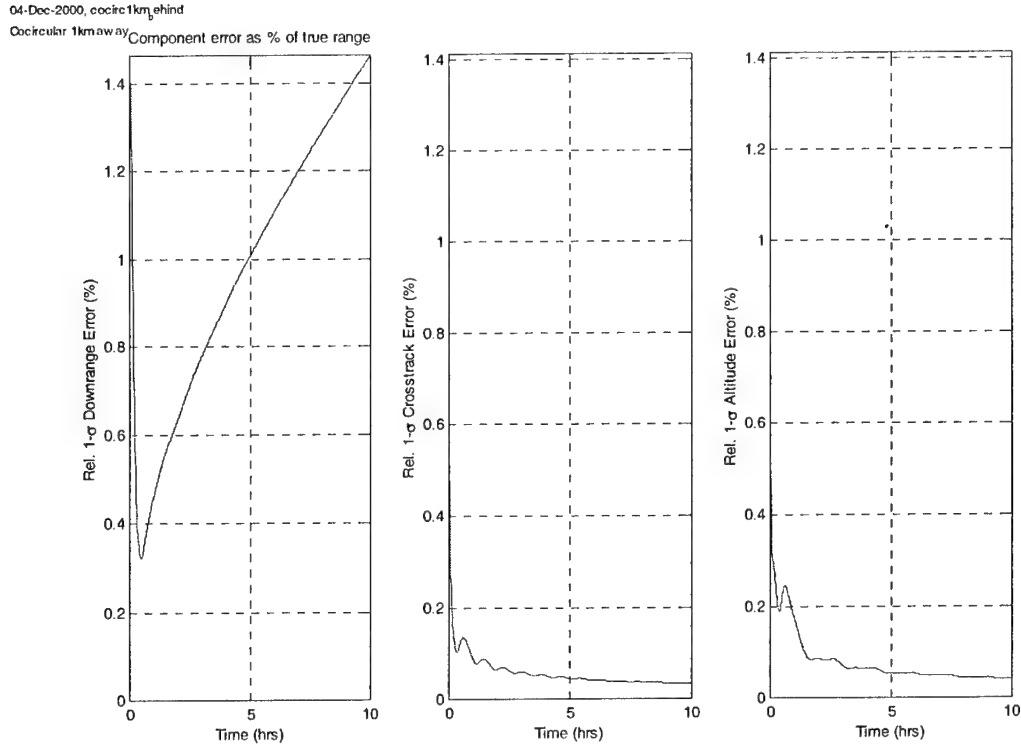


Figure 3-12: Relative position uncertainty for Co-circular station-keeping 1km away

The initial drop in downrange uncertainty during approximately the first half-hour is due to two effects. First, the navigation system initially undergoes transient behavior as the measurements begin to provide additional information beyond the *a priori* knowledge. Secondly, the level of *a priori* velocity uncertainty is mismatched with the *a priori* position uncertainty. This means that during the transient period, the filter's position uncertainty decreases while the velocity uncertainty increases until the two values are balanced. This will be shown again in section 3.3.3.

Clearly the lack of any relative motion by the chaser results in unbounded downrange error growth. A simple method of introducing some line-of-sight stimulus between the chaser and target is to use natural cross-track motion. Even the smallest amount of motion, in this nearly perfect error environment, is enough to drive down the downrange uncertainty over a long enough period of time. Figure 3-13 shows the case of the same co-circular orbit as before, 1km away, except this time with the addition of 87m of cross-track motion. This is equivalent to

$$\tan^{-1}\left(\frac{87}{1000}\right) \approx 5^\circ \text{ of motion.}$$

Natural Motion Range Observability

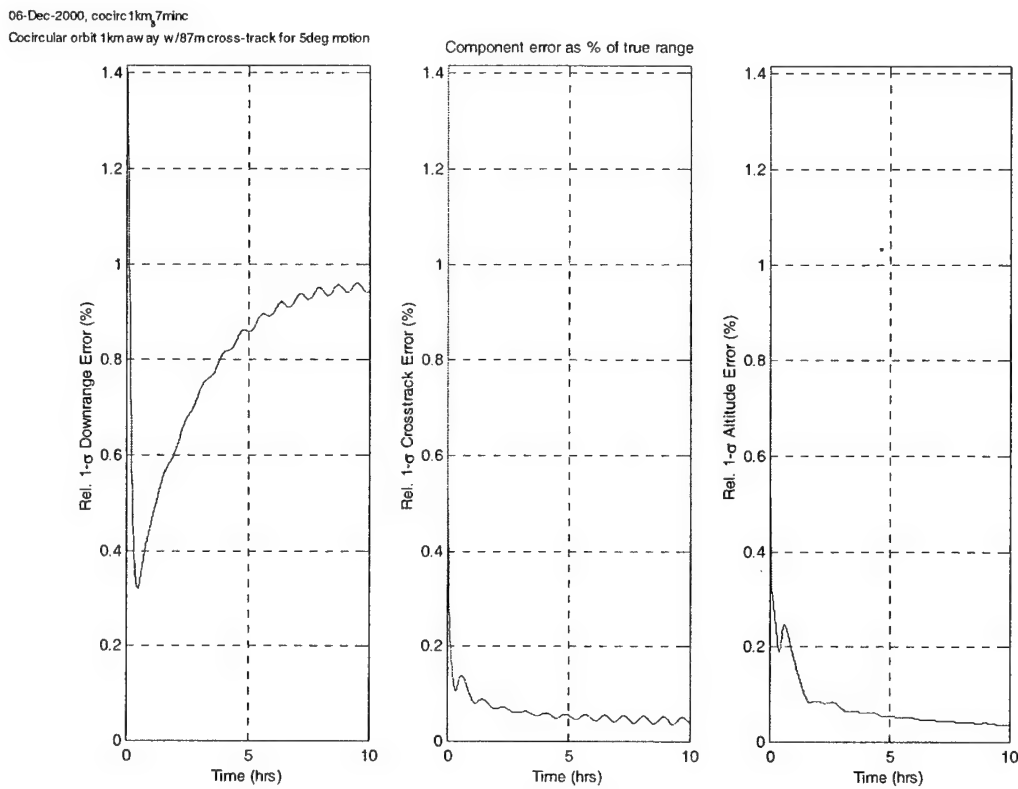


Figure 3-13: Relative position uncertainty for Co-circular station-keeping 1km away with 87m cross-track motion

Note that the addition of the cross-track motion also introduced some oscillation into the cross-track uncertainty channel that was not present in Figure 3-12. Although it does not appear that the downrange uncertainty is decreasing, by extending the time period to four days, Figure 3-14 shows that it is in fact going down.

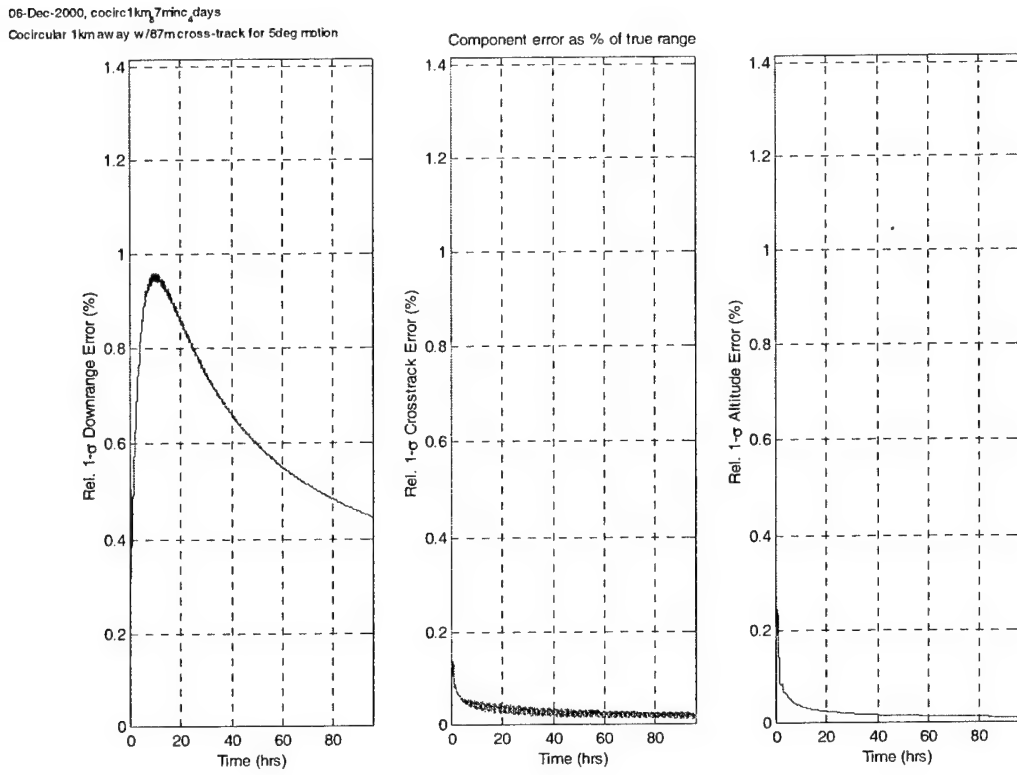


Figure 3-14: Relative position uncertainty over 4 days for Co-circular station-keeping 1km away with 87m cross-track motion

More extreme geometry changes lead to the errors decreasing faster. By increasing the cross-track motion to 268m (15°) and further still to 1km (45°), Figure 3-15 and Figure 3-16 respectively show the downrange errors decreasing progressively more quickly. Again, though, the decreasing downrange uncertainty comes at the cost of increasing the cross-track errors.

Natural Motion Range Observability

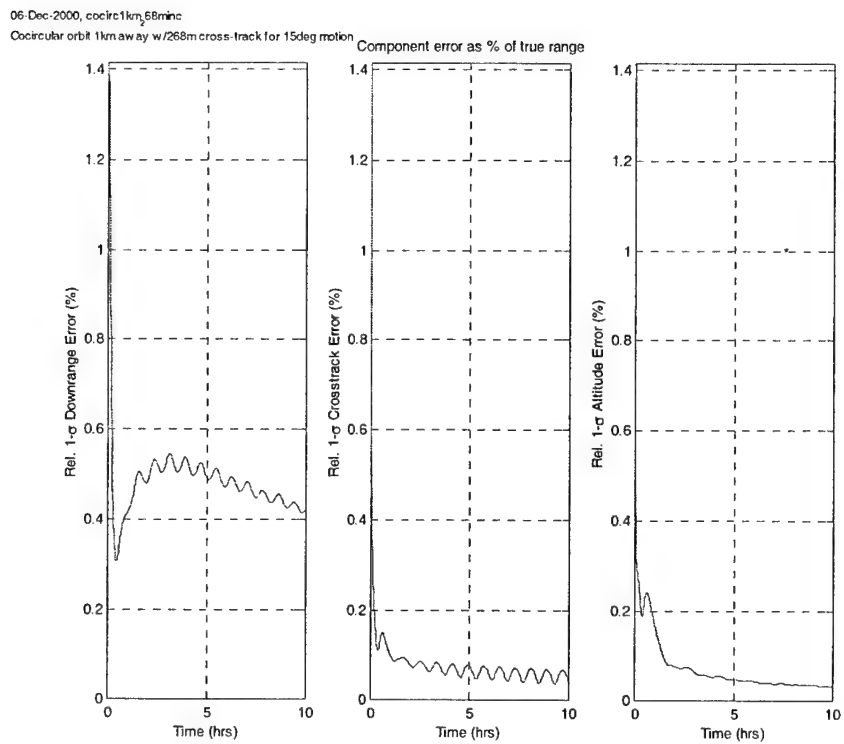


Figure 3-15: Relative position uncertainty for Co-circular station-keeping 1km away with 268m cross-track motion

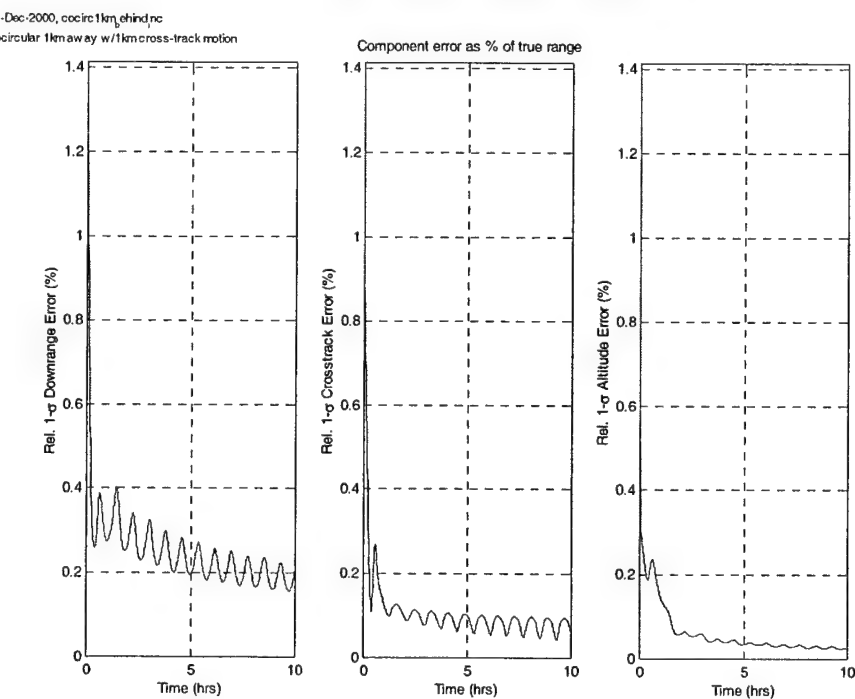


Figure 3-16: Relative position uncertainty for Co-circular station-keeping 1km away with 1km cross-track motion

Station-keeping Football

The other type of station-keeping trajectory explored is the football, shown schematically in Figure 3-17.

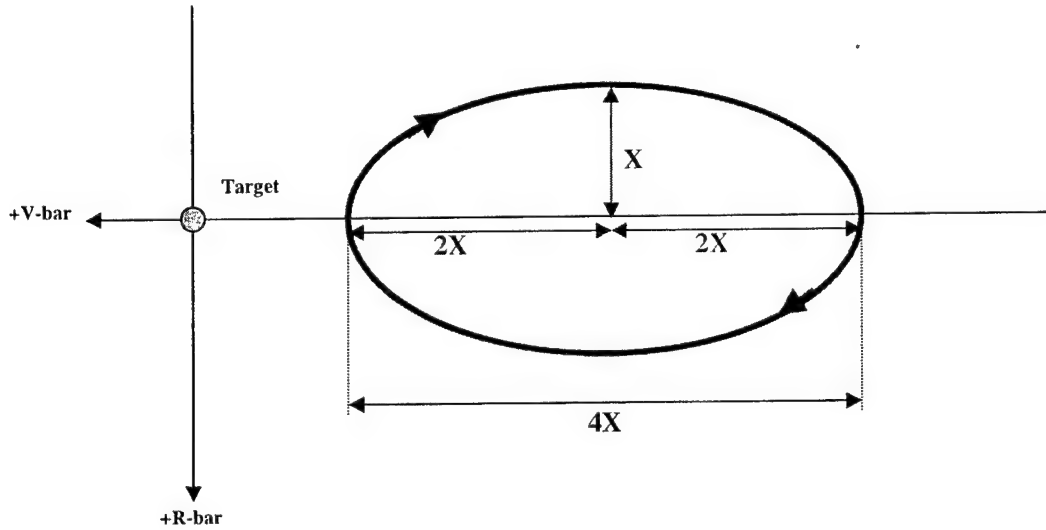


Figure 3-17: Station-keeping football relative motion schematic

Despite their vertical motion, football orbits actually wind up generating similar results to the co-circular cases for equivalent amounts of motion normal to the line-of-sight to the target. For example, the case shown in Figure 3-18 is a football centered 100m away from the target with 10m vertical motion. This is approximately the same amount of motion perpendicular to the line-of-sight as for the case of the co-circular orbit 1km away with 87m of cross-track motion in Figure 3-13. Even though one is a football orbit and one is co-circular, the results look somewhat similar when comparing the downrange uncertainty. The one significant difference though is that the football's vertical motion introduces oscillation into the altitude uncertainty channel much as the cross-track motion affected the co-circular orbit's cross-track uncertainty.

Natural Motion Range Observability

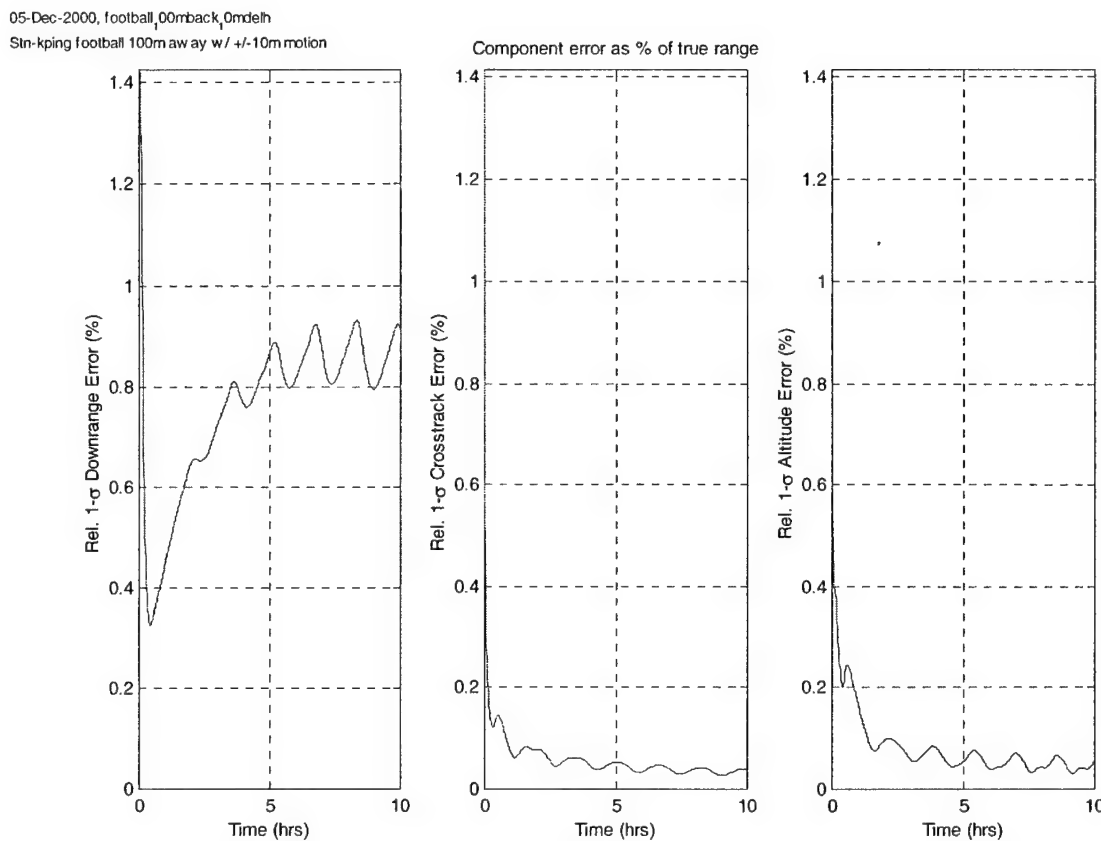


Figure 3-18: Relative position uncertainty for Football station-keeping 100m away with 10m vertical motion .

As the geometry provided by the football increases, the downrange errors decrease more quickly, similar to the behavior of co-circular cases. The case of a football centered 300km from the target with 100km of vertical motion and 100km of cross-track is shown in Figure 3-19. After an initial filter transient the downrange errors do decrease although the significant amounts of cross-track and altitude motion lead to uncertainty persisting in those components.

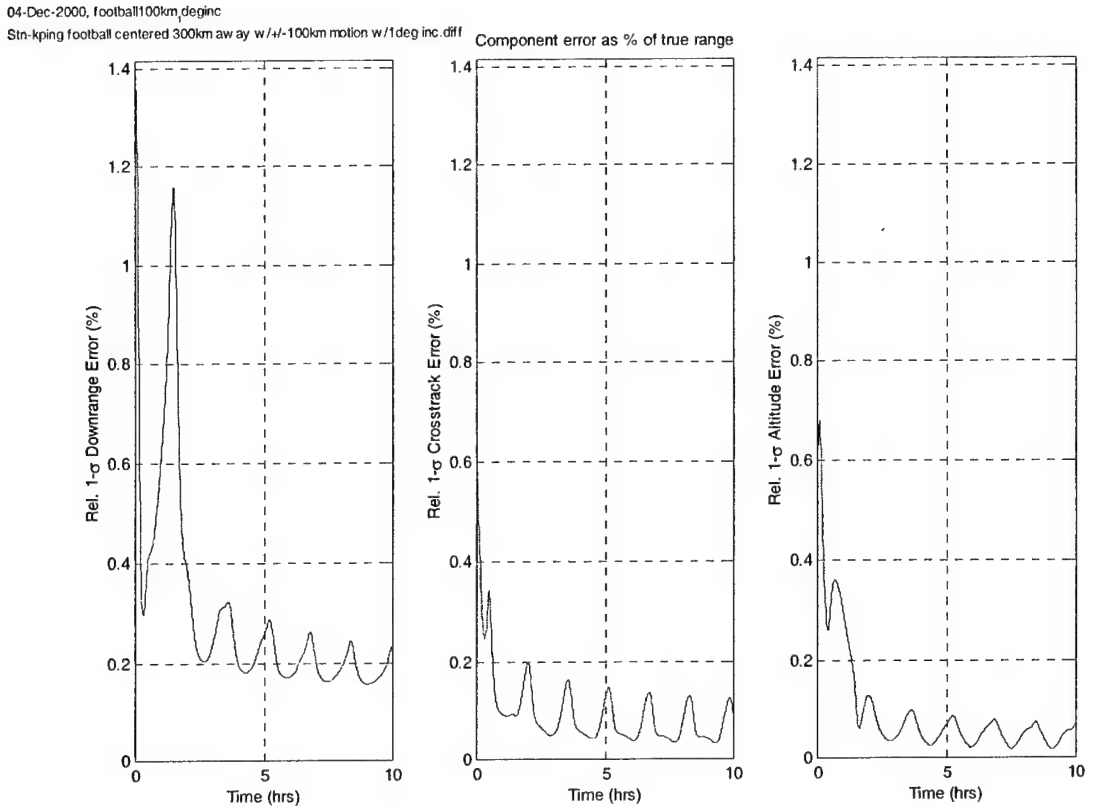


Figure 3-19: Relative position uncertainty for Football station-keeping 300km away with 100km vertical motion and 100km cross-track motion

The best results from the station-keeping football tend to occur when the target is enclosed by the football. The result for a football centered on the target with 1km of vertical motion is shown in Figure 3-20. Interestingly, as is the case with other footballs, even though there is no cross-track motion, there is still an oscillation in the cross-track uncertainty. The oscillations in the altitude and downrange directions are nearly 180° out of phase with one another. This is a concept that will be more fully explored in section 3.4.1.

Natural Motion Range Observability

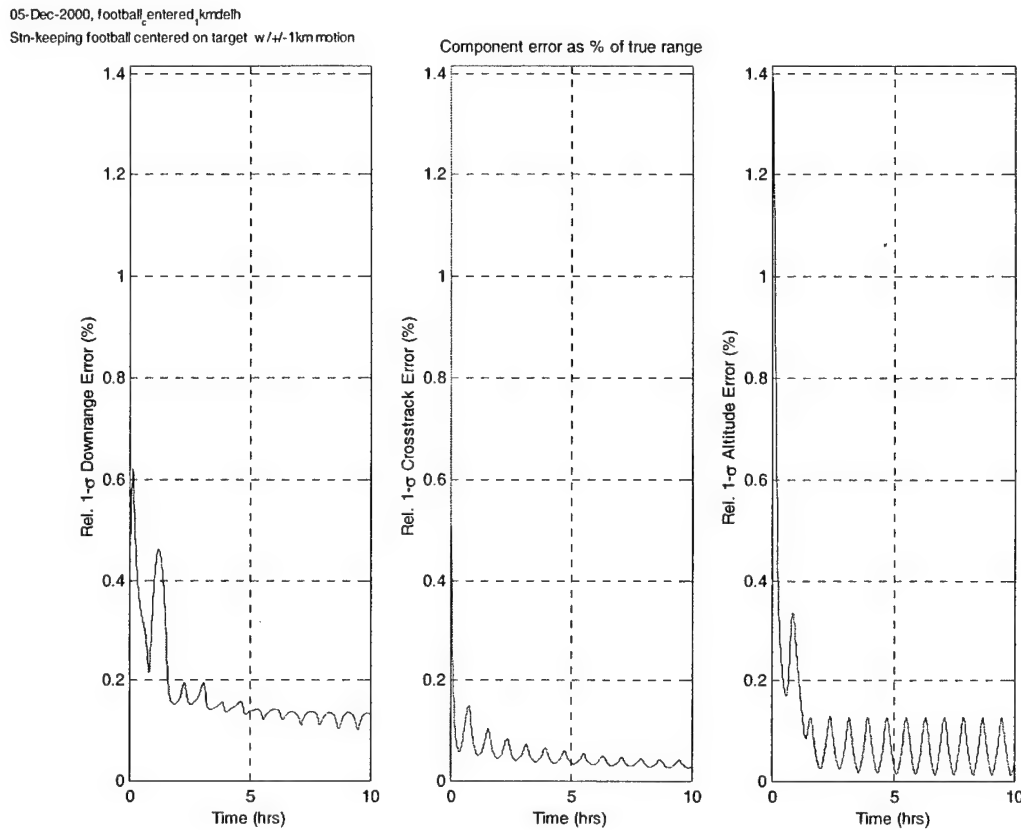


Figure 3-20: Relative position uncertainty for Football station-keeping centered on target with 1km vertical motion

The final point to be made regarding station-keeping footballs is that adding cross-track motion to them does not have any positive effects unless that motion exceeds the existing vertical geometry. For example, the previous case of a football centered on the target is modified to also have 1km of cross-track motion. However, as the results in Figure 3-21 show, it is essentially identical to the case with no cross-track. This is because the football is already providing 1km of motion perpendicular to the line-of-sight so adding 1km of motion in another direction does not have a significant impact.

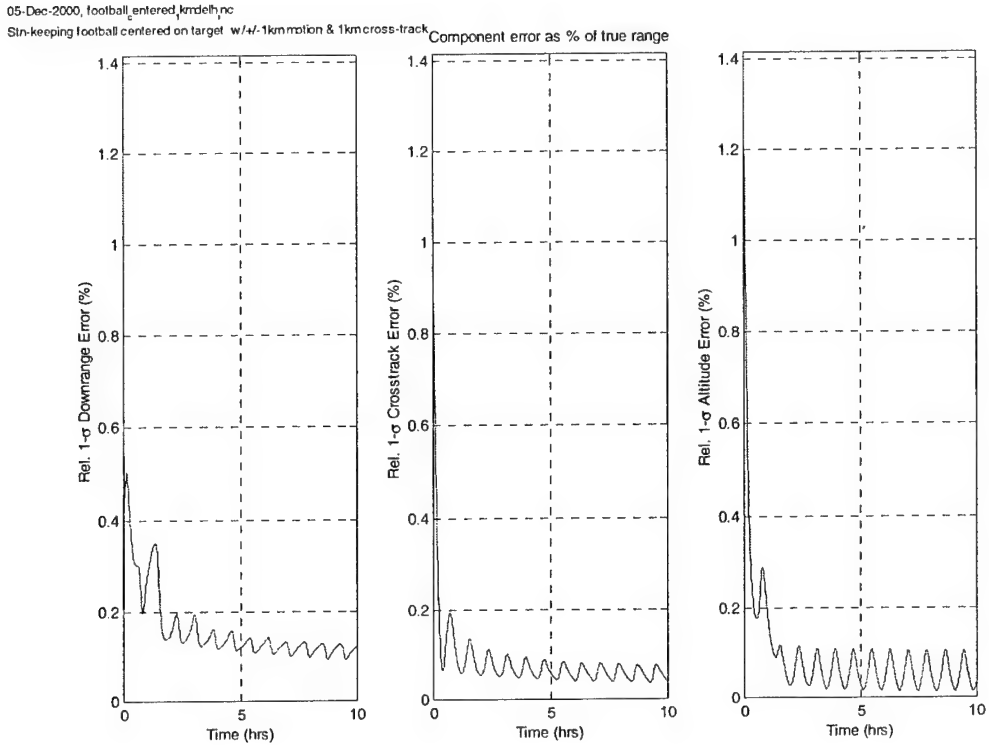


Figure 3-21: Relative position uncertainty for Football station-keeping centered on target with 1km vertical motion and 1km cross-track motion

For the station-keeping cases, it would seem that motion perpendicular to the line-of-sight, no matter how small, results in improving downrange uncertainty. This conclusion follows from intuitive reasoning, considering that this motion can be thought of as similar to triangulating on the target. As a reminder though, the results thus far are only qualitative and although they provide the basis for trajectory comparisons, they are not representative of situations where more realistic error sources and models are considered. With the qualitative knowledge of station-keeping trajectories in hand, the next step is to consider the closure cases.

3.3.3 Closure

As with the station-keeping cases, the LINCOV results for closure trajectories are grouped by the trajectory: coelliptic, V-bar hops, and traveling footballs.

Coelliptic Orbits

The simplest type of closing trajectory to visualize and implement is the coelliptic. Figure 3-22 serves as a reminder of what the relative motion plot looks like.

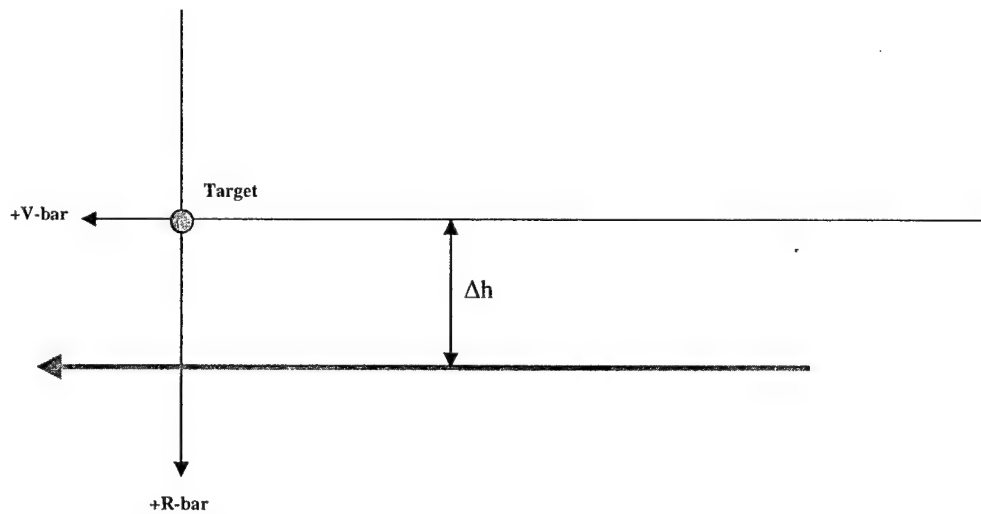


Figure 3-22: Coelliptic relative motion schematic

The most interesting characteristic about the coelliptic trajectory is that the downrange uncertainty is driven to its lowest level at the point when the chaser flies underneath the target. This is clearly shown in Figure 3-23 which shows the actual uncertainty values, not the percentages, for a coelliptic with a 100m Δh where flyby occurs at five hours. Including the velocity uncertainties demonstrates a phenomenon that arises in all trajectories, due to orbital mechanics, where the downrange uncertainty is coupled to the altitude rate uncertainty and the altitude uncertainty is coupled to the downrange rate uncertainty. It also shows a clearer picture of the filter transient due to the *a priori* values. During the transient period, the position uncertainties initially decrease while the velocity uncertainties increase until a balance is struck between the two.

04-Jan-2001, concentric, 00m
Coelliptic orbit w/100m delta h

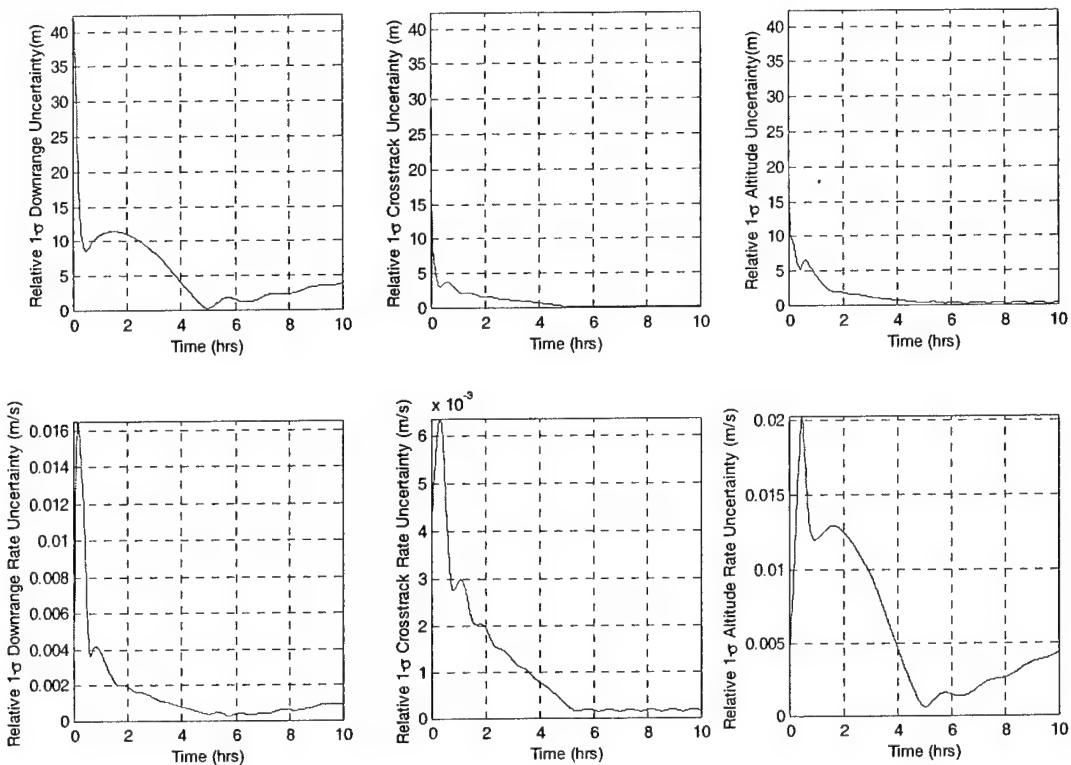


Figure 3-23:Actual relative position & velocity uncertainty values for Coelliptic with 100m Δh

Although the errors for the coelliptic trajectory begin to immediately increase again after the flyby, an important thing to notice is that they do not rise as fast as the chaser is actually moving away from the target. The results with uncertainty as a percent of the actual range clearly show this as the percent error remains at lower levels after the flyby. However, after longer time periods the error will begin to grow again as it would if there were additional error sources. Figure 3-24 shows the same 100m coelliptic, but using the percent errors to demonstrate the post flyby error levels.

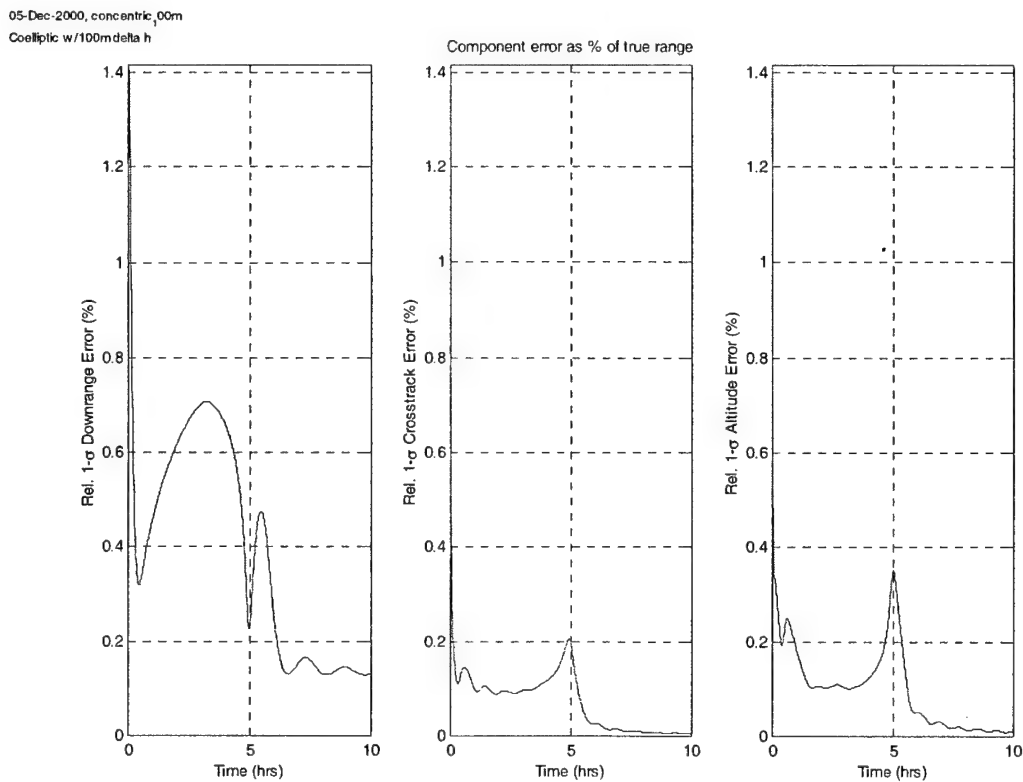


Figure 3-24: Relative position uncertainty for Coelliptic with 100m Δh

Unlike the co-circular station-keeping case, the coelliptic orbits do not seem to benefit from the use of cross-track motion. A large part of the reason for this difference is the difficulty in picking the right amount of natural cross-track motion. For example, in the case of a 1km Δh coelliptic, the chaser starts nearly 3km behind the target in order to pass under it at 5 hours. At this distance, an additional 1km of cross-track motion would not be that significant in terms of geometry. However, at the point of flyby, it would be extreme. Based on this line of thought, the point where the uncertainty would be most improved from cross-track motion is at flyby, however this is already the place that the coelliptic naturally does very well. Therefore, even if the cross-track motion is aiding the range observability, it is difficult to pick that out of the results without resorting to excessively large cross-track values that would improve the results when the chaser was still hours away from flyby. Figure 3-25 and Figure 3-26 show the results for a 1km Δh coelliptic with and without 1km of cross-track motion, respectively.

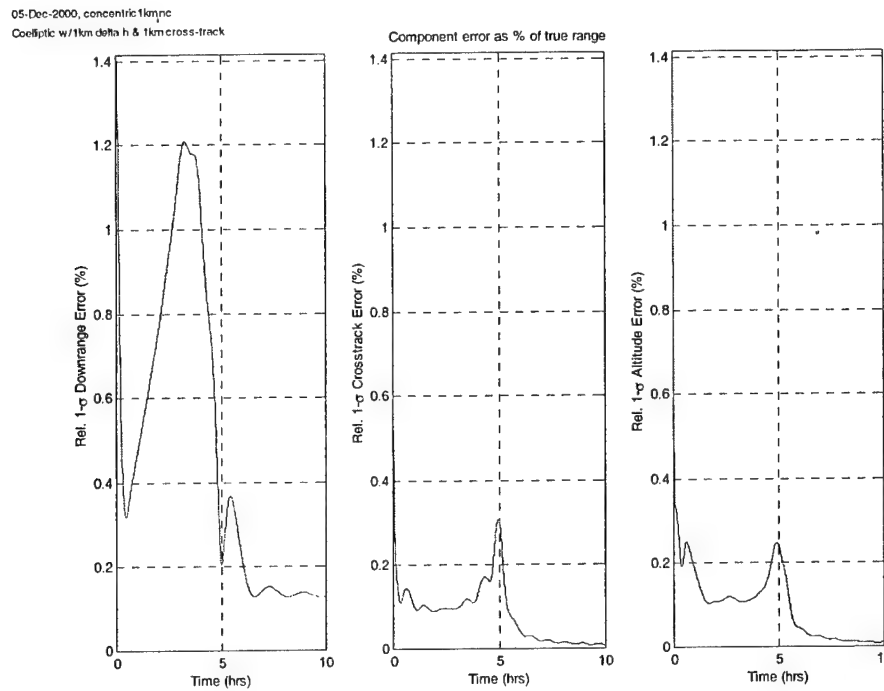


Figure 3-25: Relative position uncertainty for Coelliptic with 1km Δh and 1km cross-track motion

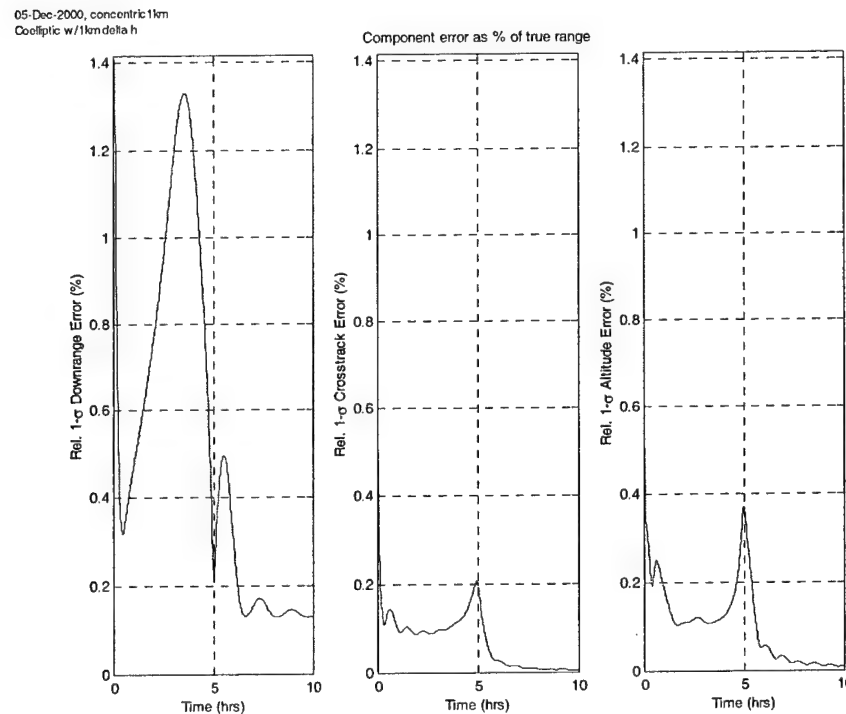


Figure 3-26: Relative position uncertainty for Coelliptic with 1km Δh

V-bar Hop Trajectories

The next type of closing trajectory is the V-bar hop, shown in Figure 3-27.

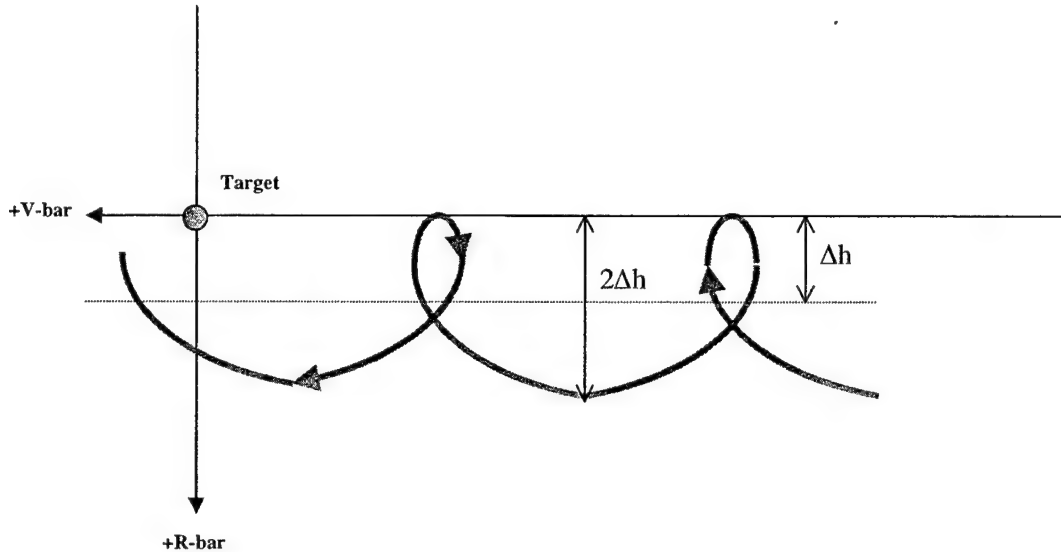


Figure 3-27: V-bar hop relative motion schematic

There is very little to say about these trajectories because the results are virtually identical to those for the coelliptic orbits. The relative vertical motion caused by the eccentricity difference does not appear to aid in improving downrange uncertainty, and in fact induces oscillation in the altitude channel that was not present before, as the station-keeping football had also done. Cross-track motion also has the same general effect on V-bar hops as it did on coelliptics. For comparison, Figure 3-28 and Figure 3-29 below are for the case of a V-bar hop orbit that is centered 1km below the V-bar and fluctuates between -2km and 0 in altitude. Figure 3-28 is the case with 1km of cross-track motion and Figure 3-29 is the standard case with no cross-track motion. Besides being similar to one another, they can also be compared to Figure 3-25 and Figure 3-26 which were the equivalent cases for the coelliptic trajectory.

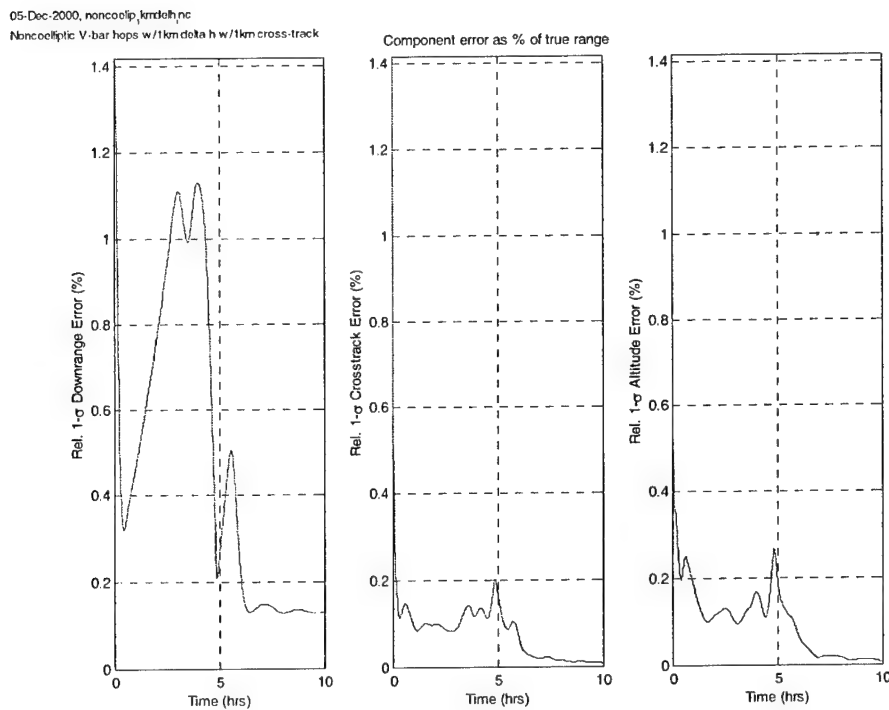


Figure 3-28: Relative position uncertainty for V-bar hops with 1km Δh and 1km cross-track motion

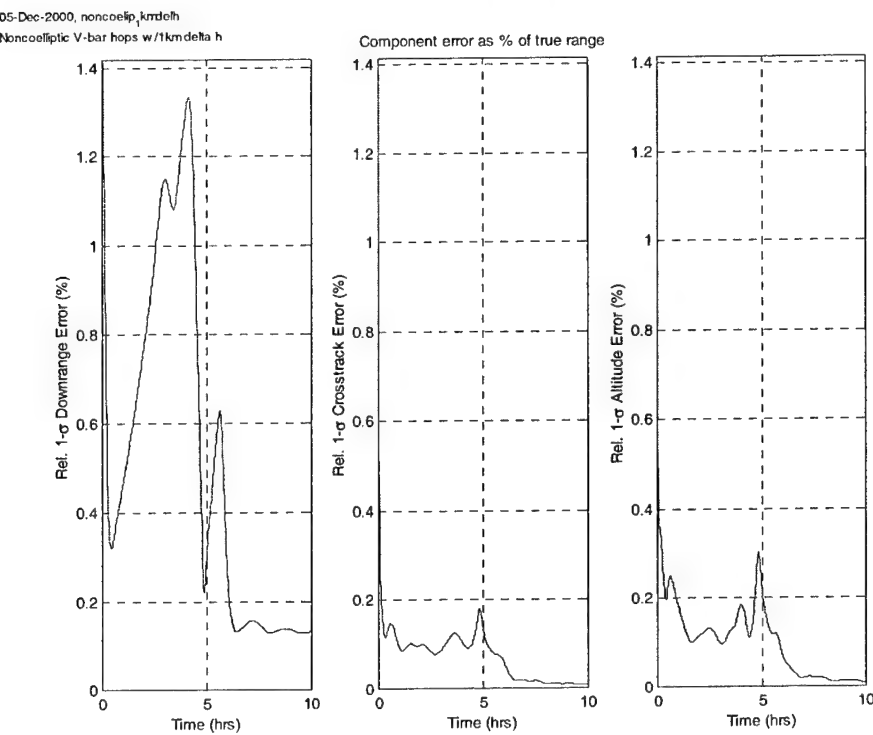


Figure 3-29: Relative position uncertainty for V-bar hops with 1km Δh

Traveling Football Trajectories

The final type of natural motion closing trajectory considered was the traveling football orbit shown schematically in Figure 3-30.

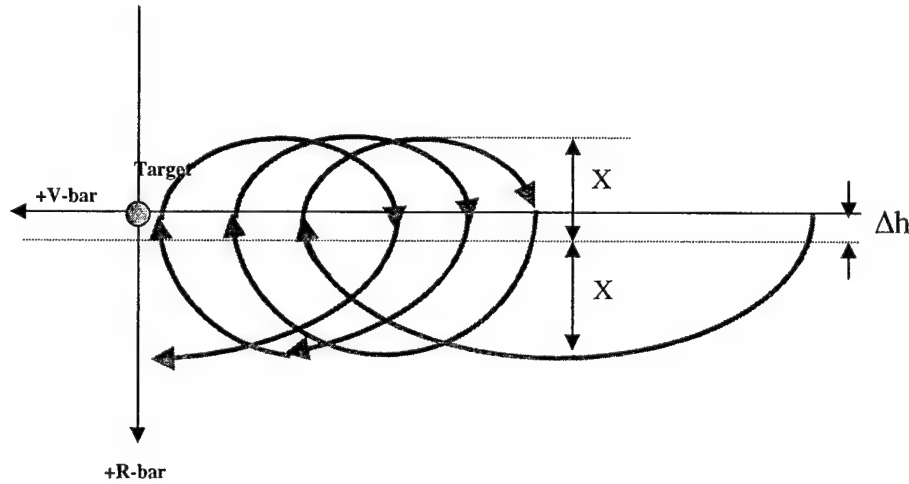


Figure 3-30: Traveling football relative motion schematic

The traveling football trajectories are similar to the other closing trajectory results with one notable exception. Although the traveling footballs do not decrease the downrange uncertainty to lower levels than the other cases in an absolute sense, they do succeed in maintaining the errors at a lower level for a longer period of time. Due to the drifting nature of the football it provides several flybys of the target from above and below, as the relative motion of the chaser encircles the target multiple times. The results for the case of a traveling football with 10m Δh and 100m of vertical motion are shown in Figure 3-31. The sudden downrange uncertainty drop near two hours corresponds to the time when the chaser first goes under the target and then the uncertainty fluctuates as the chaser sees the target from different perspectives.

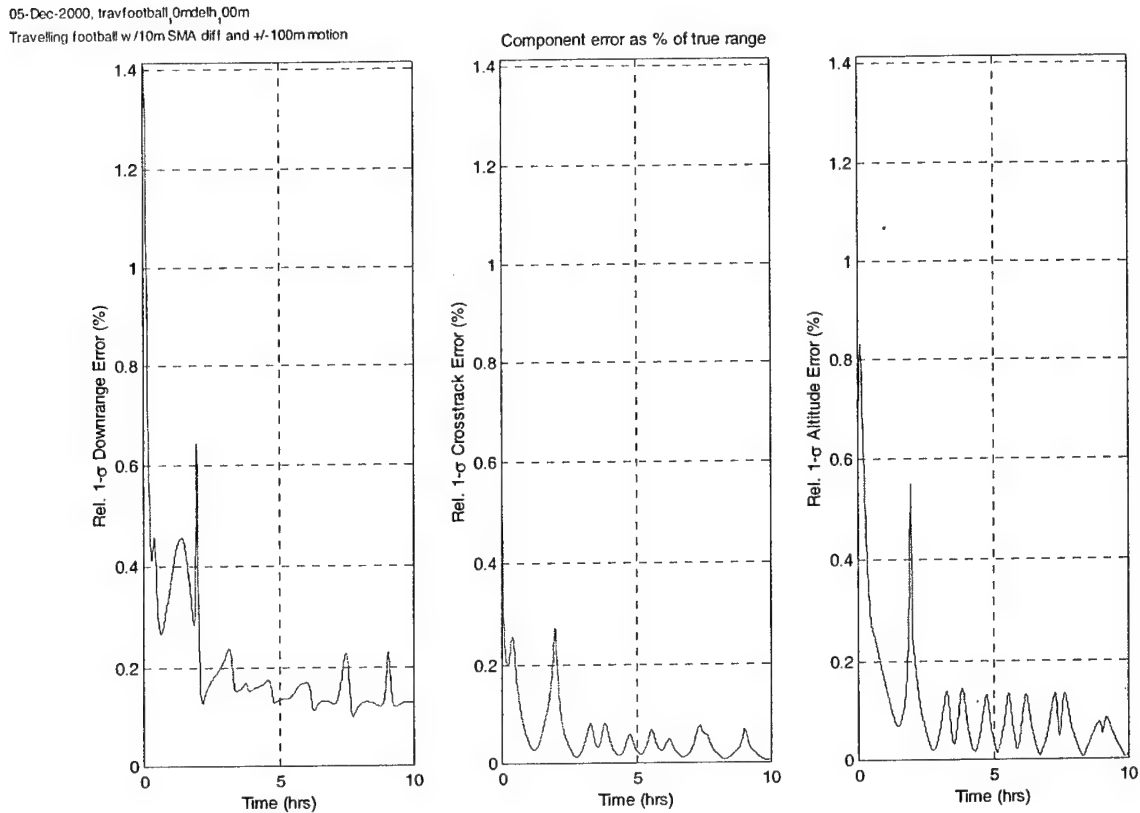


Figure 3-31: Relative position uncertainty for Traveling football with 10m Δh and 100m vertical motion

Similar to the past trends for other trajectories, adding cross-track motion to the traveling football does not make a significant difference unless the motion exceeds the geometry already being provided. Simply adding 10m of cross-track motion to the case just considered does not improve the downrange uncertainty in any significant way as shown in Figure 3-32. Increasing the cross-track motion to 100m makes a noticeable difference, but still not a significant improvement as shown in Figure 3-33.

Natural Motion Range Observability

05-Dec-2000, travfootball, 0mdebt, 00m, 00minc
Travelling football w/10m SMA diff and +/-100m motion & 10m cross-track

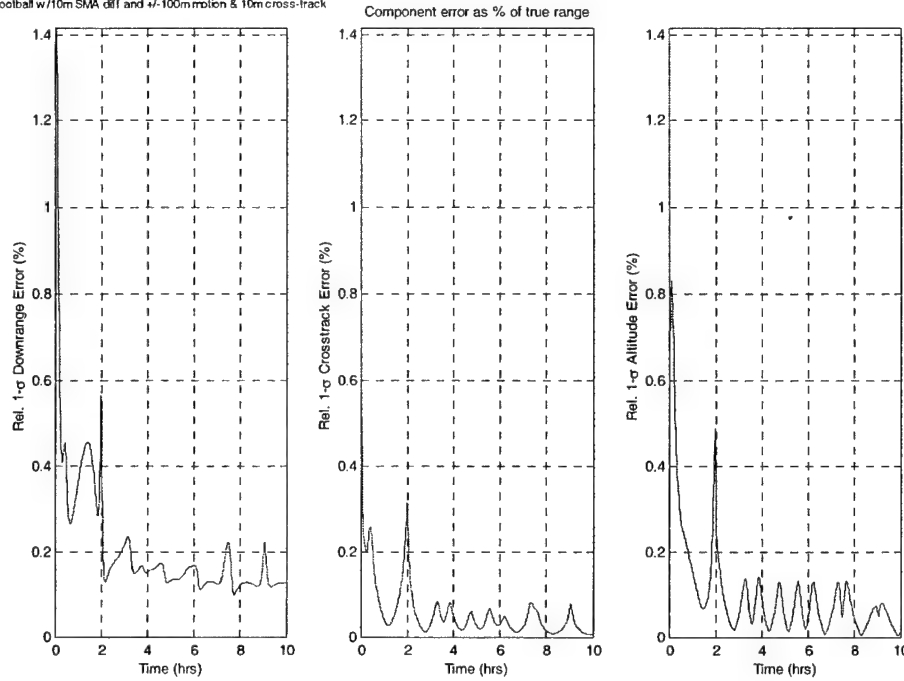


Figure 3-32: Relative position uncertainty for Traveling football with 10m Δh and 100m vertical motion with 10m cross-track motion

05-Dec-2000, travfootball, 0mdebt, 00m, 00minc
Travelling football w/10m SMA diff and +/-100m motion & 100m cross-track

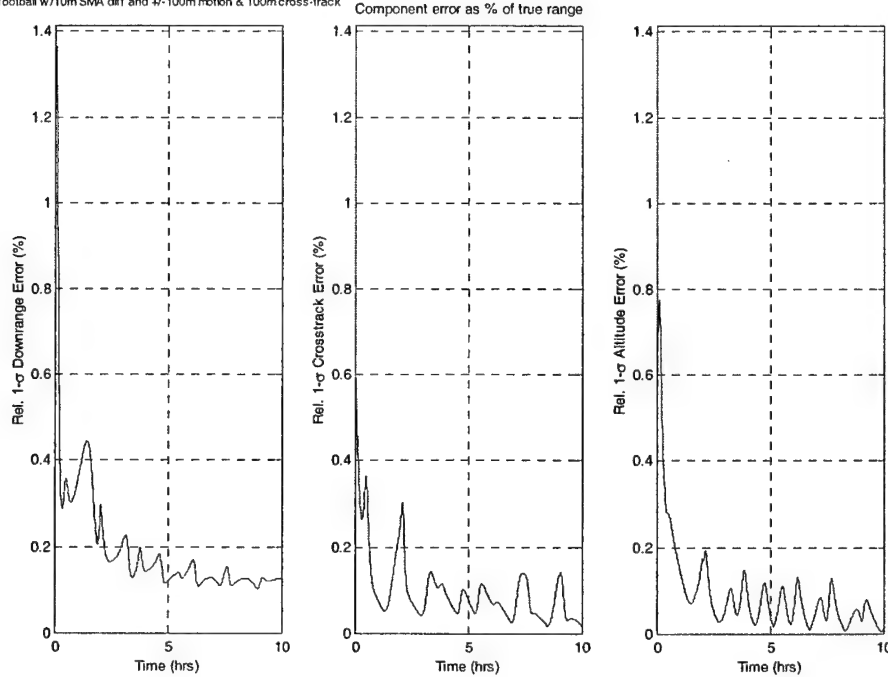


Figure 3-33: Relative position uncertainty for Traveling football with 10m Δh and 100m vertical motion with 100m cross-track motion

3.4 ADDITIONAL ANALYSIS CONSIDERATIONS

After completing the LINCOV analysis on the natural motion trajectories, there remain a few issues that merit additional consideration. The majority of these involve validating assumptions that were made in the natural motion analysis to show that the qualitative conclusions would remain the same. First, though, a more intuitive understanding of the evolution of the navigation uncertainties will be developed.

3.4.1 Error Ellipse Behavior

At the start of the chapter, Figure 3-2 showed one concept of how angles-only navigation might be able to determine range using natural motion geometry. If this concept is correct, then over time the downrange uncertainty should asymptotically approach zero. The results thus far have shown that geometry changes can help keep the downrange uncertainty from growing unbounded, but has not shown the uncertainty actually being driven all the way to zero. At issue, then, is whether these trajectories were not run for long enough periods of time to see the uncertainty reach zero, or if in fact some other effect is preventing the uncertainty from decreasing according to Figure 3-2.

Conventional wisdom in the field says that navigation with angles-only measurements does not work in a maneuver free situation. Since the majority of the natural motion trajectories exhibit a good deal of relative motion, the question arises as to why this motion in and of itself is not enough to stimulate range observability. To answer this question an attempt is made to demonstrate intuitively and pictorially the evolution of the navigation uncertainty over time in a maneuver free environment. The best way to watch the development of the uncertainty is by looking at error ellipses that represent a two-dimensional picture of the 1σ altitude vs. downrange navigation uncertainty. It is possible to actually use three-dimensional ellipsoids including the cross-track uncertainty, but since this motion is uncoupled from the in-plane relative motion it only complicates the picture.

To quickly review how these error ellipses are formed recall that the covariance analysis generates a series of covariance matrices, \mathbf{P} . If only the inertial position and velocity of each vehicle makes up the state \vec{x} then the relative inertial state is:

$$\begin{aligned}\vec{x}_{rel} &= \mathbf{T}\vec{x} \\ \mathbf{T} &\equiv [\mathbf{I}_{6 \times 6} : -\mathbf{I}_{6 \times 6}]\end{aligned}\quad (3.6)$$

Furthermore, the relative state can be rotated into any arbitrary frame through the use of a rotation matrix \mathbf{C} . In this case, the frame is the target LVLH frame. As long as these are linear transformations, the covariance matrix can be transformed into the relative LVLH frame using [5]

$$\mathbf{P}_{LVLH} = \mathbf{CTPT}^T \mathbf{C}^T \quad (3.7)$$

The 2×2 partition of the covariance matrix corresponding to altitude and downrange uncertainty can then be removed and turned into an ellipse representing the 1σ position uncertainty. Calling the 2×2 partition, \mathbf{m} , and the correlation coefficient between altitude and downrange uncertainty, ρ , then the matrix will have the form

$$\mathbf{m} = \begin{bmatrix} \sigma_{dwn-rng}^2 & \rho\sigma_{dwn-rng}\sigma_{alt} \\ \rho\sigma_{dwn-rng}\sigma_{alt} & \sigma_{alt}^2 \end{bmatrix} \quad (3.8)$$

The axes of the error ellipse will correspond to the eigenvectors, \vec{v}_1, \vec{v}_2 of \mathbf{m} and the semi-major and semi-minor axes lengths correspond to the square root of the eigenvalues, λ_1, λ_2 of \mathbf{m} , as shown in Figure 3-34 [29].

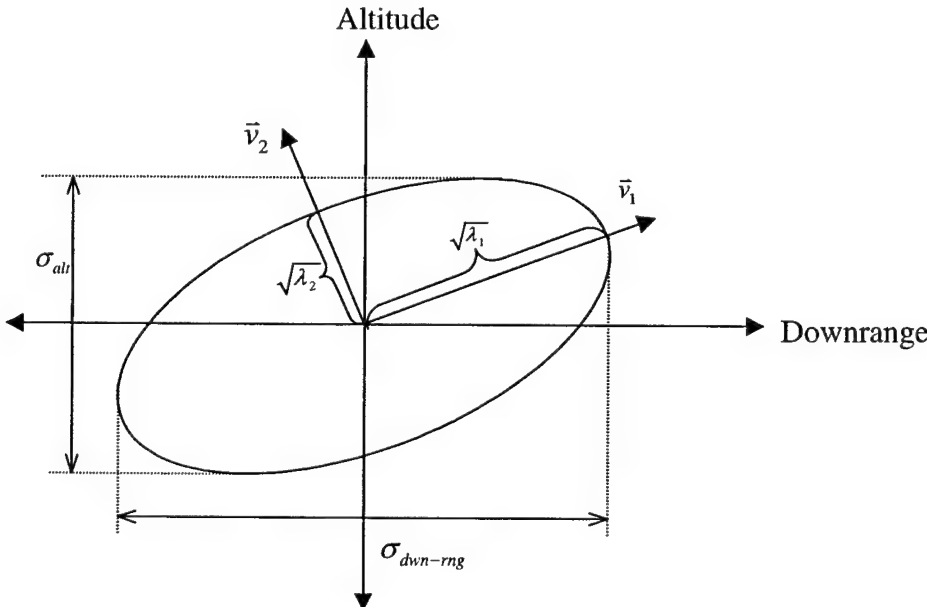


Figure 3-34: Two dimensional error ellipse dimensions

The next step is to examine the error ellipses for some of the natural motion trajectories that have been presented in an attempt to show why gaining downrange observability requires the chaser to perform a maneuver.

Centered Station-keeping Football

The first case examined is the station-keeping football centered on the target. If the behavior shown in Figure 3-2 is the correct explanation of how natural motion geometry provides downrange observability, then one would expect the error ellipses to evolve as shown in Figure 3-35. The chaser is continuously slicing down the error ellipse to smaller sizes as it proceeds around the football. Recall the LVLH coordinate frame is defined in Figure 3-3.

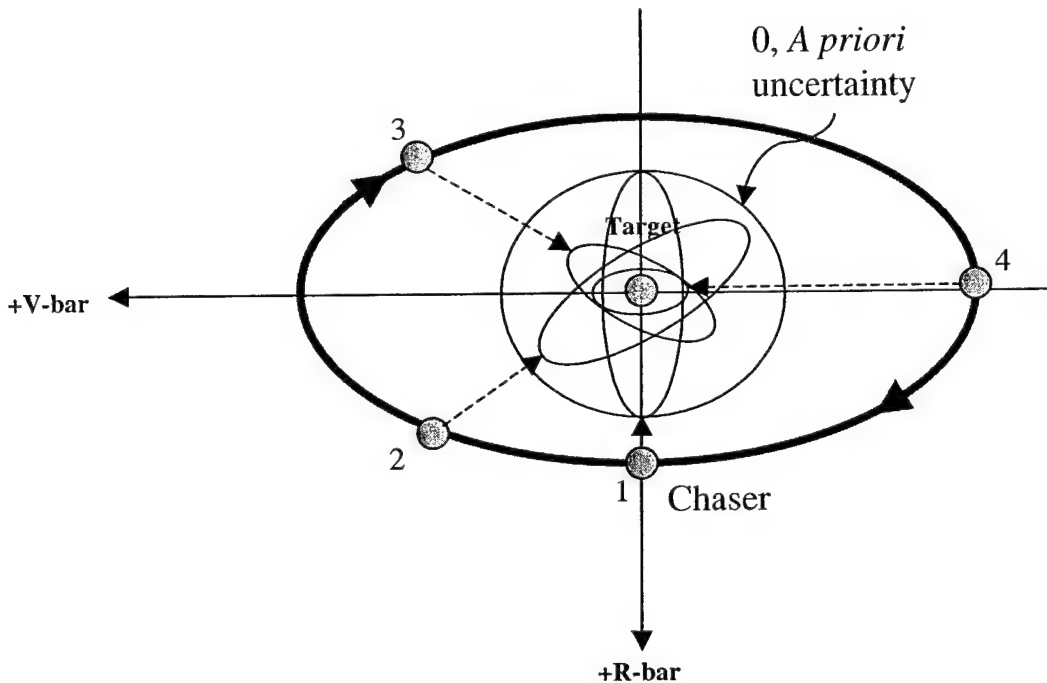


Figure 3-35: Incorrect expected error ellipse behavior for Centered station-keeping football

Unfortunately, based on the results already shown from the covariance analysis in Figure 3-20 it is apparent that the downrange uncertainty does not continue decreasing with time, but rather it develops a steady-state oscillation. The hypothesis as to why this happens is that the error ellipse in fact *follows* the line-of-sight between the chaser and the target around the football itself moving at orbital rate as shown in Figure 3-36.

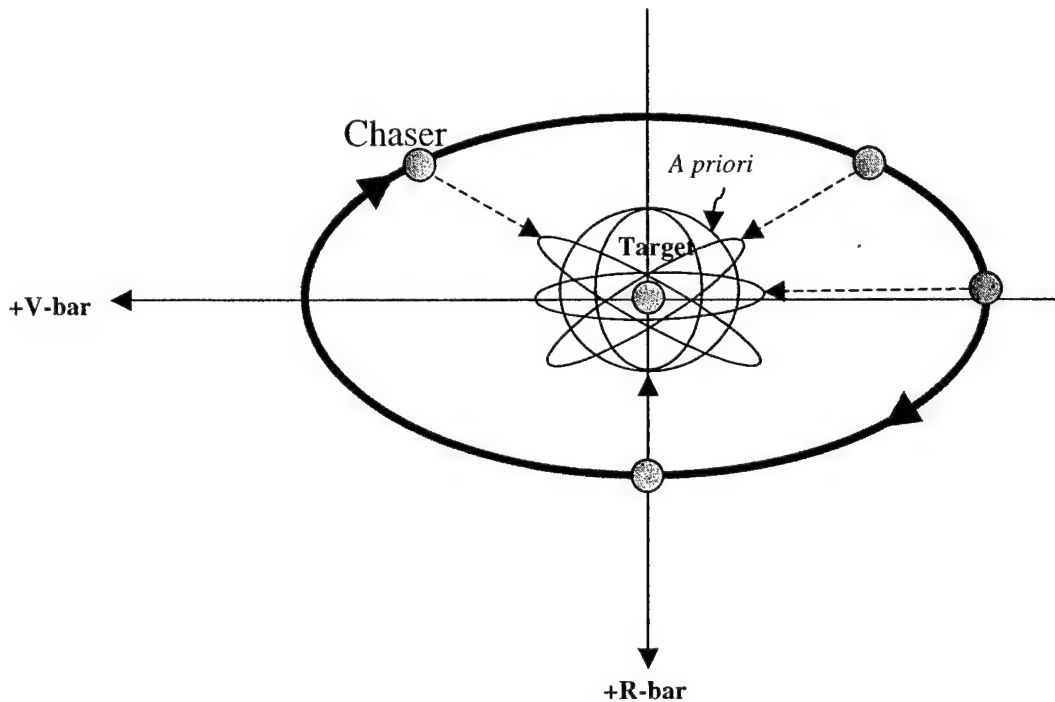


Figure 3-36: Expected error ellipse behavior for Centered station-keeping football

Extracting data from the existing covariance results shows that this is in fact exactly what happens. Figure 3-37 shows the correlation coefficient relating the altitude and downrange uncertainty. The X axis is marked in $\frac{1}{2}$ orbit increments. The first few hours the filter is undergoing transient behavior, but after approximately 2 hours, the oscillations synchronize themselves with the orbital period. At the top, bottom, and sides of the football shape, the correlation is zero meaning the semi-major/minor axes of the error ellipse are aligned with the V-bar/R-bar axes. The sign of the correlation coefficient indicates that the orientation of the ellipse follows the line-of-sight between the vehicles. Another way of making this point is by looking at Figure 3-38 which are the actual error ellipses overlaid on one another at approximate $\frac{1}{2}$ hour intervals during the last 5 hours of the trajectory.

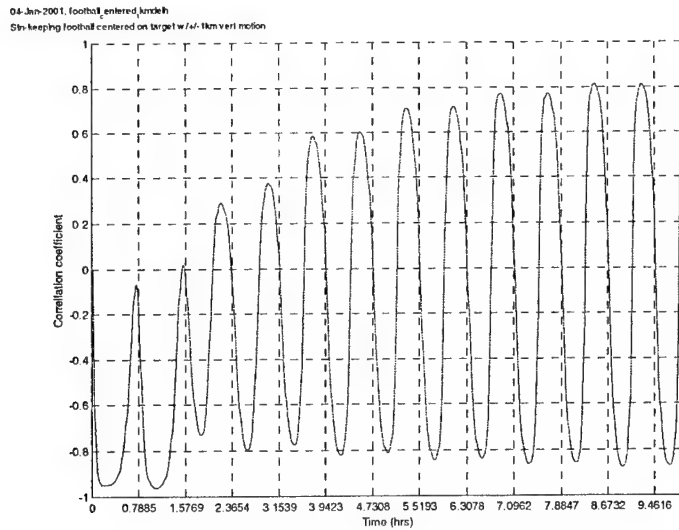


Figure 3-37: Correlation coefficient time history for Centered station-keeping football

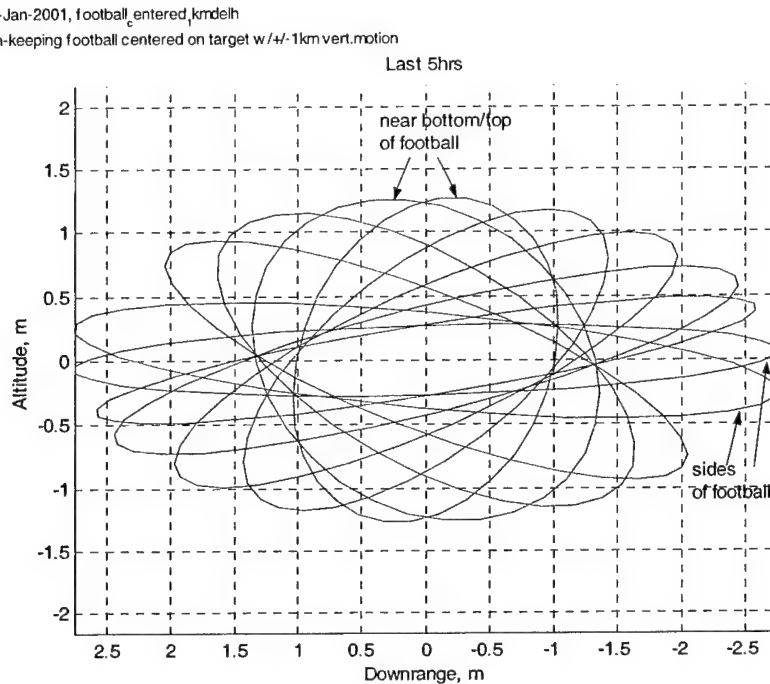


Figure 3-38: Error ellipse behavior for Centered station-keeping football

Offset Station-keeping Football

Since the centered football is a unique case, it would seem sensible to verify this concept of an error ellipse following the line-of-sight with a more conventional offset football. If the

hypothesis were to hold true, one would expect the error ellipse to simply “wobble” back and forth rather than rotate completely around as shown in Figure 3-39.

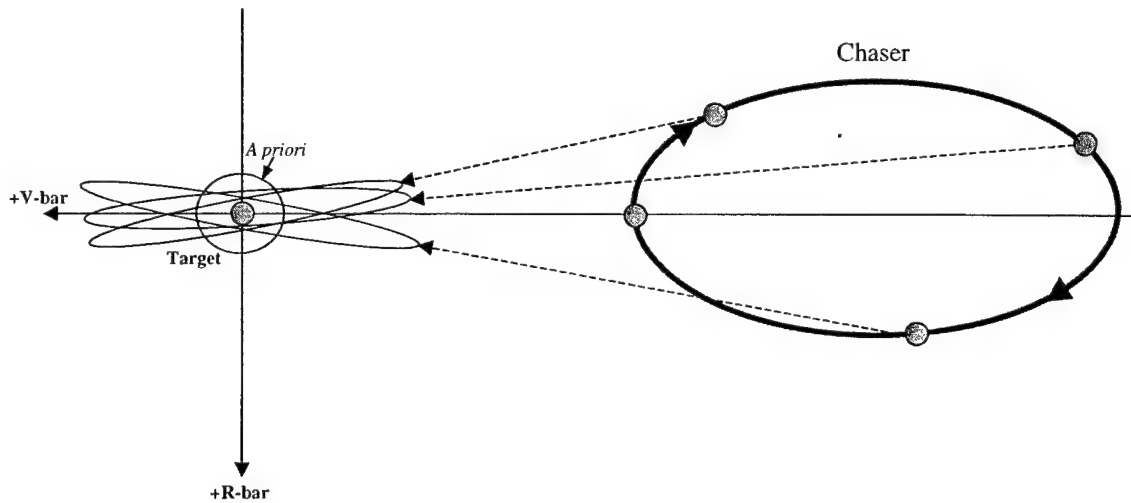


Figure 3-39: Expected error ellipse behavior for Offset station-keeping football

Looking at the time history of the correlation coefficient in Figure 3-40 there is once again oscillation that is related to orbital motion. Again, the actual covariance results show that the error ellipse does move as expected. Once the transient has passed, the maximum correlation values correspond to the times when the chaser is at the top and bottom of the football because the line-of-sight is the most “tilted” here. When the chaser crosses through the V-bar the correlation is 0, as it was for the centered football case. The wobbling motion of the ellipse can be seen more clearly in Figure 3-41 looking at the ellipses overlaid for the last 5 hours of the trajectory.

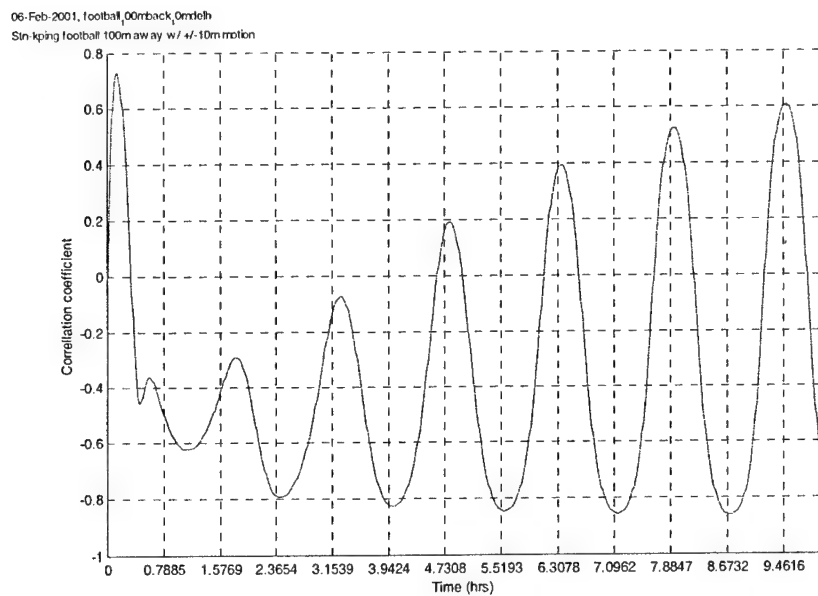


Figure 3-40: Correlation coefficient time history for Offset station-keeping football

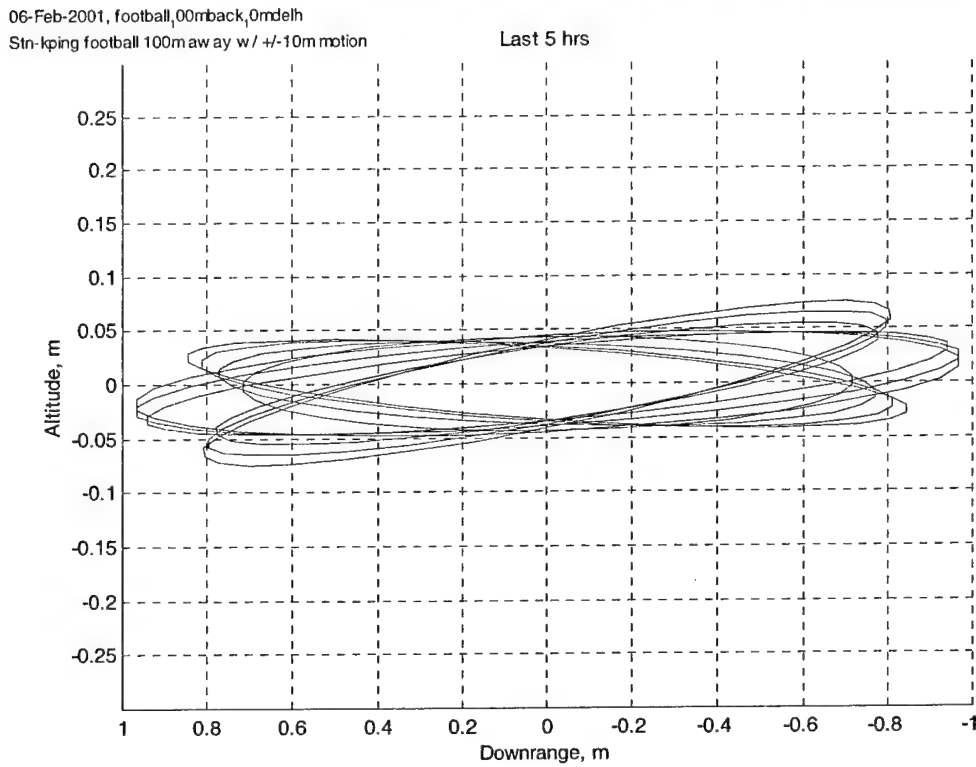


Figure 3-41: Error ellipse behavior for Offset station-keeping football

These two station-keeping cases demonstrate why using maneuvers would be ideal in order to improve downrange observability with angles-only measurements. Even though both cases have relative motion that seems to be providing adequate measurement geometry, the fact that the error ellipse is also moving at the natural motion orbital rate defeats much of the potential improvement. In other words, the intuition that lead to Figure 3-2 and Figure 3-35 is incorrect, the chaser does not slice down the size of the error ellipse using natural motion. By introducing a maneuver, however, the line-of-sight would be moving faster relative to the error ellipse's natural motion and provide the desired slicing effect in the form of additional downrange information.

Coelliptic

Although it has just been shown that for station-keeping cases the error ellipse follows the line-of-sight when natural motion is relied upon, the question of whether or not this occurs for naturally closing trajectories is still unanswered. If in fact the error ellipse does follow the line-of-sight, Figure 3-42 shows a view of how the ellipses would evolve. A key indicator that this is taking place is that the steady state downrange-altitude correlation value should switch signs abruptly at the point of flyby as the orientation of the ellipse switches direction.

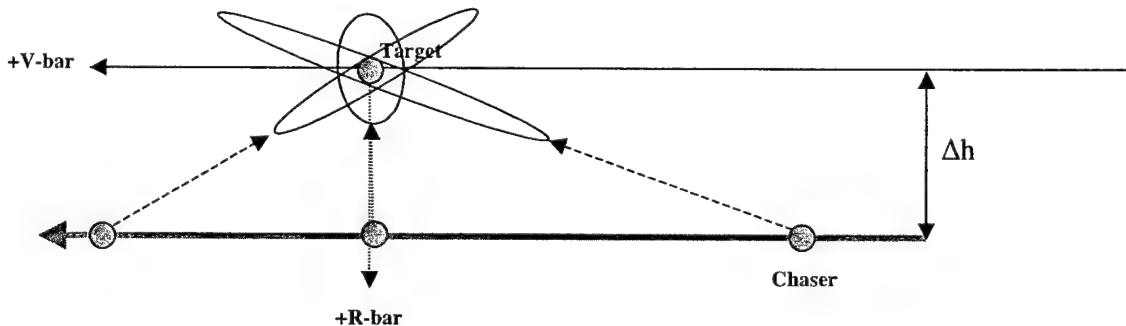


Figure 3-42: Expected error ellipse behavior for Coelliptic

The closing nature of the trajectory required some modifications to the original covariance results in order to test whether the error ellipse was tracking the line-of-sight. The transient time of the navigation filter is even longer than the station-keeping cases so in order to allow the correlation coefficient to reach a steady state value, the coelliptic was run over 4 days. However, running it this long implied that the chaser started much farther away from the target and hence the noise on the angle measurements was decreased so that the early uncertainty ellipses would not be overly large. With these changes, the results showed that once again the error ellipse followed the natural motion of the line-of-sight between the chaser and target. Figure 3-43 shows

the correlation coefficient time history, and the tell tale sign change at 24 hours, the flyby point. The overlaying of the error ellipses throughout the run in Figure 3-44 also shows how the ellipses are oriented primarily along two directions corresponding to being on either side of the target.

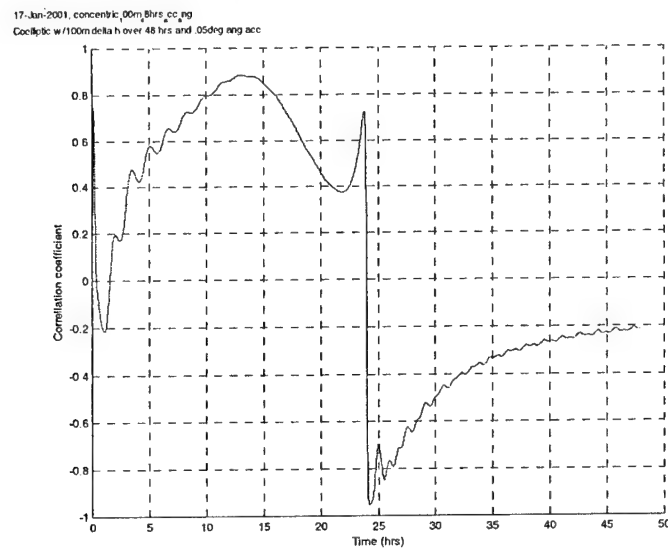


Figure 3-43: Correlation coefficient time history for Coelliptic

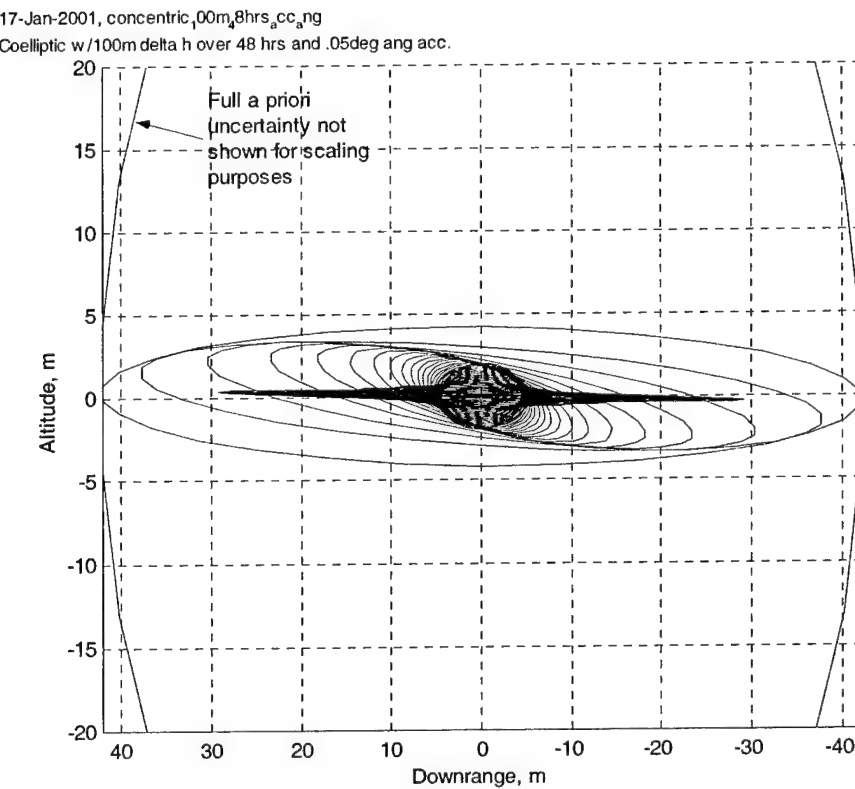


Figure 3-44: Error ellipse behavior for Coelliptic

Another method of demonstrating the same phenomenon for the coelliptic is by examining the growth of the altitude uncertainty at the point of flyby. As indicated in Figure 3-45, two coelliptics with different Δh values can have identical line-of-sight time histories. At the point of flyby, the downrange uncertainty component will be at a minimum, although the altitude uncertainty will be at a maximum since there is ambiguity as to exactly which coellipse the chaser is on. In section 3.3.3 the effect was not as noticeable due to the *a priori* values, but Figure 3-46 more clearly illustrates what happens at flyby by setting the *a priori* values to much higher values of 500m and 50 cm/sec for a 100m Δh coelliptic. At this level, although unrealistic in mission practice, the *a priori* position uncertainty is actually larger than the coelliptic Δh , and this results in over 15%- 1σ altitude uncertainty at the flyby point. In other words, the navigation filter only knows that the chaser is somewhere between 85m and 115m below the target, but can not tell these two extremes apart.

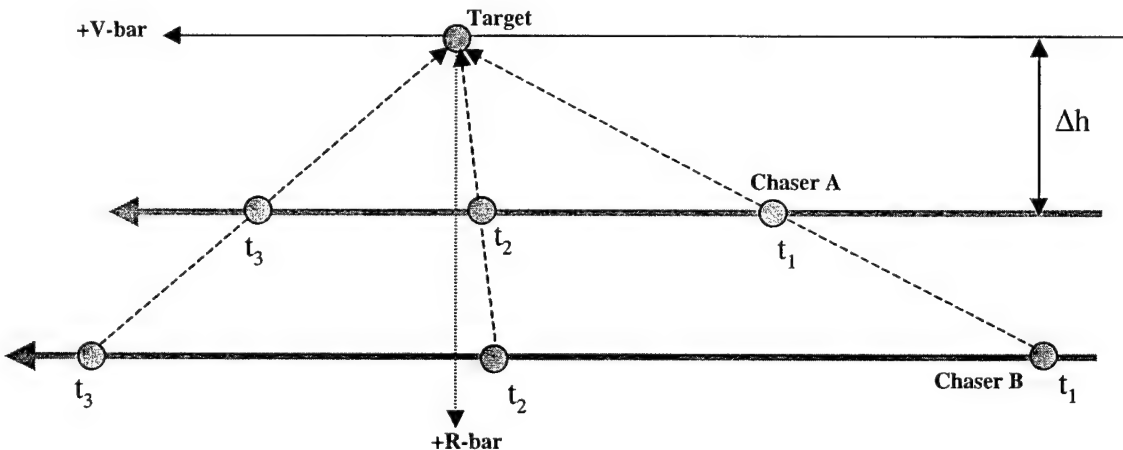


Figure 3-45: Identical line-of-sight history for different coelliptic orbits

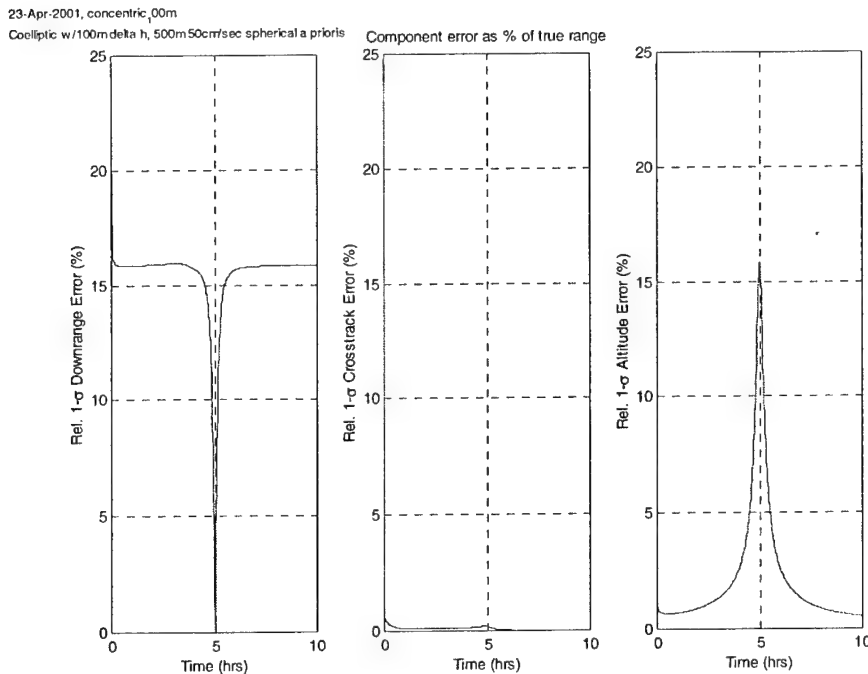


Figure 3-46: Relative position uncertainty for Coelliptic with 100m Δh and increased *a priori* uncertainty

The analysis of the error ellipse over time for the coelliptic shows that, like the station-keeping cases, the natural motion closure trajectories could gain improved range observability by using maneuver-assisted trajectories.

3.4.2 Measurement Availability

One of the assumptions used in the covariance analysis was that angular measurements were always available, but this may not always be a realistic assumption. In a number of potential mission scenarios, the availability of measurements could be dependent on factors such as solar illumination for power generation or heat signature, sensor range specifications, or spacecraft pointing requirements to name a few. To verify that non-constant measurement availability would not adversely affect any of the qualitative results from the natural motion analysis, the majority of the trajectories were run through the LINCOV model again with measurements only available when the target was illuminated by the sun. As expected, the trends and comparisons between trajectories remained the same. Somewhat unexpectedly though, the modified results actually look remarkably similar to the case where measurements are always available. In many cases, the only difference is a spike in navigation uncertainty early in the run that occurs because

the filter is still in its transient period when the target goes into eclipse. Even in these situations though, the difference in uncertainty between cases with limited and limitless measurement availability is not even noticeable after a few hours. As an example, a comparison is shown for a traveling football trajectory with 100m Δh , 1km of vertical motion, and 1km of cross-track motion. Figure 3-47 shows the case where measurements are only available when the target is in sunlight and yet the errors look very similar to the case where measurements are always available as shown in Figure 3-48.

26-Oct-2000, travfootball_00mdelh_krnnc
Traveling football centered at -100m & incl.

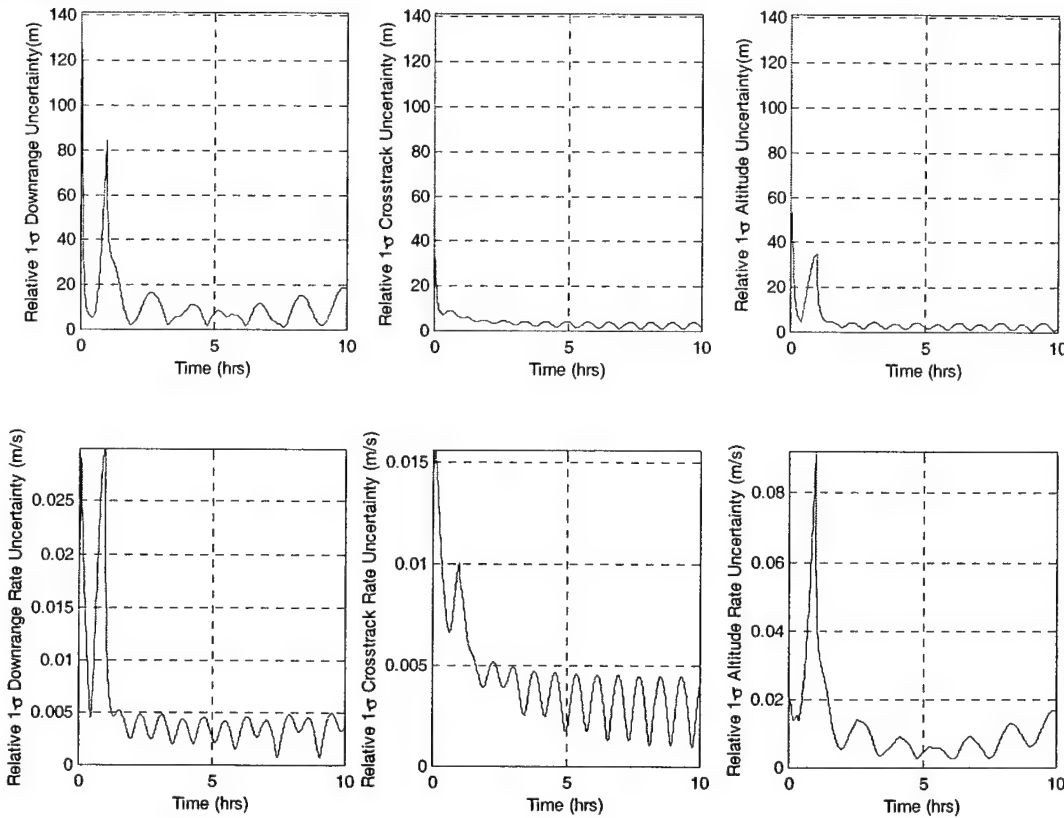


Figure 3-47: Measurements available only in sunlight – Actual relative position and velocity uncertainty values for Traveling football with 100m Δh and 1km vertical motion with 1km cross-track motion

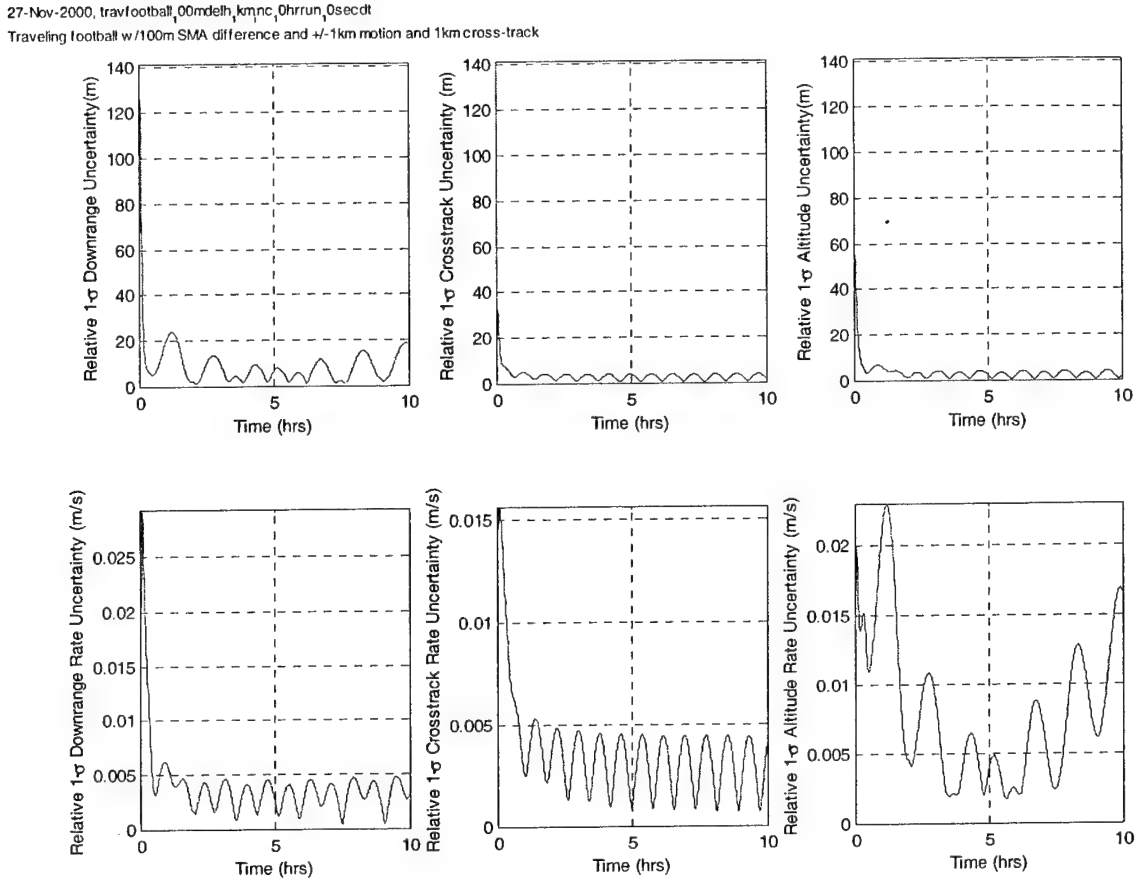


Figure 3-48: Measurements always available – Actual relative position and velocity uncertainty values for Traveling football with 100m Δh and 1km vertical motion with 1km cross-track motion

Based on a number of comparisons similar to this, it is validated that the assumption of constant measurement availability does not significantly alter the conclusions drawn from the qualitative covariance analysis.

3.4.3 Noise Vs. Number of Measurements

Another potential concern regarding the covariance analysis setup is whether the measurement noise level or measurement frequency has an effect on the results. The two are implicitly tied to one another since a system with a higher level of noise is countered with more measurements. Specifically if one increases the noise level by \sqrt{n} while at the same time taking n times as many measurements, there will be no change in the results. As a demonstration of this consider the case of a V-bar hop relative motion trajectory with a 1km Δh . Figure 3-49 shows the

results with the normal noise levels (1° - 3σ) and measurements every minute. Following this is the same trajectory but this time with $\sqrt{3}^\circ$ - 3σ noise on the angular measurements which are taken every 20 seconds. As expected Figure 3-49 and Figure 3-50 are identical. For both cases, measurements are only available during sunlight which is why there is an uncertainty spike due to eclipse near one hour.

26-Oct-2000, noncoelip, knadelh
Non-coelliptic orbit w/ 1km SMA difference

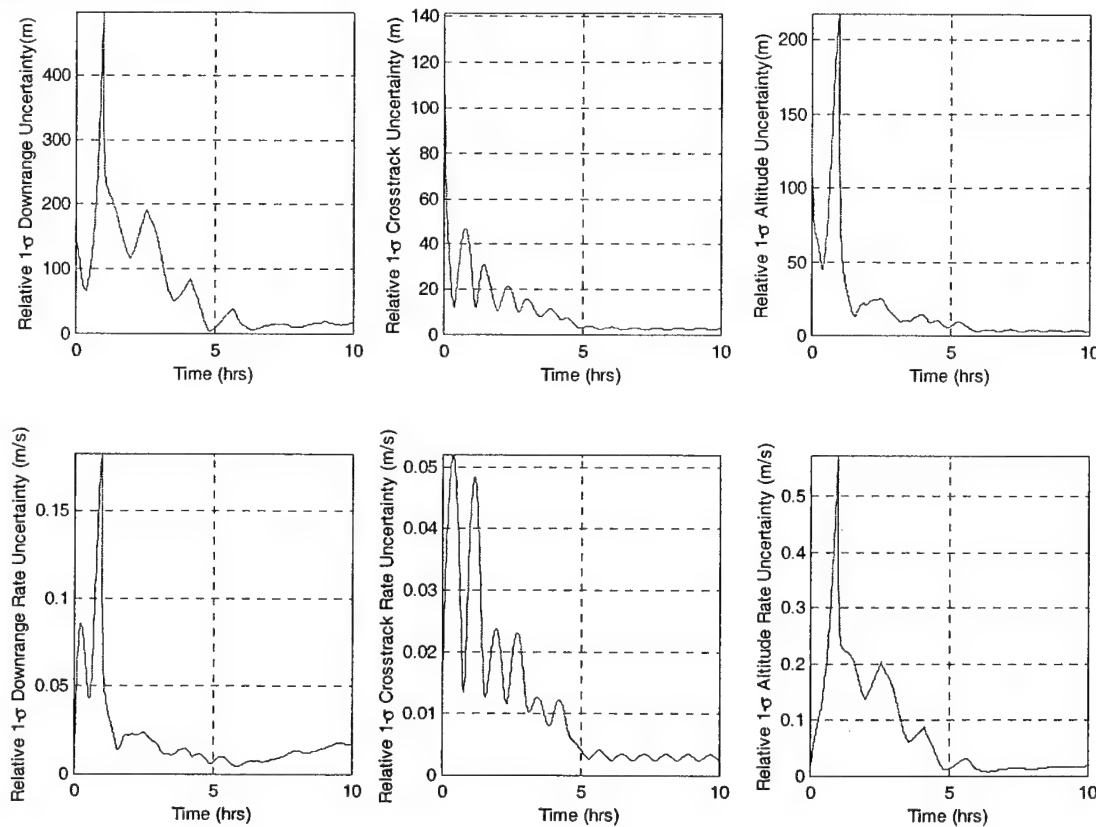


Figure 3-49: Actual relative position and velocity uncertainty values for V-bar hops with 1km Δh

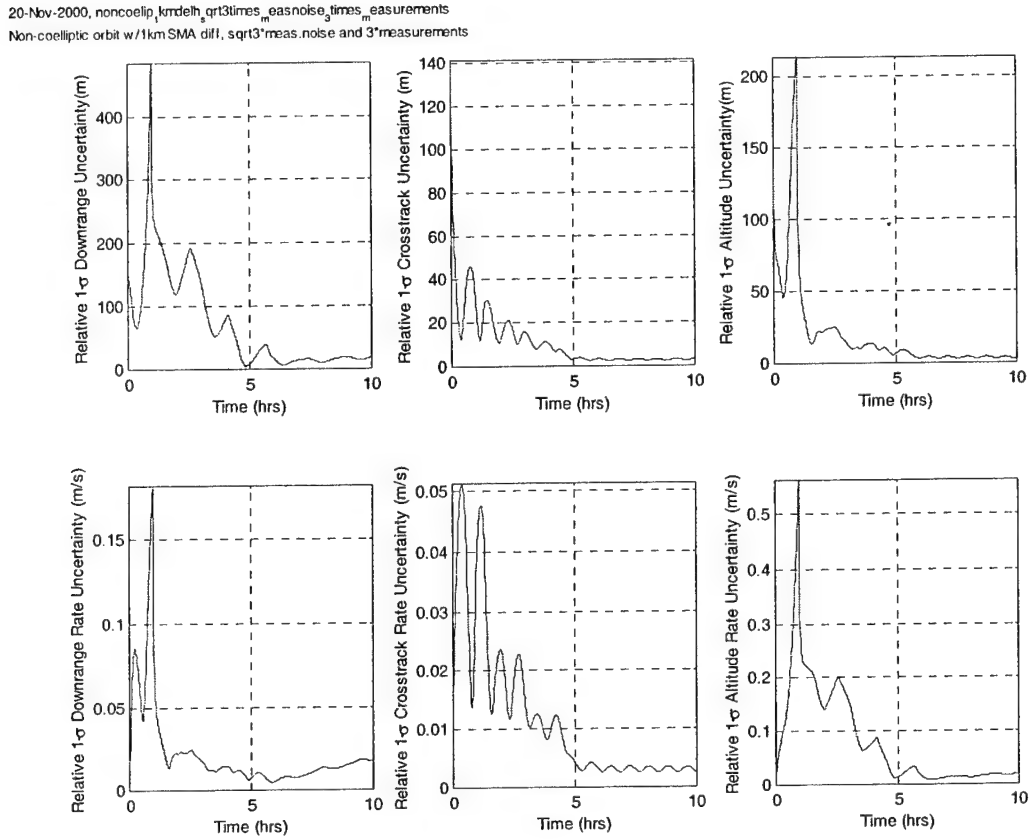


Figure 3-50: Increased noise and measurement frequency – Actual relative position and velocity uncertainty values for V-bar hops with 1km Δh

3.4.4 Biases

The last item explored in more detail is the fact that no biases were considered in the natural motion analysis. In order to verify that this would not significantly alter the results, a number of cases were run with bias terms added to isolate their effects. Biases were added in the forms of a static alignment error as well as an angle measurement bias on the azimuth and elevation angles (see sections 2.2.2 and 5.2 for details on how these were actually implemented). In general, the tests showed that although the filter was not able to estimate all components of the bias values it did not have an adverse effect on the navigation's relative position uncertainty values. This results because the bias elements that are unobservable to the filter are ones that do not impact the relative uncertainties. The one exception to this statement is the case of a co-circular orbit in which the biases cause much faster downrange error growth. In actual practice these non-

observable bias elements would not be a problem because a simple attitude maneuver, rolling the chaser about the line-of-sight vector, would allow the filter to calibrate the biases out.

An example is shown in the next few figures for the case of a station-keeping football centered 100m away from the target with 10m of vertical motion. The static alignment bias is $1^\circ/\text{axis}-3\sigma$ and the measurement biases on the azimuth and elevation angles are $0.35^\circ-3\sigma$. Figure 3-51, Figure 3-52, and Figure 3-53 show a comparison between the filter's relative uncertainty values for the case with just the static alignment bias, with both biases, and with zero biases, respectively. It is very difficult to detect any changes between the cases.

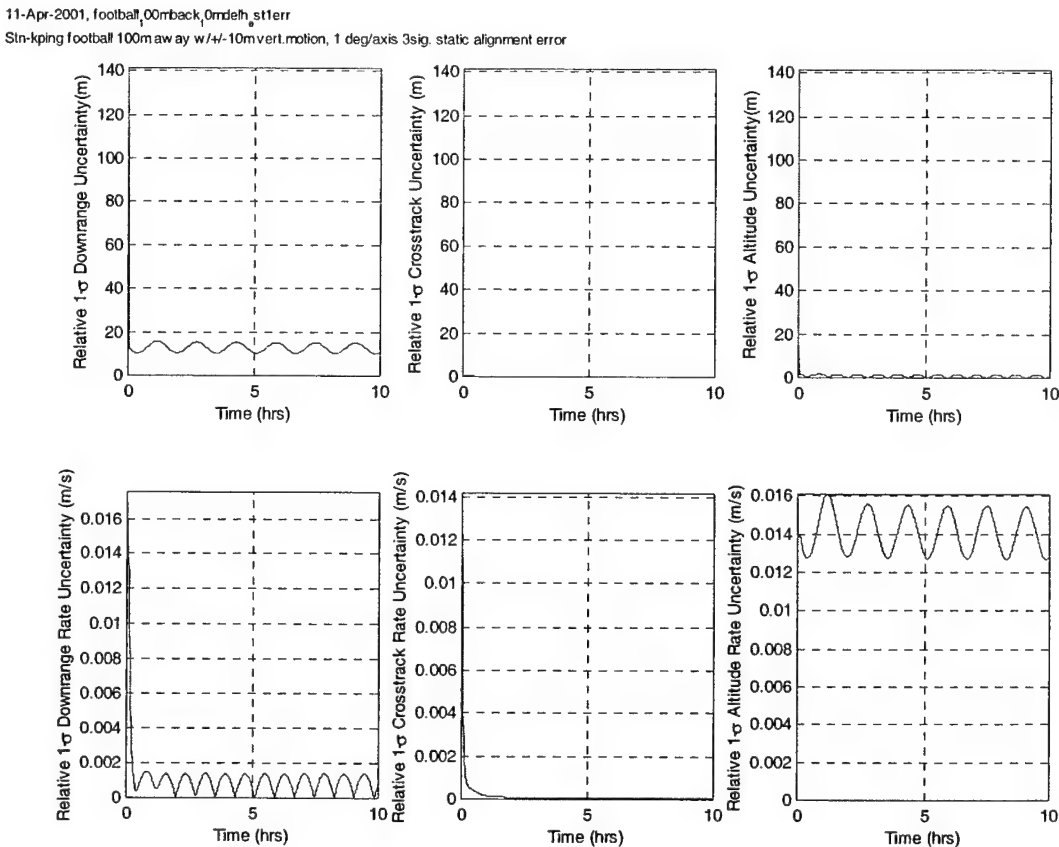


Figure 3-51: Actual relative position and velocity uncertainty values for Football station-keeping 100m away with 10m vertical motion – With one bias

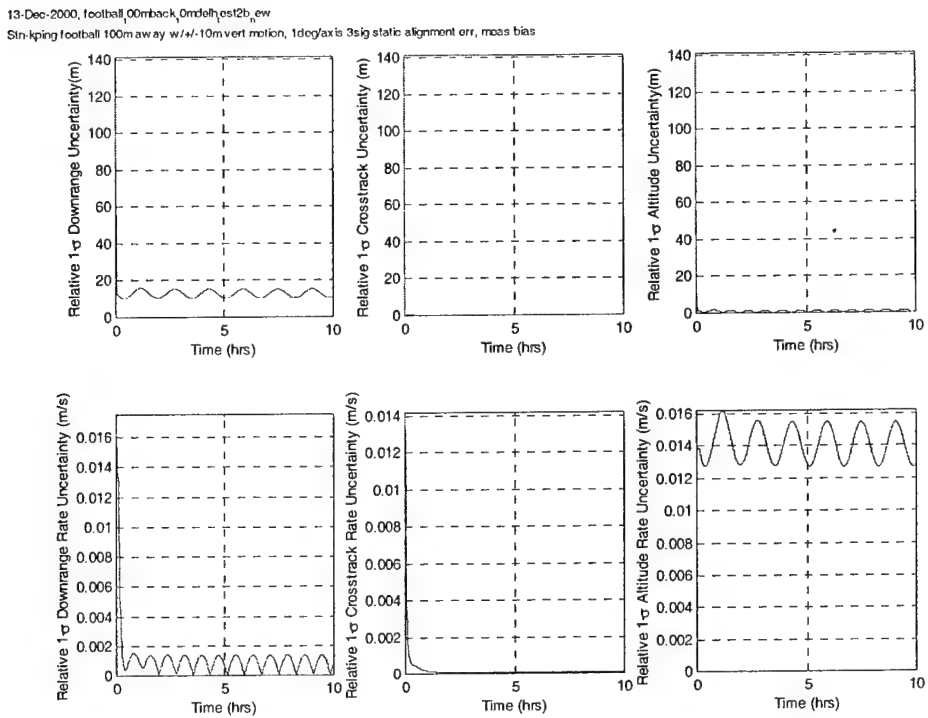


Figure 3-52: Actual relative position and velocity uncertainty values for Football station-keeping 100m away with 10m vertical motion – With both biases

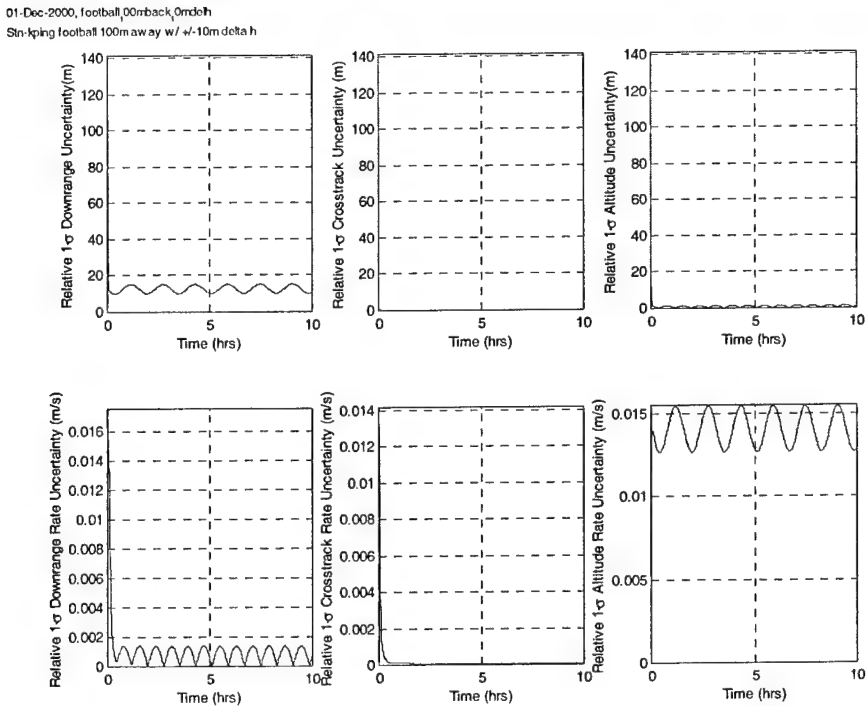
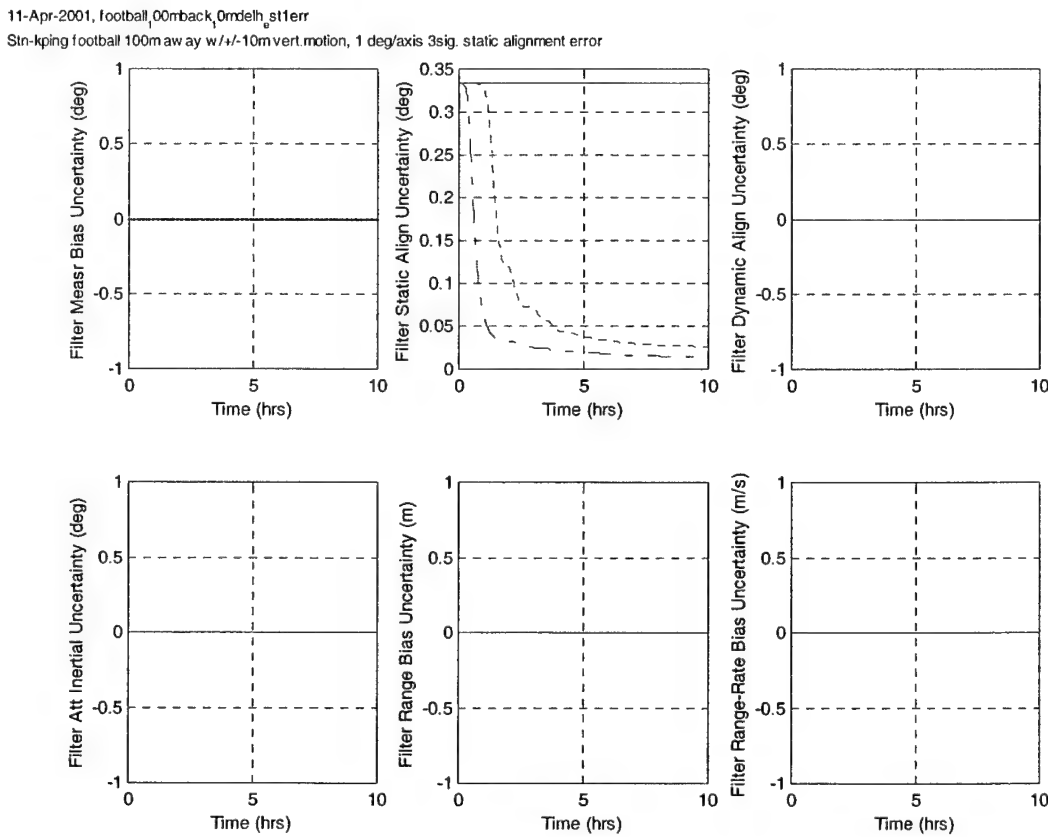
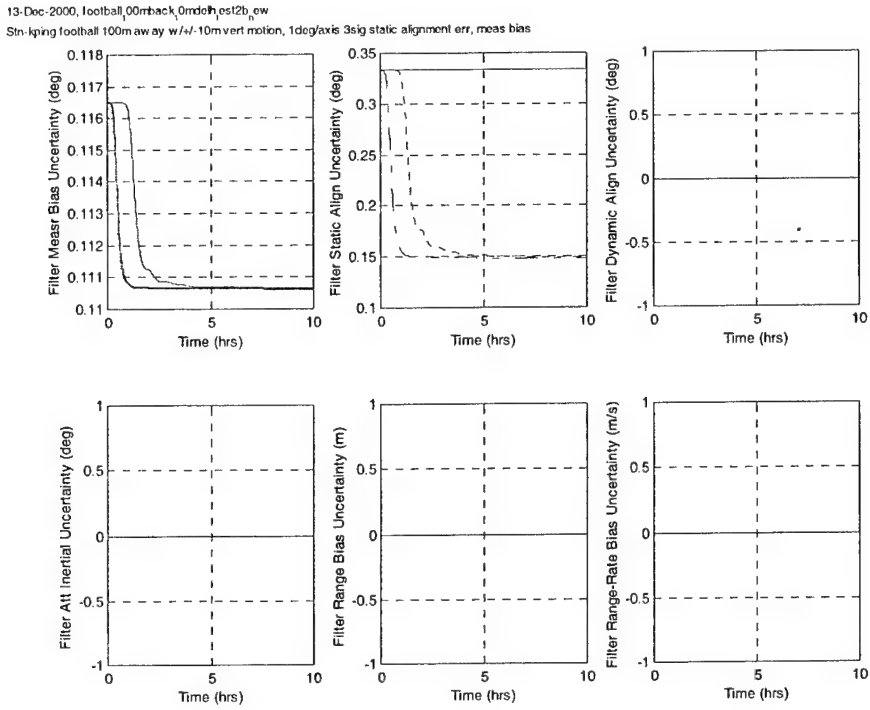


Figure 3-53: Actual relative position and velocity uncertainty values for Football station-keeping 100m away with 10m vertical motion – Without biases

Finally, Figure 3-54 and Figure 3-55 show the filter error in estimating the bias values. This demonstrates that although the filter is not improving its estimate of the biases very quickly, or at all in the case of one static alignment component, it is not adversely affecting the overall results. Another point that these last two figures illustrate is the effect of having multiple biases. The uncertainty of the static alignment bias (Figure 3-54) is driven to lower levels when it is the only bias present, whereas in the presence of additional biases, the uncertainty stays at a higher value (Figure 3-55). Similarly, if the measurement bias had been isolated, the filter would have more success in estimating its value. This difference occurs because when multiple biases are present, the linear combination of them that affects the results is estimated quite effectively. However, there will also be a linear combination of the errors that do not effect the navigation results, and this is the same combination that will not be observable to the navigation filter.



**Figure 3-54: Filter bias value uncertainty for one bias - Football station-keeping
100m away with 10m vertical motion**



**Figure 3-55: Filter bias value uncertainty for both biases - Football station-keeping
100m away with 10m vertical motion**

3.5 GENERAL CONCLUSIONS

In addition to the explanations accompanying the previous results, some of the key conclusions from the natural motion analysis are presented here. Keep in mind that these statements stem from LINCov analysis in a virtually error free environment and therefore are idealized versions of angles-only navigation performance.

First and foremost for the station-keeping cases, it is clear that the downrange errors will grow unbounded if there is no changing geometry, and the chaser is just following the target around the same orbit. Adding geometry in the form of either footballs or relative cross-track eliminates this effect and prevents the errors from growing. In a perfect situation, any amount of deviation from the exact co-circular case will eventually lead to decreasing downrange estimation errors. However, the less extreme the geometry, the more time it takes for this decrease to occur. Also, the direction of the geometry does not make a difference. For example, cross-track motion will yield approximately the same gains as the vertical motion of a football orbit. Along a similar

line of thought, if there is already one source of geometry variations, adding in more in another direction does not necessarily improve the results. This concept can be visualized by way of a cone emanating from the target as shown in Figure 3-56. Regardless of the range from the target, a given angular deviation due to orbital motion will result in the same percent downrange error. The lower bound of how low the error can be driven is a function of the angular measurement accuracy and potentially the sensor's field of view. Using the idealized analysis to this point, 5° of geometric motion in terms of the cone angle was adequate to keep the error from growing beyond the *a priori* uncertainties over a 10 hour period while increasing this to 15° yields much more favorable results with the uncertainty decreasing within this same time period.

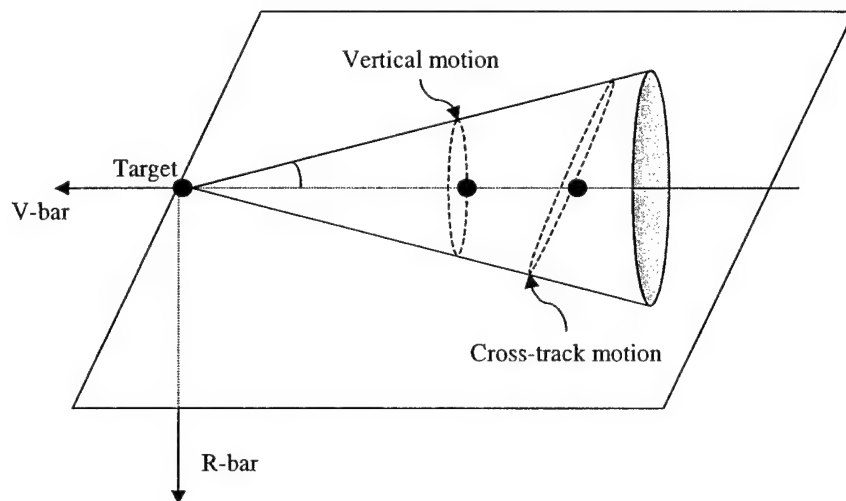


Figure 3-56: Cone of equivalent relative motion geometries

The most prominent conclusion from the closure trajectories is that for both the coelliptic and non-coelliptic cases, the navigation uncertainty of the downrange position to the target is at a minimum at the point of target flyby. This is true regardless of whether there is also cross-track motion or not. This implies, similar to the concept in the station-keeping conclusions, that additional geometry is not always helpful when other factors are already providing it. In this case, the closing motion of the chaser leads to sufficient angular variation to cause the downrange errors to decrease. The only difference cross-track motion makes is how quickly the initial errors start going down. A similar effect comes from using a traveling football approach. Although it does not provide any better absolute performance than what is normally achieved at flyby, it does drive the downrange percent uncertainty to lower levels earlier than the other cases. In general then, inclination or additional geometry changes will only have an effect on how quickly the initial errors decay but will not improve upon the best values achieved.

To ensure that these conclusions are truly qualitative and not sensitive to the conditions used to generate the LINCOV results (other than the use of zero error sources) a few more checks are warranted.

3.5.1 Effects of Measurement Noise

One of the first questions drawn from the conclusions and results is whether the numerical values of downrange uncertainty achieved in different cases have an absolute lower limit due to the trajectory itself or if it is truly just a function of the angular measurement noise. For example, if the noise were increased, would the corresponding minimum percent error values achieved correspondingly increase? The answer to this question, as one might expect, is yes, they are correlated. To show this, Figure 3-57 and Figure 3-58 compare the results for the case of chaser in a co-circular orbit 1km from the target with 1km cross-track motion, for 1° and 5° per axis 3 σ angle measurement noise values respectively. The results are clearly related to this noise value because the minimum downrange percent uncertainty no longer reaches 0.2% but rather only gets to 0.6%. Going the other direction, Figure 3-59 shows the results when the noise is only 0.1°/axis and the downrange percent error now stays well below 0.2% steadily.

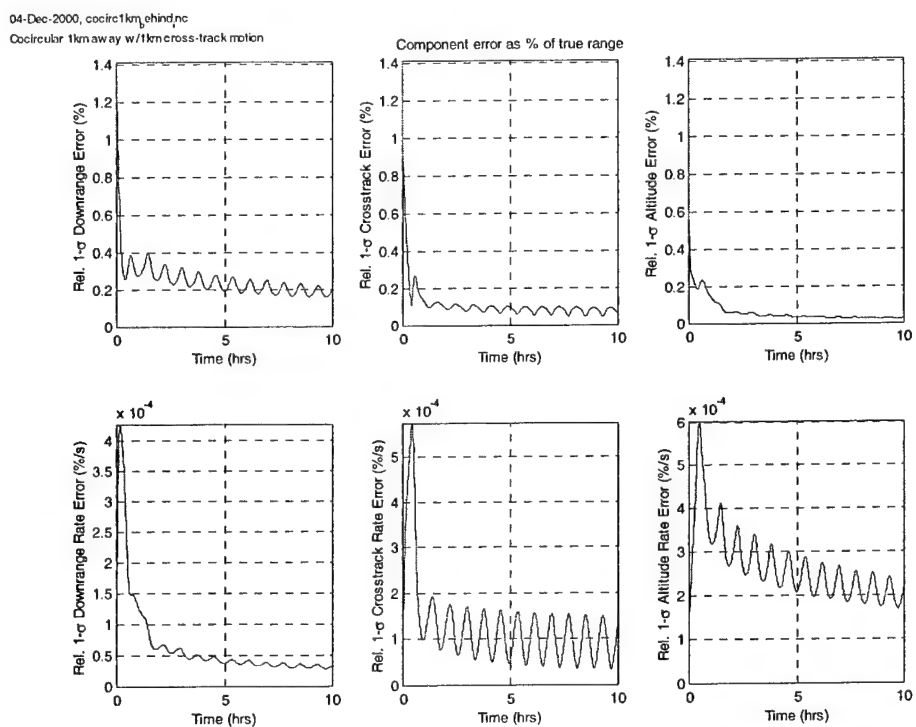


Figure 3-57: Relative position and velocity uncertainty for Co-circular station-keeping 1km away with 1km cross-track, 1°/axis 3 σ angular measurement noise

Natural Motion Range Observability

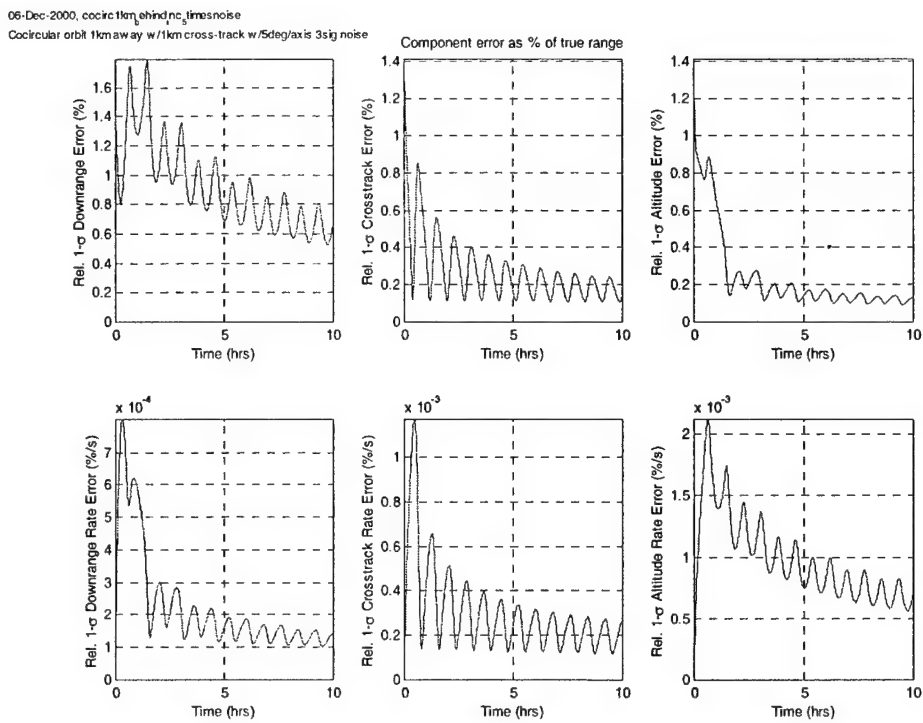


Figure 3-58: Relative position and velocity uncertainty for Co-circular station-keeping 1km away with 1km cross-track motion, 5°/axis 3 σ angular measurement noise

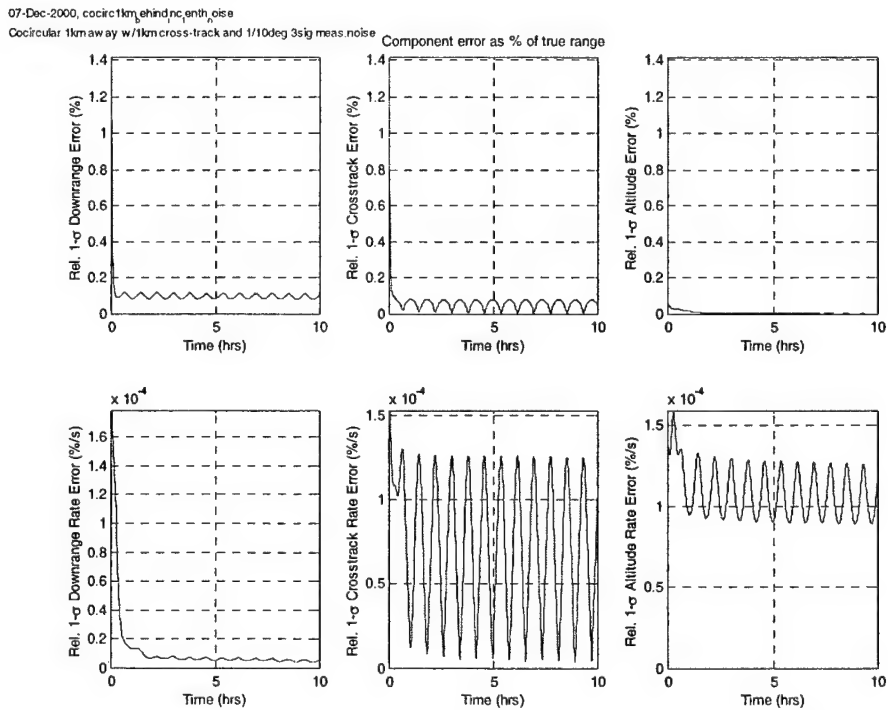


Figure 3-59: Relative position and velocity uncertainty for Co-circular station-keeping 1km away with 1km cross-track motion, 0.1°/axis 3 σ angular measurement noise

3.5.2 A Priori Effects on Benefits of Geometry

Another question arising from the conclusions is how dependent the ability of geometry to reduce downrange uncertainty errors is on *a priori* navigation uncertainties. One particular concern is whether the uncertainty will still improve if the magnitude of the geometry changes due to relative motion is less than the initial *a priori* magnitude. Figure 3-60 shows the LINCOV results for a case where the chaser is 1km away from the target in a co-circular orbit with 87m of cross-track motion, and the *a priori* downrange uncertainty is on the order of 10m. Following this in Figure 3-61 is the same scenario except with an *a priori* uncertainty of 100m so the cross-track motion is smaller than the uncertainty. Despite the larger *a priori* values, the downrange uncertainty curve takes on the same trend. However, the uncertainty values for the increased *a priori* case are not as low as they were in the previous case at the end of the 10 hour period.

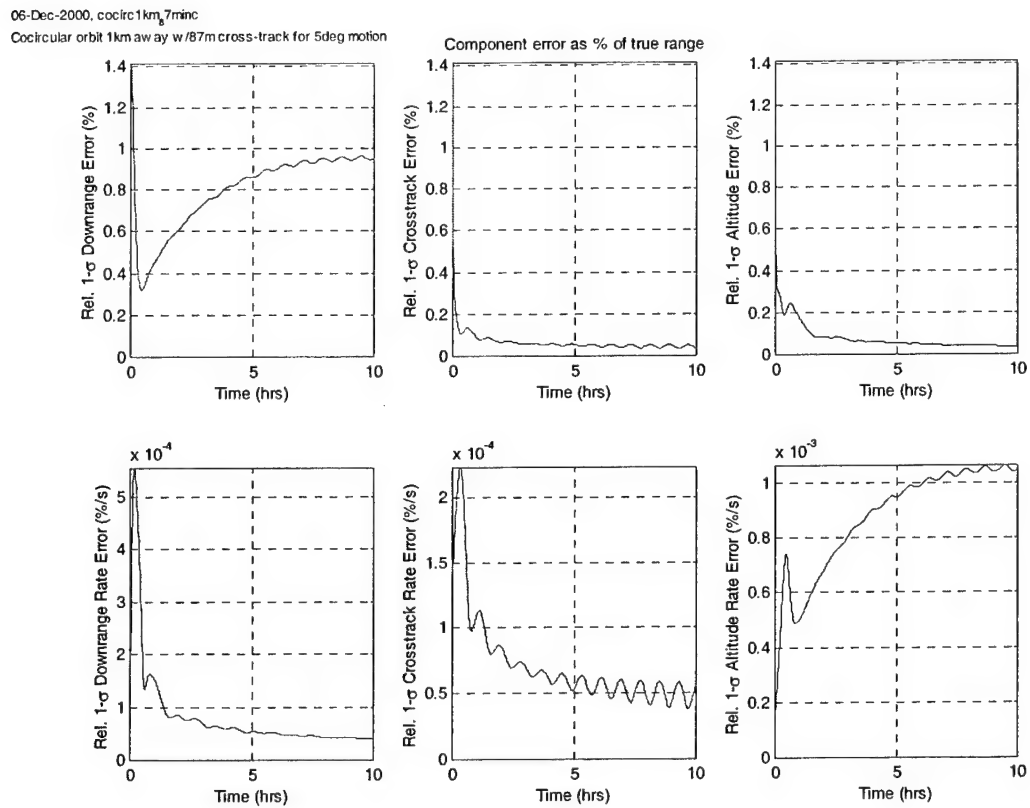


Figure 3-60: Relative position and velocity uncertainty for Co-circular station-keeping 1km away with 87m cross-track motion, normal *a priori* uncertainty

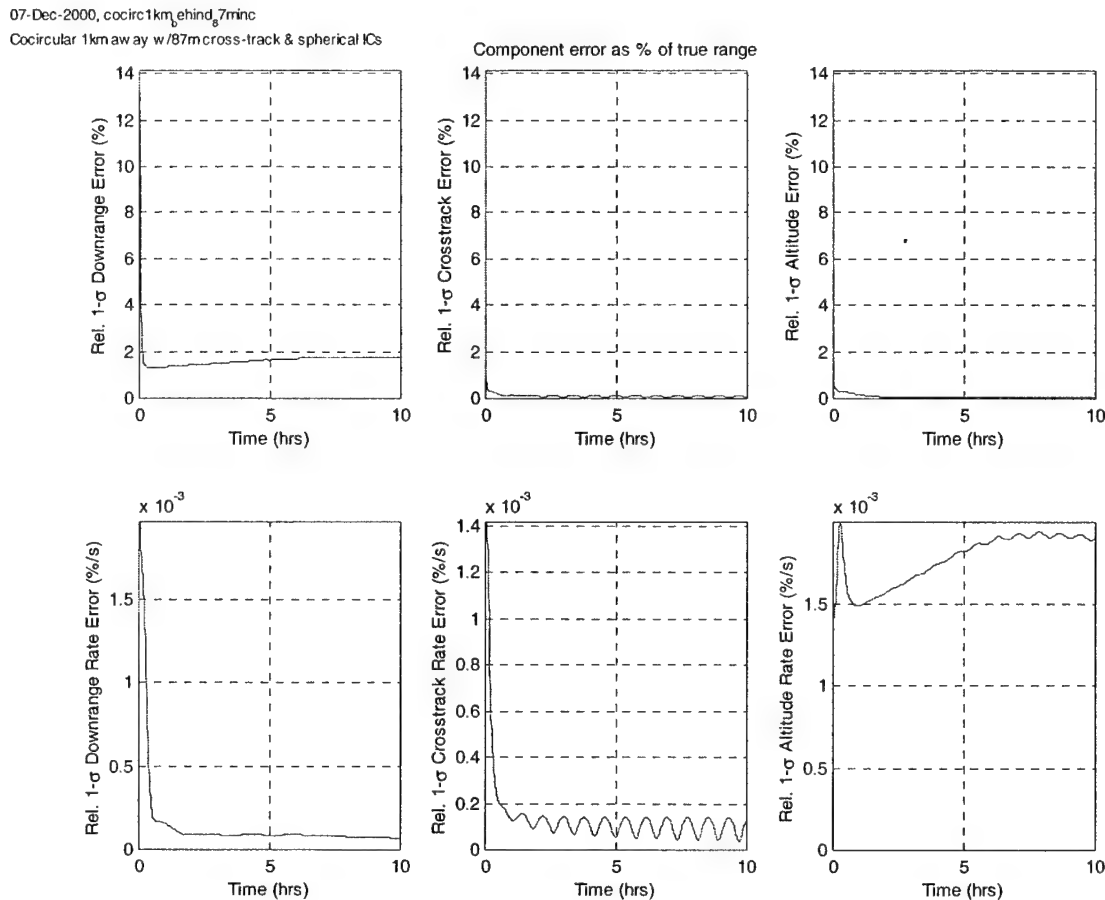


Figure 3-61: Relative position and velocity uncertainty for Co-circular station-keeping 1km away with 87m cross-track motion, increased *a priori* uncertainty

Recall that it was shown that any changing geometry will eventually lead to error reduction, but that small variations may take very long to have an effect. With that in mind, Figure 3-62 shows the results running the previous case over 4 days instead of 10 hours. The downrange uncertainty is now down to 1.3% which is not yet as low as in Figure 3-60, but the error is still steadily decreasing and would eventually reach the same level. Therefore, it seems that larger *a priori* uncertainty translates (for a fixed geometry) into longer times to reach the same error level as for a case with lower *a priori* values.

08-Dec-2000, cocirc1km_s7minc
Cocircular 1km away w/87m cross-track motion, spherical ICs over 4 days Component error as % of true range

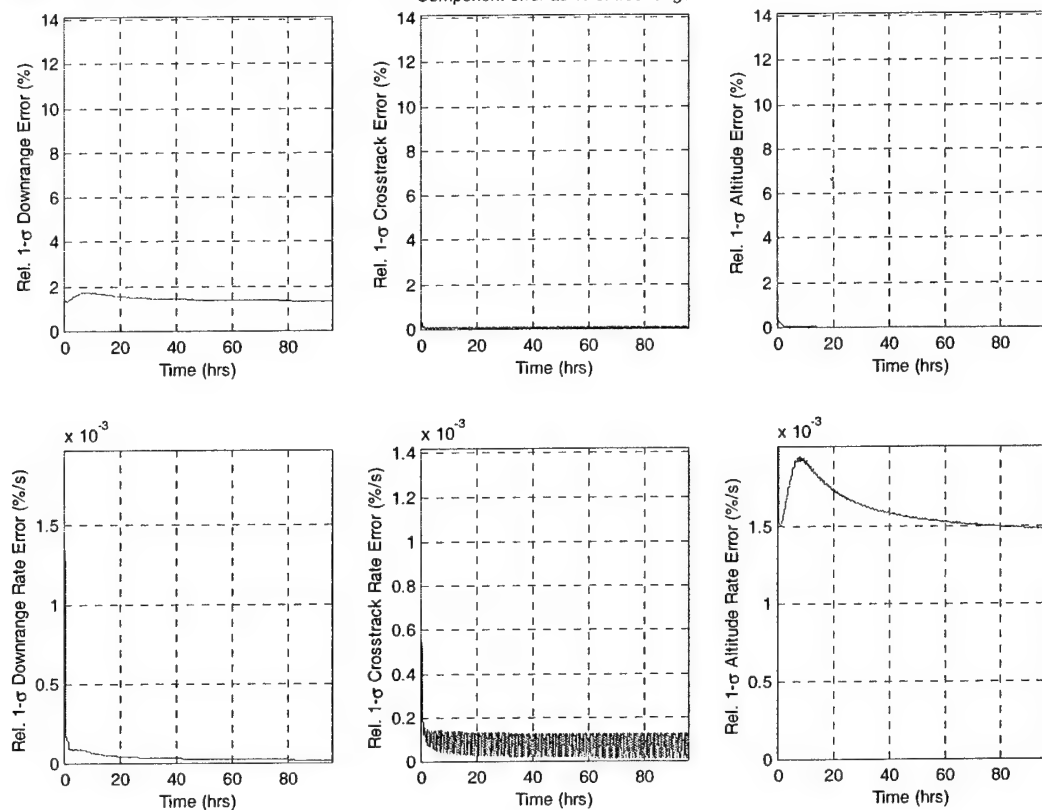


Figure 3-62: Relative position and velocity uncertainty over 4 days for Co-circular station-keeping 1km away with 87m cross-track motion, increased *a priori* uncertainty

To ensure that this phenomenon always occurs due to the poorer *a priori* uncertainty, and not just as a result of that particular trajectory having geometry which was less than the uncertainty, another case is examined where the *a priori* uncertainty is again 100m, but the cross-track motion is 268m. Figure 3-63 shows the results with the *a priori* values at their original levels and Figure 3-64 shows the increased *a priori* results.

Natural Motion Range Observability

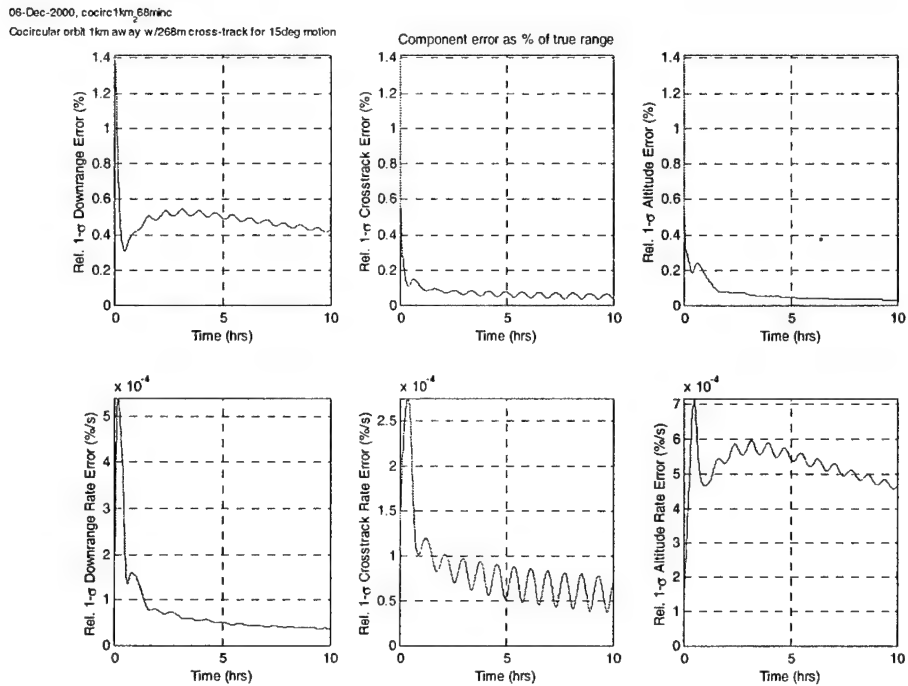


Figure 3-63: Relative position and velocity uncertainty for Co-circular station-keeping 1km away with 268m cross-track motion, normal *a priori* uncertainty

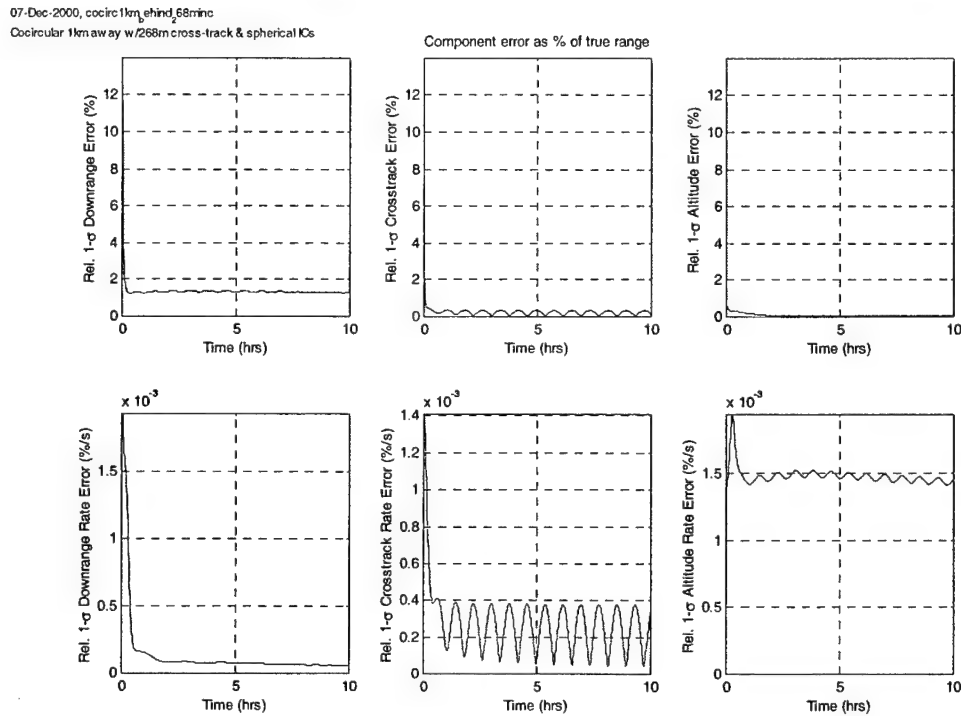


Figure 3-64: Relative position and velocity uncertainty for Co-circular station-keeping 1km away with 268m cross-track motion, increased *a priori* uncertainty

Since the lowest downrange uncertainty value increases from ~0.4% to 1.2% this indicates that it is the poor *a priori* knowledge itself and not the fact that the cross-track motion does not exceed the *a priori* information that causes the results to degrade.

The rules of thumb that come out of the natural motion angles-only navigation analysis in an error-free environment then are as follows:

First, relative motion geometry with any components normal to the line-of-sight will eventually drive down the downrange uncertainty value. Higher or lower amounts of geometry simply equate to shorter or longer times for this reduction to take place.

Secondly, angular measurement noise will not alter the qualitative results. Regardless of the noise level the downrange error will eventually decrease, assuming the trajectory contains some relative motion line-of-sight geometry changes. The larger the magnitude of the angular measurement noise, the longer it will take to decrease the downrange uncertainty, similar to the relationship between the magnitude of geometry and the time required to decrease the uncertainty.

Finally, there is an independent relationship between the *a priori* uncertainty and angle measurement noise. If the *a priori* uncertainty is larger than the angular spheroid due to the measurement noise, then initially the downrange uncertainty will decrease very rapidly since the measurements are providing much better information than the *a prioris*. If, on the other hand, the *a priori* uncertainty is smaller than the angular spheroid due to measurement noise then the downrange uncertainty will increase very quickly to the level that is measurable by the angle sensor. The behavior after these initial transients is then governed by whether or not there is relative motion line-of-sight geometry.

Although these conclusions are valid for the qualitative results obtained from the idealized LINCOV analysis, the error ellipse analysis in section 3.4.1 clearly demonstrates the need for maneuvers to further improve angles-only navigation performance. Whether or not these maneuvers will create downrange observability in the strict sense is still an unanswered question despite several unsuccessful attempts by the author to determine this analytically. Regardless of this uncertainty though, the previous conclusions are still valid and lend themselves towards designing natural motion trajectories that generate better range observability (in the loose sense). However, as more error sources are modeled, the need for maneuvers in addition to natural motion aids will become more apparent.

4 MANEUVER-ASSISTED TRAJECTORY ANALYSIS

After considering a wide variety of natural motion orbital trajectories in Chapter 3, the next logical step is to develop orbital trajectories with maneuvers to improve range observability using angles-only measurements. By removing the constraint of requiring only natural relative motion, it is possible to model an accelerating chaser vehicle capable of altering its trajectory. The previous analysis will hopefully prove useful as it guides the choice of maneuvers that will yield better range observability. This chapter will first review results from dual control literature before explaining the various maneuver-assisted trajectories that were developed and their analysis. Finally, elements of the most promising trajectories are combined to form hybrid trajectories that are later used as a basis for Orbital Express mission design.

4.1 COMPARISON TO PREVIOUS WORK

There are essentially two areas in the existing literature that relate to the issues of angles-only navigation. The first is work done on bearings-only tracking applications, typically for earth based dynamic systems. The second area involves the field of dual control. Although neither area directly addresses the problem in this study, it is useful to examine their results in order to add this to the knowledge gleaned from chapter 3.

The field of bearings-only tracking derives heavily from naval applications as well as work on homing missiles. In either case, the necessary use of maneuvers to gain target observability has been a fact re-discovered in a variety of methods. Chang [7][8] takes the approach of formulating the dynamics of a system where the range, azimuth, and elevation angles themselves are the states. Alternatively, Nardone [20] uses the conditions from the solution of a complex differential equation while Aidala and Hepner [1][10] construct matrices they use to generate similar conditions. The end results in all cases are analytic conditions that require the chaser to initiate a maneuver in order to generate navigation filter observability of the range. However, Hepner and Nardone [10][20] also show that blindly executing a maneuver without regard to its

direction will not necessarily lead to improved observability. Specifically, the ideal maneuver is normal to the line-of-sight between the chaser and target while a maneuver parallel to the line-of-sight will not yield any observability improvements.

The other field that relates to the problem of angles-only navigation is dual control. As explained in [27], A.Fedlbaum first put forth the concept of dual control in 1960. Put simply, dual control is a recognition that a given control signal serves two purposes. It affects the state directly, but also will affect future estimation of that state. From a qualitative standpoint, the method of generating an appropriate control algorithm is similar to the Linear Quadratic Regulator (LQR) problem. In the LQR case, a cost function that has penalties on both the state error and amount of controller energy is minimized [9]. For the dual control problem, the cost function would include the state error, the controller energy, and also a measure of the future filter uncertainty. The interested reader can find various solution approaches to the dual control problem for non-linear stochastic systems in [6] or [26], but in all cases the numerical results are very similar to the angles-only analysis. For target intercept applications, the dual control laws introduce some amount of motion normal to the line-of-sight in order to improve the observability of the target.

Although these two areas give helpful results, they are limited in terms of direct application to the angles-only orbital navigation problem of interest here. First of all, the dynamics associated with orbital motion makes the problem more complex than most of the cases previously examined. Also, solving the dual control problem is a computationally intensive approach that makes its potential use in a real-time feedback system questionable. The more practical solution is to use maneuvers to create relative motion orbital trajectories that, while they may not be mathematically optimal, enable the navigation filter to perform effectively with angles-only measurements. Even though the results of dual control and bearings-only analysis did not involve orbital dynamics, their insight that maneuvers normal to the line-of-sight provide target observability is consistent with the lessons learned in Chapter 3. In some sense then, the analytic results provided by these fields verify the conclusions that will now be used to form actual maneuver-assisted trajectories for angles-only navigation.

4.2 REFERENCE TRAJECTORY DEVELOPMENT

As with the natural motion trajectories, the maneuver-assisted trajectories are classified as either station-keeping or closure cases. These characterizations make it easier to compare results

as well as being practical from the standpoint of an end-user who may be only concerned with one phase or the other for mission design.

Within this section the relative motion plots are broken down into four sub-plots in order to highlight the effects of the maneuvers. The top-left plot is the relative in-plane motion. The remaining three plots are the time histories of the downrange, altitude, and cross-track components of relative motion. The following sections describe in detail the various trajectory designs as well as explaining the actual calculations for the maneuvers used.

4.2.1 Station-keeping

Similar to the natural motion cases, the station-keeping category contains co-circular and football type orbits. Unlike the natural motion study, however, maneuver-assisted trajectories are not developed for all the possible range regimes. Rather, the focus lies in prox ops and short range cases, since these are the areas generally of most interest for rendezvous and close approach operations. Also, it has already been shown that quantifying uncertainty results in terms of percentages of the actual range removes the range dependence. Hence, many of these maneuver-assisted trajectories at short ranges can be extrapolated to longer ranges, as will be shown in section 4.3.2.

Although the maneuver-assisted co-circular and football station-keeping orbits start in exactly the same manner as their natural motion counterparts, they are modified with maneuvers that introduce cross-track motion in one of two ways. In both cases, the cross-track motion is intended to generate a stimulus perpendicular to the line-of-sight that will be useful in improving range observability.

The first method is shown in Figure 4-1 which is the case of a football shaped relative trajectory centered 10m away from the target with 1m of vertical motion. The induced cross-track motion involves doing a maneuver at 5 hours that introduces natural cross-track motion into the trajectory through the use of a plane change maneuver. The motion is allowed to continue without modification for 2.5 orbits when it is nulled with a second maneuver. For the purposes of this study, this type of maneuver will be referred to as ‘slow cross-track motion.’ Specifically, slow cross-track motion is any maneuver pair where the first maneuver induces natural cross-track motion and the second maneuver takes place a $\frac{1}{2}$ orbit multiple later to null this motion.

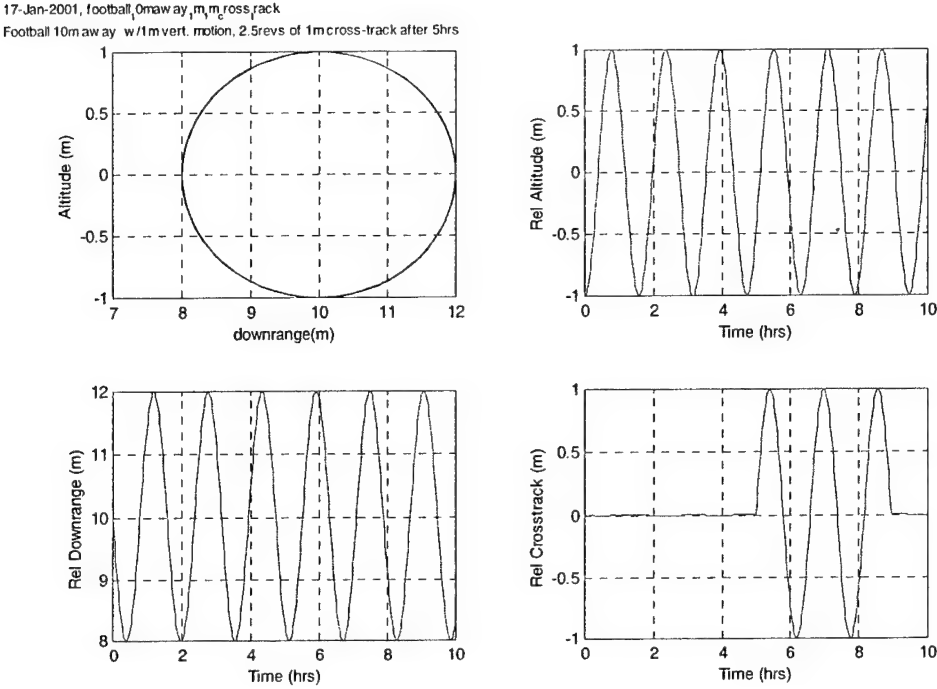


Figure 4-1: Football station-keeping 10m away with 1m vertical motion, 2.5 orbits of 1m cross-track motion starting at 5 hours, $\Delta V=2\text{mm/s}$

This type of maneuver is the simplest to actually implement. The inertial direction of the ΔV is determined by calculating the unit vector in the cross-track direction which is opposite the direction of the angular momentum vector or:

$$\hat{i}_{crs-trk} = \frac{-(\vec{R}_{tgt} \times \vec{V}_{tgt})}{|\vec{R}_{tgt} \times \vec{V}_{tgt}|} \quad (4.1)$$

where \vec{R}_{tgt} and \vec{V}_{tgt} are the inertial position and velocity vectors of the target respectively. The corresponding magnitude of the maneuver is based on the desired amount of slow cross-track motion and the magnitude of the position and velocity vectors [22]

$c \equiv$ desired crosstrack motion

$$|\Delta V_{inertial}| = 2|\vec{V}_0| \sin \left[\frac{\tan^{-1} \left(\frac{c}{|\vec{R}|} \right)}{2} \right] \quad (4.2)$$

The slow cross-track motion can be nulled at any $\frac{1}{2}$ orbit increment corresponding to the intersection of the target and chaser orbital planes, and the maneuver is exactly equal in magnitude to the initial ΔV . Another example of slow cross-track motion is shown in Figure 4-2 which is the co-circular station-keeping case with the chaser 100m away.

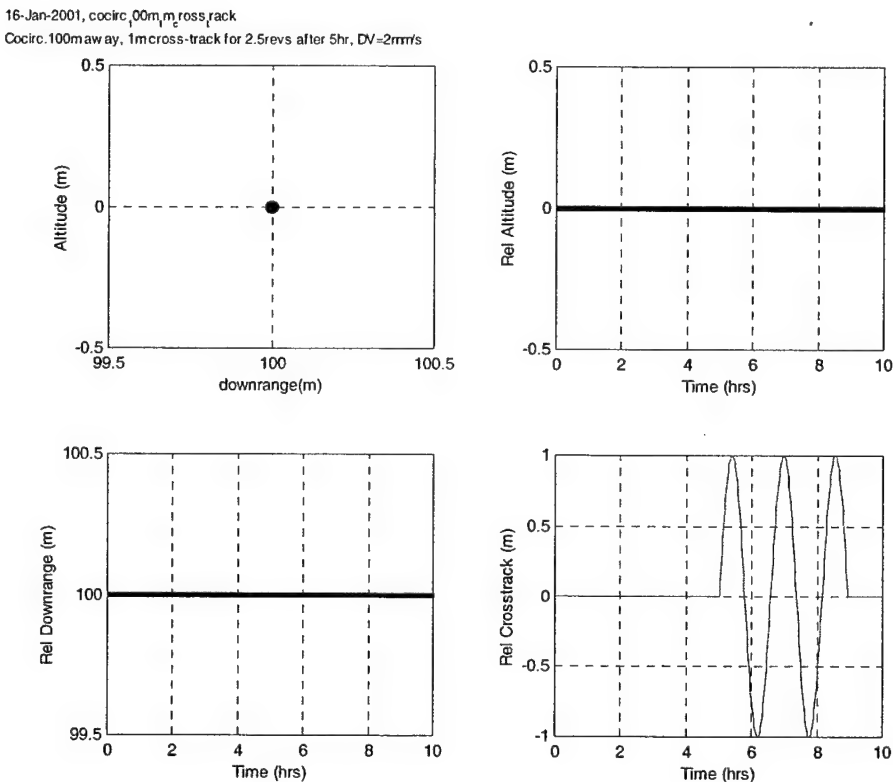


Figure 4-2: Co-circular station-keeping 100m away, 2.5 orbits of 1m cross-track motion starting at 5 hours, $\Delta V=2\text{mm/s}$

The second type of cross-track maneuver is referred to as an ‘observation maneuver’ which creates and nulls cross-track motion in an arbitrary time. Unlike slow cross-track motion, the observation maneuver is not constrained to performing maneuvers only at $\frac{1}{2}$ orbit intervals. Figure 4-3 shows an example where a station-keeping football is centered on the target and is augmented by observation maneuvers that move the chaser out approximately 10m in the cross-track direction over 10 minutes every hour beginning at 5 hours.

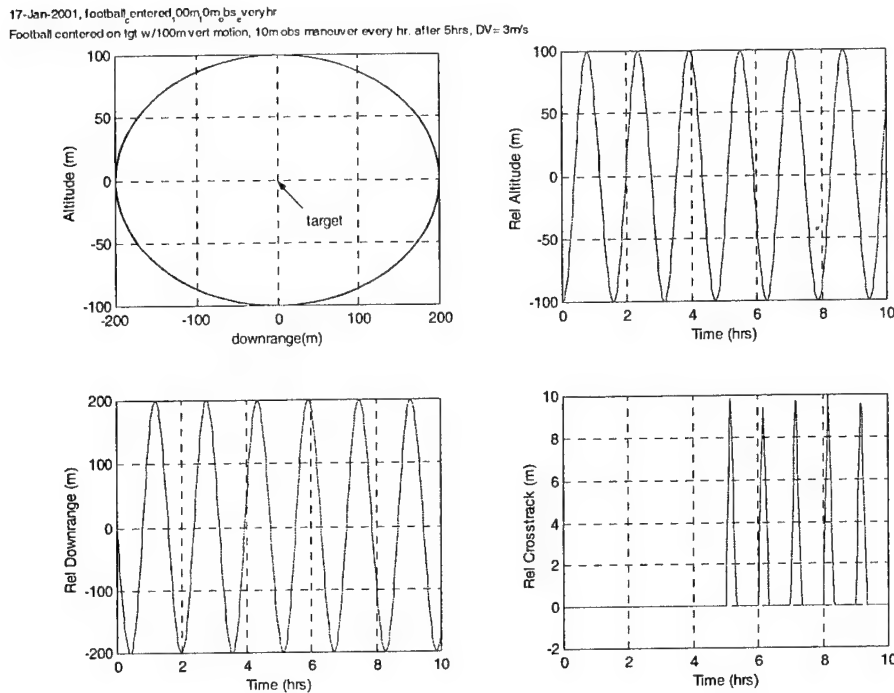


Figure 4-3: Football station-keeping centered on target with 100m vertical motion, 10m observation maneuvers every hour starting at 5 hours, $\Delta V=0.3\text{m/s}$

Although the observation maneuver can occur at any arbitrary time, the disadvantage is that three maneuvers are required to bring the chaser back to its original position since the natural oscillation of cross-track motion is no longer being taken advantage of. The direction of the burns is determined using (4.1) and the magnitudes are calculated by manipulating the C-W equations to give:

$$\begin{aligned}\Delta V_1 &= \frac{c\omega}{\sin(\omega\Delta t)} \\ \Delta V_2 &= \frac{-c\omega \cos(\omega\Delta t)}{\sin(\omega\Delta t)} - \Delta V_1 \cos(\omega\Delta t) = -\Delta V_1(1 + \cos(\omega\Delta t)) \\ \Delta V_3 &= c\omega \sin(\omega\Delta t) + \frac{c\omega \cos^2(\omega\Delta t)}{\sin(\omega\Delta t)} = \Delta V_1\end{aligned}\quad (4.3)$$

where c is again the desired cross-track motion, ω is orbital rate, and Δt is the desired time it should take for the chaser to extend c meters. The first maneuver, ΔV_1 , takes place at a user-selected time = t_0 while the chaser is in the target orbital plane. The second maneuver, ΔV_2 , takes place at time = $t_0 + \Delta t$ when the chaser is at its user-selected maximum out-of-plane point. Finally,

the third maneuver, ΔV_3 , takes place at time= $t_0+2\Delta t$ when the chaser is once again in the target orbital plane. ΔV_3 nulls the cross-track velocity.

The complete list of station-keeping maneuver-assisted trajectories generated is shown in Table 4-1 along with the associated ΔV requirements. The baseline cases, without any maneuvers, are also shown so they can be used for comparison. For all cases, the cross-track maneuvers took place according to the same schedule as the examples presented previously in this section. Specifically, ‘XX observation maneuvers’ refers to observation maneuvers moving the chaser out XX meters in the cross-track direction over 10 minutes every hour starting at five hours, and ‘YY revs ZZm cross-track’ means that slow cross-track motion moving the chaser out ZZ meters started at five hours and continued for YY orbits when the motion was nulled.

Station-Keeping	ΔV (cm/sec)
Cocircular, 100m separation	0
2.5 revs 1m cross-track	0.2
1m observation maneuvers	3
2.5 revs 10m cross-track	2
10m observation maneuvers	30
2.5 revs 100m cross-track	22
100m observation maneuvers	320
Cocircular, 1km separation	0
2.5 revs 100m cross-track	22
100m observation maneuvers	320
Football, Centered w/100m vert.motion	0
2.5 revs 10m cross-track	2
10m observation maneuvers	32
2.5 revs 100m cross-track	22
100m observation maneuvers	320
Football, 10m away w/1m vert.motion	0
2.5 revs 1m cross-track	0.2
1m observation maneuvers	3.2
2.5 revs 10m cross-track	2.2
10m observation maneuvers	32

Table 4-1: Maneuver-assisted station-keeping reference trajectories

4.2.2 Closure

The various maneuver-assisted closure trajectories include V-bar and R-bar approaches as well as modified coelliptic and traveling football orbits. In addition to the in-plane maneuvers that create the closing trajectory, all of these trajectories are also further modified with the addition of slow cross-track motion and observation maneuvers. Although the principle is the same as the station-keeping trajectories, the implementation of cross-track maneuvers must change for reasons of practicality. For the closing scenarios, it does not seem realistic to have a

fixed value of cross-track motion since the chaser no longer has a constant downrange distance to the target. For example, if the chaser started 100m away from the target on the V-bar with an additional 100m of cross-track motion there might not be any problems. However, by the time the chaser is only 5m away from the target, 100m of cross-track motion is more than excessive and would create the potential for unwanted collisions. To address this problem, the magnitude of both slow cross-track motion and observation maneuvers must be changed based on the range between the target and chaser.

The first type of closing trajectory shown in Figure 4-4 is the V-bar approach. The chaser starts 360m away from the target and is closing on it at 1cm/sec (10hr total closing time). This case also shows an example of how the slow cross-track motion is reduced in magnitude every $\frac{1}{2}$ orbit as the range to the target decreases.

18-Jan-2001, vbar_360mback_cmsec_armed_crosstrack

Vbar approach from 360m @ 1cm/sec,Damped cross-track oscillations, DV=1.59m/s

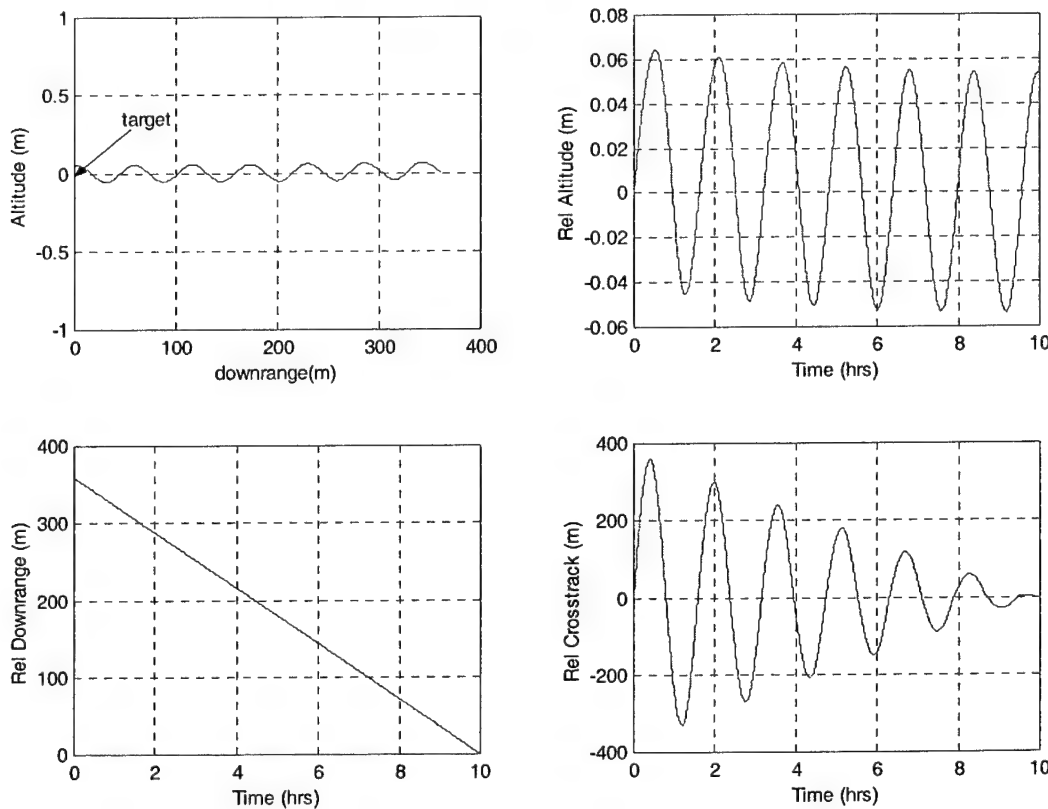


Figure 4-4: V-bar approach from 360m at 1cm/sec with damped cross-track oscillations, $\Delta V=1.59\text{m/s}$

A true V-bar approach is possible only with continuous thrust. However, a V-bar approach may be approximated by executing a maneuver at each time step. The magnitude of the first maneuver is simply the value of the desired closing rate applied in the V-bar direction which is in the direction of the target velocity vector or:

$$\hat{i}_v = \frac{\vec{V}_{tgt}}{|\vec{V}_{tgt}|} \quad (4.4)$$

After this initial maneuver, the remaining maneuvers are executed in the radial direction or:

$$\hat{i}_r = \frac{\vec{R}_{tgt}}{|\vec{R}_{tgt}|} \quad (4.5)$$

Where the magnitude is calculated according to:

$$\Delta V = 2\omega (\text{Closing Rate}) \delta t \quad (4.6)$$

where δt is the time step interval being used in propagating the trajectory. This approximation to the true continuous thrust approach is the reason for the small oscillations in the altitude of Figure 4-4.

Another possible closure trajectory is an R-bar approach. Figure 4-5 shows an example where the chaser is closing on the target at 1cm/sec from 360m below and uses several observation maneuvers during the approach. Note that these maneuvers grow smaller as the chaser gets nearer to the target.

18-Jan-2001, rbar,60mbelow,1cm/sec,ult,bs
 Rbar approach from 360m @ 1cm/sec, Mult Observation Man., DV=27.1m/s

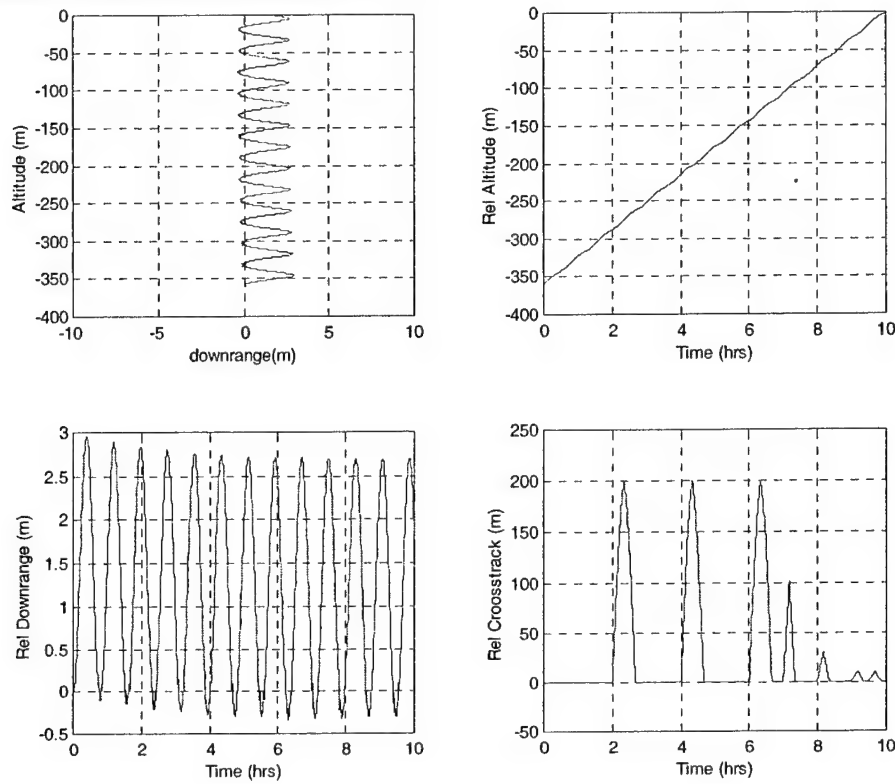


Figure 4-5: R-bar approach from 360m at 1cm/sec with multiple observation maneuvers, $\Delta V=27.1\text{m/s}$

The maneuvers required for the R-bar approach are more complicated than the V-bar approach because the continuous thrust case actually requires a ΔV in two different directions. The first maneuver must initiate the closing rate as well as null the downrange relative velocity between the two vehicles. The start of closure is handled by simply applying a ΔV in the radial direction defined by (4.5) equal to the desired closing rate. The initial downrange relative velocity exists due to the altitude difference between the two vehicles and is eliminated by executing a maneuver in the V-bar direction defined by (4.4) equal to

$$\Delta V = -1.5\omega \Delta h \quad (4.7)$$

where Δh is the altitude difference. After this initial maneuver, each later time step requires one maneuver in the V-bar direction (4.4) whose magnitude is calculated identically to (4.6) which maintains the R-bar closing rate. The other maneuver is executed in the radial direction (4.5) in order to maintain the chaser at a fixed downrange location so that the total maneuver is

$$\Delta \bar{V} = (3\omega^2 \Delta h \delta t) \hat{i}_r + [2\omega (\text{Closing Rate}) \delta t] \hat{i}_v \quad (4.8)$$

Similar to the V-bar approach plots, the downrange oscillation in the R-bar relative motion plots in Figure 4-5 is due to the continuous thrust approximation.

Although the fuel use associated with the R-bar approach shown in Figure 4-5 seems high, this is primarily because the approach rate is rather slow and the chaser is initially so far from the target. Figure 4-6 shows the non-linear relationship between the approximate ΔV required (for 500km circular target orbit) and the initial altitude separation for R-bar approaches at three different rates.

Delta V Required for R-bar approach

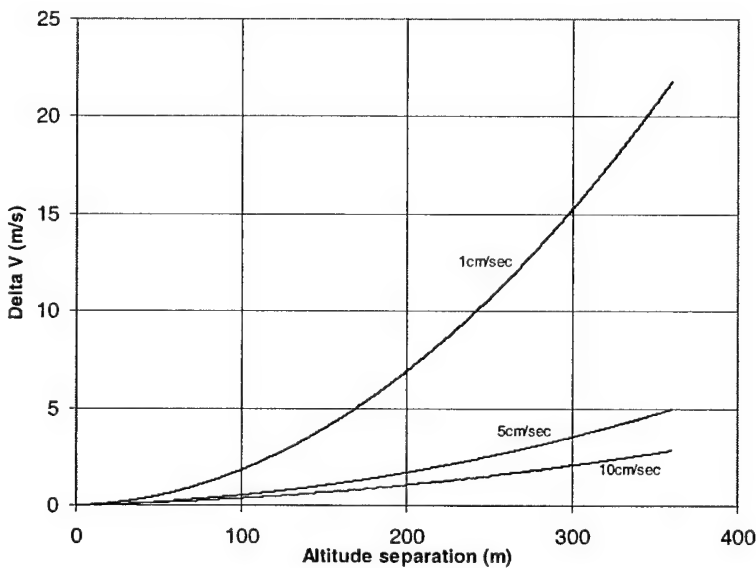


Figure 4-6: ΔV required for R-bar approaches with varying closing rates & initial separations

The third type of closing trajectory considered is the modified coelliptic. In this case, the coelliptic naturally generates the closing rate, the maneuvers are used simply to create either slow cross-track motion or observation maneuvers. Figure 4-7 shows the case of a 100m coelliptic which has slow cross-track motion that begins and ends at 2 and 8 hours respectively. The cross-track oscillations are sized based on the range to the target and are symmetric on both sides of the target flyby, which occurs at 5 hours.

26-Jan-2001, concentric, 00m damped loss/rack 2-8hrs
 Coelliptic w/100m delta h, damped cross-track motion from 2-8hrs, DV=8.85m/s

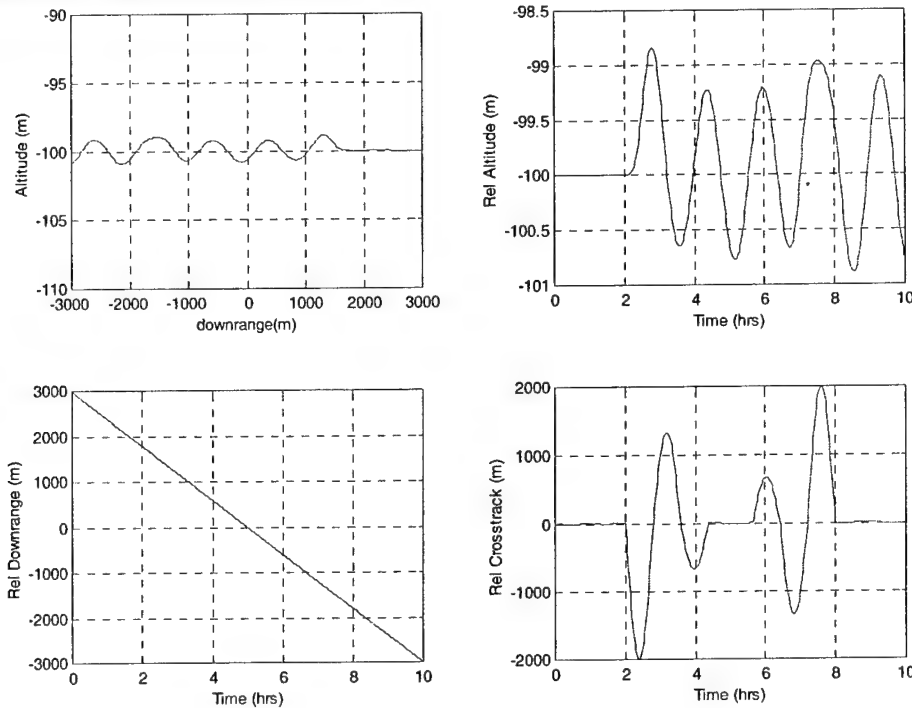


Figure 4-7: Coelliptic with 100m Δh and damped cross-track oscillations symmetric with respect to flyby point from 2-8 hours, $\Delta V=8.85\text{m/s}$

The final group of closing trajectories considered are modified traveling footballs. As explained in the natural motion analysis, these are very similar to coelliptic orbits except for an eccentricity difference that generates relative altitude motion. There are three variations of the traveling football used to approach the target. As with the cross-track motion, the motivation for these cases is that the vertical oscillations in the football should decrease as the chaser approaches the target. Additionally, altering the in-plane natural motion involves maneuvers that may improve observability.

All of the modified traveling footballs are created by using Hohmann transfer type burns in order to shift the chaser's apoapse and periapse heights. Since they are Hohmann burns, the maneuvers are in or opposite the direction of the V-bar, defined by (4.4). By performing a maneuver of magnitude

$$\Delta V = \frac{\omega}{4} (\text{height change}) \quad (4.9)$$

in the direction of the V-bar at apoapse, the periapse height will be correspondingly shifted up. Similarly, using the same magnitude burn at periapse, but opposite the V-bar direction, will shift the apoapse altitude down.

The first and simplest possible modification to the traveling football is to reduce the magnitude of the vertical oscillations while maintaining the same semi-major axis difference, Δh . Figure 4-8 shows an example of this where the traveling football maintains a 10m Δh while reducing its vertical motion from 100m to 0 over 10 hours. Note that this case also exhibits damped slow cross-track motion as it approaches the target.

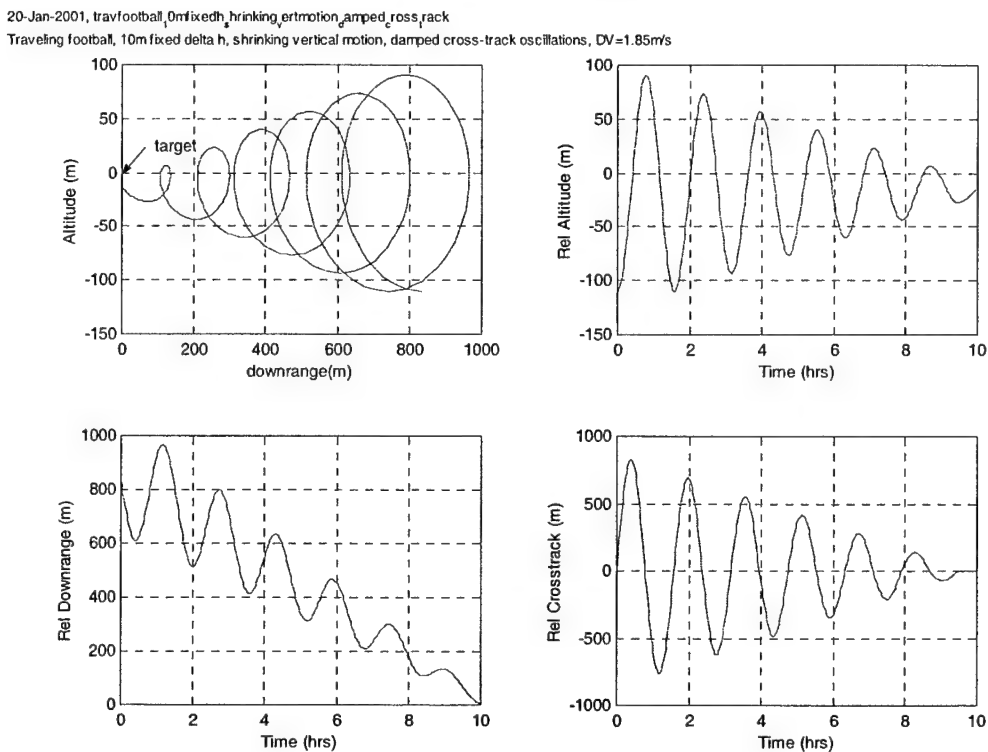
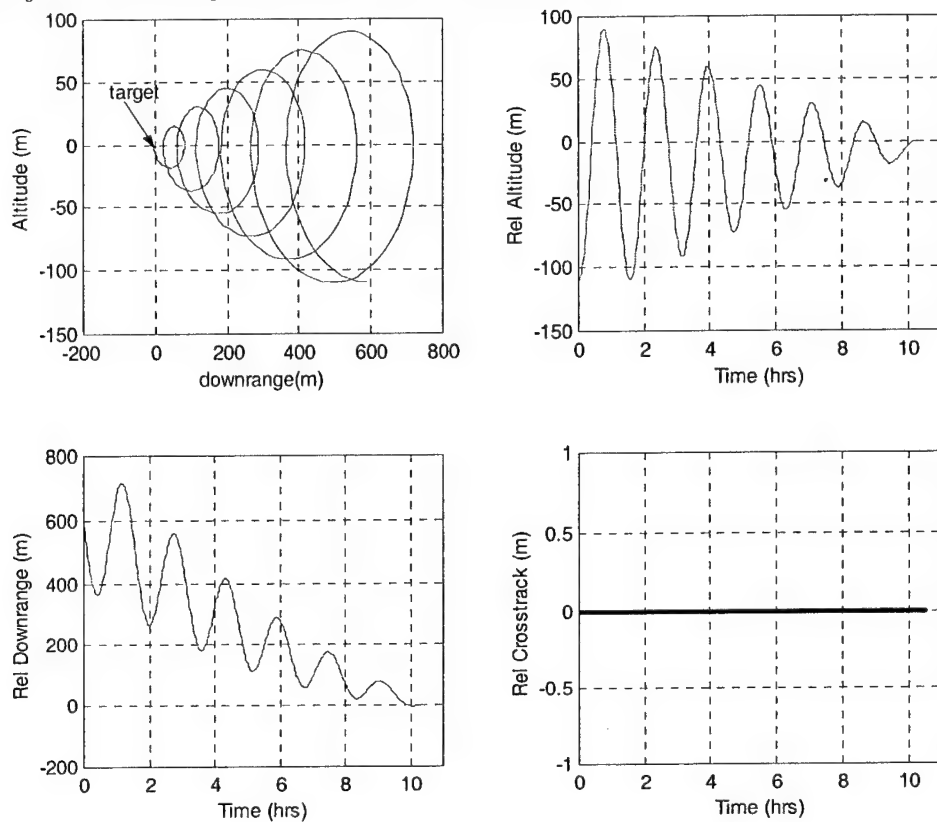


Figure 4-8: Traveling football with fixed 10m Δh and shrinking vertical oscillations with damped cross-track oscillations, $\Delta V=1.85\text{m/s}$

The second type of modified traveling football decreases both the vertical oscillations as well as the Δh as it closes on the target. The shrinking Δh has the added benefit of reducing the closing rate between the chaser and target as the range decreases. This is very appealing for docking or close approach type missions since slow closing rates are usually preferred. A case similar to the previous one is shown in Figure 4-9 except this time the Δh is also shrinking. There is no cross-track motion in this case.

20-Jan-2001, travfootball,0mshrinkingh_shrinking_vertmotion
Traveling football w/10m shrinking delta h, shrinking vert.motion from 100m, DV=5.5cm/s



**Figure 4-9: Traveling football with shrinking Δh and shrinking vertical oscillations,
 $\Delta V=0.055\text{m/s}$**

The final variation of a traveling football is the spiral case which is shown in Figure 4-10. The only difference between this case and the previous one is that the first burn takes place at apoapse rather than periapse, and the resulting relative motion spirals in towards the target. This case begins with 100m of vertical motion and 10m Δh and also makes use of multiple observation maneuvers whose magnitude decreases as the spiral moves closer to the target.

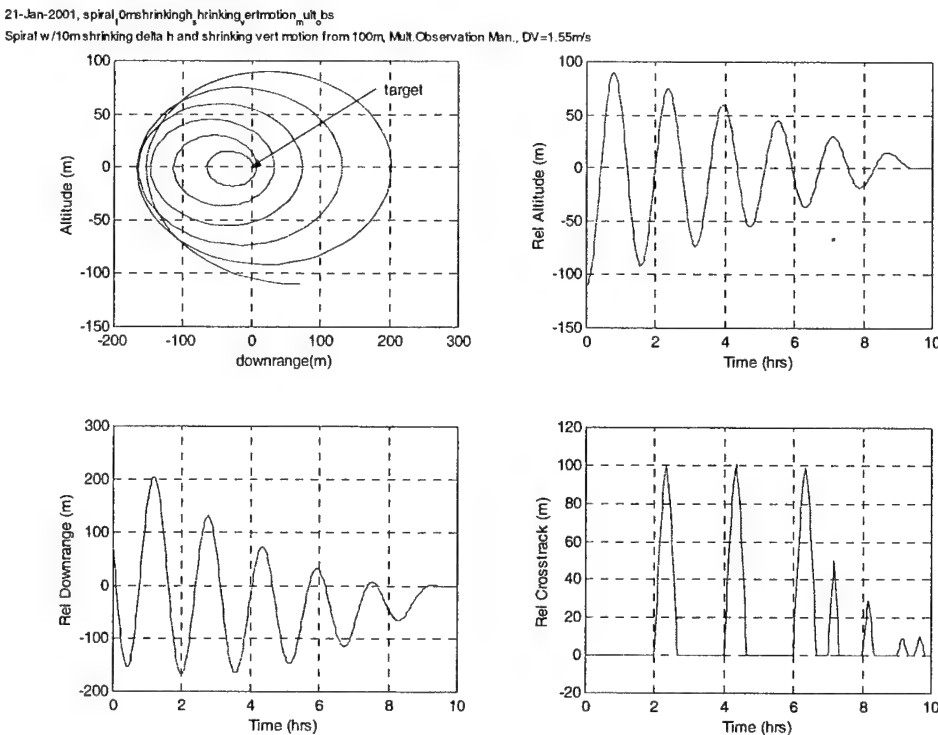


Figure 4-10: Traveling football/spiral with shrinking Δh and shrinking vertical oscillations with multiple observation maneuvers, $\Delta V=1.55\text{m/s}$

The complete listing of maneuver-assisted closure trajectories is shown in Table 4-2. Note that some of the associated ΔV values are extremely high. Although these cases may not be useful from a direct practical standpoint, the insights they provide will prove useful later. The table lists the actual values used for the cross-track maneuvers as well as the times they occurred. For example, the case of the V-bar approach with damped slow cross-track motion states “Damped cross-track, burn every 1/2 rev start at 360m and reduce by 30m each burn” which means that the trajectory starts with a maneuver to introduce 360m of slow cross-track motion and then each $\frac{1}{2}$ orbit increment after that it nulls 30m of the motion until it reaches 0. As another example, the case of the R-bar approach with multiple observation maneuvers states “Mult.obs.man. At(2, 4, 6, 7, 8, 9, 9.5) hr going out (200, 200, 200, 100, 30, 10, 10)m in (20, 20, 20, 10, 10, 10)min” which lists the times when the maneuvers start (2, 4...) hours, how far each corresponding maneuver goes in the cross-track direction (200, 200 ...) meters, and finally what the Δt value is for each case (20, 20 ...) minutes to go. In this example case, the first maneuver takes place at 2hr, the chaser goes 200m in 20 minutes at which point the second

maneuver is executed, and another 20 minutes later (40 minutes from the first maneuver) the final null maneuver is executed.

Closure	ΔV (m/sec)
V-bar approach from 360m, 1cm/s	0.81
2revs 100m cross-track starting at 5hr	1.03
Damped cross-track, burn every 1/2 rev start at 360m and reduce by 30m each burn	1.59
Mult.obs.man. At(2,4,6,7,8,9,9.5)hr going out (200,200,200,100,30,10,10)m in (20,20,20,10,10,10,10)min	3.47
30m cross-track 1/2 rev before end	0.86
50m cross-track 1/2 rev before end	0.84
R-bar approach from 360m, 1cm/s	24.4
2revs 100m cross-track starting at 5hr	24.7
Damped cross-track, burn every 1/2 rev start at 360m and reduce by 30m each burn	24.96
Mult.obs.man. At(2,4,6,7,8,9,9.5)hr going out (200,200,200,100,30,10,10)m in (20,20,20,10,10,10,10)min	27.1
Coelliptic, 100m Δh	0
Damped cross-track, burn every 1/2 rev start at 2.9km and reduce by 483m each burn to 0, increase after flyby	9.63
Damped cross-track from 2-8hrs, burn every 1/2 rev start at 2km and reduce by 667m to 0, increase after flyby	8.85
Mult.obs.man. At (1,2,3,4,4.5,5.5,6,7,8,9)hr going out (2.4,1.8,1.2,6,3,3,6,1.2,1.8,2.4)km in (20,20,10,10,10,10,10,20,20)min	50.72
Coelliptic, 1km Δh	0
Damped cross-track, burn every 1/2 rev start at 29km and reduce by 4.8km each burn to 0, increase after flyby	96.3
Trav. Football, standard	0
Shrinking Trav. Football, fixed Δh	0.051
Damped cross-track, burn every 1/2 rev start at 830m and reduce by 69m each burn	1.85
Mult.obs.man. At (2,4,6,7,8,9,9.5)hrs going out (500,500,500,250,150,75,30)m in (20,20,20,10,10,10,10)min	7.53
Shrinking Trav. Football, shrinking Δh	0.055
Damped cross-track, burn every 1/2 rev start at 600m and reduce by 50m each burn	1.35
Mult.obs.man. At (2,4,6,7,8,9,9.5)hrs going out (350,350,350,200,150,100,30)m in (20,20,20,10,10,10,10)min	6.1
Spiral	0.055
Damped cross-track, burn every 1/2 rev start at 200m and reduce by 16.7m each burn	0.46
Mult.obs.man. At (2,4,6,7,8,9,9.5)hrs going out (100,100,100,50,30,10,10)m in (20,20,20,10,10,10,10)min	1.55

Table 4-2: Maneuver-assisted closure reference trajectories

4.3 LINEAR COVARIANCE RESULTS

Following the generation of the maneuver-assisted reference trajectories, the LINCOV tool was used to analyze the downrange uncertainty. As with the case of the natural motion analysis, the results are considered separately for the station-keeping and closure cases. In order to ensure that the maneuvers were in fact significantly improving the navigation results, the *a priori* uncertainties were increased beyond those used in the natural motion analysis. The actual values used for the initialization were dependent on the specific trajectory. For station-keeping and approaches along the V-bar or R-bar, the standard deviation of the position uncertainties in every direction was 10% of the actual range. The standard deviation of the velocity uncertainties was $1/1000^{\text{th}} \text{ sec}^{-1}$ of the corresponding position uncertainties. For example, if the actual range was 1,000m then the position uncertainty would be 100m, and the velocity uncertainty would be

10cm/sec. For the cases of coelliptics and traveling footballs, the *a priori* uncertainties were no longer spherical. The downrange position uncertainty was 10% of the actual downrange value while the altitude and cross-track uncertainties were 10% of the actual altitude. Again, the velocity uncertainties were $1/1000^{\text{th}}$ sec $^{-1}$ of the corresponding position uncertainty. This methodology was used because the spherical *a prioris* were not always appropriate. For example, in the case of a 100m coelliptic, the chaser starts approximately 3km behind the target in order to pass under it at 5 hours. If the *a priori* uncertainty for all position components was 10% (or 300m) then the altitude uncertainty would be significantly larger than the desired Δh . It is unlikely that in actual practice, the chaser would be placed on a 100m coelliptic when the navigation's altitude uncertainty is three times larger. Therefore, the *a priori* uncertainty was selected to be both large enough to test the maneuver-assisted trajectories as well as to be more realistic based on the specific trajectory.

It is still assumed that applied ΔV is being measured perfectly. Clearly, errors in measuring ΔV will adversely affect the navigation performance. However, as in chapter 3, the results of this chapter are more focused on investigating angles-only navigation from a qualitative standpoint. The effects of modeling IMU errors as discussed in section 2.2.2 will be more fully explored in chapter 5. A related concern is the ability of the IMU to actually sense the mm/sec level maneuvers that some of the trajectories use. This is handled through the use of thrust modeling, and will be discussed in section 5.2.

4.3.1 Station-keeping

As expected, maneuvers made an immediate and noticeable improvement in the downrange uncertainty for station-keeping cases which included co-circular and football orbits. The first demonstration of this, in Figure 4-11, shows the case of a football centered on the target with 100m of vertical motion. At 5 hours, a maneuver is executed to start 10m of slow cross-track motion that is nulled after 2.5 orbits. These two maneuvers require a total of 2cm/sec of ΔV . The maneuver immediately reduces the error level although the oscillatory nature of the downrange and altitude errors still exists due to the error ellipse behavior explained in section 3.4.1.

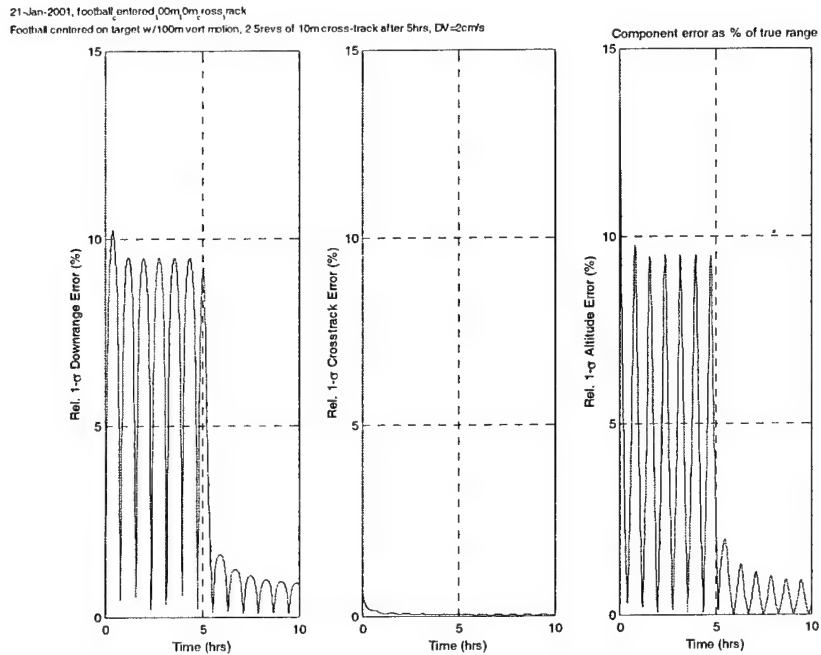


Figure 4-11: Relative position uncertainty for Football station-keeping centered on target with 100m vertical motion and 2.5 orbits of 10m cross-track motion starting at 5 hours, $\Delta V=0.02\text{m/s}$

The next point, again as expected, is that the addition of a maneuver and the corresponding additional geometry leads to improvements in downrange knowledge. The series of plots in Figure 4-12, Figure 4-13, and Figure 4-14 are all for the case of a co-circular orbit that is 100m away from the target. At 5 hours, a maneuver introduces 1, 10, and 100m of slow cross-track motion respectively for 2.5 orbits. For purposes of fuel practicality, a key piece of information to notice here is that the improvement in downrange uncertainty going from 10m to 100m of slow cross-track motion is not nearly as dramatic as that from 1m to 10m. This indicates that the relationship between the amount of cross-track motion and downrange uncertainty is non-linear, but more importantly there is a principle of diminishing returns at work. Although it is possible to expend 22cm/sec of fuel to generate 100m of slow cross-track motion, the results from using only 2cm/sec for slow 10m of cross-track motion are still a marked improvement over the initial condition. Therefore, even in fuel-constrained missions, smaller maneuvers still yield very useful information, and in some cases larger maneuvers may just be wasting fuel while not noticeably improving the navigation results.

Maneuver-Assisted Trajectory Analysis

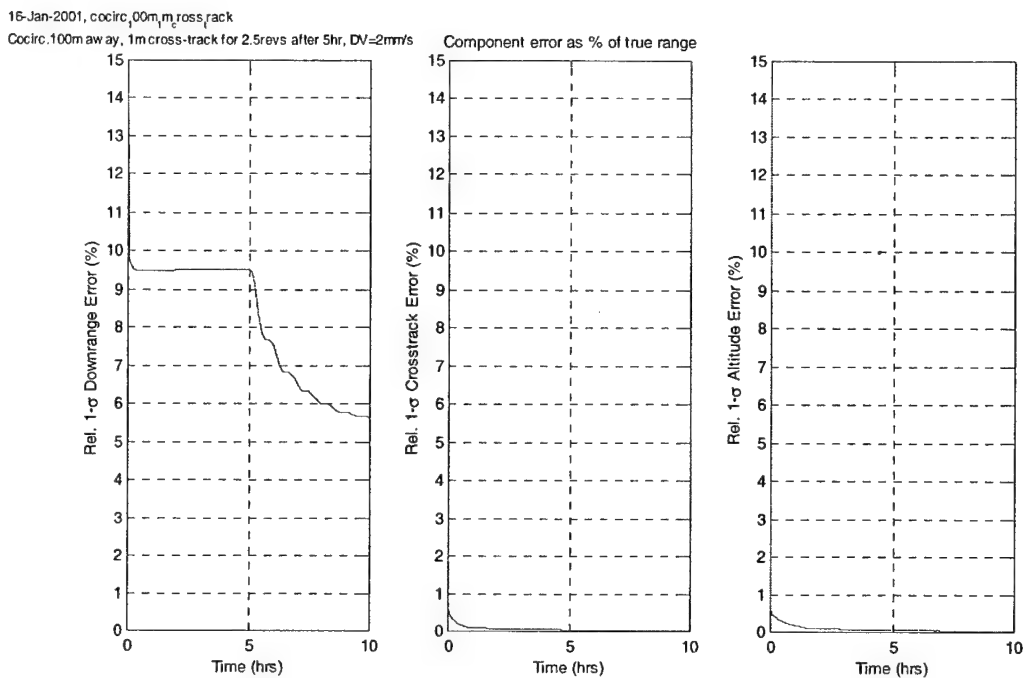


Figure 4-12: Relative position uncertainty for Co-circular station-keeping 100m away with 2.5 orbits of 1m cross-track motion starting at 5 hours, $\Delta V=2\text{mm/s}$

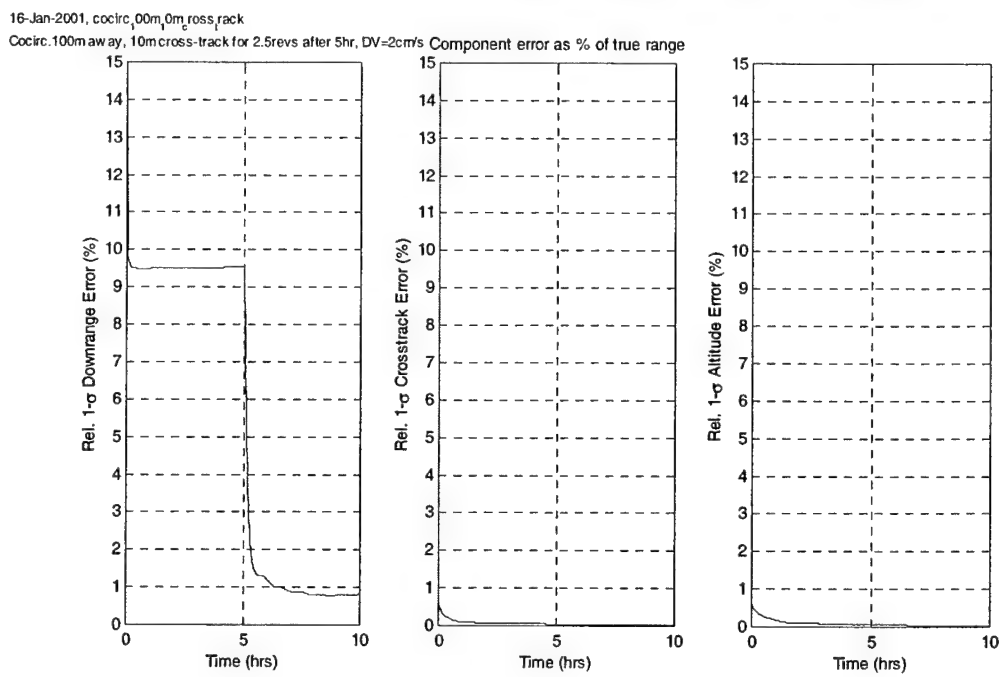


Figure 4-13: Relative position uncertainty for Co-circular station-keeping 100m away with 2.5 orbits of 10m cross-track motion starting at 5 hours, $\Delta V=.02\text{m/s}$

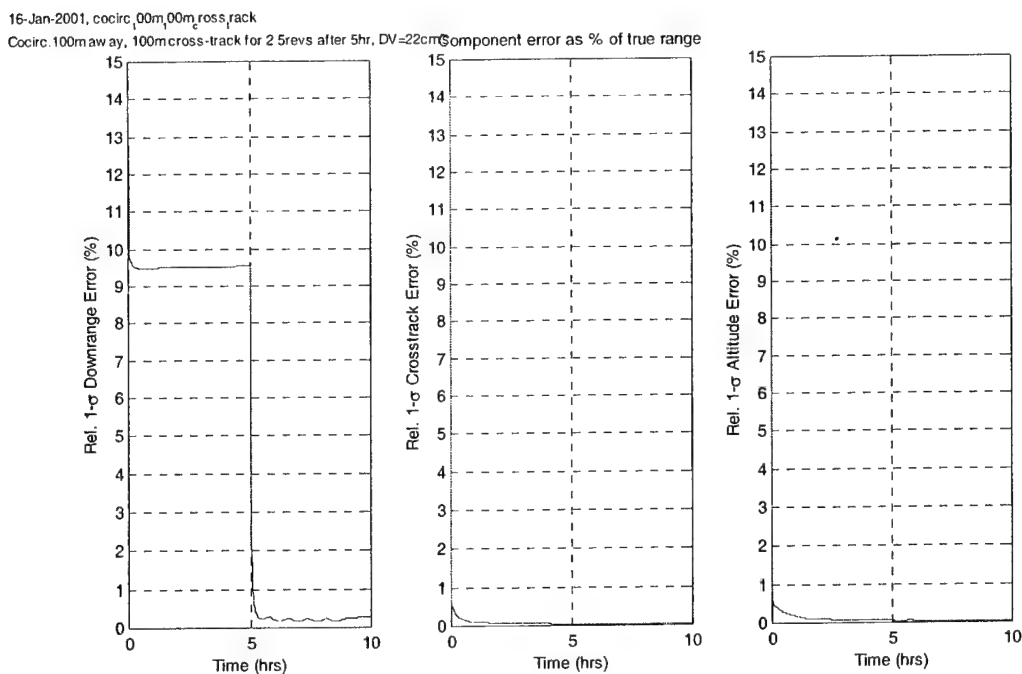


Figure 4-14: Relative position uncertainty for Co-circular station-keeping 100m away with 2.5 orbits of 100m cross-track motion starting at 5 hours, $\Delta V = .2\text{m/s}$

The effect of observation maneuvers on downrange uncertainty for station-keeping cases actually turns out to be very similar to the simpler method of adding slow cross-track motion. This could be anticipated since the two methods become identical as the length of the observation maneuver approaches the length of natural cross-track motion. In other words, if the total time for the observation maneuver is $\frac{1}{2}$ orbit then its first and third maneuvers are identical to the case of slow cross-track motion, and the second maneuver that occurs $\frac{1}{4}$ th orbit after the first one will be zero. The only real advantage provided by the observation maneuvers then is their ability to be executed in an arbitrary time period. However, this flexibility has a cost in terms of higher ΔV use. The two plots below show the results for the case of a football centered 10m away from the target with 1m of vertical motion. In Figure 4-15, 2.5 orbits of 10m slow cross-track motion begins at 5 hours while in Figure 4-16, 10m observation maneuvers (20 minutes total for each maneuver) are performed every hour starting at 5 hours. Although the effects on downrange uncertainty are extremely similar, the observation maneuvers use 0.32m/s of ΔV compared to only 2.2cm/s for the slow cross-track motion.

Maneuver-Assisted Trajectory Analysis

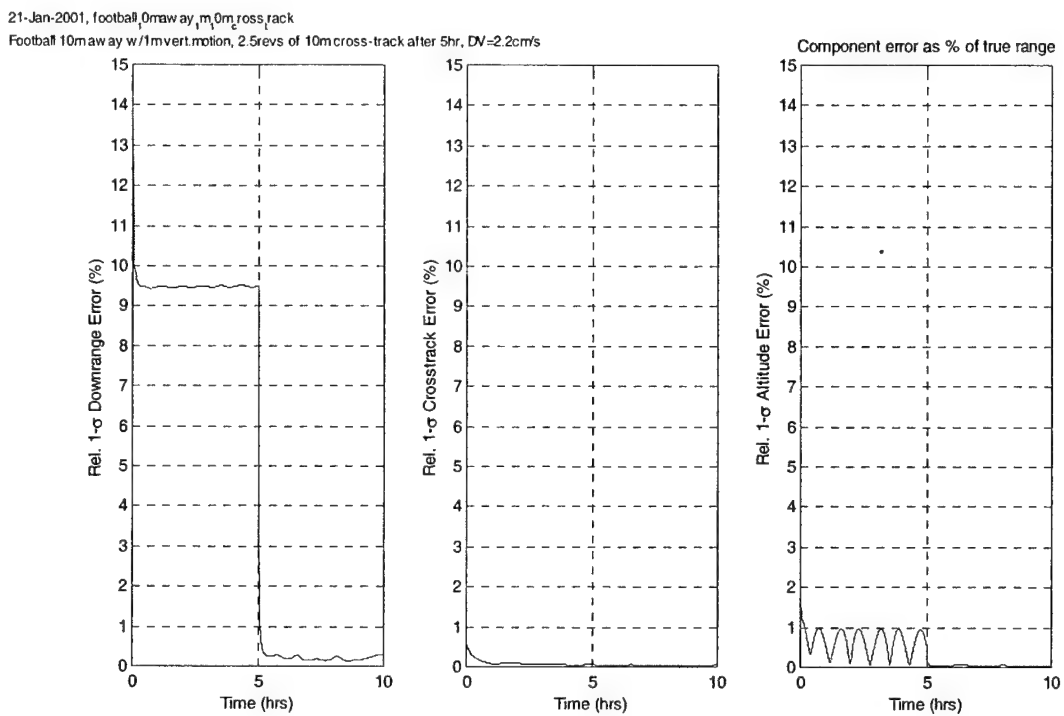


Figure 4-15: Relative position uncertainty for Football station-keeping 10m away with 1m vertical motion and 2.5 orbits of 10m cross-track motion starting at 5 hours, $\Delta V=0.02\text{m/s}$

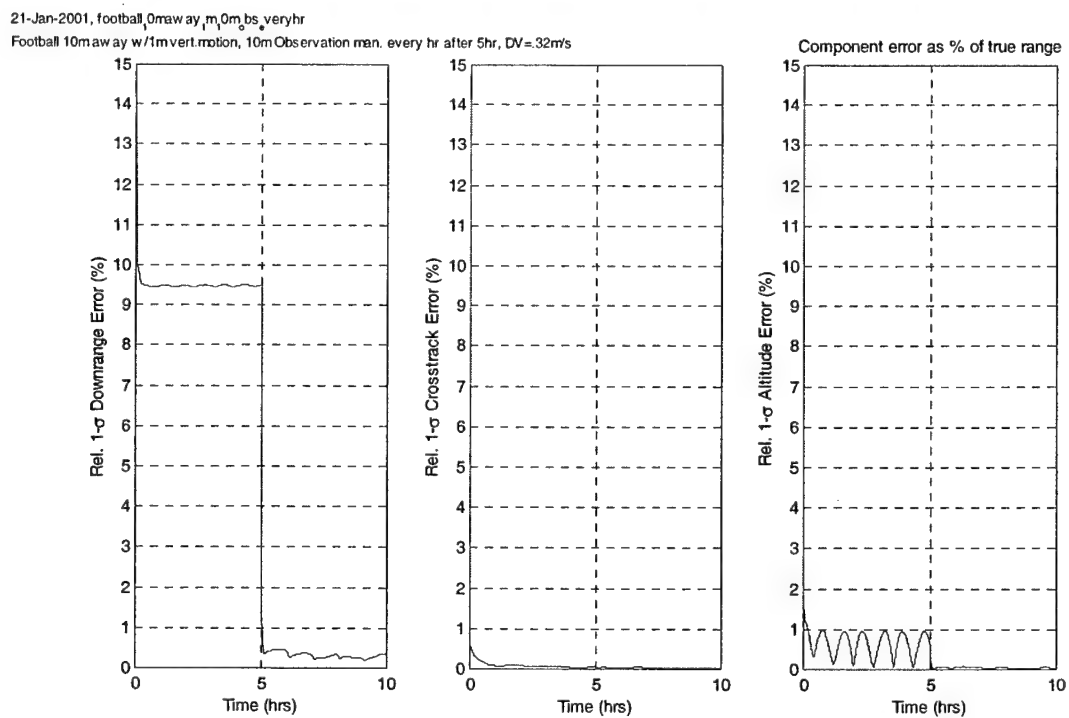


Figure 4-16: Relative position uncertainty for Football station-keeping 10m away with 1m vertical motion and 10m observation maneuvers starting at 5 hours, $\Delta V=0.32\text{m/s}$

There is one more potential benefit to using observation maneuvers, and that is the case when the chaser is subjected to un-modeled accelerations. Up to this point, the process noise parameter has not been used in the LINCOV analysis. If the process noise is non-zero, the downrange uncertainty will grow rather than just staying at a steady value. For example, in the case of Figure 4-13 and Figure 4-14, the single maneuver executed at 5 hours reduced the downrange uncertainty and it stayed nearly constant. However, Figure 4-17 shows the same case of a co-circular station-keeping orbit 100m away, but this time with process noise added to the analysis. At 5 hours, a maneuver is executed to start 100m of slow cross-track motion and the uncertainty drops, but then begins to rise again until the nulling maneuver is executed 2.5 orbits later. Compare this to Figure 4-18 which uses 100m observation maneuvers every hour also starting at 5 hours. The difference is clear and illustrates that each maneuver provides some range observability. Using the observation maneuvers uses more fuel, 3.2m/s compared to 22cm/s in this case, but provides better downrange uncertainty in the face of un-modeled accelerations.

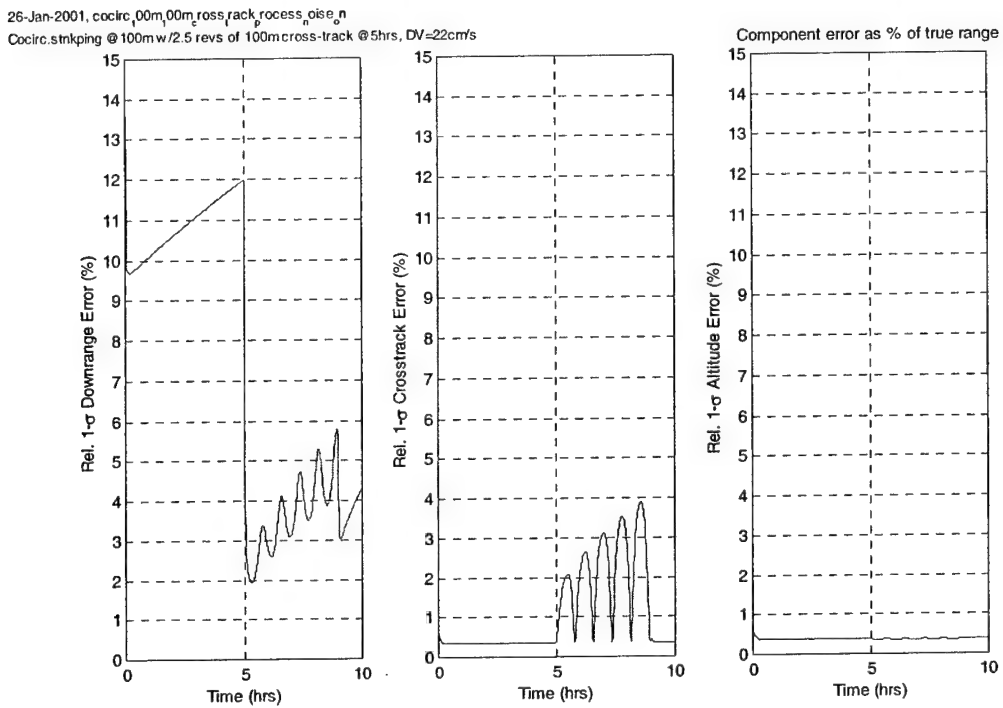


Figure 4-17: Relative position uncertainty with process noise for Co-circular station-keeping 100m away with 2.5 orbits of 100m cross-track motion starting at 5 hours, $\Delta V=0.22\text{m/s}$

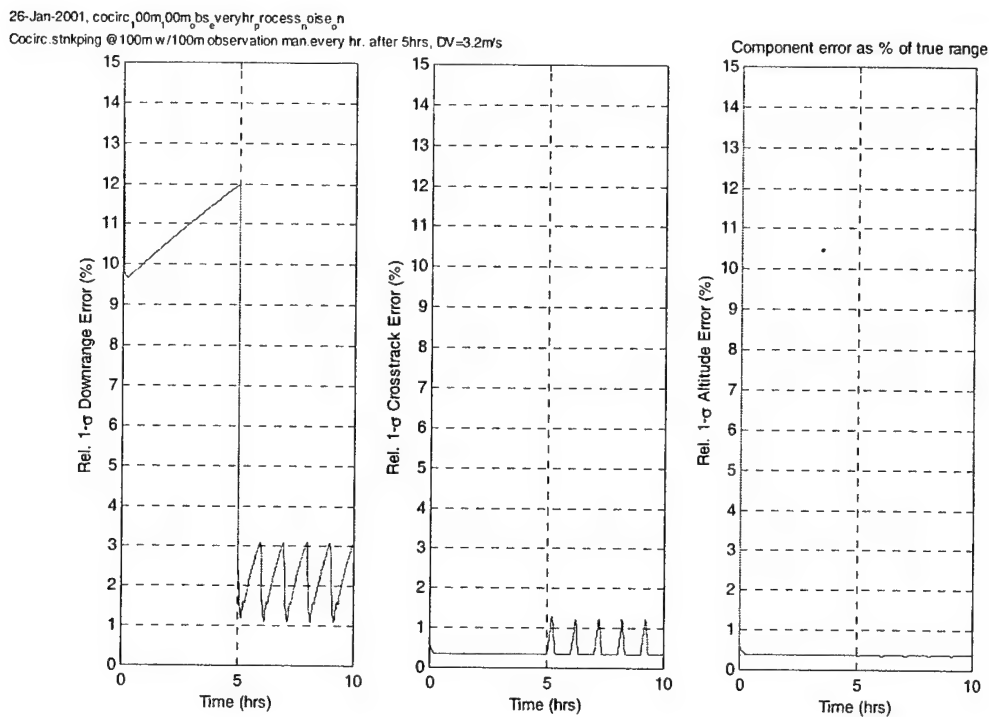


Figure 4-18: Relative position uncertainty with process noise for Co-circular station-keeping 100m away with 100m observation maneuvers every hour starting at 5 hours, $\Delta V=3.2\text{m/s}$

The preceding results and conclusions are representative of the other trajectories as well. Table 4-3 lists the required ΔV and the value of downrange percent error that the navigation filter was able to achieve for the station-keeping cases with no process noise. In cases where the uncertainty value was oscillatory, the peak value of the oscillation was recorded.

Case	Best % Errors	ΔV (m/s)
Cocircular, 100m separation	9.49	0
2.5 revs 1m cross-track	5.65	0.002
1m obs.man.	6.86	0.03
2.5 revs 10m cross-track	0.78	0.02
10m obs.man.	1.04	0.3
2.5 revs 100m cross-track	0.157	0.22
100m obs.man.	0.22	3.2
Cocircular, 1km separation	9.49	0
2.5 revs 100m cross-track	0.84	0.22
100m obs.man.	1.13	3.2
Football, Centered w/100m vert.motion	9.49	0
2.5 revs 10m cross-track	1	0.02
10m obs.man.	1.45	0.32
2.5 revs 100m cross-track	0.15	0.22
100m obs.man.	0.21	3.2
Football, 10m away w/1m vert.motion	9.45	0
2.5 revs 1m cross-track	0.71	0.002
1m obs.man.	0.97	0.032
2.5 revs 10m cross-track	0.14	0.022
10m obs.man.	0.18	0.32

Table 4-3: Maneuver-assisted station-keeping trajectory LINCOV results summary

This data can also be visualized by showing the best performing trajectories, in terms of ΔV and percent error, as in Figure 4-19.

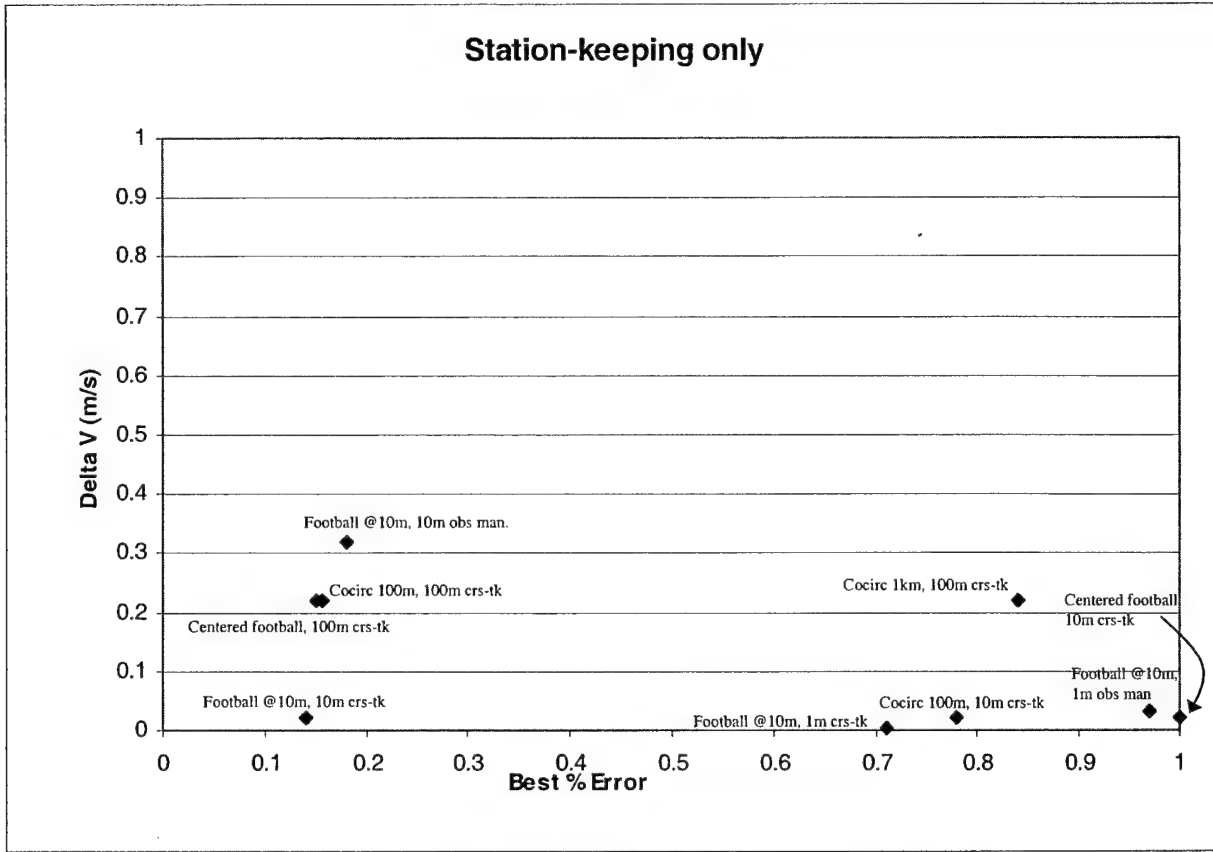


Figure 4-19: Maneuver-assisted station-keeping trajectory LINCOV results summary

4.3.2 Closure

For the case of closure maneuver-assisted trajectories, the results are considered for each general type of trajectory: V-bar, R-bar, coelliptic, and traveling football.

V-bar Approaches

First, the V-bar approach is very similar to the co-circular station-keeping case in the sense that the downrange errors grow unbounded if no cross-track maneuvers take place. Figure 4-20 shows the case of the V-bar approach from 360m behind the target at 1cm/sec. The errors are rising until a maneuver is executed at 5 hours to start 100m of slow cross-track motion. This succeeds in reducing the downrange uncertainty for 2.5 orbits when the motion is nulled and the errors immediately begin to grow again.

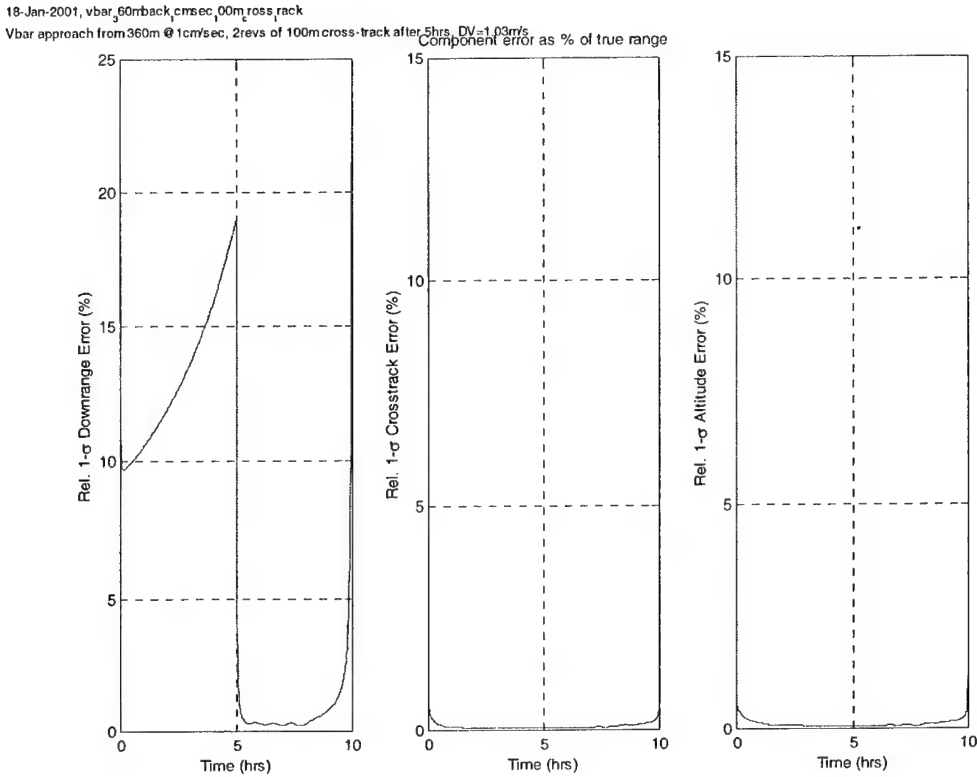


Figure 4-20: Relative position uncertainty for V-bar approach from 360m at 1cm/sec with 2 orbits of 100m cross-track motion starting at 5 hours, $\Delta V=1.03\text{m/s}$

R-bar Approaches

Unlike the V-bar approach, the R-bar approach does an excellent job of decreasing the downrange uncertainty. Using slow cross-track motion or observation maneuvers in this case does not make any difference simply because the baseline approach does so well on its own. The key that makes the R-bar approach so successful lies in the C-W equations. The range along the line-of-sight to the target can be determined based on the amount of ΔV expended to stay directly below the target according to equation (4.8). Measuring the maneuvers is indirectly providing a very accurate range estimate to the target. The major disadvantages to this approach are the large amount of fuel required as well as the potential sensitivity to IMU errors in measuring the maneuvers. Although an R-bar approach may be ideal for the terminal phase of a rendezvous, it is not practical for long range approaches or station-keeping. Figure 4-21 shows an example of the baseline R-bar approach in which the chaser closes on the target at 1cm/s from 360m below. The improvement over the V-bar approach results in Figure 4-20 is dramatic.

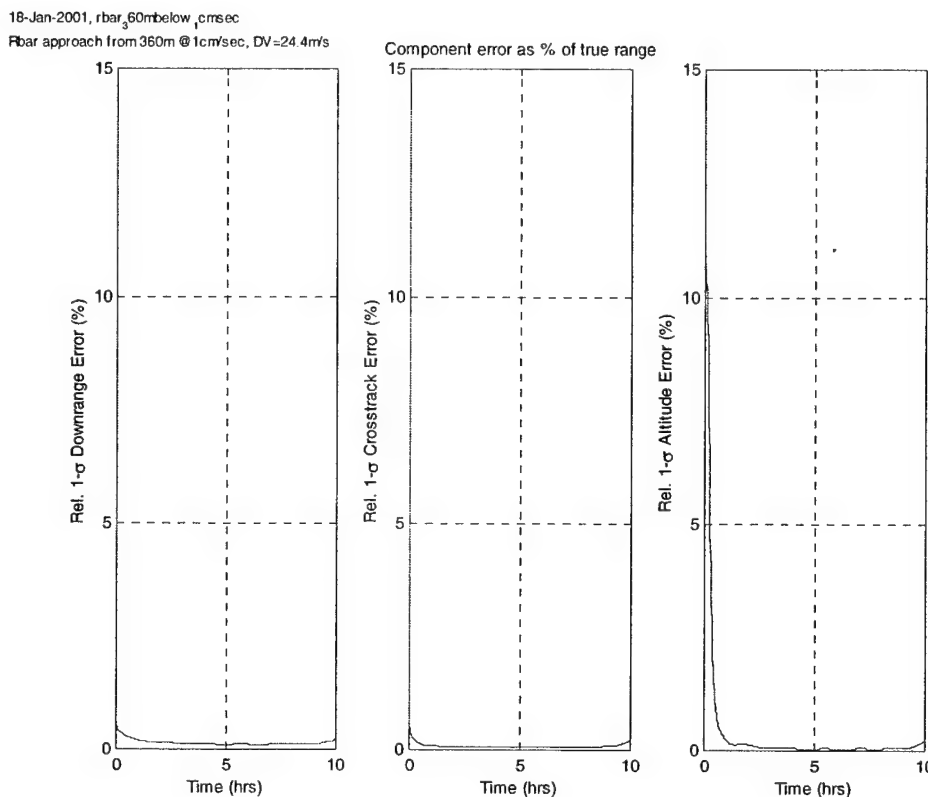


Figure 4-21: Relative position uncertainty for R-bar approach from 360m at 1cm/sec, $\Delta V=24.4\text{m/s}$

Modified Coelliptics

The third type of maneuver-assisted trajectories considered are the modified coelliptics. In general, the results were not significantly improved by the addition of cross-track maneuvers before the point of flyby. Figure 4-22 shows an overlay that has the results for a normal coelliptic with a 100m Δh as well as those for a case with damped slow cross-track motion. Although the downrange uncertainty is slightly improved by the slow cross-track motion, the cross-track uncertainty is much larger before flyby (5 hours). However, after the flyby point the characteristic first noted in the natural motion analysis appears again as the downrange percent uncertainty grows very slowly. Also, the cross-track uncertainty is no longer as large demonstrating that coelliptics with cross-track maneuvers tend to exhibit their best performance in the time following a flyby of the target.

25-Jan-2001, concentric, 00m
Coelliptic w/100m delta h, 0 DV

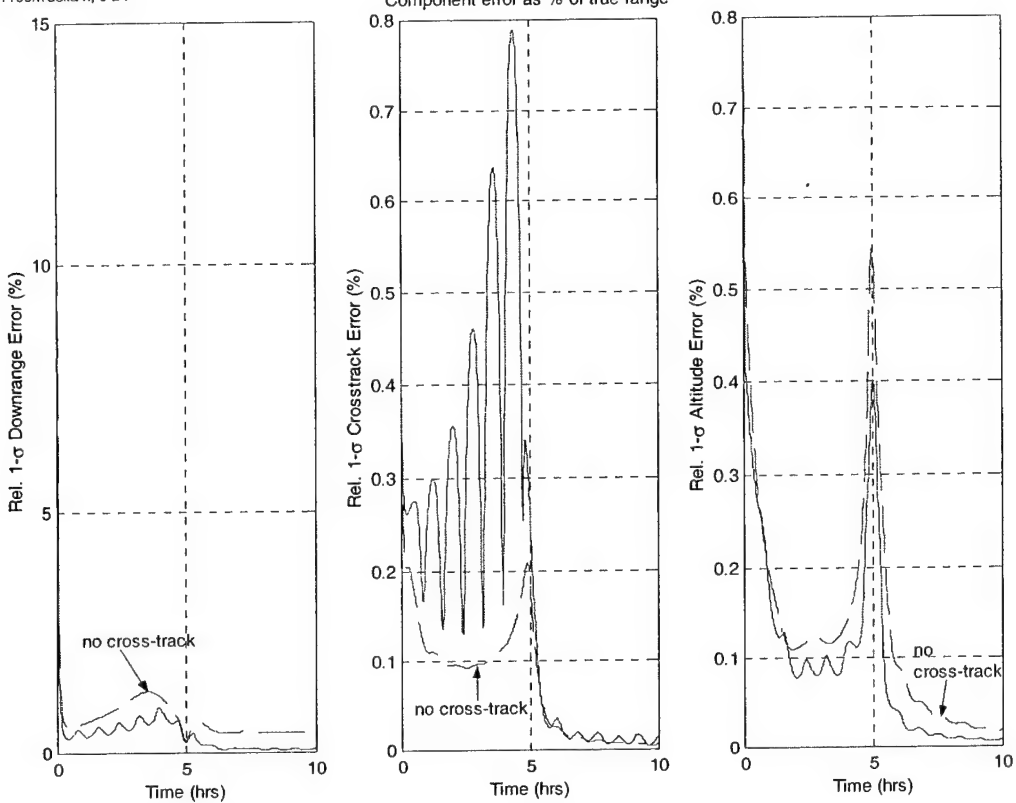


Figure 4-22: Relative position uncertainties for Coelliptic with 100m Δh case with no cross-track motion overlaid on case with damped cross-track oscillations symmetric with respect to flyby point, $\Delta V=9.63\text{m/s}$

As an aside, the modified coelliptics are used to verify that scaling the distances involved in the trajectories does not have an impact on the results in terms of percent uncertainty. By comparing two coelliptics, one with 10m Δh and the other with 100m Δh shown in Figure 4-23 and Figure 4-24 respectively, it is clear the results are in fact nearly identical. In both cases, maneuvers are being executed to induce slow cross-track motion approximately equal to the downrange distance. The 100m Δh case has maneuvers that are exactly ten times the value of the 10m Δh case. This fact is what allows all of the results from various closing trajectories to be extrapolated to different range regimes without actually having to generate different reference trajectories and run the LINCOV tool.

Maneuver-Assisted Trajectory Analysis

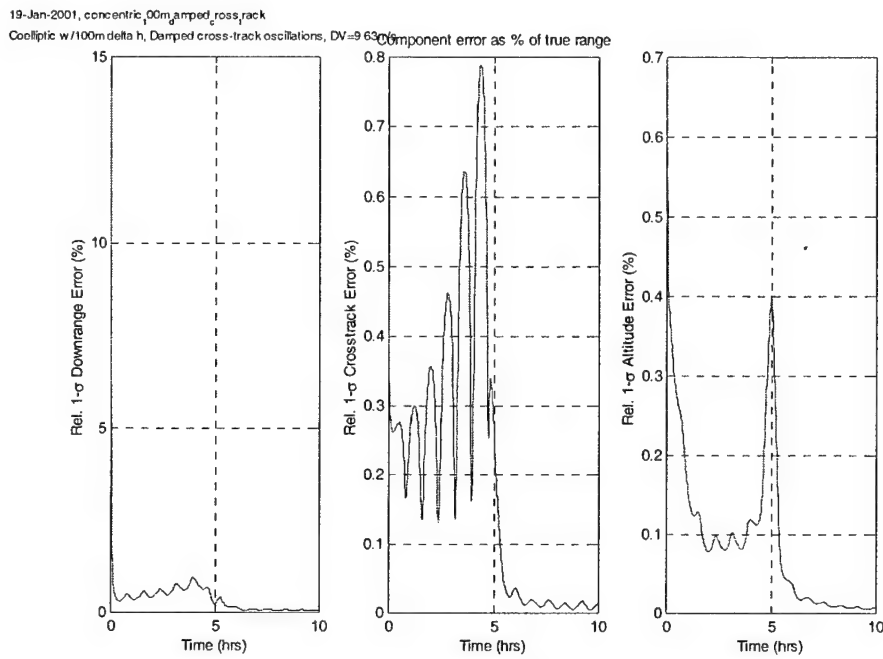


Figure 4-23: Relative position uncertainty for Coelliptic with 100m Δh case with damped cross-track oscillations symmetric with respect to flyby point, $\Delta V=9.63\text{m/s}$

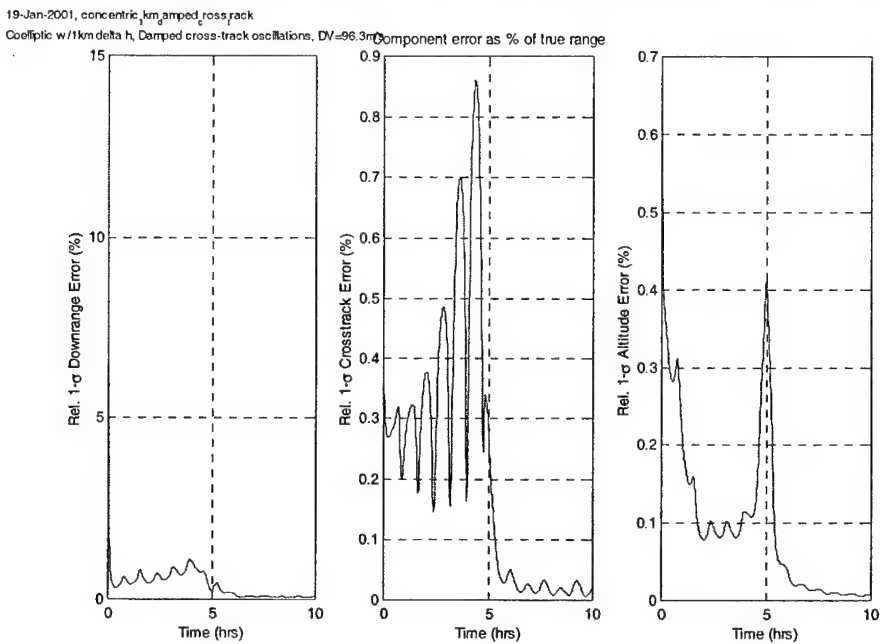


Figure 4-24: Relative position uncertainty for Coelliptic with 1km Δh case with damped cross-track oscillations symmetric with respect to flyby point, $\Delta V=96.3\text{m/s}$

Modified Traveling Footballs

The last type of maneuver-assisted closing trajectory is the modified traveling football. From a range uncertainty standpoint, these trajectories are not that much more attractive than their natural motion equivalent. It is difficult to notice any significant difference between a typical traveling football that does not require any maneuvers, Figure 4-25, and one that has in-plane maneuvers to reduce its Δh and vertical motion, Figure 4-26. However, the modified traveling footballs may still be attractive because of other characteristics such as their naturally slowing closure rate or spiraling motion towards the target.

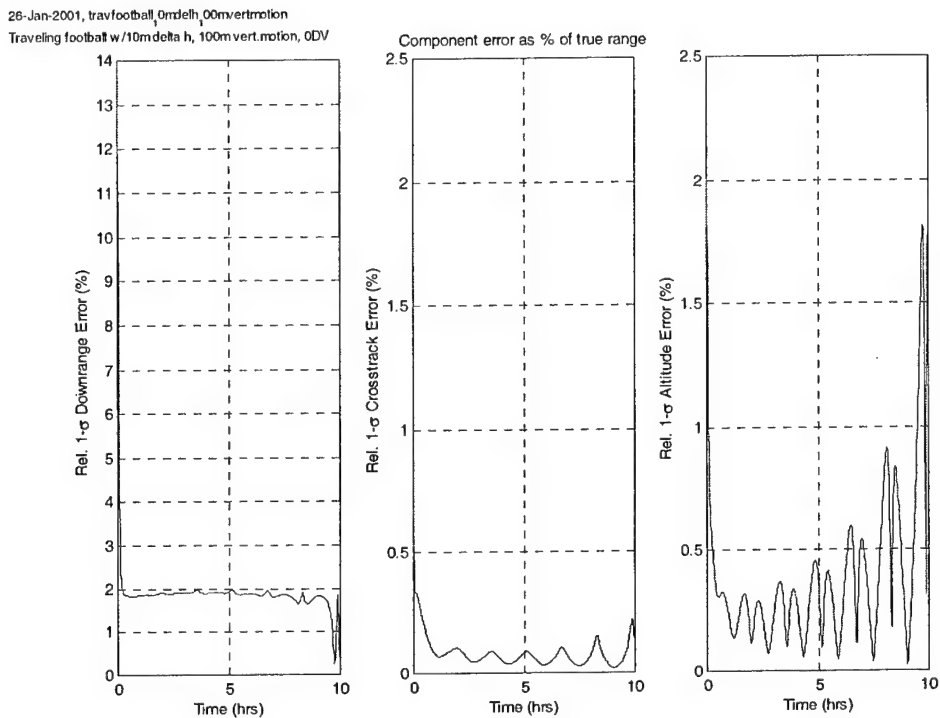


Figure 4-25: Relative position uncertainty for Traveling football, unmodified, with 10m Δh and 100m vertical oscillations, $\Delta V=0\text{m/s}$

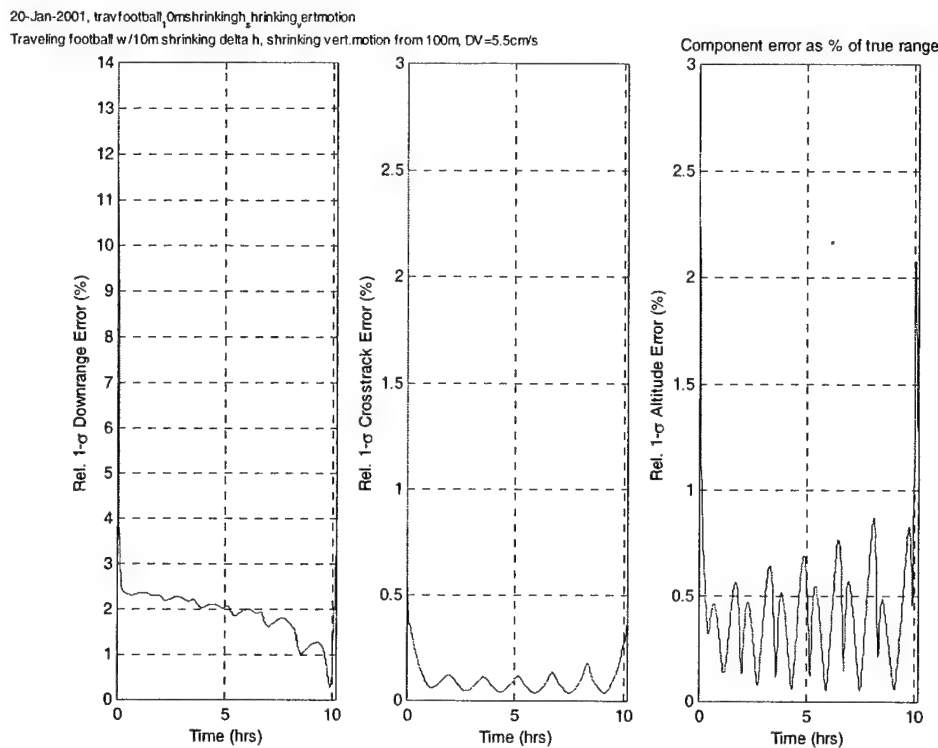


Figure 4-26: Relative position uncertainty for Traveling football with shrinking Δh and shrinking vertical oscillations, $\Delta V=0.055\text{m/s}$

Generally, the addition of damped slow cross-track motion did not aid the modified traveling footballs. The downrange and altitude uncertainties exhibit oscillatory motion, similar to the case of the centered station-keeping football, so the additional cross-track oscillations induced by maneuvers seemed to not only add uncertainty to the cross-track channel but the other components as well. On the other hand, the observation maneuvers did tend to improve the downrange uncertainty in all cases although this difference would disappear as the length of the maneuvers approached slow cross-track motion as discussed earlier. The best performing case is the spiral from Figure 4-10 with multiple observation maneuvers. The results in Figure 4-27 clearly show the impact of the first maneuver at 2 hours. The sudden error growth at the very end of the run is due to fact that the range between the chaser and target is approaching 0 so the percent range error approaches ∞ .

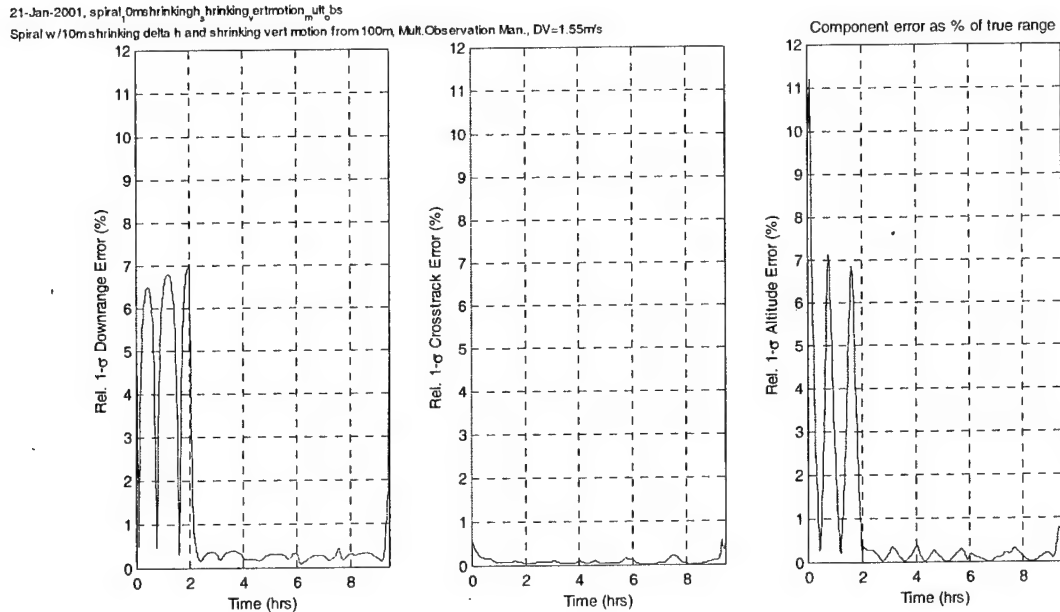


Figure 4-27: Relative position uncertainty for Traveling football/spiral with shrinking Δh and shrinking vertical oscillations with multiple observation maneuvers, $\Delta V=1.55\text{m/s}$

Effects of Process Noise

One last concept remains to be checked for the closure cases and that is the effect of process noise/un-modeled accelerations. For the station-keeping cases, it turned out that although the observation maneuvers were more fuel costly, they provided better results in cases where un-modeled accelerations were present. For the closure cases, the damped slow cross-track motion requires maneuvers every $1/2$ orbit in order to keep the magnitude proportional to the downrange separation. This more frequent maneuvering removes the advantage the observation maneuvers had so that for closure cases the two are very similar in terms of results although the observation maneuvers are still more fuel costly. The cases below are both for a 100m Δh coelliptic in the presence of un-modeled accelerations. Figure 4-28 uses maneuvers between 2 and 8 hours to maintain slow cross-track motion proportional to downrange distance while Figure 4-29 uses multiple observation maneuvers. Although the observation maneuvers require considerably more fuel than the damped slow cross-track motion (50.7m/s compared to 8.9m/s), the downrange uncertainty is not significantly improved.

Maneuver-Assisted Trajectory Analysis

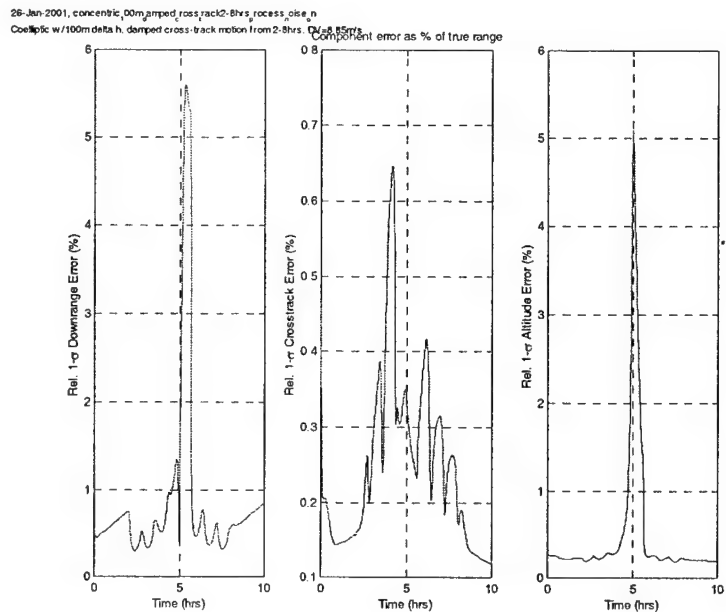


Figure 4-28: Relative position uncertainty with process noise for Coelliptic with 100m Δh and damped cross-track oscillations symmetric with respect to flyby point from 2-8 hours, $\Delta V=8.85\text{m/s}$

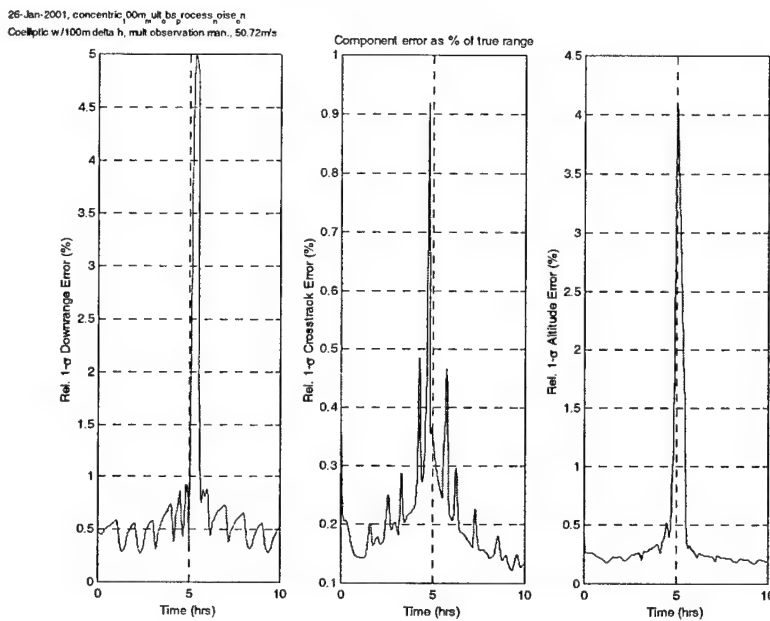


Figure 4-29: Relative position uncertainty with process noise for Coelliptic with 100m Δh and multiple observation maneuvers, $\Delta V=50.72\text{m/s}$

Results Summary

The previous sections have shown samples representative of all the cases considered. Table 4-4 shows the results for all closure cases in terms of ΔV use and the value of downrange percent error that the navigation filter was able to achieve for the closure cases with no process noise. In cases where the uncertainty value was oscillatory, the peak value of the oscillation was recorded.

Case	Best % Errors	ΔV (m/s)
V-bar approach from 360m, 1cm/s	14.14	0.81
2revs 100m cross-track	0.22	1.03
Damped cross-track	1.1	1.59
Mult.obs.man.	0.22	3.47
30m cross-track 1/2 rev before end	0.3	0.86
50m cross-track 1/2 rev before end	0.25	0.84
R-bar approach from 360m, 1cm/s	0.095	24.4
2revs 100m cross-track	0.097	24.7
Damped cross-track	0.112	24.96
Mult.obs.man.	0.085	27.1
Coelliptic, 100m Δh	0.229	0
Damped cross-track	0.056	9.63
Damped cross-track from 2-8hrs	0.074	8.85
Mult.obs.man.	0.084	50.72
Coelliptic, 1km Δh	0.229	0
Damped cross-track	0.057	96.3
Trav. Football, standard	0.167	0
Shrinking Trav. Football, fixed Δh	0.27	0.051
Damped cross-track	1	1.85
Mult.obs.man.	0.23	7.53
Shrinking Trav. Football, shrinking Δh	0.28	0.055
Damped cross-track	0.7	1.35
Mult.obs.man.	0.14	6.1
Spiral	0.63	0.055
Damped cross-track	2	0.46
Mult.obs.man.	0.27	1.55

Table 4-4: Maneuver-assisted closure trajectory LINCOV results summary

This data can also be visualized by showing the best performing trajectories, in terms of ΔV and percent error, as in Figure 4-30.

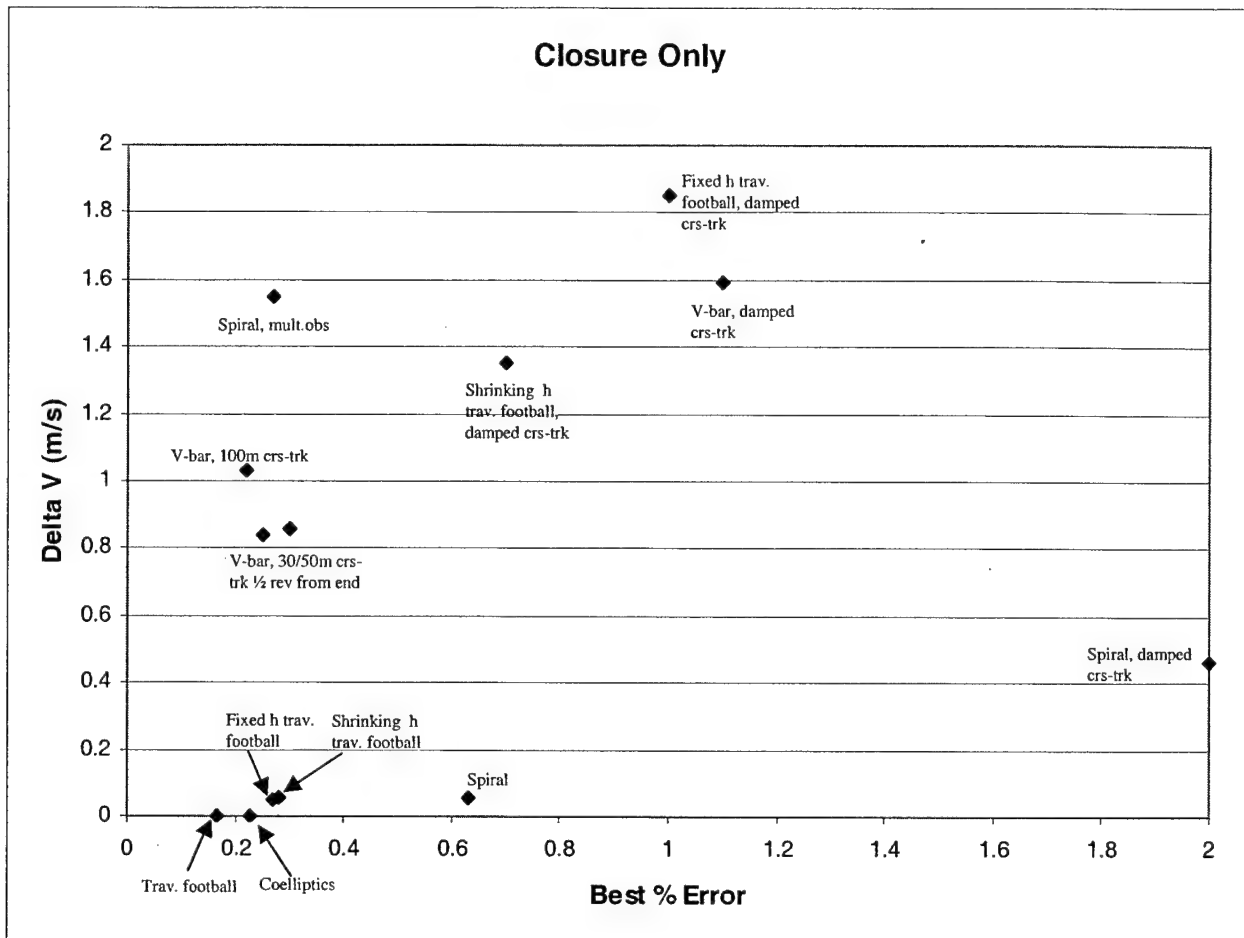


Figure 4-30: Maneuver-assisted closure trajectory LINCOV results summary

4.4 GENERAL CONCLUSIONS AND HYBRID TRAJECTORY DEVELOPMENT

In addition to the maneuver-assisted trajectories in the previous sections, several hybrid trajectories are designed in order to combine the best characteristics of different maneuvers. For instance, it was mentioned earlier that the R-bar approach provides excellent range observability to the navigation filter, but the high fuel use makes long approaches costly. An improved technique would be to use other methods to get closer to the target and then transition to an R-bar final approach. Three trajectories are proposed as an example of how to create complete

maneuver-assisted trajectories. Both the trajectories and LINCOV results, tested under the same conditions as in section 4.3.2, are shown.

These hybrid trajectories are also representative of the general conclusions that can be drawn from this chapter in the sense that they represent techniques for maneuver-assisted trajectories that improve downrange observability. Although the maneuver-assisted trajectories may not yield downrange observability in the strict sense, the results clearly showed that using maneuvers to augment natural orbital motion significantly helps navigation filter performance. However, it was also shown that the simple addition of a maneuver without regard to its direction is not recommended. Specifically, the V-bar approach demonstrated that maneuvers leading to motion parallel to the line-of-sight can actually make the downrange uncertainty worse. The analytical results in the dual control field support the qualitative conclusion in this chapter that motion normal to the line-of-sight generally yields significant improvements in downrange uncertainty. Also, the principle that downrange uncertainty is greatly reduced during chaser flybys of the target is still a useful technique in maneuver-assisted trajectories even though it was first established in the natural motion analysis.

The first hybrid trajectory is shown in general schematic form in Figure 4-31. The chaser starts in a co-circular station-keeping orbit a fixed distance from the target. At some point, a maneuver induces slow cross-track motion to keep the chaser oscillating and drive down the downrange errors. The second maneuver transfers the chaser to a coelliptic that takes the chaser past the target to a third maneuver point. At this point, the chaser can either transition to the V-bar or to a coelliptic on the opposite side of the target. If the chaser comes in along its final approach on the V-bar, it damps out any remaining cross-track motion as it approaches the target. In the case where it transfers to another coelliptic, at the next flyby point the chaser nulls all cross-track motion and begins a final approach along the R-bar. Although the approach along the V-bar does not offer range observability, it is a typical approach used in many current rendezvous applications and so is considered herein.

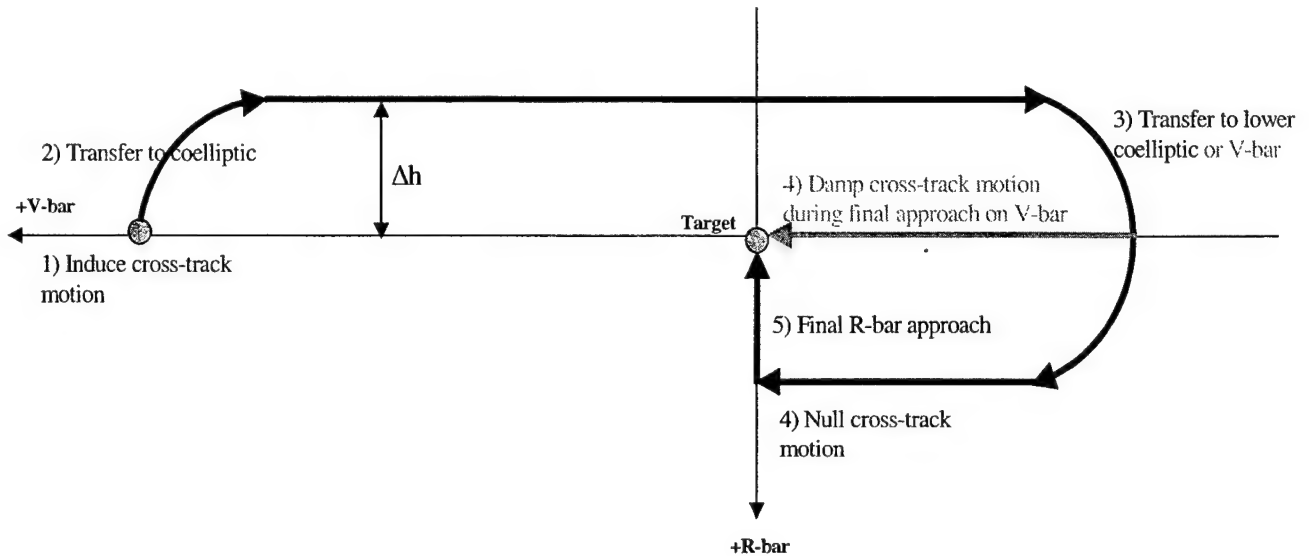


Figure 4-31: Hybrid trajectory 1– Co-circular station-keeping to coelliptic to final approach

The reference trajectory and linear covariance results for hybrid case 1, with a final R-bar approach, are shown in Figure 4-32 and Figure 4-33. In this case, the coelliptic Δh is 100m and the R-bar approach is from 100m at a closing rate of 5cm/sec. The results with a final V-bar approach at 5cm/sec from approximately 250m away are shown in Figure 4-34 and Figure 4-35. Total ΔV usage for the R-bar variation is 3m/s and 2.97m/s for the V-bar approach case.

As expected, the R-bar approach performs quite well. The use of the hybrid helps to improve the V-bar approach's normally poor range observability. However, the downrange uncertainty begins to grow dramatically as the chaser gets near the target. The LINCOV results do not show the last 17m of the V-bar approach to preserve the scaling.

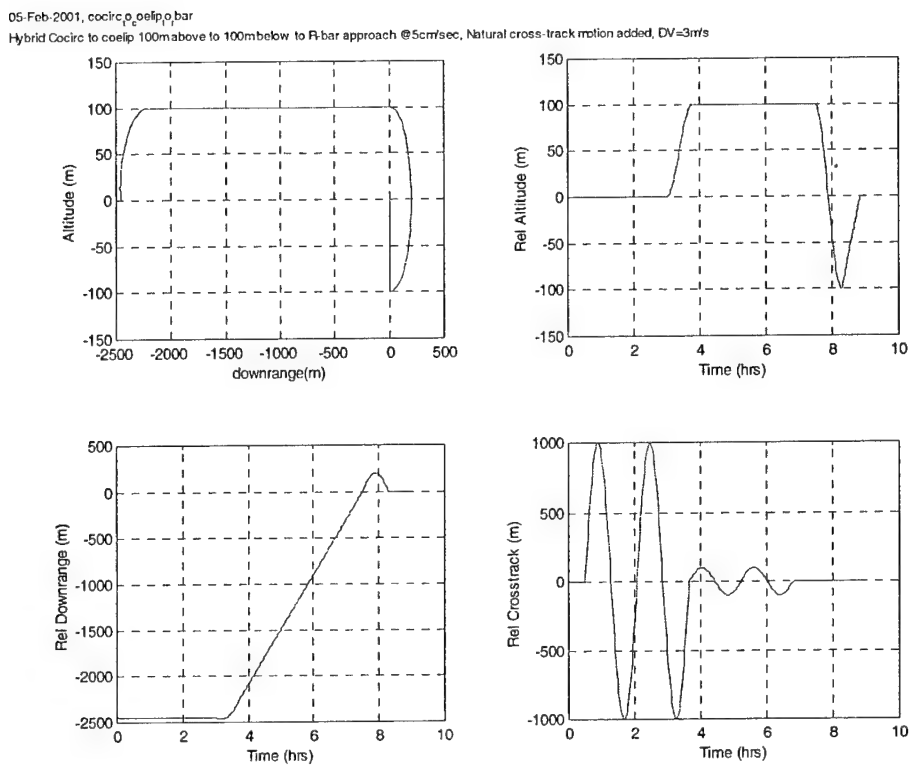


Figure 4-32: Hybrid trajectory 1 – R-bar final approach, $\Delta V=3\text{m/s}$

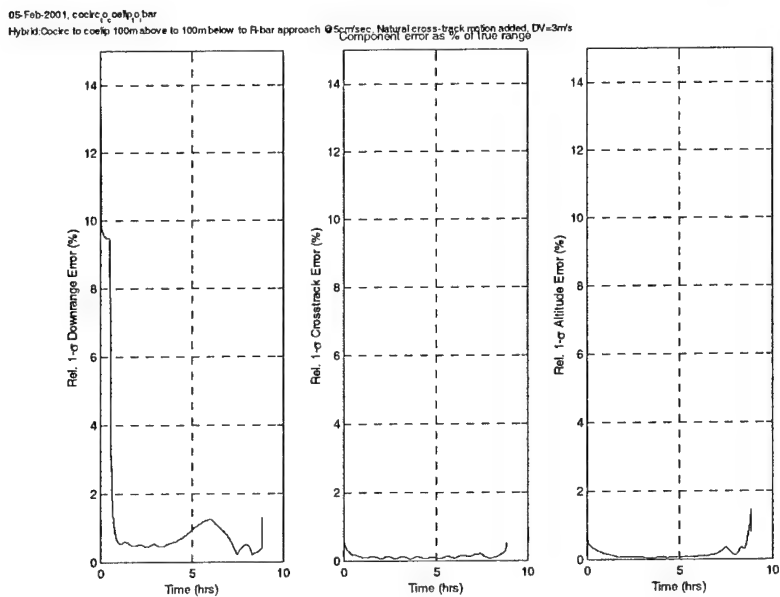


Figure 4-33: Hybrid trajectory 1 – Relative position uncertainty for R-bar final approach, $\Delta V=3\text{m/s}$

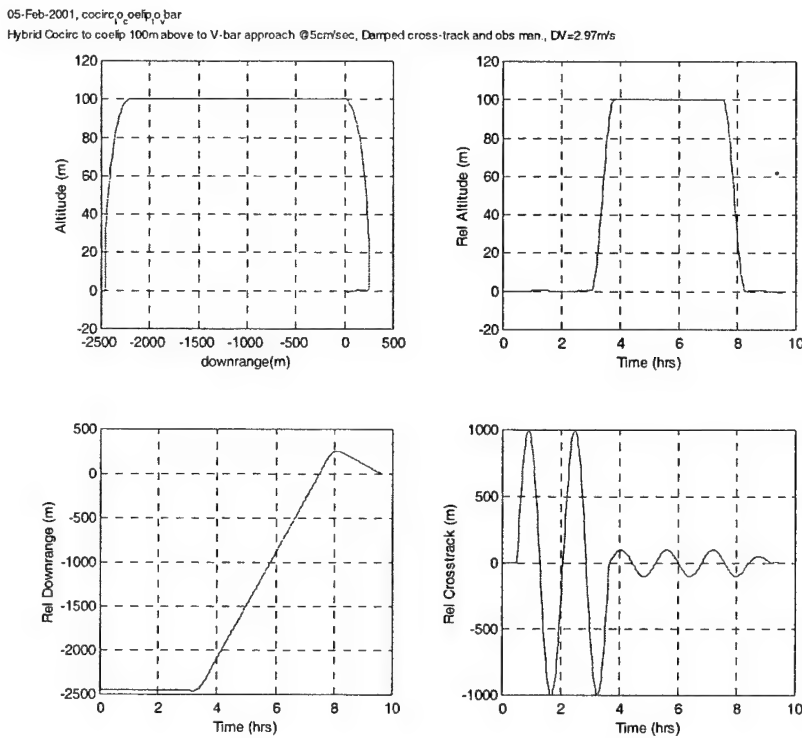


Figure 4-34: Hybrid trajectory 1 – V-bar final approach, $\Delta V=2.97\text{m/s}$

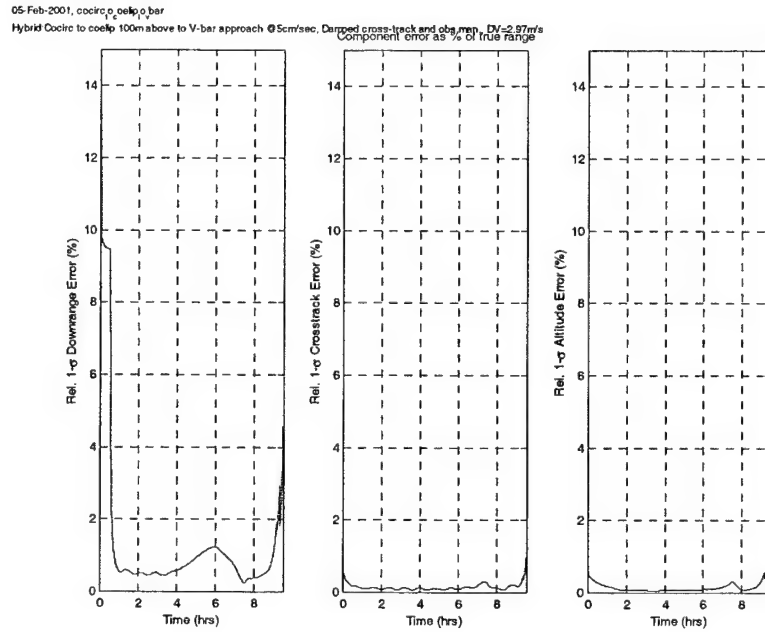


Figure 4-35: Hybrid trajectory 1 – Relative position uncertainty for V-bar final approach to 17m, $\Delta V=2.97\text{m/s}$

The second hybrid trajectory makes use of the spiral, or modified traveling football, along with a final approach along the V-bar or R-bar. As shown in general form in Figure 4-36, the chaser begins in a spiral orbit closing on the target. Throughout the approach, several observation maneuvers are performed and timed to occur during the V-bar crossings since these are points of poor range observability. At either a V-bar or R-bar crossing, the chaser transitions to a final approach and moves to intercept the target.

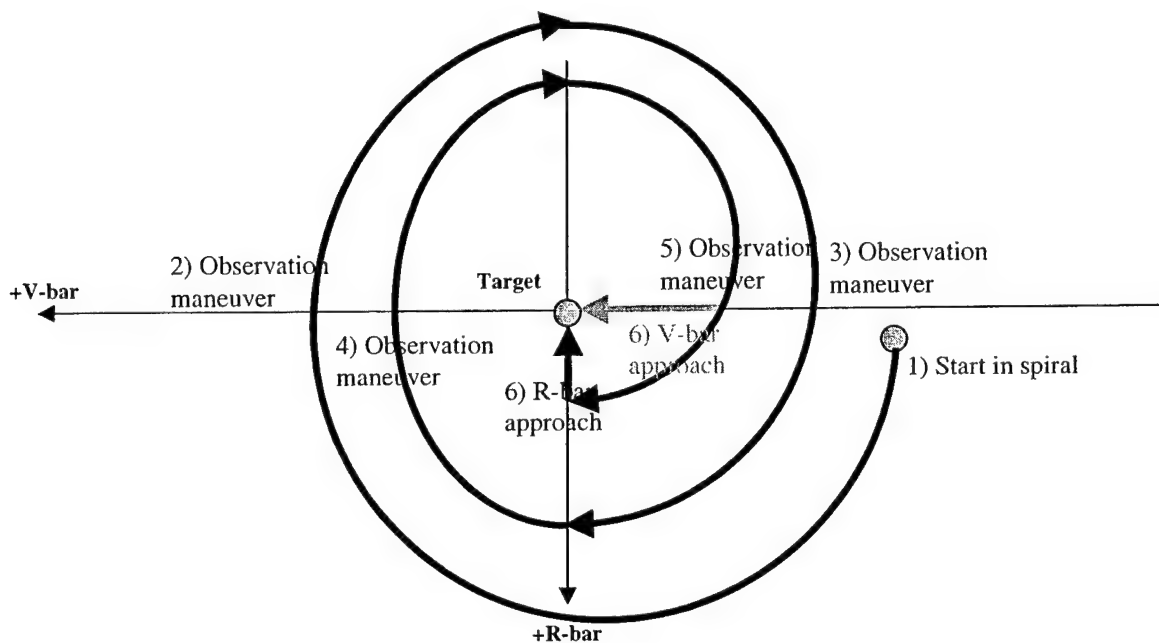


Figure 4-36: Hybrid trajectory 2–Spiral to final approach

The reference trajectory and linear covariance results for this second hybrid case with a final R-bar approach from 55m at 5cm/sec are shown in Figure 4-37 and Figure 4-38. The spiral altitude shifts approximately from -110m to 90m to -80m to 70m and then to the point where final approach is initiated. The results with a final V-bar approach from 108m at 5cm/sec are shown in Figure 4-39 and Figure 4-40. Total ΔV usage for the R-bar variation is 1.12m/s and 1.01m/s for the V-bar approach case.

In this case, the final approaches do not perform as well as they did for the first hybrid. This is due to the fact that the first hybrid has larger R-bar burns since it approaches from a further distance. Also, since there is no process noise, the benefits of using observation maneuvers in the second hybrid compared to the slow cross-track motion in the first may not be as apparent. The R-bar LINCOV results stop when the chaser is 8m away from the target and the V-bar results stop 32m away to preserve the scaling of the plots since the final errors grow very large.

Maneuver-Assisted Trajectory Analysis

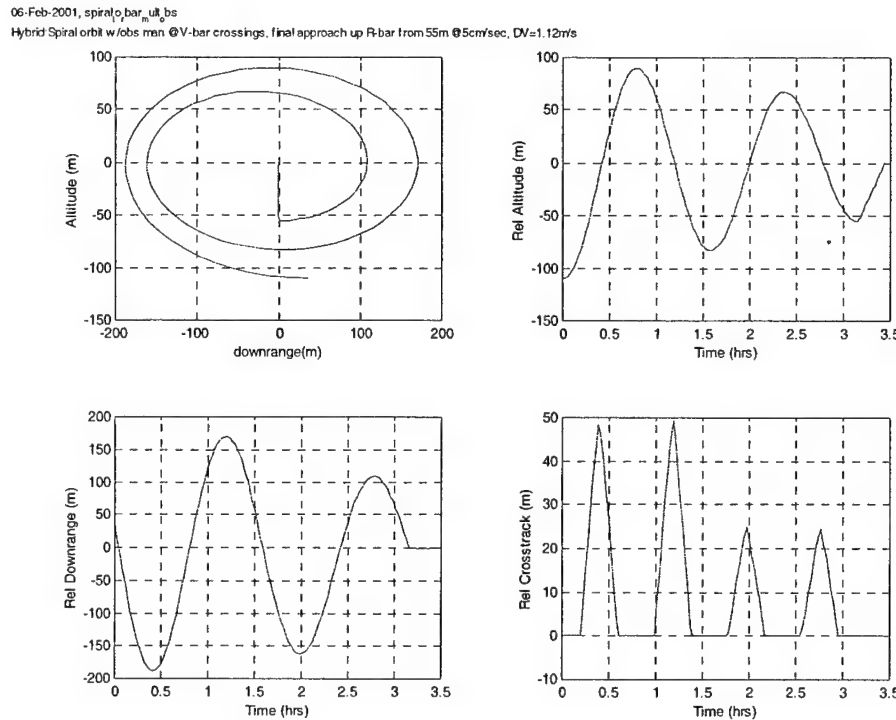


Figure 4-37: Hybrid trajectory 2 – R-bar final approach, $\Delta V=1.12\text{m/s}$

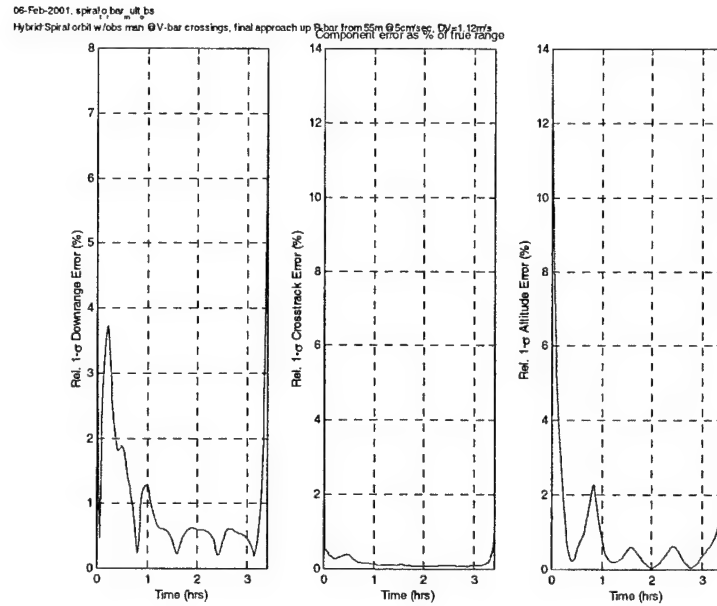


Figure 4-38: Hybrid trajectory 2 – Relative position uncertainty for R-bar final approach to 8m, $\Delta V=1.12\text{m/s}$

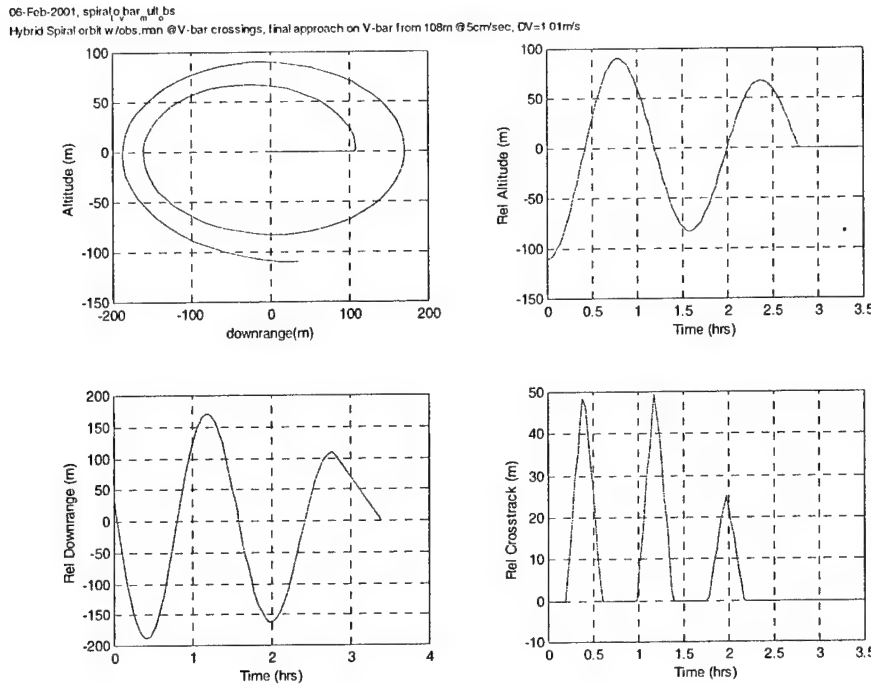


Figure 4-39: Hybrid trajectory 2 – V-bar final approach, $\Delta V=1.01\text{m/s}$

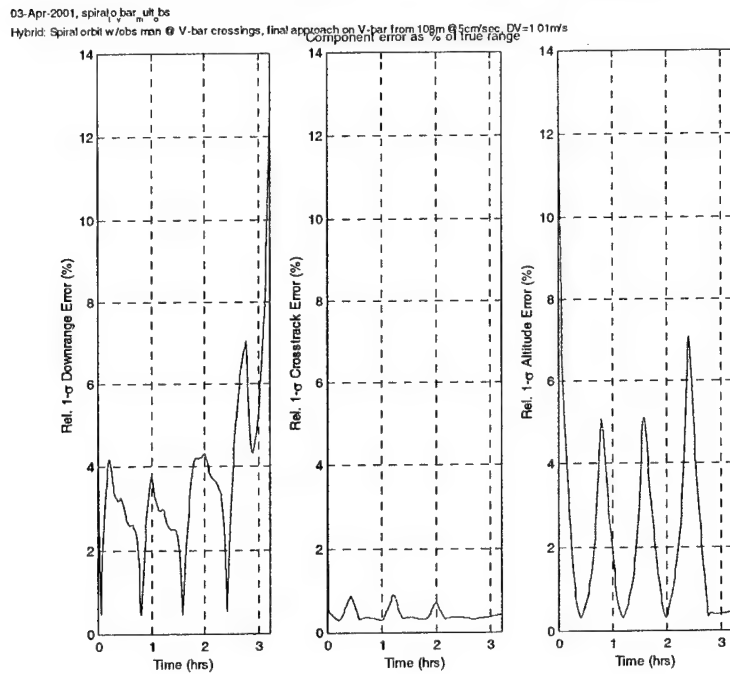


Figure 4-40: Hybrid trajectory 2 – Relative position uncertainty for V-bar final approach to 32m, $\Delta V=1.01\text{m/s}$

The third and final hybrid trajectory is a combination of a centered station-keeping football followed by an R-bar or V-bar approach. The schematic in Figure 4-41 shows how the chaser starts in a centered football and executes a maneuver to induce slow cross-track motion. This is done to improve the downrange uncertainty so that a second maneuver can be made to transition the chaser into either a V-bar or R-bar approach. As in the first hybrid trajectory, the cross-track motion is damped out for V-bar approach while for the R-bar case it is nulled completely when the final approach begins.

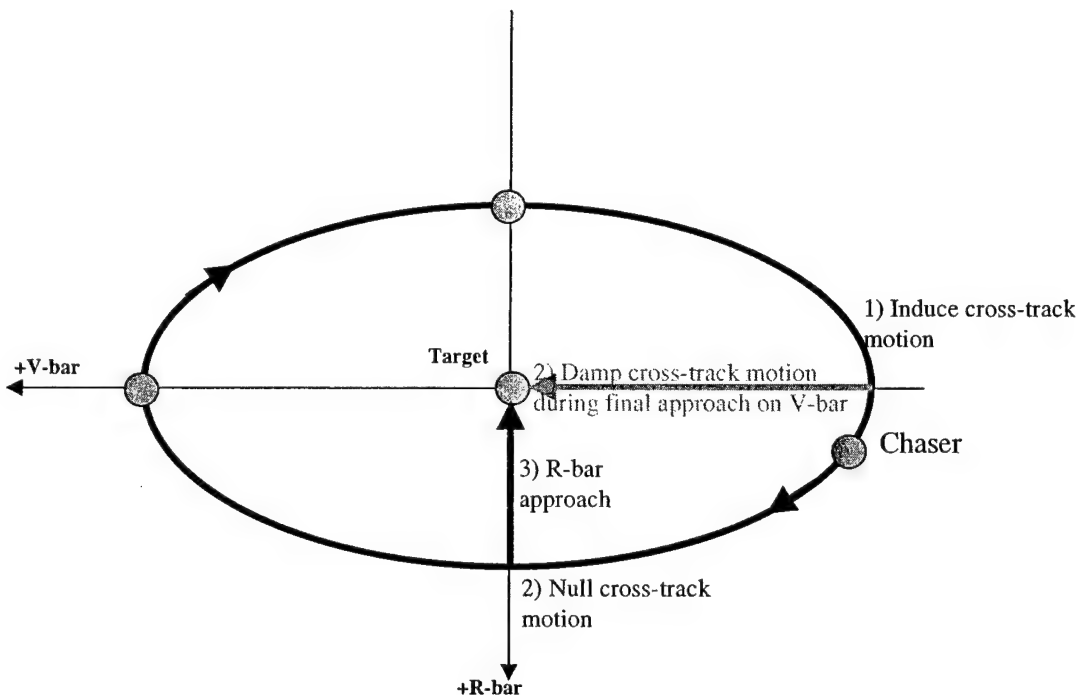


Figure 4-41: Hybrid trajectory 3– Centered football station-keeping to final approach

The trajectory and LINCOV results for hybrid trajectory 3 with an R-bar approach are shown in Figure 4-42 and Figure 4-43, and the final V-bar approach results are given in Figure 4-44 and Figure 4-45. For both variations, the relative motion football has $\pm 100\text{m}$ of vertical motion and $\pm 200\text{m}$ of downrange motion. This hybrid does a good job of maintaining the downrange uncertainty at low levels throughout the run. Initially the downrange and altitude uncertainty is oscillating, characteristic of the football shape, but the first cross-track maneuver has a very noticeable effect. The V-bar approach expectedly begins to cause downrange error growth as it approaches the target and the LINCOV results stop when the chaser is still 8m from the target. Total ΔV usage for the R-bar variation is 0.81m/s and 0.85m/s for the V-bar approach case.

02-Feb-2001, centered football, 00m vert motion, 00m cross-track, R-bar approach @6revs

Centered football w/100m vert motion and 100m cross-track @1rev, transferring to R-bar approach @5cm/sec, DV=81m/s

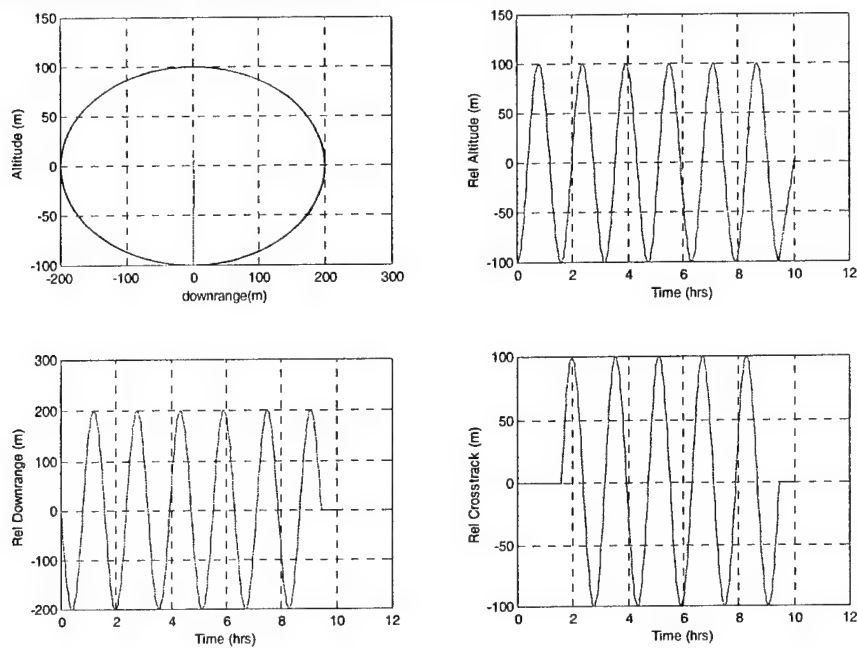


Figure 4-42: Hybrid trajectory 3 – R-bar final approach, $\Delta V=0.81\text{m/s}$

04-Feb-2001, centered football, 00m vert motion, 00m cross-track, R-bar approach @6revs
Hybrid Centered football 100m vert motion, 100m crs-trk @ 1rev-null w/ no final approach from 100m @5cm/sec, @6rev starts, DV=81m/s
Component error as % of true range

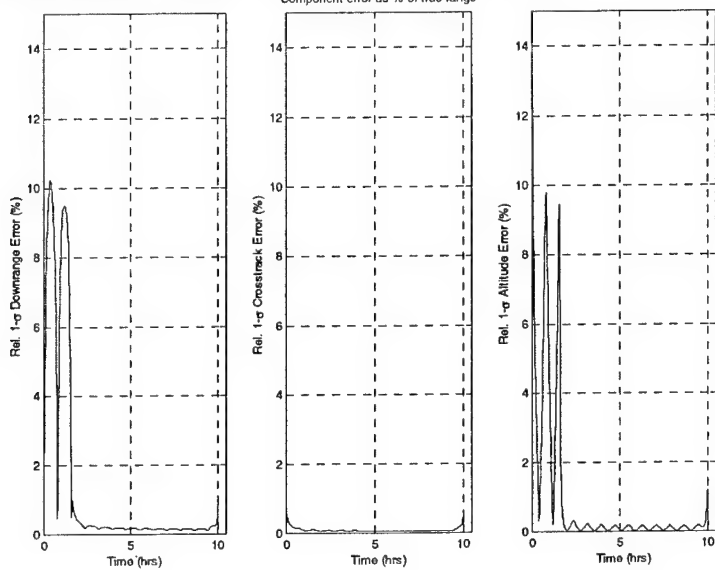


Figure 4-43: Hybrid trajectory 3 – Relative position uncertainty for R-bar final approach, $\Delta V=0.81\text{m/s}$

Maneuver-Assisted Trajectory Analysis

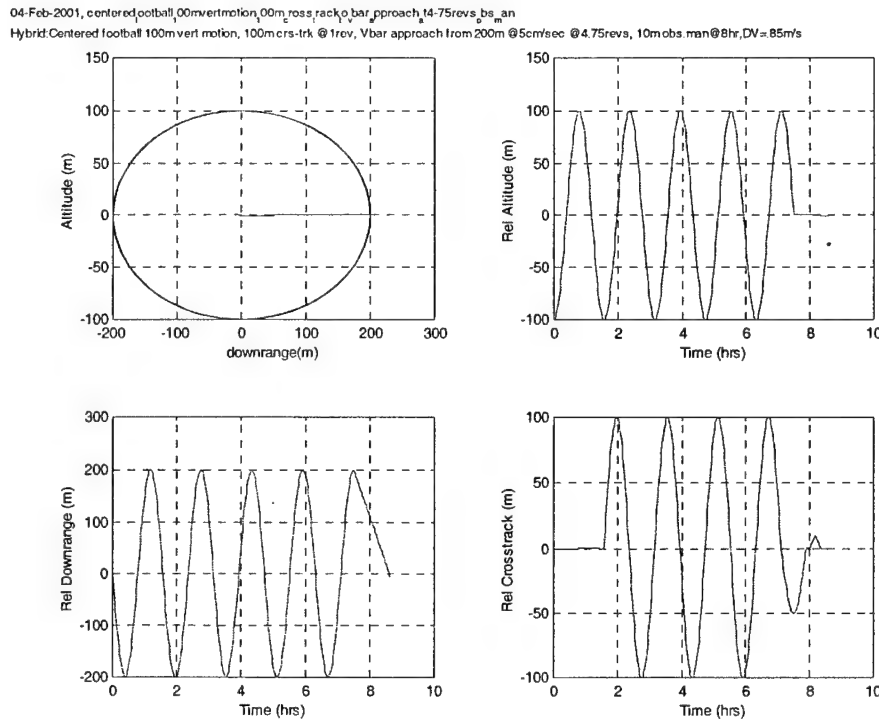


Figure 4-44: Hybrid trajectory 3 – V-bar final approach, $\Delta V=0.85\text{m/s}$

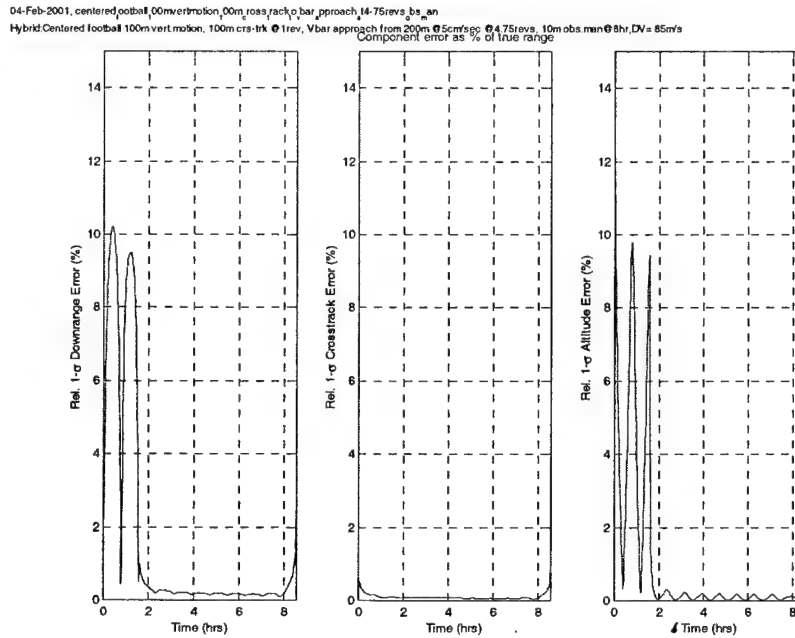


Figure 4-45: Hybrid trajectory 3 – Relative position uncertainty for V-bar final approach to 8m, $\Delta V=0.85\text{m/s}$

The hybrid trajectories demonstrate that using well-chosen maneuvers can lead to excellent performance in rendezvous and close approach scenarios using angles-only navigation. As expected, the lessons learned from natural motion analysis paid dividends as they helped to create maneuvers that effectively stimulated line-of-sight changes. Thus, while maneuver-assisted trajectories may not lead to strict observability, they decrease downrange uncertainty to levels acceptable for close approach applications. However, these results came using ideal conditions in terms of error sources and measurement availability. The next step will be to use these hybrid trajectories, along with other selected maneuver-assisted trajectories, to form the basis for the next phase of testing, eventually leading to trajectories which are useful in actual mission scenarios.

5 MISSION ANALYSIS

Although the previous chapter provided a number of potential trajectories that would be useful in an angles-only navigation situation, the results came primarily from idealized scenarios in terms of the error models that were used. In order to verify that these maneuver-assisted trajectories work in practice, the Orbital Express mission is explored as a typical mission that could benefit from the techniques presented in this work. This chapter will briefly explain the background of the Orbital Express mission, present some of the error parameters that are reasonably expected, utilize selected maneuver-assisted trajectories to accomplish the mission goals in the face of more complete error modeling, and show a sensitivity analysis of how these errors affect navigation performance.

5.1 MISSION OVERVIEW

The ASTRO (Autonomous Space Transport and Robotic Orbital) Orbital Express mission is a DARPA (Defense Advanced Research Projects Agency) Advanced Technology Program. As shown in Figure 5-1, the long-term goal of the program is to eventually have modular spacecraft that can be serviced on-orbit by an ASTRO spacecraft [19]. This will allow spacecraft to have their lifetimes extended by being refurbished with new supplies such as fuel or avionic unit replacements. These supplies would be placed in bulk into a parking orbit where they would be later retrieved, on demand, by the ASTRO vehicle. The ASTRO vehicle would then rendezvous with the spacecraft being re-supplied. The target vehicle would not have the capability to aid in the rendezvous so the burden is on ASTRO to perform all relative navigation, and execute the corresponding maneuvers. Additionally, ASTRO must be able to act autonomously and have the capability of achieving rendezvous without ground control monitoring.

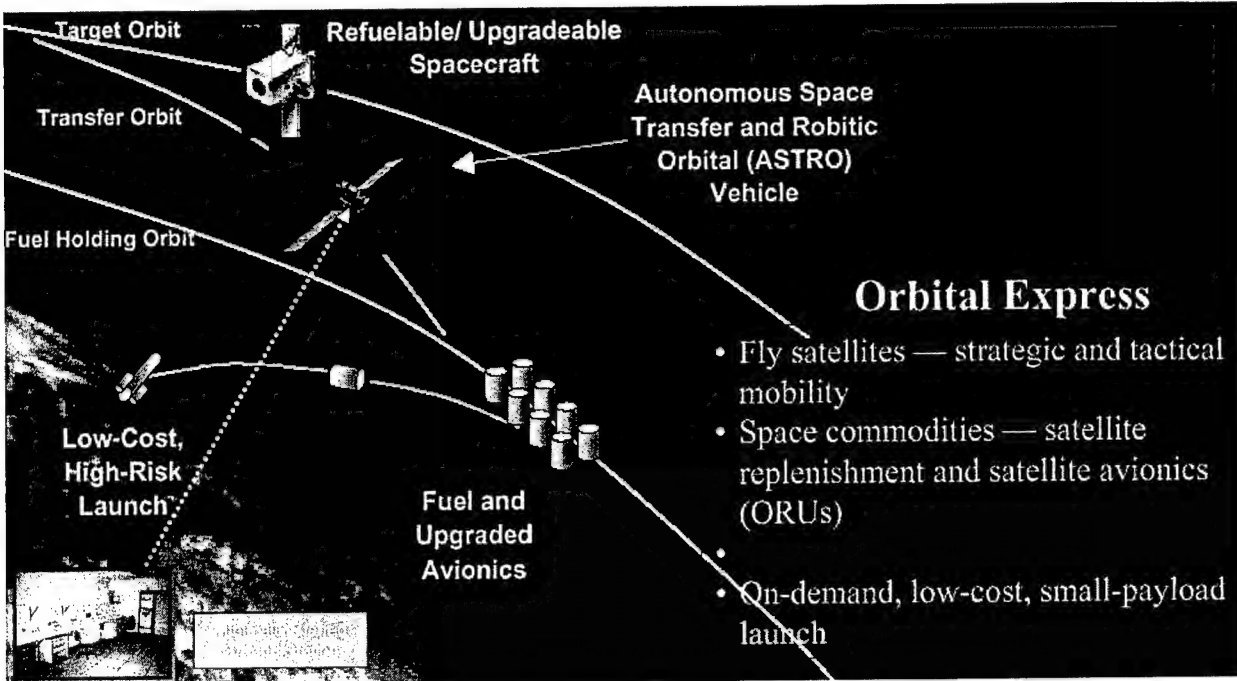


Figure 5-1: Orbital Express system elements

The concept of using ASTRO serviced spacecraft could eventually extend to a broad array of vehicles and orbits, but for the purposes of this study only the near-term demonstration mission will be considered. This demonstration involves a number of aerospace design teams competing for the chance to do an actual flight demonstration in the 2003-2004 time-frame. In one scenario, the simulated ASTRO vehicle, or chaser, must first move from a position 20km downrange and 1km above/below the target to a station-keeping point 50m downrange as in Figure 5-2. Then, the chaser must show the ability to maintain this station-keeping position for an extended period of time. The question, though, is how should the chaser proceed from its initial position to the terminal offset point. There are obviously a number of systems and events that play a role in mission success; however, this portion of the study will only examine the impact of the ASTRO navigation system on mission success. More precisely, the question is whether an angles-only navigation system, using maneuver-assisted trajectories, can accomplish the desired mission of placing the ASTRO at the desired point(s) with acceptable error uncertainties. For this study, the desired uncertainty value is less than 10%-1 σ downrange error at the 50m offset point. This equates to a navigation downrange 1 σ error of 5m or less by the time the chaser reaches its final targeted position.

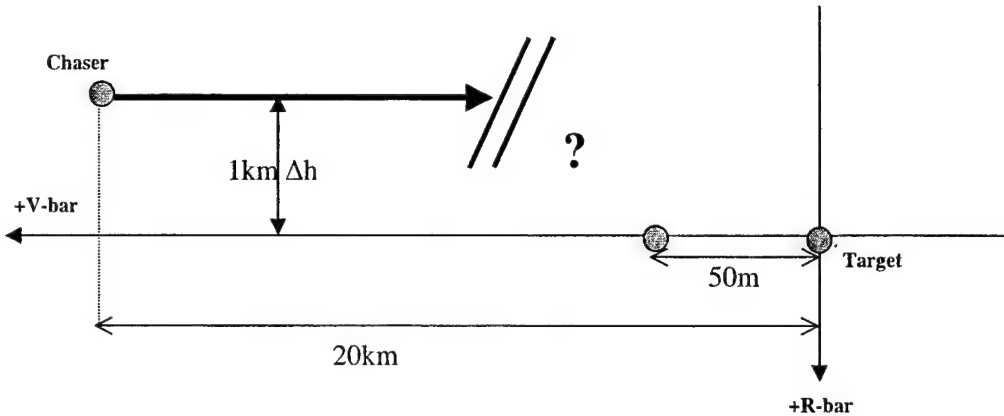


Figure 5-2: Orbital Express mission endpoints

5.2 INCORPORATION OF MISSION SPECIFICATIONS

The Orbital Express mission is expected to take place in low to medium altitude earth orbits. Specifically, the target orbit was designated to be circular at 800km altitude. The actual inclination is unspecified so a value of 45° was selected. In practice, the absolute orbital element values of the target and chaser vehicle have little, if any, impact on the results reported here. The more important values are the differences between them.

The first mission related constraint is that angular measurements are only available when the target is illuminated by sunlight. Even though the exact sensor suite for the Orbital Express mission is unknown, the general constraint of selective measurement availability is realistic for a variety of different scenarios such as optical sensors requiring lighting, infrared sensors requiring a deep space background, a modified star tracker requiring the earth and sun to be outside the field of view, or a solar-powered target beacon. Although section 3.4.2 discussed how measurement availability did not significantly change navigation performance, that conclusion was for cases with no process noise. The present addition of error models including process noise may turn out to have adverse effects on navigation where measurement updates are not consistent.

Selecting actual error parameter values for navigation performance evaluation is a rather subjective process that is dominated by two considerations. The error sources must be chosen so that the results are broad enough to be generally applied to other missions. Although the Orbital Express construct is being used to generate initial and final conditions for the trajectories, simply applying all of the expected mission values to the present study would strip away its generality

for future use. Secondly, the list of errors must not be so long that the dimensionality of the problem becomes overwhelming, but must be long enough that the final results are a reasonable representation of reality. With this in mind, four different error sources are modeled as described below, and implemented in the linear covariance analysis according to section 2.2.2.

The first error model affects the angular measurements themselves. For a typical line-of-sight sensor, the measurement error comes largely from two sources. The first source of angular measurement error is simply the noise on the measurements which was the sole error being modeled in previous chapters. This noise is independent of target-chaser position and is therefore fixed at $0.03^\circ - 1\sigma$. This is representative of a simple 1,000x1,000 pixel measurement array with a 15° field of view. Assuming the target is a point source that occupies one pixel (two if it falls onto a neighboring one as well) the error to fully displace the target would be 0.03° . Although this model is realistic at distances where the target appears to be a point source, at shorter ranges, most angular measurement sensors will have errors relating to finite body effects. As the chaser approaches the target, taking accurate angular measurements implies that the centroid of the target is known perfectly which is not usually the case. In fact, even if the centroid were known, there would still be errors since the center of gravity of the target vehicle would not be known perfectly. To account for these effects, it is assumed, for the current testing, that the sensor has a 10% error determining the center of a target that can be contained inside a 2.5m radius sphere. Thus, the standard deviation of the angular measurement error resulting from finite body effects

is $\left(\frac{0.25}{r} * \frac{180}{\pi} \right)^\circ$, 1σ where r is the relative range between the target and chaser. For different

sized target vehicles or errors, the results are still valid by scaling the range, e.g. 10% error centering a 2.5m target at 25m is the same as 10% error centering a 5m target at 50m or 30% error centering a 2.5m target at 75m, etc. Also, this finite body effect is not necessarily white noise but may rather appear as a time-varying bias due to varied lighting conditions. Assuming that this occurs about once every half orbit due to lighting constraints, this error is modeled as a first order Markov process with a time constant, $\tau=1/2*\text{Period}$ (see section 2.2.2). Thus, the total error model for angular measurements includes both a range independent noise value and a range dependent dynamic bias.

The second error model accounts for the IMU inaccuracies in measuring maneuvers implemented by the chaser vehicle. Since the previous chapter dealt with the benefits of using maneuver-assisted trajectories to aid in angles-only navigation, the measurement of these maneuvers is a key parameter. As with the angular measurement error model, the ΔV

measurement error model consists of two portions. For maneuvers that are larger than 2cm/sec, the measurement error is 1mm/sec- 1σ which is representative of the quantization error of an IMU [12]. For smaller maneuvers on the order of mm/sec used in proximity operations, spacecraft may use thrust models rather than attempting to actually measure the maneuver with an IMU. In this study, maneuvers smaller than 2cm/sec have an associated modeling error equal to 5% of the ΔV magnitude. Both the quantization error and modeling error are added in the linear covariance tool as spherical measurement errors according to equation (2.81). Note that the modeling error for small burns is being added spherically, as opposed to along the direction of the burn, because for such small maneuvers it would be very impractical to align the spacecraft in the direction of each maneuver. Rather a combination of thrusters would impulsively fire for maneuvers less than 2cm/sec, and the resulting thrust model error would be closer to a spherical shape rather than directed along a particular direction.

The next error modeled is the ability of the chaser to determine its inertial attitude. The angular measurements of the line-of-sight to the target are referenced to inertial attitude and therefore errors in the chaser's inertial attitude will enter into the relative navigation uncertainty values. It is reasonable to assume that star tracker updates will be frequent enough that the details of a gyrometer model are not required for this study. Instead, two forms of error will be placed on the inertial attitude measurements. The first is a bias of $0.01^\circ/\text{axis-}1\sigma$ that is representative of a static misalignment between the star tracker and the chaser spacecraft. The second is a time-varying or dynamic attitude bias, conservatively set to $0.1^\circ/\text{axis-}1\sigma$, and modeled as a first order Markov process with a time constant, $\tau=300$ seconds, based on the time increment between star tracker measurements [24].

The final error source model for the mission analysis is process noise, or un-modeled accelerations. The level of un-modeled acceleration that is important is not the absolute values of process noise on each vehicle, but rather the difference between them. For example, if the gravity field is poorly modeled it will have a similar effect on both the chaser and the target so the effect on relative navigation will be small. The level of un-modeled acceleration is then driven by the assumed effective differences between the two vehicles. It is assumed that the target is essentially a passive non-maneuvering vehicle and has a process noise variance of

$$1 \times 10^{-13} \frac{m^2}{s^3}, \text{ or a standard deviation of } 0.0019 \frac{cm/s}{\sqrt{hr}}, \text{ which equates to approximately } 1/2 \text{ m}$$

of error per orbit [15]. The chaser vehicle, however, is active and will potentially be subject to more un-modeled accelerations in the form of un-coupled jet firings or venting. Also, the chaser

process noise value should account for differential effects between it and the target such as drag, solar radiation pressure, or other perturbations that affect the vehicles unequally. In light of these variables, two different values of process noise are used to represent a ‘quiet’ and ‘noisy’ chaser vehicle. The quiet vehicle has a process noise variance of $9 \times 10^{-10} m^2/s^3$, or a standard deviation of $0.18 \frac{cm}{\sqrt{hr}}$, which translates into slightly more than 50m of error per orbit. The noisy chaser vehicle’s process noise variance is $7 \times 10^{-9} m^2/s^3$, or a standard deviation of $0.5 \frac{cm}{\sqrt{hr}}$, which is about 150m of error per orbit and is nearly on the order of un-modeled accelerations experienced by the space shuttle, which is an extremely noisy vehicle.

Although not an actual error model, another important factor to consider for linear covariance testing is the *a priori* initialization of the covariance matrix. Although the Orbital Express mission does not yet have set values, it does have a mission concept and associated expected values that are still general enough to handle other potential missions. For closure scenarios, the chaser vehicle is assumed to have GPS measurement capability and therefore have an initial *a priori* 1σ uncertainty of 30m and 3cm/sec. The target vehicle is assumed to have been tracked with ground based systems, and thus have an initial *a priori* 1σ uncertainty of 100m and 10cm/sec. These values are clearly too large to be used for station-keeping cases since the initial position of the chaser is only 50m from the target. For these station-keeping cases, both vehicles have *a priori* uncertainties such that the relative position uncertainty values are initially 10%, the meet-or-beat goal of the closure trajectories. This equates to 3.5m and 3.5mm/sec of inertial position and velocity uncertainty initially placed on each vehicle.

5.3 DESIGN OF MISSION TRAJECTORIES

The next step for mission analysis is to design the actual maneuver-assisted trajectories subject to Figure 5-2 taking the chaser vehicle from its starting point to the 50m offset in addition to station-keeping trajectories that maintain the chaser near the 50m point. Besides combining the techniques of Chapter 4, several other considerations come into play. Maneuvers must be realistic in the sense that they could actually be executed based on the current navigation state

estimate. For example, the chaser could not perform a maneuver going from a 1km coelliptic to a 100m coelliptic if the 1σ altitude uncertainty was much more than 30m. In addition, the final portion of the closure trajectories should ideally be during a period of sunlight illumination. Since the final minutes of the trajectory are the most crucial, it would be unwise to attempt to reach the 50m point without the benefit of any angular measurements. Associated with this concept is the idea that in actual practice it would be desirable to only execute maneuvers during sunlight. This is generally the case for the closure and station-keeping trajectories that will be considered. However, in a few instances maneuvers are executed during eclipse periods. Although this is not recommended for actual mission operations, the results from this practice are used as an illustrative tool in this study.

The maneuver-assisted trajectories for the Orbital Express mission presented in this section are shown in ‘cartoonish’ format. Since the actual scaling involved would make it prohibitive for the reader to note key characteristics if looking at actual data, all key dimensions, times, and maneuvers are noted within the schematics. For notational convenience, observation maneuvers are labeled in the format “ $t=X.XXhr$, start obs.man., $\Delta t=YYmin$, ZZm ” which means that the observation maneuver initiates at $X.XX$ hours and goes out ZZ meters in the cross-track direction in YY minutes before returning to 0 YY minutes later. In other words, the entire three-burn sequence described by equation (4.3) takes $(2*YY)$ minutes. There are a total of four closure trajectories designed to bring the chaser to the 50m offset point and three station-keeping trajectories designed to hold this position for an extended period of time.

5.3.1 Closure

The first closure trajectory, shown in Figure 5-3, begins with a 1km coelliptic flyby. Transferring from the 1km coelliptic above the target to a lower coelliptic 100m below the target is ideal since the flyby point is the point of best downrange error. Once the chaser is directly below the target on the 100m coelliptic, it begins final approach along the R-bar at 10cm/sec. The reason for choosing to close only 75m of the 100m along the R-bar is two-fold. First, the desired final position is 50m on the V-bar, not actual rendezvous. It would be possible to simply fly past the target 50m on the lower coelliptic and then move directly up along the radial direction. However, this approach is not as effective as the approach from directly below since the angular measurements once again begin to form a ‘cigar-shaped’ uncertainty ellipse due to the downrange offset. The other reason to stop short during the R-bar approach is that, unlike the error free cases, the downrange percent uncertainty begins to increase at the end of an R-bar

approach. By only approaching to within 25m of the target, the benefits of the R-bar approach are gained without getting close enough to see degradation of the navigation uncertainty. The transfer from the R-bar approach to the V-bar offset point is done using a Lambert transfer maneuver. This Lambert calculation determines the required initial and final velocity, \bar{V}_0^I, \bar{V}_F^I , required to take a spacecraft from an initial to a final position, \bar{R}_0^I, \bar{R}_F^I , in a fixed amount of time, $t_{transfer}$. The interested reader can find extensive coverage of the mechanics of calculating these maneuvers in [3] and [4]. The Lambert maneuver is used as opposed to a $\frac{1}{2}$ orbit Hohmann type transfer because at such close range to the target, the effects of process noise are much more pronounced in terms of percent downrange error growth. Waiting $\frac{1}{2}$ orbit between maneuvers is much less effective than using a Lambert maneuver pair whose burn times are much closer together. The total fuel use for this trajectory is 1.63m/s.

The thickened gray portions of the trajectory schematics represent times when measurements are not available due to periods of eclipse.

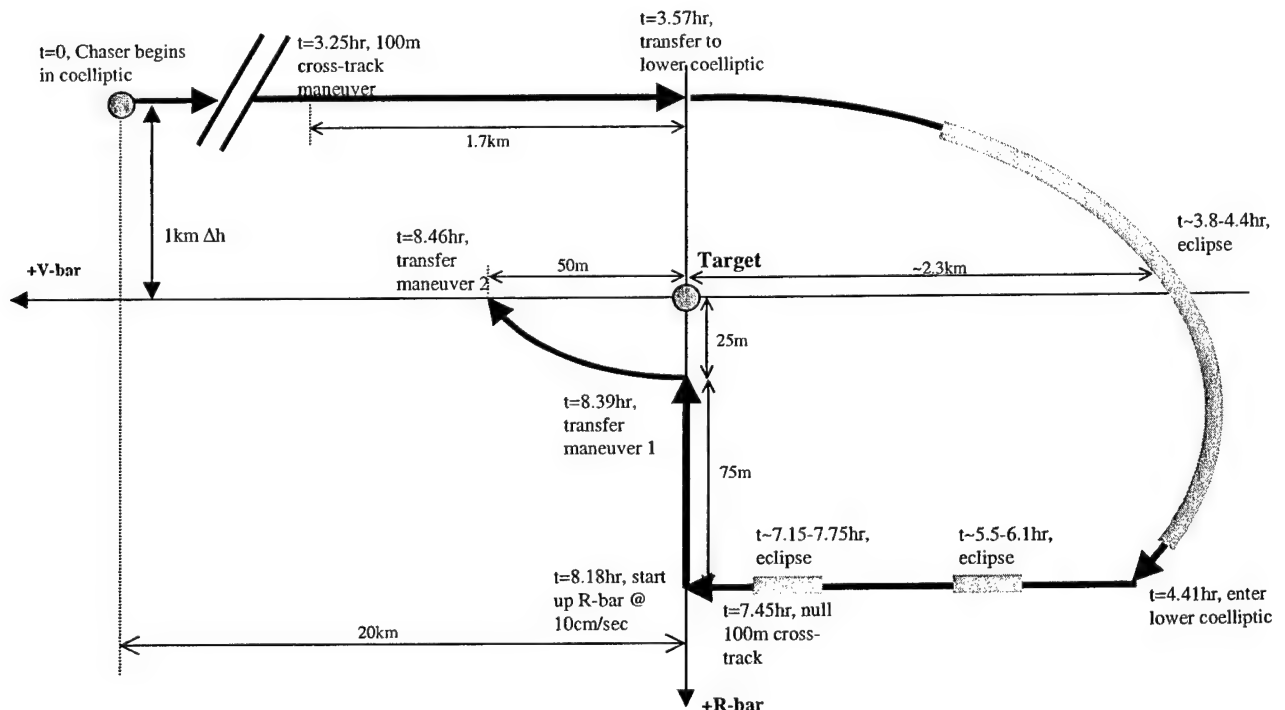


Figure 5-3: Orbital Express trajectory option 1 schematic

The second closure trajectory is similar to the first except that it makes use of a V-bar final approach, as shown in Figure 5-4. Although V-bar approaches suffer from poor angles-only observability characteristics, they are a common method of spacecraft rendezvous and therefore one was incorporated into the current study. Note that unlike the R-bar approach, observation maneuvers are used to compensate for the loss of observability due to approaching the target along the line-of-sight. The maneuver from the lower coelliptic to the V-bar is once again a Lambert transfer and is applied directly below the target to take advantage of the low navigation errors at that point. Two observation maneuvers are performed before beginning the 10cm/sec V-bar approach during which the target reaches the 50m point at 8.93hrs. This scenario was also used to examine navigation ability at closer offset points by allowing the chaser to close to within 10m of the target. Fuel use for this trajectory, including the approach to 10m, is 3.91m/s.

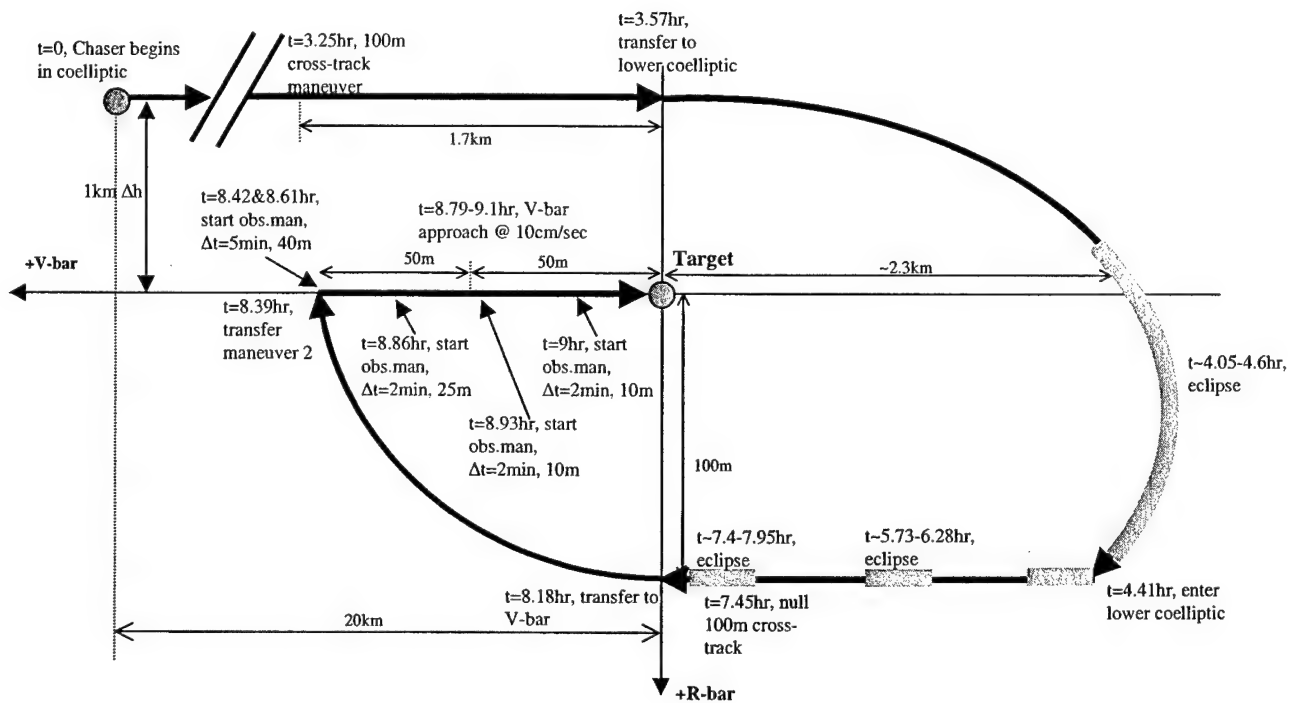


Figure 5-4: Orbital Express trajectory option 2 schematic

The third Orbital Express trajectory uses a spiral approach to place the chaser directly at the desired offset point as shown in Figure 5-5. In addition to the in-plane motion, observation maneuvers are also used at V-bar crossing points. Note that two of these maneuvers take place in eclipse periods. As discussed earlier, this is not the most desirable situation, but they are used here to see the effects of employing maneuvers during periods of unavailable measurements. The in-plane maneuvers are all simply Hohmann type transfers and the resulting total fuel use for this trajectory is 1.69m/s.

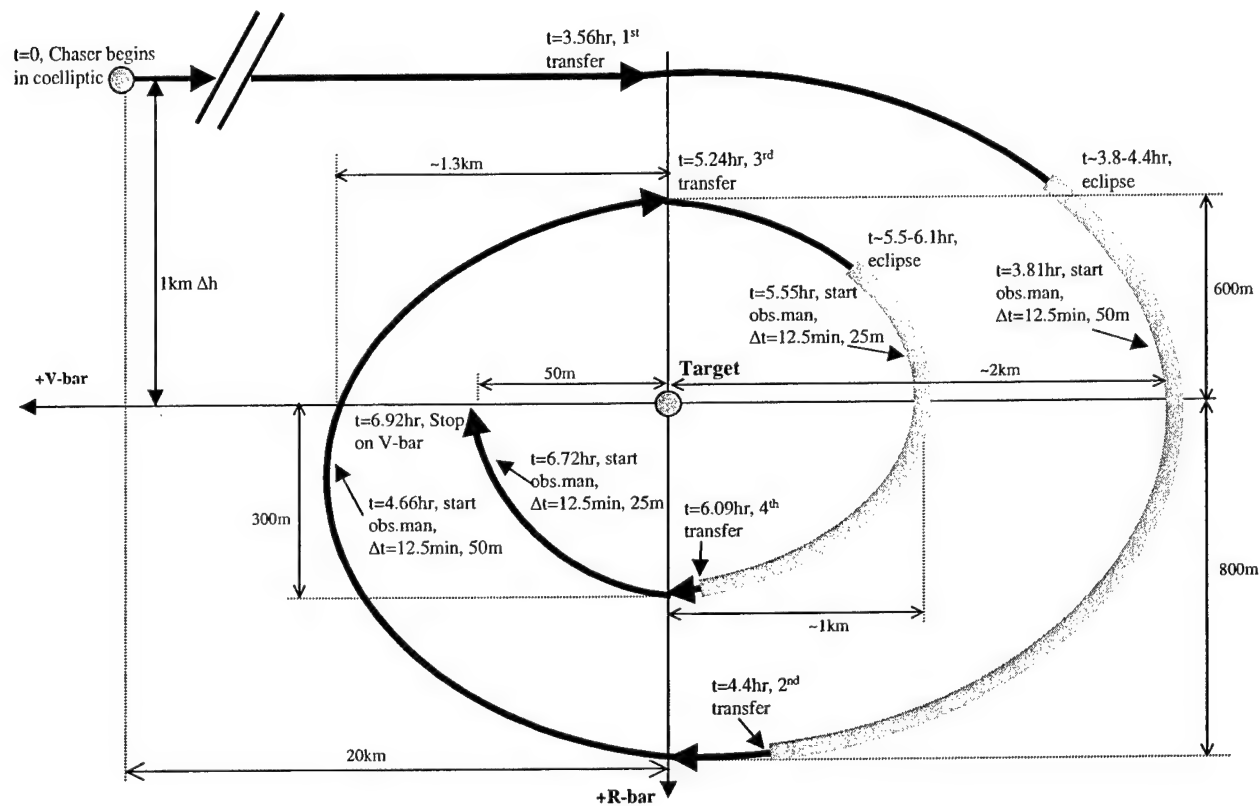


Figure 5-5: Orbital Express trajectory option 3 schematic

The fourth and final closure trajectory transitions from the initial coelliptic to a temporary station-keeping football to a final approach along a glide-slope as shown in Figure 5-6. The initial transfer from the 1km coelliptic is done above the target to a coelliptic 50m below the target. As the chaser passes directly below the target it places itself into a football orbit centered on the target. After two orbits on the football with observation maneuvers to maintain the navigation accuracy, the chaser transitions to a ~20cm/sec glide-slope approach towards the target. This glide-slope is accomplished by combining the maneuvers associated with both R and V-bar approaches to achieve a closing velocity along an angle relative to the target, 30° in this case. As with closure trajectory option 2, this case is used to examine the ability of angles-only navigation to function beyond the 50m offset point. The glide-slope approaches the target to within 10m at 14.25hr. The total fuel use for the entire trajectory is 2.42m/s.

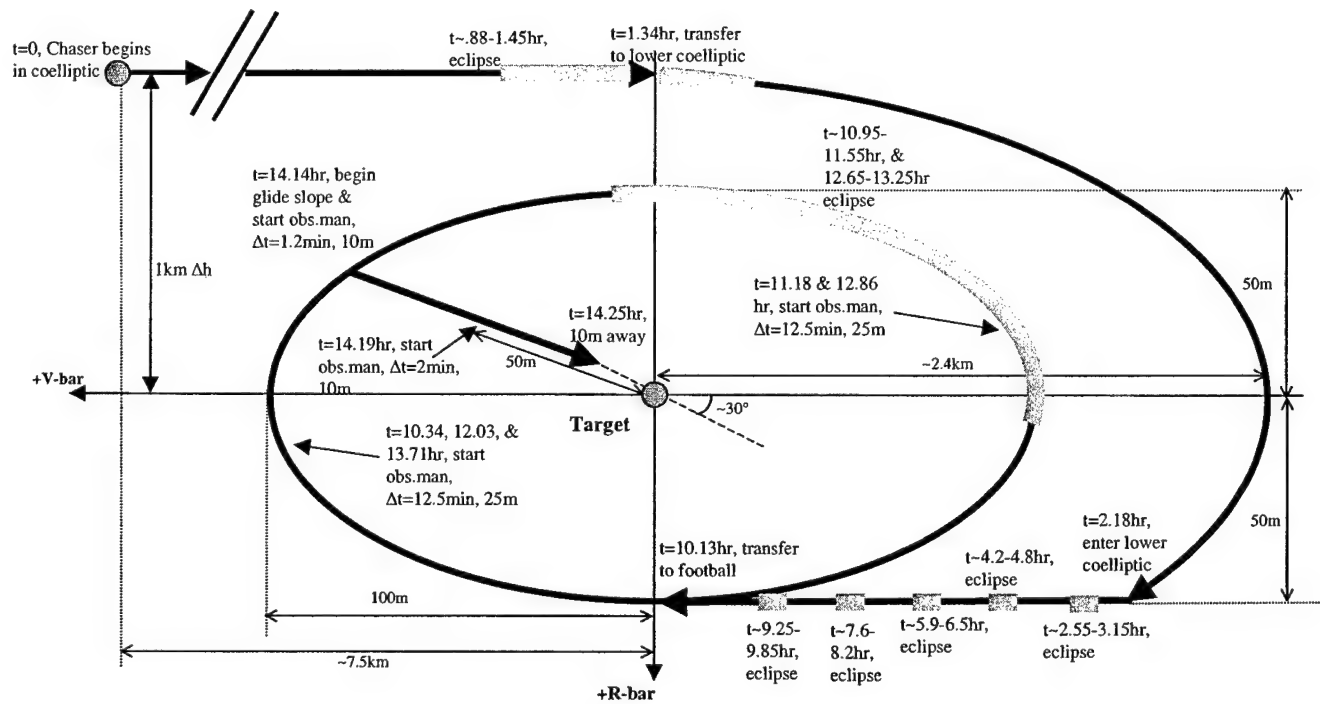


Figure 5-6: Orbital Express trajectory option 4 schematic

5.3.2 Station-keeping

In addition to the four trajectories designed for the closure portion of the Orbital Express mission, three methods of station-keeping are proposed for maintaining the chaser at the 50m V-bar offset. Since the underlying assumption of station-keeping is that the chaser can not deviate from a given point relative to the target, all three methods are similar in nature and are considered at once as shown in Figure 5-7.

The first station-keeping technique is for the chaser to simply stay in a co-circular orbit with the target with 50m of separation. As demonstrated in Chapters 3 and 4 this type of station-keeping is far from ideal from an angles-only navigation standpoint, but it is a common method in actual practice since it is the only point where zero relative motion can be maintained indefinitely with zero fuel use (in an idealized situation). To overcome the problem of navigating in a co-circular orbit, observation maneuvers are used three times per orbit to keep the navigation uncertainty errors at acceptable levels. The times of the observation maneuvers, along with eclipse periods, are shown along with the trajectory in Figure 5-7. The fuel use over approximately five orbits is 4.97m/s. As in the previous section, the Δt listed for an observation maneuver refers to the time it takes the chaser to reach the maximum out-of-plane point.

The next type of station-keeping trajectory is very similar to the first except that instead of using a co-circular orbit for zero relative motion, the chaser is in a small football centered on the 50m offset point. The chaser gets as close as 40m to the target and is 60m away at its farthest separation. The observation maneuvers are identical to those used for the co-circular case which take place three times per orbit and are timed to avoid eclipse periods. Since these observation maneuvers are the same, the fuel use for this trajectory over five orbits is still 4.97m/s.

The third and final station-keeping trajectory also makes use of a relative motion football, but uses maneuvers to stop and start the football motion. Since maneuvers generally tend to improve observability, this trajectory replaces some of the cross-track observation maneuvers used in the first two methods with in-plane maneuvers that induce and then null a football. In between the footballs, the chaser is in a co-circular orbit sitting motionless at the 50m offset point. The chaser performs two observation maneuvers during every football as shown in Figure 5-7. Note that for this third trajectory, some of the maneuvers take place during eclipse periods which is done only for illustrative purposes and is not usually desirable in practice. The fuel use over four cycles is 1.32m/s where a cycle consists of waiting on the V-bar for $\frac{1}{2}$ hour, inducing a football and then nulling it one orbit later.

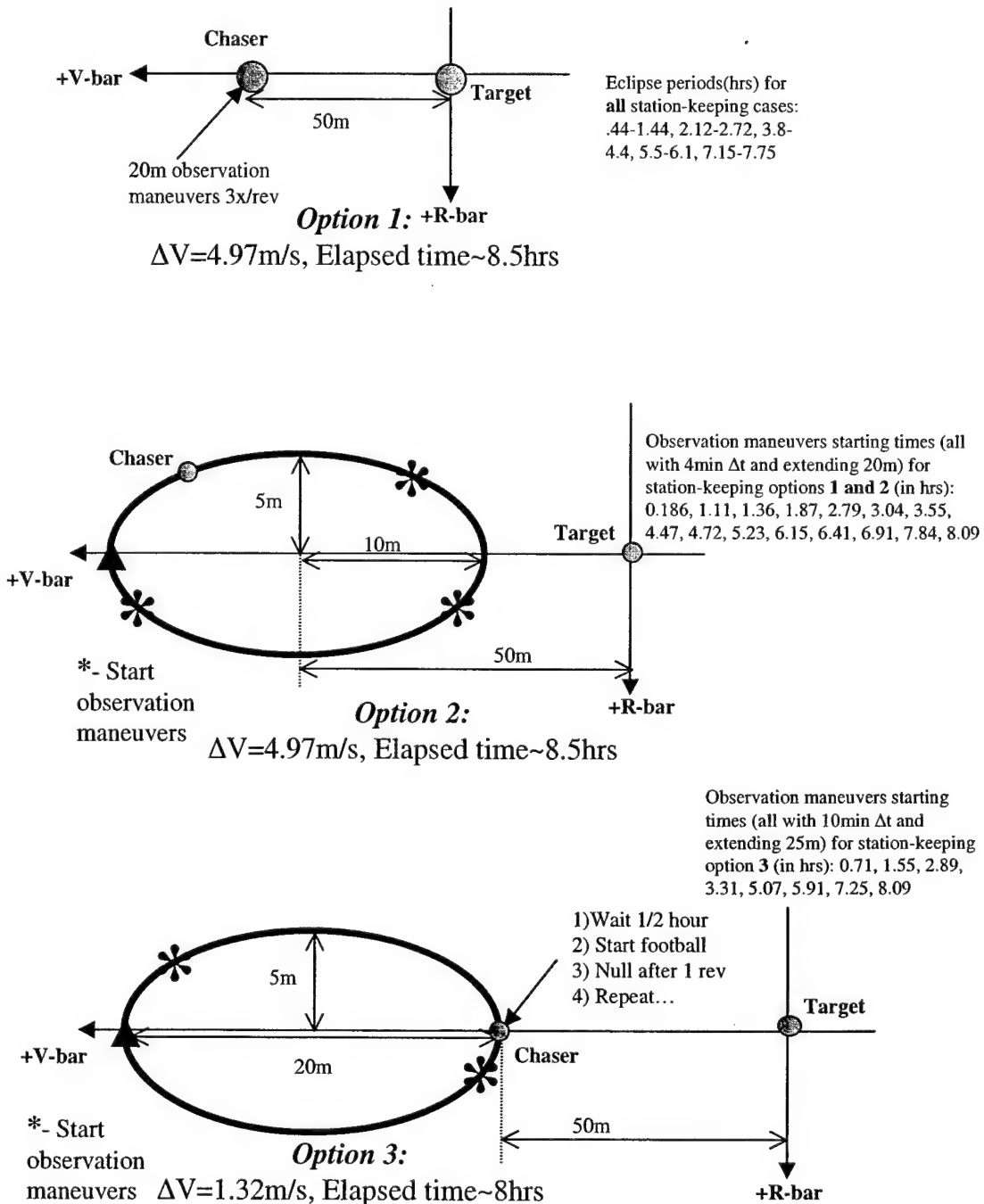


Figure 5-7: Orbital Express station-keeping trajectory schematics

5.4 RESULTS

With several potential Orbital Express trajectories designed, the next step is to gauge the ability of angles-only navigation to achieve mission success. This simply requires a LINCOV analysis of the problem as specified by the reference trajectories and the error models given in section 5.2. However, a more useful set of results would include not only the navigation performance in the presence of all the errors sources but also a demonstration of the sensitivity to these errors. The underlying motivation to this approach is that the current study would be much more useful to future mission design if a potential user could easily judge whether or not a given trajectory might work subject to their mission specific error models. In light of this desire, the following test plan was used for generating LINCOV results with the trajectories in the previous section.

Each of the station-keeping and closure trajectories was tested in the presence of sixteen different error model combinations designed to span as much of the study space as possible. The results provide useful information about the individual effects of error sources as well as reference trajectory dependencies. First, the value of process noise/un-modeled accelerations was set for the chaser vehicle. The first LINCOV run then uses zero error sources in order to establish a baseline for the trajectory for its given *a priori* information and un-modeled accelerations. The next three runs consist of turning on each error model individually while leaving the others at zero (e.g. the ΔV measurement error model is used while still using error free attitude determination and angular measurement models). These results show the relative effects of each error source compared to the baseline error free results. The fifth run is a case with all three error sources set at their nominal values, and is considered the anchor point, or most realistic representation, of what the Orbital Express mission results would actually be like. The sixth through eighth cases are stress tests to examine the sensitivity of the trajectories to higher error values. Each error model is increased by three times its nominal value while leaving the other two error sources at their nominal values. For example, the attitude error stress case would set the static misalignment bias to $3 \times 0.01^\circ = 0.03^\circ/\text{axis-}1\sigma$ and the attitude measurement noise to $3 \times 0.1^\circ = 0.3^\circ/\text{axis-}1\sigma$ while leaving the angular and ΔV measurement errors at their nominal non-zero values. These same eight runs are then repeated for a different value of chaser vehicle un-modeled accelerations.

For the closure trajectories, the final downrange percent uncertainty upon arrival at the 50m offset point was the key value to focus on. Again, though, simply recording this value and moving on would remove the generality from this study that could make it potentially useful to future missions. The presence of eclipse periods means that there are portions of each trajectory where the downrange percent error values may be of interest. Therefore, in addition to recording the downrange percent uncertainty at the end of each trajectory, the highest value encountered during the entire trajectory is also recorded. In almost all cases, this occurs during an eclipse period. An additional figure of merit recorded for closure trajectories 2 and 4 only is the downrange percent uncertainty when the chaser reaches a point 10m away from the target. For the station-keeping trajectories, there are really only two values of interest. One is the highest value of downrange percent error experienced. This value always occurs during an eclipse period. Since other missions may have more constant measurement availability, the highest value of downrange percent error during a sunlight period is also recorded. All of these values were recorded for each of the above tests.

The results for the quiet and noisy chaser vehicle are tabulated in Table 5-1 and Table 5-2 respectively. Preceding these results is Figure 5-8 which illustrates how to extract data of interest from the tables. The data is also shown in a more graphical form following the tables.

Data for given trajectory contained in this column

Indicates level of un-modeled accelerations on chaser

PROCESS NOISE - CHASER					SK1	SK2	SK3
					Sun	Eclipse	
Final downrange % uncertainty @50m offset point	Closure 1	Closure 2	Closure 3	Closure 4	0 error	Sun	
0 error	Final					Eclipse	
	High						
	at 10m						
ΔV Meas.	Final				ΔV Meas.	Sun	
	High					Eclipse	
	at 10m						
Ang.Meas.	Final				Ang.Meas.	Sun	
	High					Eclipse	
	at 10m						
Att.Err.	Final				Att.Err.	Sun	
	High					Eclipse	
	at 10m						
All Errors	Final				All Errors	Sun	
	High					Eclipse	
	at 10m						
3x ΔV	Final				3x ΔV	Sun	
	High					Eclipse	
	at 10m						
3x Ang Err.	Final				3x Ang Err.	Sun	
	High					Eclipse	
	at 10m						
3x Att.Err.	Final				3x Att.Err.	Sun	
	High					Eclipse	
	at 10m						
<i>ΔV required (m/s)</i>					<i>ΔV required (m/s)</i>		
<i>Closure cases</i>					<i>Station-keeping cases</i>		
Nominal value rows							
Highest downrange % uncertainty PRIOR to final approach							
Stress test rows							
Downrange % uncertainty at 10m point (only for closure cases 2&4)							

Figure 5-8: Orbital Express trajectory testing results legend

"QUIET" PROCESS NOISE - CHASER

		Closure 1	Closure 2	Closure 3	Closure 4
0 error	Final	0.3	0.75	0.6	1
	High	1.4	2.5	0.9	6
	at 10m		5.6		3.5
ΔV Meas.	Final	0.5	4	1.2	1.7
	High	1.5	3.2	1.2	6.5
	at 10m		29		11
Ang.Meas.	Final	0.5	1.2	1.1	1.75
	High	2.25	3.5	1.25	9
	at 10m		7		5.4
Att.Err.	Final	0.5	1.5	1.2	1.8
	High	3.4	5.5	2.5	10
	at 10m		7.9		5.2
All Errors	Final	1	4.8	1.75	2.7
	High	3.5	6	2.6	12
	at 10m		32		12.5
3x ΔV	Final	1.4	12	2.5	4.6
	High	4	8	3.25	16
	at 10m		94		32
3x Ang.Err	Final	1.5	5	2.4	3.6
	High	4	6.5	2.75	17
	at 10m		38		15
3x Att.Err	Final	1.5	5	2.7	3.75
	High	7	10	6.2	19
	at 10m		36		18
ΔV required (m/s)		1.63	3.91	1.69	2.42

Nominal 1σ Error Values:

ΔV measurement error: Burn>2cm/sec-->1mm/sec spherical; Else 5% spherical
 Angular measurement noise: 0.03°; Measurement bias: 0.25/Range rad, $\tau=1/2$ *Period
 Attitude error: 0.01%/axis static misalignment; 0.1%/axis attitude error ($\tau=300$ sec)

		SK1	SK2	SK3
0 error	Sun	1.3	1	2
	Eclipse	6.5	7.5	7
ΔV Meas.	Sun	1.5	1.25	3
	Eclipse	6.75	8	9
Ang.Meas.	Sun	1.5	1.5	3.5
	Eclipse	8	9.5	8.5
Att.Err.	Sun	1.5	1.25	3
	Eclipse	8	9.5	9
All Errors	Sun	2.5	2	4.5
	Eclipse	11	13.5	11
3x ΔV	Sun	3.25	3	6
	Eclipse	14	18.5	22
3x Ang.Err	Sun	3.5	4	10
	Eclipse	14.75	18	14
3x Att.Err	Sun	3.25	3	6
	Eclipse	15	18	15
ΔV required (m/s)		4.97	4.97	1.32

Process noise on target: $1 \times 10^{-13} (\text{m}^2/\text{s}^3) - 0.5 \text{m/rev}$
 Process noise on chaser: $9 \times 10^{-10} (\text{m}^2/\text{s}^3) - 50 \text{m/rev}$

Table 5-1: Summary of results for Orbital Express trajectories with quiet chaser vehicle

"NOISY" PROCESS NOISE - CHASER

		Closure 1	Closure 2	Closure 3	Closure 4	SK1	SK2	SK3
0 error	Final	0.75	2.1	1.7	2.75	Sun	2.75	2.75
	High	4	6.75	2.6	16	Eclipse	17.8	20.9
	at 10m		15		10			18
ΔV Meas.	Final	1	4.5	2.25	3.2	Sun	2.9	3
	High	4	7	2.7	16.5	Eclipse	18.2	21.2
	at 10m		32		14.75			19
Ang. Meas.	Final	1	2.5	2.3	3.7	Sun	3.2	3.1
	High	5	8.5	2.75	20	Eclipse	19.5	22.5
	at 10m		16		12			21
Att.Err.	Final	1	3	2.5	3.9	Sun	3.25	3
	High	6.8	10.8	3.2	20	Eclipse	19.5	22.75
	at 10m		17		12.1			21
All Errors	Final	1.2	5.2	3	4.5	Sun	3.4	3.25
	High	7	11	3.4	22	Eclipse	21	24.5
	at 10m		33		17			22.5
3x ΔV	Final	1.8	12.5	3.8	6.2	Sun	3.9	3.8
	High	7	12.5	4.2	24	Eclipse	22.75	27.5
	at 10m		95		35			28
3x Ang.Err	Final	1.9	6	3.5	5.5	Sun	4.6	4.5
	High	7.5	12	3.9	27.5	Eclipse	24.1	28
	at 10m		39		19			25
3x Att.Err	Final	1.9	6	3.75	5.6	Sun	4.1	4
	High	10.5	16	7	29	Eclipse	24.1	29
	at 10m		39		19			26
ΔV required (m/s)		1.63	3.91	1.69	2.42	ΔV required (m/s)	4.97	4.97
								1.32

Nominal 1σ Error Values:

ΔV measurement error: Burn>2cm/sec-->1mm/sec spherical; Else 5% spherical
Angular measurement noise: 0.03°; Measurement bias: 0.25/Range rad, $\tau=1/2$ /Period
Attitude error: 0.01°/axis static misalignment; 0.1°/axis attitude error ($\tau=300$ sec)

Process noise on target: $1 \times 10^{-13} (\text{m}^2/\text{s}^3) \sim 0.5 \text{m/rev}$
Process noise on chaser: $7 \times 10^{-9} (\text{m}^2/\text{s}^3) \sim 140 \text{m/rev}$

Table 5-2: Summary of results for Orbital Express trajectories with noisy chaser vehicle

Although the tables are complete, an alternate and perhaps easier way of quickly viewing the data is through time histories of the LINCOV results for the various trajectories. The following pages show the results of the error sensitivity studies. For each trajectory, the results with all errors at their nominal values are overlaid with the stress cases where two errors are at their nominal values and one is at 3x its nominal value. Refer to Figure 5-3 through Figure 5-6 for the key times and maneuvers in the closure trajectories. Figure 5-9 is a collection of the results for all four closure trajectories with a quiet chaser vehicle, and Figure 5-10 is the same set of trajectories except using the noisy chaser vehicle. Following this are the results for the station-keeping cases. Refer to Figure 5-7 to compare the trajectories to the results. Figure 5-11 shows the results for all station-keeping trajectories with quiet un-modeled accelerations on the chaser vehicle while Figure 5-12 contains the results for the noisy un-modeled accelerations.

The time histories for the closure trajectories begin at 3.5 hours since the early portion of the runs is generally of little interest. The square wave at the top of each plot represents the solar illumination and eclipse periods. Also, only the downrange component of navigation uncertainty (as a percent of range) is shown since estimating the other components is not problematic using angles-only measurements. In the case of closure trajectories 2 and 4, the plots terminate when the chaser is 50m away from the target in order to better preserve the scaling of the figures.

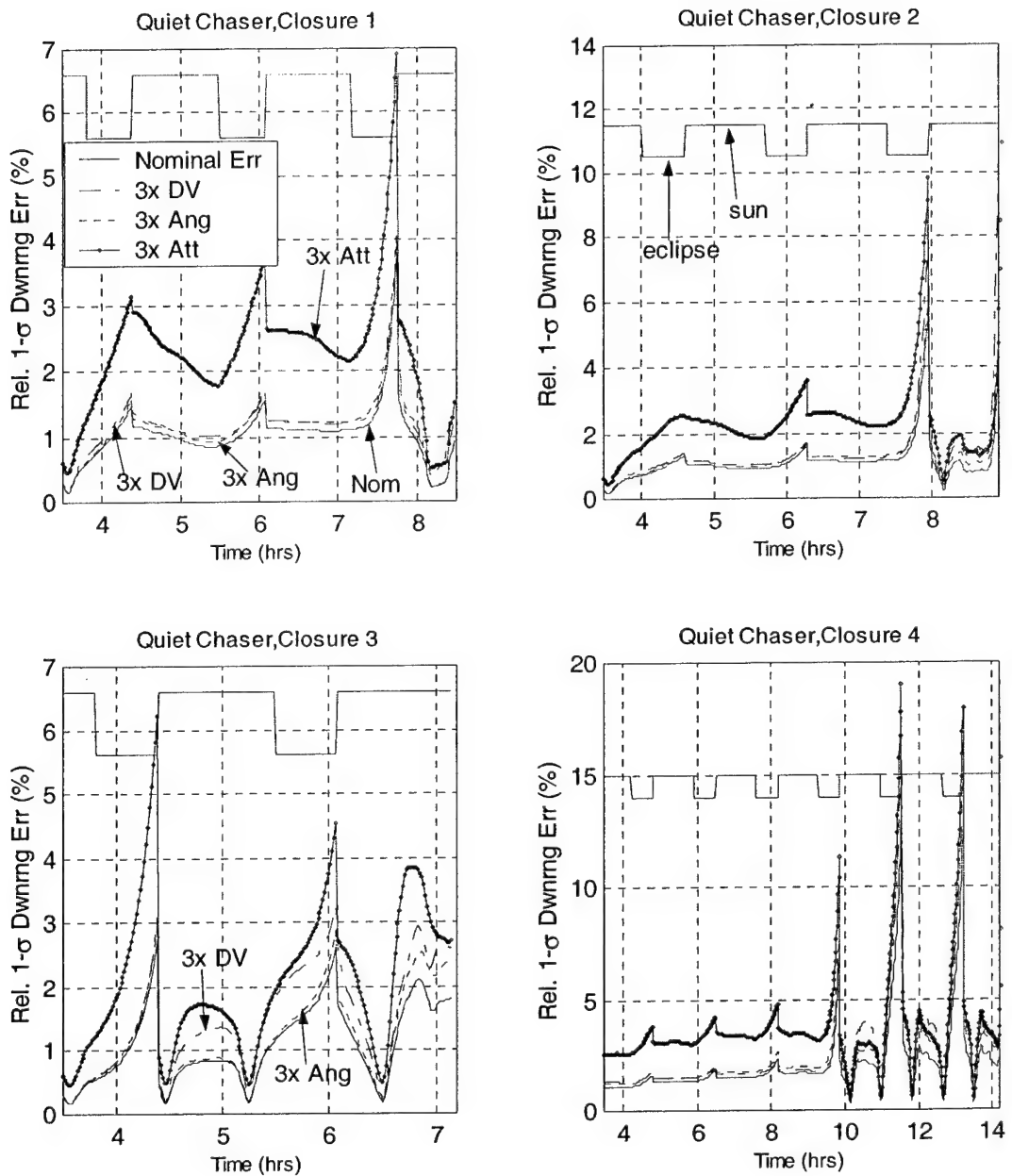


Figure 5-9: Results for closure trajectories with quiet chaser vehicle using nominal error cases and stress cases

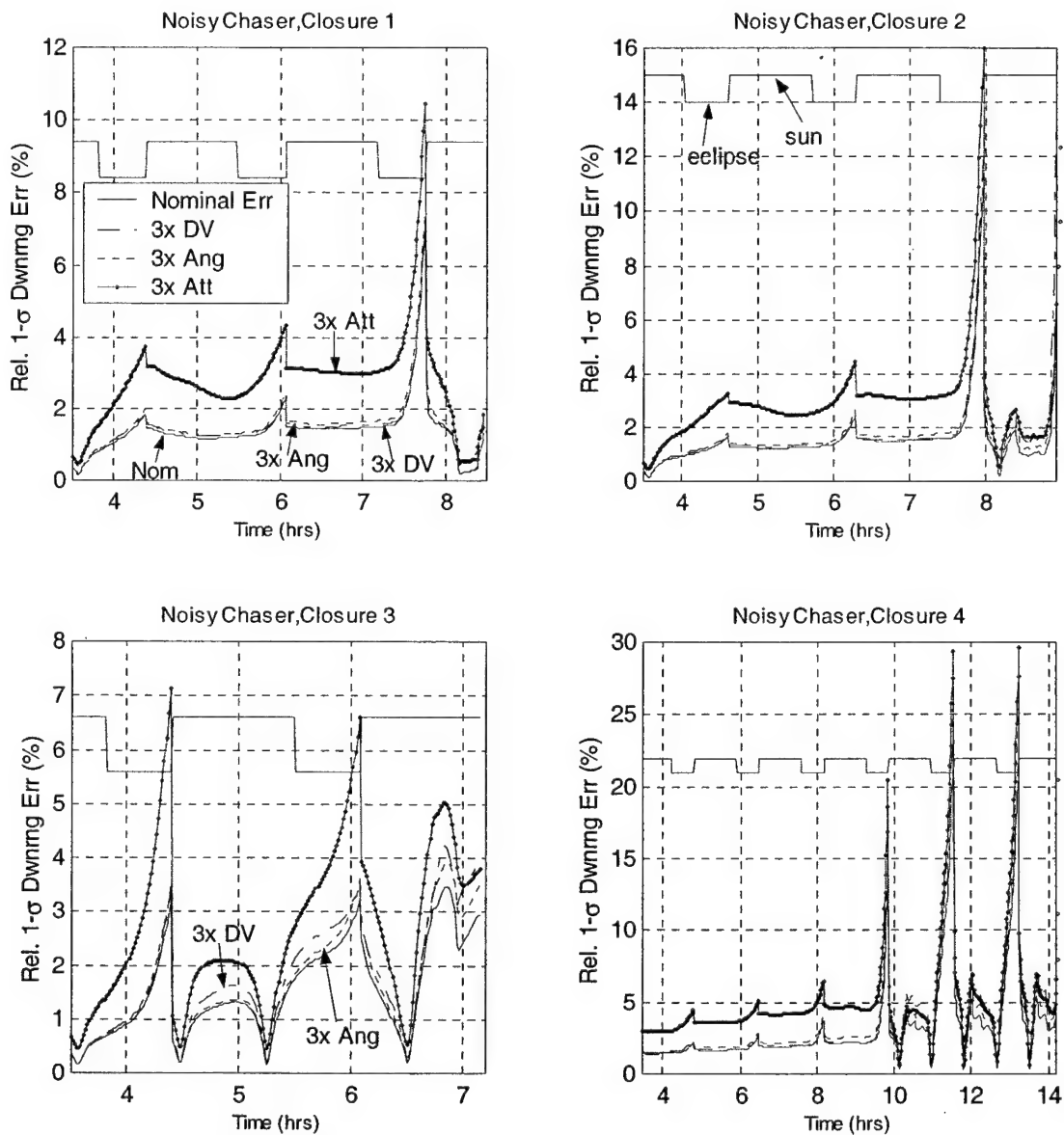


Figure 5-10: Results for closure trajectories with noisy chaser vehicle using nominal error cases and stress cases

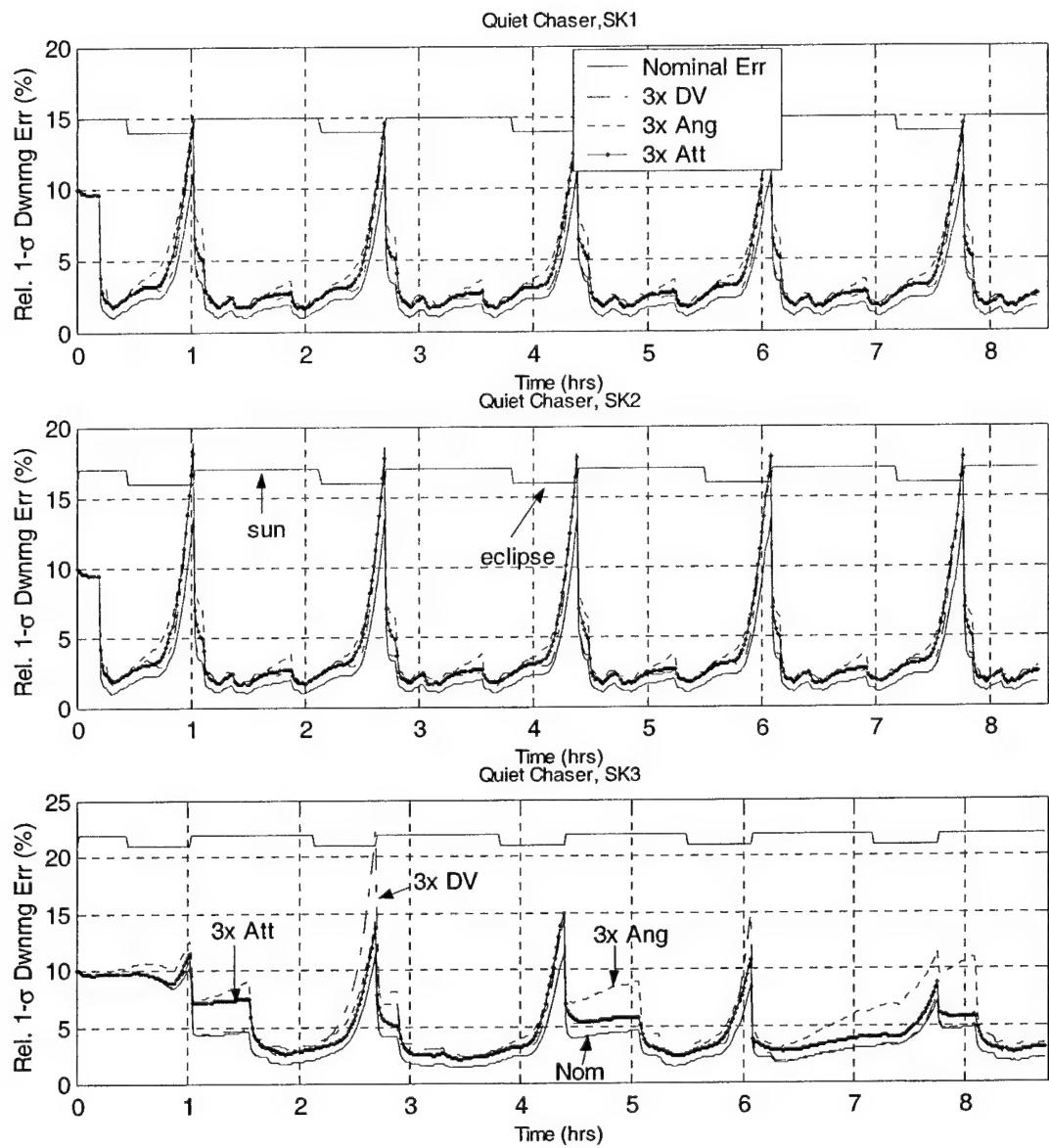


Figure 5-11: Results for station-keeping trajectories with quiet chaser vehicle using nominal error cases and stress cases

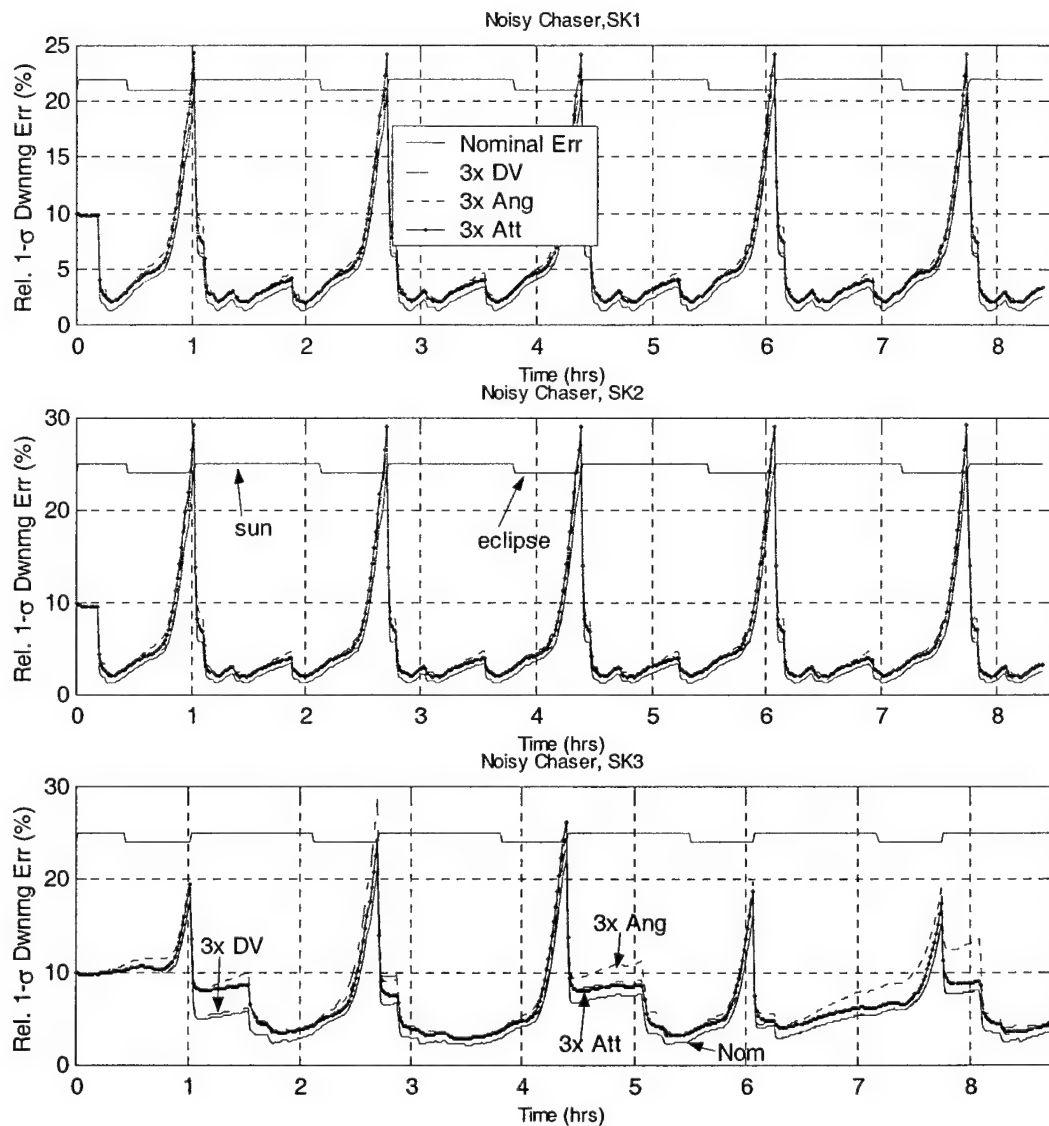


Figure 5-12: Results for station-keeping trajectories with noisy chaser vehicle using nominal error cases and stress cases

The results show that the maneuver-assisted trajectories are quite effective at making angles-only navigation successful. For the chaser vehicle with quiet un-modeled accelerations, only closure trajectory 4 did not reach the 50m offset point with less than 10% downrange uncertainty with all errors at their nominal values. In fact, the first three closure trajectories were able to maintain this performance even under the higher stress case error values. Increasing the un-modeled accelerations to the noisy case eliminates closure trajectory 2 from being able to meet the success criteria. However, trajectories 1 and 3 again maintain the downrange error values below 10% even in the presence of the largest error models.

For the station-keeping trajectories, the results are largely dominated by the combination of un-modeled accelerations and eclipse periods. Regardless of whether the trajectory maintains downrange uncertainty at low levels during sunlight, the amount of un-modeled accelerations greatly degrades navigation performance during eclipse. A quick thought experiment explains why. If the noisy chaser vehicle experiences on the order of 150m of error growth per orbit due to un-modeled accelerations, then it would only take $1/3^{\text{rd}}$ of an orbit for this error alone to create 100% error while station-keeping at a 50m offset point. During eclipse periods, measurements are not available to keep this growth in check. Despite these problems, though, all three station-keeping trajectories came very near to maintaining less than 10% downrange uncertainty for the case of a quiet chaser vehicle with all errors at their nominal values.

Finally, the results illustrate the danger of blindly placing maneuvers into a trajectory in the hopes of improving navigation performance. As mentioned earlier, several maneuvers were intentionally executed in eclipse periods to examine the effects of this practice. In a sense, the difference in executing a maneuver in eclipse versus sunlight is similar to executing commands in an open versus closed loop system. Performing a maneuver initially adds to the navigation uncertainty due to ΔV measurement error. In sunlight, however, this additional uncertainty is not only eliminated, but the original uncertainty is reduced thanks to angular measurements of the target, in effect closing the loop. In eclipse, though, the uncertainty from the maneuver is not removed since there are no measurements available.

5.4.1 End-to-End Testing

As an additional test, one end-to-end trajectory was created that merged a closure and station-keeping trajectory to form one large maneuver-assisted trajectory for LINCOV analysis. Station-keeping trajectory 3 was added to the end of closure trajectory 3 with several slight

modifications. First, all maneuvers were timed to occur during periods of sunlight, as would be desirable for actual mission operations. Second, the station-keeping point was shifted during the course of the run from 50m to 30m to 10m progressively at 6.92hrs, 17.2hrs, and 24.7hrs respectively. This was to investigate the performance of angles-only navigation at closer distances than the 50m offset. Finally, the LINCOV analysis was conducted under varying measurement availability conditions. Besides the standard case of solar illumination dependence, one case was run with constant measurement availability, and another case had constant availability only during the station-keeping phase. The trajectory is shown in detail in Figure 5-13 with the accompanying LINCOV results in Figure 5-14. Total fuel use for the trajectory was 5.35m/s and the entire scenario lasts approximately 32 hours.

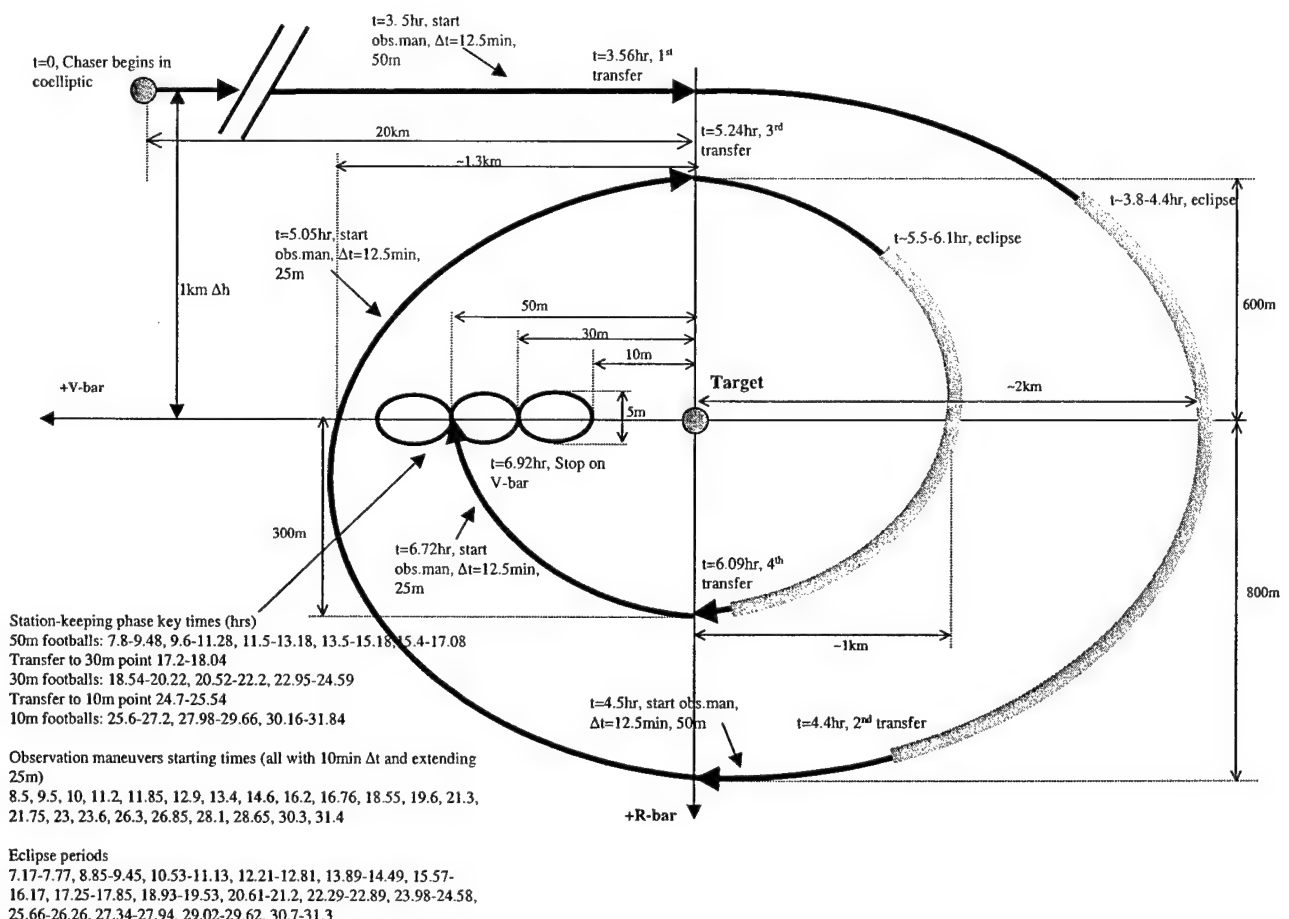


Figure 5-13: Orbital Express end-to-end trajectory schematic

The results for the end-to-end trajectory shown below are for the case of all error sources at their nominal values and the quiet chaser vehicle.

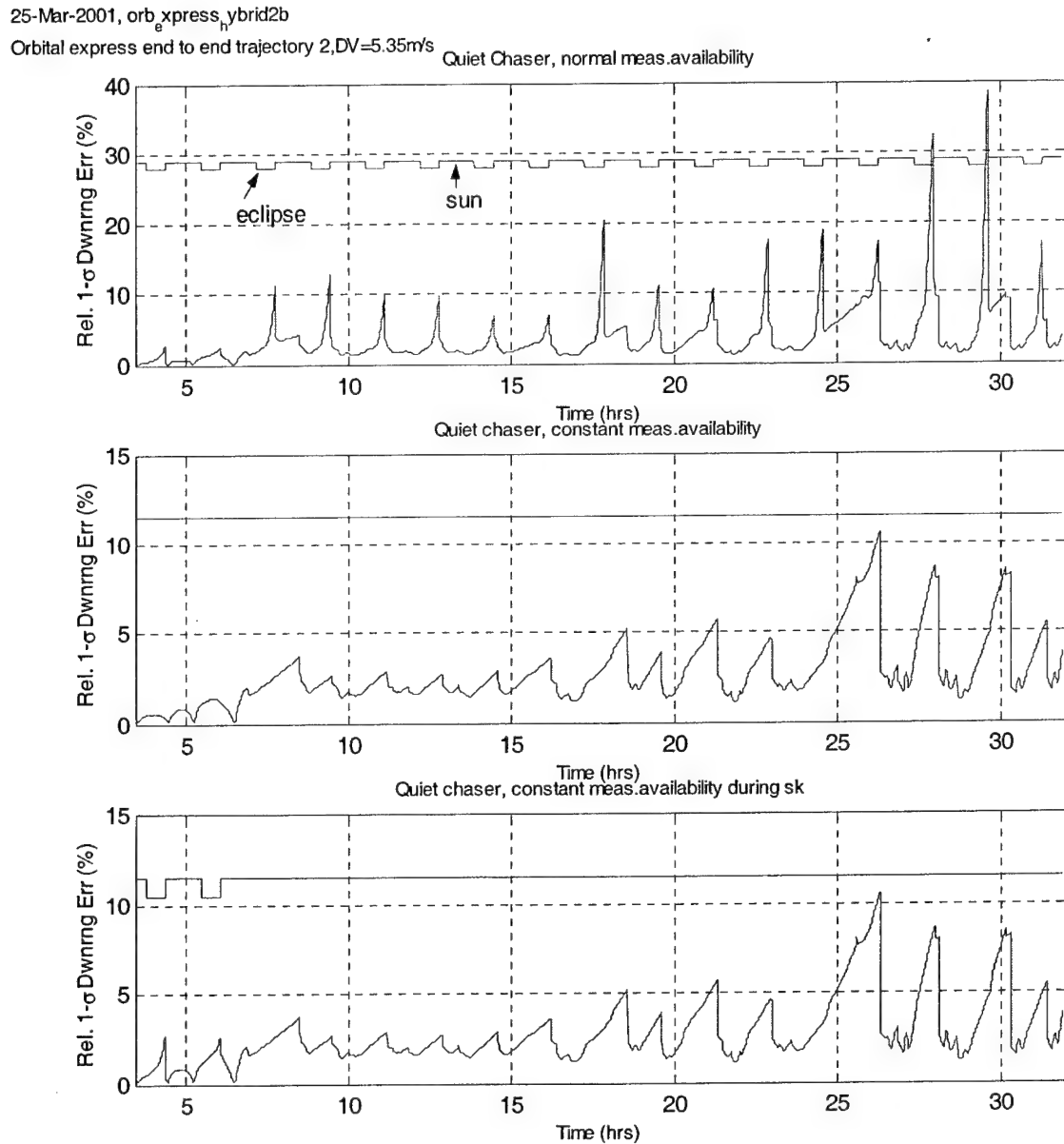


Figure 5-14: End-to-end trajectory results for quiet chaser with all errors at nominal values and varying measurement availability conditions

Once again, the results are extremely encouraging in showing that angles-only navigation can be effective when using well designed maneuver-assisted trajectories. Except for eclipse periods, the navigation filter maintains downrange uncertainty values to less than 10% even while at the 10m offset point. Eliminating the eclipse periods makes the results even more attractive. The results also serve to highlight the effectiveness of observation maneuvers. Note that the downrange uncertainty grows during eclipse times even when measurements are always available. This is because the trajectory was originally designed to avoid maneuvers during these periods. For potential missions where constant measurement availability was assured these navigation uncertainty growth periods would be eliminated by simply scheduling observation maneuvers to maintain the uncertainty at a lower steady state level.

Dispersions Due to Velocity Uncertainty

One aspect of angles-only navigation performance that has not been discussed in detail up to this point is the effect of velocity uncertainties. Although some of the LINCOV results in previous chapters showed relative velocity uncertainty values, it is difficult to visualize their effects on estimating the target position. In mission practice, the presence of velocity uncertainties during maneuver execution would lead to future trajectory dispersions. Thus, a better method of quantifying the effects of velocity uncertainties on angles-only navigation is to examine the dispersions they would cause after maneuvers.

The end-to-end trajectory shown in Figure 5-13 is used to briefly demonstrate how velocity uncertainties turn into position dispersions. As mentioned in section 2.2.1, the current study deals with filter performance rather than dispersion analysis. In light of this, the analysis of dispersions due to velocity uncertainties is significantly simplified and proceeds as follows. At a given maneuver execution time, it is assumed that the position is known perfectly. The current velocity uncertainty values along with their cross-correlations are then propagated forward one hour using the C-W equations (3.1) to create a time history of the position dispersion as a percentage of the range to the target.

Figure 5-15 shows a sampling of the relative position dispersions resulting from six different maneuvers. The maneuver times are selected from various portions of the trajectory. The first maneuver shown at 3.5 hours is an observation maneuver that takes place while the chaser is still on the initial incoming coelliptic. The second example is at 5.24 hours which is the third transfer burn in the spiral approach. The third maneuver corresponds to 6.92 hours when the chaser

arrives and stops on the V-bar 50m from the target. The last three maneuver times all correspond to the start of station-keeping footballs at the 50, 30, and 10m offset points respectively.

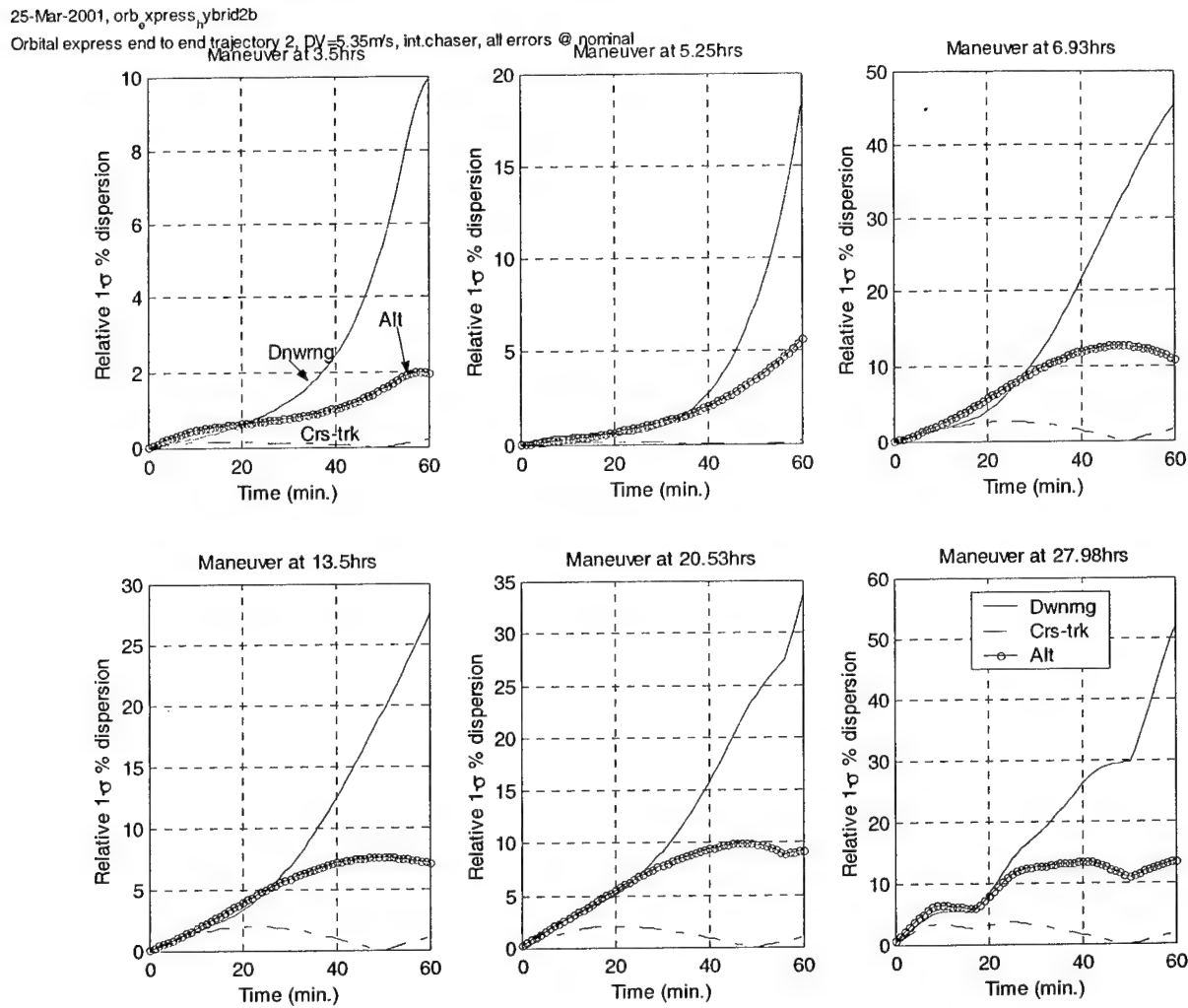


Figure 5-15: Relative position dispersions resulting from velocity uncertainty at maneuver execution times for Orbital Express end-to-end trajectory

As was the case for position uncertainties, the position dispersions due to velocity uncertainties grow worse the closer the chaser is to the target, when comparing percent values. Another key point that this analysis demonstrates is the potential need for mid-course correction maneuvers when the time between normally scheduled maneuvers is greater than 30 minutes, or about one-third of the orbital period. Figure 5-15 shows that when the time between maneuvers is approximately less than thirty minutes, the trajectory dispersions generally stay at acceptable levels near 10%. However, if a given maneuver is not followed by another maneuver within

thirty minutes, the dispersions begin to grow to unacceptable levels. In actual practice, this problem could be mitigated by using mid-course corrections.

Geo-Synchronous Test Case

Another area of interest is the potential of angles-only navigation to work at higher orbital altitudes, specifically geo-synchronous orbits. The same end-to-end trajectory shown in Figure 5-13 was adapted slightly for geo-synchronous use. The relative motion shape is exactly the same although the key times are shifted, and the chaser initially starts 1.4km downrange of the target rather than 20km since the relative motion at geo-synchronous altitude is much slower. The spiral approach now begins at 3.43 hours and ends at 51.3 hours (~2.1 days) when the chaser reaches the 50m offset point. Following five station-keeping footballs at the 50m offset point, the chaser arrives at the 30m offset point at 193 hours (~8 days). After another three station-keeping footballs here, the chaser finally arrives at the 10m offset point at 296.4 hours (~12.3 days) where it does an additional three station-keeping footballs.

Besides these timing changes, many more observation maneuvers were used for the geo-synchronous case. In the LEO case, there were generally about two observation maneuvers per orbit. However, at geo-synchronous altitude this would mean doing observation maneuvers nearly 12 hours apart. In the presence of all the error models this was not sufficient to keep the downrange error at acceptable levels. Observation maneuvers are begun at 37.6 hours starting approximately every 1.25 hours and extending 25m with a $\Delta t=1/2$ hour. Once the chaser reaches the station-keeping point, the frequency of observation maneuvers is increased. From 51.3 hours through the end of the trajectory, observation maneuvers begin every 48 minutes. Each one extends 25m with the $\Delta t=12$ minutes. This repeating 48 minute pattern essentially mimics how often observation maneuvers occurred in the LEO case. All of these additional maneuvers wind up increasing the total fuel use to 52.8m/s which seems rather large. Considering this is used over a 16 day period, though, the number is not that high since it equates to roughly 3.3m/s per day.

The downrange percent uncertainty for the end-to-end geo-synchronous trajectory with all errors at their nominal values and the quiet chaser vehicle is shown in Figure 5-16. Additionally, constant measurement availability is assumed. This is a reasonable assumption since the chaser and target are now at geo-synchronous altitudes and neither encounters the earth's shadow. The results show that the navigation filter successfully keeps the downrange error below 10% until the chaser moves to the 10m offset point. At this closer distance, the observation maneuvers are not

frequent enough to further reduce the error. However, this can be easily fixed by simply adding more observation maneuvers, and the more important conclusion is that angles-only navigation was largely successful in a geo-synchronous orbit using a trajectory originally designed for use in LEO.

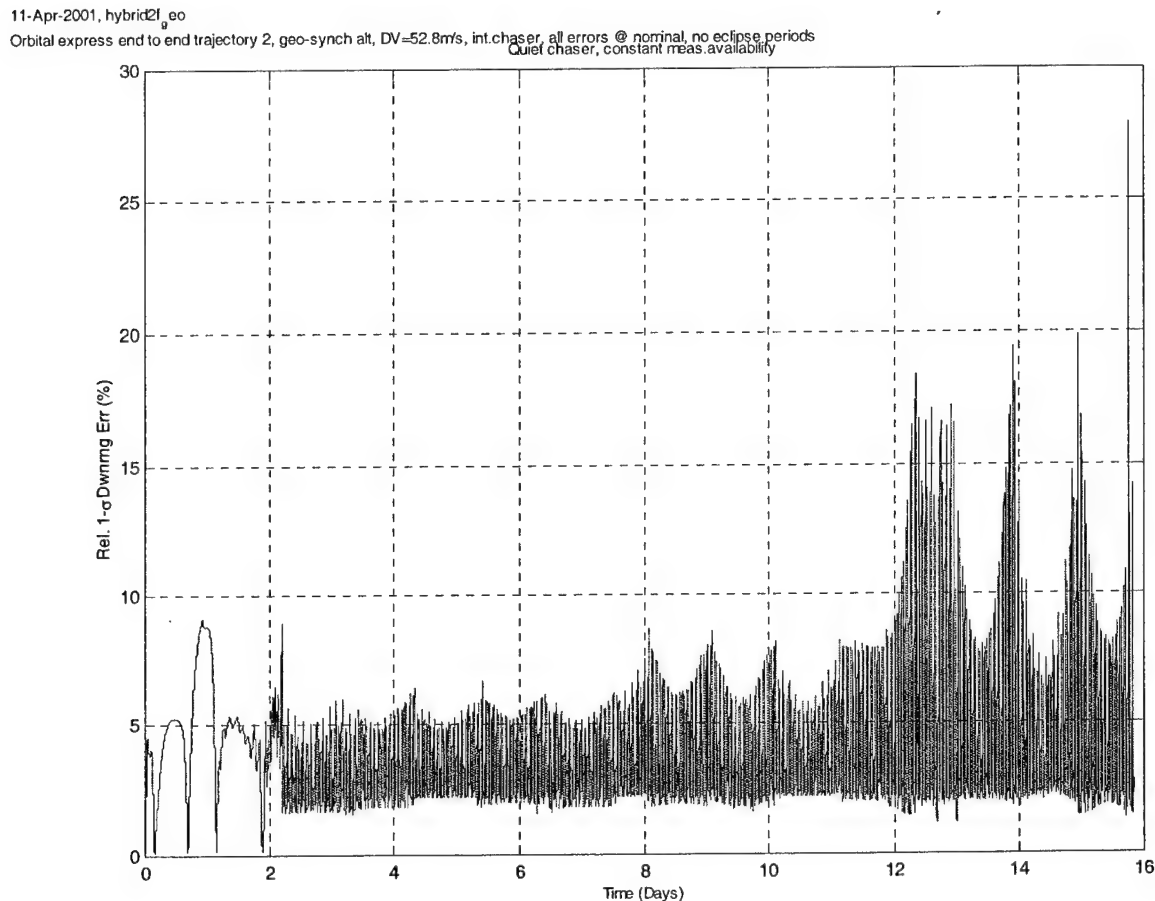


Figure 5-16: Geo-synchronous end-to-end trajectory results for quiet chaser with all errors at nominal values and constant measurement availability

6 CONCLUSIONS

6.1 SUMMARY OF RESULTS

This study addressed the use of angles-only navigation in orbital rendezvous and close approach situations. There are currently several potential missions which demand sensor suites that can safely and robustly achieve autonomous orbital rendezvous. Although there are a variety of sensors that can provide line-of-sight information to a target vehicle, relative navigation with line-of-sight sensors is usually not considered feasible since the range to the target along the line-of-sight can not be directly measured. This study proposes enhancing the performance of the relative angles-only navigation filter, specifically generating improved range observability, through a combination of two techniques. First, natural motion relative trajectories that involve a changing target-chaser line-of-sight improve estimation of all relative position components. Second, maneuvers are used to augment these trajectories to improve range observability, even in the presence of typical navigation error sources. The results show that, although there is still much work to be done, angles-only navigation using maneuvers-assisted trajectories is a promising method of achieving autonomous orbital rendezvous.

6.1.1 Natural Motion Navigation

The first set of results corresponded to the study of natural motion orbital trajectories. These showed that a lack of relative motion leads to unbounded downrange uncertainty growth when navigating with angles-only measurements. Relative line-of-sight geometry changes between the chaser and target allow this downrange error to be reduced over time, although this did not account for models such as un-modeled accelerations, attitude determination errors, or angular measurement biases. It was also shown that motion normal to the line-of-sight has similar effects on range observability regardless of the direction normal to the line-of-sight. Specifically, cross-track motion is just as effective as vertical motion and is actually more desirable since it is decoupled from in-plane motion. Another key observation from this study was that downrange navigation errors were reduced the most during flybys of the target. A study of the evolution of the navigation uncertainty ellipses over time also showed that they followed the natural motion of the line-of-sight between the target and chaser vehicles. This fact, coupled

with the positive effects of geometry changes lead to the conclusion that introducing maneuvers into the relative motion trajectory would improve angles-only navigation performance.

6.1.2 Maneuver-Assisted Navigation

The next set of results came from studying trajectories that incorporated maneuvers. The maneuvers were used to create typical rendezvous trajectories, such as R and V-bar approaches; as well as more un-conventional trajectories such as cross-track oscillations that shrank as the chaser approached the target, cross-track observation maneuvers, traveling footballs with naturally slowing closing rates, and even spirals. The results clearly demonstrated the benefit of performing maneuvers. Besides showing the trade-offs between navigation performance and fuel use, several suggested hybrid trajectories were created that combined the best characteristics of several different approaches.

6.1.3 Orbital Express Mission Analysis

The last portion of this study applied maneuver-assisted trajectories to the Orbital Express mission in the presence of realistic error models, in order to judge whether angles-only navigation was a viable method of helping to achieve orbital rendezvous. Several trajectories were designed and used for error sensitivity analyses. These cases demonstrated that well-chosen trajectories could lead to excellent navigation performance, even when subjected to large errors introduced in the form of process noise, IMU ΔV measurement, attitude determination, and angular measurements. In light of these results, the final conclusion is that angles-only navigation is an extremely promising method of relative navigation for rendezvous and close-approach applications.

6.2 FUTURE WORK

Although angles-only navigation seems to be viable, actually using the suggested maneuver-assisted trajectories in mission practice will require future studies involving higher fidelity modeling. This study attempted to capture the error sources that might be primary drivers of angles-only navigation degradation, but only additional study will ensure there are no undiscovered problems. In the near-term, four areas could be explored that could offer more insight into the problem and hopefully confirm that the techniques of maneuver-assisted trajectory design are sound.

6.2.1 Dispersion Analysis

As described in section 2.2.1, the LINCOV tool not only provides the navigation filter's uncertainty as to the state estimates, but can also provide the actual dispersions about the nominal states. This study focused only on the filtering aspects of angles-only navigation and used maneuver-assisted trajectories to make it effective. However, another part of the overall problem is the dispersions that would develop in real use. To fully characterize the performance of angles-only navigation, the maneuver-assisted reference trajectories need to be modeled with dispersions added onto them to ensure that the navigation performance is not significantly changed, and that the mission can be achieved in a dispersed environment.

6.2.2 Monte Carlo Analysis

Another, and arguably most definitive, verification technique is Monte Carlo analysis. The concepts and results put forth up to this point have been based on the results of LINCOV analysis. Therefore, a significant concern is whether or not there are potential non-linearities in the problem that may nullify some of the LINCOV results.

A Monte Carlo analysis could be performed by constructing a three degree-of-freedom simulation including an orbital environment model and sensor models corresponding to those used in the LINCOV tool. Rather than exhaustively studying all of the trajectories considered for LINCOV analysis, one or two of the trajectories used for the Orbital Express mission analysis could be subjected to Monte Carlo analysis. The results could readily support the LINCOV analysis' accuracy, or illustrate the need to revisit some of the assumptions made for this problem.

6.2.3 Formulation of problem in relative frame

Another attractive technique to approaching the angles-only problem would be to formulate the dynamics purely in a relative motion framework. In this study, both the target and chaser vehicle states were handled in inertial frames, and then the relative results were derived from this. An alternative approach would be to use the Clohessy-Wiltshire relative motion equations as the system dynamics, and then formulate the measurements and other error models in terms of these relative states. In mission practice, though, implementing a relative navigation filter would also require some type of sensor to determine the exact direction of the local vertical, just as the current study relies on a star tracker to determine inertial attitude. The motivation for this relative approach is the hope that it might lend itself to reducing the angles-only navigation problem to a

few analytic conditions that would need to be satisfied in order to guarantee range observability. This approach is similar to some of the methods discussed in section 4.1. Despite several brief attempts by the author to do exactly this, the desired results never materialized, but the potential ways to approach this problem are far from exhausted.

6.2.4 Observability Calculation

If the concept of having a purely analytic method of determining range observability in an angles-only environment does not work, another alternative is a semi-analytical method of calculating the observability matrix. As shown in [17], the observability matrix for a system can be calculated using

$$\mathbf{M}(t_0, t_1) \triangleq \int_{t_0}^{t_1} \Phi^T(\tau, t_0) \mathbf{H}^T(\tau) \mathbf{H}(\tau) \Phi(\tau, t_0) d\tau \quad (6.1)$$

Where the rank of the matrix \mathbf{M} determines the number of observable states. Therefore, a non-full rank observability matrix \mathbf{M} implies that one or more states is unobservable. This calculation is currently performed in the LINCOV analysis, however, the result is a 12x12 \mathbf{M} matrix corresponding to the inertial position and velocity of both target and chaser vehicles. Unfortunately, this matrix can not be manipulated into an equivalent 6x6 relative motion form. However, by reformulating the entire problem in a relative frame as described in section 6.2.3 and generating new Φ and \mathbf{H} matrices over the course of a relative motion trajectory, the corresponding \mathbf{M} matrix may contain useful information as to the observability problems in an angles-only system. Specifically, looking at the null space of the matrix \mathbf{M} would provide insight as to vector(s) in the state space would make the system strictly observable.

7 REFERENCES

- [1] Aidala, Vincent. "Kalman Filter Behavior in Bearings-Only Tracking Applications." *IEEE Transactions on Aerospace and Electronic Systems*. Vol. AES-15, No.1, pp.29-39, January 1979.
- [2] Bate, R., D.Mueller, J.White. *Fundamentals of Astrodynamics*. Dover Publications, Inc., New York, 1971.
- [3] Battin, Richard H. *An Introduction to the Mathematics and Methods of Astrodynamics, Revised Edition*. AIAA, Inc., United States, 1999.
- [4] Battin, Richard H. Course notes from "Astrodynamics I", MIT Course 16-346, 1999.
- [5] Brown, Robert and Patrick Hwang. *Introduction to Random Signals and Applied Kalman Filtering, 3rd Edt.* John Wiley and Sons, Inc., New York, 1997.
- [6] Casler, Richard J. "A Dual-Control Guidance Strategy for Homing Interceptors Taking Angle-Only Measurements." Charles Stark Draper Laboratory, Inc., P-433, Cambridge, Massachusetts, March 1977.
- [7] Chang, Chaw-Bing and John Tabaczynski. "Application of State Estimation to Target Tracking." *IEEE Transactions on Automatic Control*. Vol. AC-29, No.2, pp.98-109, February 1984.
- [8] Chang, C.B. "Ballistic Trajectory Estimation with Angle-Only Measurements." *IEEE Transaction son Automatic Control*. Vol. AC-25, No.3, pp.474-480, June 1980.
- [9] Dahleh, M.A. Class notes from "Dynamic Systems and Control", MIT Course 6-241, 1999.
- [10] Hepner, Stephen A. and Hans P. Geering. "Observability Analysis for Target Maneuver Estimation via Bearing-Only and Bearing-Rate-Only Measurements." *Journal of Guidance, Control, and Dynamics*. Vol.13, No.6, pp. 977-983. Nov-Dec 1990.
- [11] Gelb, A. *Applied Optimal Estimation*, MIT Press., Cambridge, MA, 1974.

- [12] "Guidance Systems." Litton Guidance and Control Systems [online], URL: <http://www.littongcs.com/products/2guidance/fiber/02description/overview.html> [cited 26 March 2001].
- [13] Kalman, R.E. "A New Approach to Linear Filtering and Prediction Problems," *Trans. ASME, Journal of Basic Engineering Series D*, Vol.83, pp 35-45, March, 1960.
- [14] Lear, William M. *Kalman Filtering Techniques*. NASA JSC Mission Planning and Analysis Division 85FM18 JSC-20688, September 1985.
- [15] Lear, William M. *Navigation at Mars Using Ground Transponders*. NASA JSC Mission Planning and Analysis Division 89-FM-8 JSC-23709, July 1989.
- [16] "Mars Observer Planetary Constants and Models." NASA JPL D-3444, November 1990.
- [17] Maybeck, Peter S. *Stochastic Models, Estimation, and Control, Volume 1*. Academic Press, Inc., New York, 1979.
- [18] Murphy, D.J., "Noisy Bearings-Only Target Motion Analysis." Ph.D. Dissertation, Department of Electrical Engineering, Northeastern University. Medford, MA, 1970.
- [19] "Orbital Express Space Systems Architecture/ASTRO." DARPA website [online], URL: <http://www.darpa.mil/tto/programs/astro.html> [cited 30 April 2001].
- [20] Nardone, Stephen C. and Vincent Aidala. "Observability Criteria for Bearings-Only Target Motion." *IEEE Transactions on Aerospace and Electronic Systems*. Vol. AES-17, No.2, pp.162-166, March 1981.
- [21] Papoulis, Athanasios. *Probability, Random Variables, and Stochastic Processes*, 3rd Edt. WCB/McGraw-Hill, Inc., Boston, 1991.
- [22] Sellers, JJ., W.Astore, K.Crumpton, C.Elliott, and R.Giffen. *Understanding Space, An Introduction to Astronautics*. McGraw-Hill, Inc., New York, 1994.
- [23] Song, Taek Lyul and Tae Yoon Um. "Practical Guidance for Homing Missiles With Bearings-Only Measurements." *IEEE Transactions on Aerospace and Electronic Systems*. Vol.32, No.1, pp. 434-443, January 1996.
- [24] "Star Trackers." Ball Aerospace [online], URL: <http://www.ball.com/aerospace/senst.html> [cited 26 March 2001].

- [25] Stoll, John C. "Performance Analysis of a GPS Interferometric Attitude Determination System for a Gravity Gradient Stabilized Spacecraft." Master of Science Thesis, Department of Aeronautics and Astronautics, MIT, May 1995.
- [26] Tse, Edison and Yaakov Bar-Shalom. "Adaptive Dual Control for Stochastic Nonlinear Systems with Free End-Time." IEEE Transactions on Automatic Control, pp. 670-675, October 1975.
- [27] Tse, Edison, Yaakov Bar-Shalom, and Lewis Meier III. "Wide-Sense Adaptive Dual Control for Nonlinear Stochastic Systems." IEEE Transactions on Automatic Control, Vol. AC-18, No.2, pp. 98-108, April 1973.
- [28] Vallado, David A. *Fundamentals of Astrodynamics and Applications*. McGraw-Hill, Inc., New York, 1997.
- [29] Vander Velde, Wallace E. Course notes from "Stochastic Estimation and Control", MIT Course 16-322, 2000.

[This page intentionally left blank]